Universidade de São Paulo
Instituto de Astronomia, Geofísica e Ciências Atmosféricas
Departamento de Ciências Atmosféricas

Anderson Augusto Bier

Changes in the South Atlantic Dipole and impacts on the climate of South America under the aspect of climate change (Alterações no Dipolo do Atlântico Sul e impactos sobre o clima da América do Sul sob o aspecto de mudanças climáticas)

São Paulo
2023

Anderson Augusto Bier

Changes in the South Atlantic Dipole and impacts on the climate of South America under the aspect of climate change (Alterações no Dipolo do Atlântico Sul e impactos sobre o clima da América do Sul sob o aspecto de mudanças climáticas)

Tese apresentada ao Departamento de Ciências Atmosféricas do Instituto de Astronomia, Geofísica e Ciências Atmosféricas da Universidade de São Paulo como requisito parcial para a obtenção do título de Doutor em Ciências.

Area de Concentração: Meteorologia
Orientador: Prof. Dr. Tercio Ambrizzi

Versão corrigida. O original encontra-se disponível na unidade

São Paulo

2023

Acknowledgements

I would like to express my gratitude to my advisor, Dr. Tercio Ambrizzi, for all the support and exchange of ideas throughout this journey. To my thesis defense committee members, Professors Simone, Rita, Anita, and Everaldo, for their valuable insights and observations that helped enhance this work.

To my family, who have been part of my life in São Paulo since I began my doctoral journey in 2018. My girlfriend, Izabella, and our cats, Dom and Soliclelson, for their unwavering support.

To my mother, Cristina, my father, Norberto (in memoriam), my brother Eduardo, sister-in-law Luciane, and my dear niece Milena.

To the University of SÃ£o Paulo, a renowned public institution that provided me with a rich academic environment and excellent infrastructure for the development of my research.

I would also like to acknowledge FAPESP for their financial support under project number 2018/06806-0.

Thank you all for your contributions and support.

Resumo

BIER, A. A., 2023. **Alterações no Dipolo do Atlântico Sul e impactos sobre o clima da América do Sul sob o aspecto de mudanças climáticas**. 2023. Tese (Doutorado) - Instituto de Astronomia, Geofísica e Ciências Atmosféricas, Universidade de São Paulo, São Paulo, 2023.

Nas últimas décadas, o Oceano Atlântico Sul (OAS) experimentou mudanças notáveis em suas características físicas devido às mudanças climáticas produzidas pelo homem. Essas mudanças abrangem vários aspectos como o aumento do vazamento de Agulhas, alterações na circulação oceânica induzida pelo vento, mudanças na salinidade e na temperatura da superfície do mar (TSM). Nesse contexto, o Dipolo do Atlântico Sul (DAS), o principal modo acoplado de variabilidade oceano-atmosfera na região, também pode sofrer alterações. Este estudo visa examinar as mudanças históricas no DAS (1851-presente) e suas projeções sob diferentes cenários futuros de aquecimento global (2015-2100), utilizando dados de reanálise e de saídas de modelos do CMIP6. A análise incorpora períodos associados às fases da Oscilação Interdecadal do Pacífico (OIP), que estão ligados à variabilidade climática no OAS, para avaliar as mudanças no DAS e os impactos climáticos resultantes na América do Sul durante o período histórico. Uma ênfase é dada para compreender a sazonalidade do DAS, em particular sua evolução durante o verão austral, quando o modo apresenta uma dinâmica importante com o clima sul-americano. As principais descobertas para o período histórico indicam um deslocamento para o sul de todo o padrão DAS, consistente com as mudanças oceânicas e atmosféricas observadas e atribuídas ao aquecimento global. Esta mudança é acompanhada por uma transição de um padrão tripolo para um dipolo de anomalias de precipitação sobre o continente sul-americano durante a

estação de verão. Adicionalmente, o DAS demonstra uma relação alternada com as fases do OIP, exibindo uma relação positiva (negativa) com as anomalias de TSM do Niño do Pacífico durante a fase negativa (positiva) do OIP. Quanto à representação do DAS pelos melhores modelos do CMIP6 durante o período histórico, eles geralmente captam as características essenciais dessa oscilação. Esses modelos reproduzem efetivamente recursos como a formatação do modo, período de oscilação e variabilidade sazonal. No entanto, não conseguem captar o sinal associado ao Niño do Atlântico (tipicamente acoplado ao DAS) e ao deslocamento para sul do DAS observado nas últimas décadas. Nos cenários climáticos futuros projetados pelos modelos CMIP6, os principais achados relativos ao DAS destacam uma intensificação das anomalias de TSM, pressão média do nível do mar (PNMM) e precipitação relacionada. Essas anomalias são mais pronunciadas no cenário SSP3-7.0. Além disso, os diferentes cenários sugerem que o DAS está associado a um padrão dipolo de precipitação entre o norte e o sudeste da América do Sul.

Palavras-chave: Dipolo do Atlântico Sul. Oscilação Interdecadal do Pacífico. Aquecimento global. CMIP6.

Abstract

BIER, A. A., 2023. **Changes in the South Atlantic Dipole and impacts on the climate of South America under the aspect of climate change**. Thesis (Doctorate) - Institute of Astronomy, Geophysics and Atmospheric Sciences, University of São Paulo, São Paulo, 2023.

Over the past few decades, the South Atlantic Ocean (SAO) has experienced notable changes in its physical characteristics due to human-induced climate change. These changes encompass various aspects such as increased Agulhas leakage, alterations in wind-driven ocean circulation, salinity shifts, and changes in sea surface temperature (SST). In this context, the South Atlantic Dipole (SAD), the main coupled ocean-atmosphere variability mode in the region, may also be subject to modifications. This study aims to examine the historical changes in the SAD (1851-present) and its projections under different future global warming scenarios (2015-2100), utilizing reanalysis data and outputs from the CMIP6 models. The analysis incorporates periods associated with the phases of the Interdecadal Pacific Oscillation (IPO), which are linked to climate variability in the SAO, to evaluate changes in the SAD and the resulting climate impacts on South America during the historical period.Emphasis is placed on understanding the SAD's seasonality, particularly its evolution during the austral summer when it exhibits important dynamics with the South American climate. Key findings for the historical period indicate a southward displacement of the entire SAD pattern, consistent with observed oceanic and atmospheric changes attributed to global warming. This shift is accompanied by a transition from a tripole to a dipole pattern of precipitation anomalies over the South American continent during the summer season. Additionally, the SAD demonstrates an alternating relationship with the

IPO phases, exhibiting a positive (negative) relationship with Pacific Niño SST anomalies during the IPO's negative (positive) phase. Regarding the representation of the SAD by the best CMIP6 models during the historical period, they generally capture the essential characteristics of this oscillation. These models effectively reproduce features such as the mode's characteristics, oscillation period, and seasonal variability. However, they fail to capture the signal associated with the Atlantic Niño (typically linked to the SAD) and the southward shift of the SAD observed in recent decades. In future climate scenarios projected by the CMIP6 models, the main findings concerning the SAD highlight an intensification of SST anomalies, mean sea level pressure (MSLP), and related precipitation. These anomalies are most pronounced under the SSP3-7.0 scenario. Additionally, the different scenarios suggest that the SAD is associated with a dipole pattern of precipitation between North and Southeast South America.

Keywords: South Atlantic Dipole. Interdecadal Pacific Oscillation. Global warming. CMIP6.

List of Figures

List of Tables

List of Abbreviations

20C3M	20th century climate scenario
AMOC	Atlantic Meridional Overturning Circulation
CEBR	central-eastern Brazil
CMIP	Coupled Model Intercomparison Project
CMIP6-HS	CMIP6 historical simulations
CPC	Climate Prediction Center
CPW	Circumpolar Water
DAS	Dipolo do Atlântico Sul
DJF	Dezembro-Janeiro-Fevereiro
ENSO	El Niño-Southern Oscillation
GCMs	general circulation models
GPCC	Global Precipitation Climatology Center
GYR	Guyanas region
IPCC	Intergovernmental Panel on Climate Change
IPO	Interdecadal Pacific Oscillation
IPO+	IPO positive phase
IPO-	IPO negative phase
ITCZ	Intertropical Convergence Zone
JJA	June-July-August
MAM	March-April-May
MSLP	mean sea level pressure
NNE	northern portion of Northeastern Brazil
NOAA	National Oceanic and Atmospheric Administration

NOAA-CIRES	NOAA-CIRES 20th Century V2c
OAS	Oceano Atlântico Sul
OIP	OscilaÃ§Ã£o Interdecadal do PacÃfico
ONI	Oceanic Niño Index
PCA	principal component analysis
PNMM	pressão ao nível médio do mar
PSL/NOAA	Physical Sciences Laboratory/NOAA
RCP	Representative Concentration Pathways
RMSE	root mean square error
SACZ	South Atlantic Convergence Zone
SAD	South Atlantic Dipole
SAD+	SAD positive phase
SAD-	SAD negative phase
SAO	South Atlantic Ocean
SASH	South Atlantic Subtropical High
ScenarioMIP	Scenario Model Intercomparison Project
SESA	southeastern South America
SCF	squared covariance fraction
SON	September-October-November
SPAs	Shared Climate Policy Assumptions
SSH	sea surface height
SSP	Shared Socioeconomic Pathways
SST	sea surface temperature
SVD	singular value decomposition
$SVD1_{MSLP}$	Expansion coefficient associated with the MSLP for the first mode of covariability
$SVD1_{SST}$	Expansion coefficient associated with the SST for the first mode of covariability
TPI	Tripole Index
TSM	temperatura de superfície do mar
WCRP	World Climate Research Programme

Contents

Chapter 1

Introduction

The South Atlantic Ocean (SAO) refers to the vast body of water situated in the southern hemisphere part of the Atlantic Ocean. A schematic representation of the average upper-level geostrophic circulation in the SAO, along with the main superficial currents, can be verified in Figure 1.1, after Peterson and Stramma (1991). In its most superficial layer, which directly interacts with the atmosphere, the SAO's tropical section consists of the Tropical Surface Water and the surface mixed layer (STRAMMA; ENGLAND, 1999). Moving southward beyond the Subantarctic Front near the latitude of 45°, the oceanic dynamics in the SAO are primarily influenced by the presence of Circumpolar Water (CPW), characterized by distinctive temperature and salinity properties that differ from those found in tropical regions.

Regarding to the importance of SAO to the global climate, it becomes essential to direct our attention towards understanding the dynamic interplay between the ocean and atmosphere in this specific region. A crucial approach to achieve this understanding is by analyzing the covariability modes that exist between these two fundamental components (ocean and atmosphere). In this context, the South Atlantic Dipole (SAD) represents the main mode of coupled variability observed over the SAO, which plays a relevant role in the interaction between the ocean and atmosphere on a climatic scale, exerting a special influence on neighboring areas like South America and Africa (BOMBARDI *et al.*, 2014; HAARSMA; CAMPOS; MOLTENI, 2003; NNAMCHI; LI; ANYADIKE, 2011; STERL; HAZELEGER, 2003; VENEGAS; MYSAK; STRAUB, 1997). This mode exhibits a distinct pattern characterized by a dipole of sea surface temperature (SST) anomalies between tropics and extratropics of the SAO (FAUCHEREAU *et al.*, 2003; STERL; HAZELEGER, 2003; VENEGAS; MYSAK; STRAUB, 1997). This oscillation occurs primarily on inte-

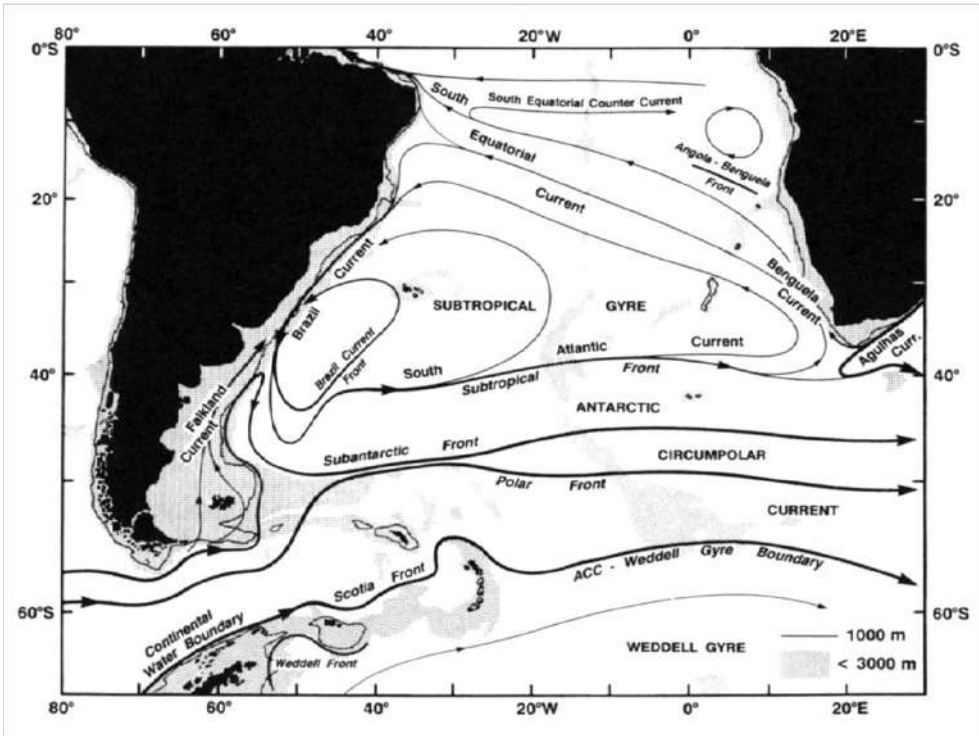

Figure 1.1: Large-scale currents and fronts over the South Atlantic Ocean. Source: Peterson and Stramma (1991).

rannual and interdecadal timescales. Furthermore, the observed dipole of SST anomalies interact with the just above South Atlantic Subtropical High (SASH) and its mean sea level pressure (MSLP) variations.

Haarsma, Campos and Molteni (2003) utilized numerical simulations to demonstrate that turbulent heat fluxes, Ekman transport, and wind-induced mixing within the surface layers of the ocean are the main drivers shaping the observed SAD pattern. Plus, Nnamchi, Li and Anyadike (2011) conducted research that confirmed the genuine nature of the SAD as a physical oscillation rather than a result of analysis techniques. However, it is worth noting that the SAD exhibits coupling with the Atlantic Niño at given moments, as noticed by Nnamchi, Li and Anyadike (2011) and Nnamchi *et al.* (2016). Morioka, Tozuka and Yamagata (2011) conducted a study employing both observational data and an ocean general circulation model to elucidate the important role of mixed layer depth in the growth and dissipation of SST anomalies at each pole of the mode. Their findings reveal that during the initial phase of development, the positive (negative) pole of the oscillation exhibits a shallower (deeper) mixed layer, thereby facilitating (impeding) heating and resulting in positive (negative) SST anomalies. Subsequently, during the decay phase,

the combined effects of net heat flux and entrainment work to restore the mixed layer anomalies. Still according to Morioka, Tozuka and Yamagata (2011), the growth phase of the SAD takes place in late austral spring, followed by its developed phase in summer, and finally, the decay phase in early autumn. Furthermore, Haarsma, Campos e Molteni (2003) identified that the most robust atmospheric response to the SAD occurs during the austral summer.

In this work, we define the positive (negative) SAD phase as being characterized by positive (negative) SST anomalies over the tropical pole and negative (positive) anomalies over the extratropical pole. Different studies define the SAD phases differently, with some following the same definition as presented here (e.g. BOMBARDI *et al.*, 2014), while others adopt the opposite definition (e.g. MORIOKA; TOZUKA; YAMAGATA, 2011). Considering this, SAD can be associated with several climatic features in the SAO surroundings. One significant atmospheric response to the SAD positive phase is the southward shift of the Atlantic Intertropical Convergence Zone (ITCZ) related rainfall, mainly during the austral autumn (KAYANO; ANDREOLI; FERREIRA DE SOUZA, 2013; NNAMCHI; LI, 2011). Conversely, during the negative phase, ITCZ precipitation areas tend to move northward. Over South American continent, SAD positive (negative) phase has been associated with less (more) rainfall during summer months in southeastern Brazil and rainier (drier) summers in northeastern Brazil (BOMBARDI; CARVALHO, 2011; BOMBARDI *et al.*, 2014). In this sense, Bombardi *et al.* (2014) have discovered that during neutral years of the El Niño-Southern Oscillation (ENSO), the negative phase of the SAD is associated with an increase in cyclogenesis near the southeastern coast of Brazil, as well as the migration of extratropical cyclone activity towards the north during the austral summer months. Consequently, this configuration promotes increased precipitation accumulation over the southeastern region of Brazil. These cyclones, along with their associated fronts, play a crucial role as key modulators of the South Atlantic Convergence Zone (SACZ). The SACZ, in its turn, accounts for the majority of rainfall in the warm months of the southern hemisphere, particularly over the Brazilian southeast and central-eastern regions (NUNES; VICENTE; CANDIDO, 2009). Plus, Bombardi and Carvalho (2011) discovered that the SAD positive phase is linked to delayed onsets of the rainy season in southeastern Brazil, while the negative phase is associated with early onsets in the same region. Conversely, northeastern Brazil experiences early onsets during the positive phase and late

onsets during the negative phase of the SAD. In the boreal summer monsoon season over the African continent, positive SST anomalies in the tropical Atlantic, which are linked to the SAD positive phase, have been found to be correlated with enhanced precipitation along the Guinea coast and reduced precipitation in the Sahel region (NNAMCHI; LI, 2011). Regarding the SASH, it has been observed that the negative phases of the SAD are associated with its intensification and southward displacement (FAUCHEREAU *et al.*, 2003; MORIOKA; TOZUKA; YAMAGATA, 2011).

In terms of the relationship between the SAD and the ENSO, Kayano, Andreoli and Ferreira de Souza (2013) have made noteworthy findings. They observed that during the periods of 1920-1930 and 1940-1980, the SAD positive (negative) phases tended to follow El Niño (La Niña) events by up to six months. However, in the period of 1975-2000, the SAD positive (negative) phase was seen to precede the onset of La Niña (El Niño) by up to one year. The authors propose that the ENSO is influenced by SAD through the Walker circulation. The positive (negative) SST anomalies in the tropical Atlantic, during the SAD positive (negative) phase, contributes to the persistence of convection, which leads to subsidence over the eastern equatorial Pacific region. This results in the strengthening (weakening) of surface divergence over this Pacific region and subsequently decreases (increases) the depth of the thermocline. These conditions create a favorable environment for the development of La Niña (El Niño) events within a timeframe ranging from three months to one year. Conversely, some studies (e.g. KAYANO; ANDREOLI, 2006; RODRIGUES *et al.*, 2011; RODRIGUES; CAMPOS; HAARSMA, 2015) have investigated and demonstrated that central Pacific ENSO conditions modulate the SAD through teleconnection patterns formed by stationary waves.

Lopez *et al.* (2016) have highlighted the influence of the Interdecadal Pacific Oscillation (IPO) on the sea surface height (SSH) variability of the SAO on an interdecadal timescale. They determine that approximately 45% of the SSH variability in the SAD can be attributed to the IPO. The first mode of SSH variability over the SAO exhibits similarities to the SAD summer pattern, that is shifted southward compared to the annual pattern. This SSH mode is predominantly characterized by low-frequency variability, operating on an interdecadal timescale. While it may contribute to the variability observed in the SAD, it is not directly linked to the higher frequencies of the oscillation. During the positive phase of the IPO, the jet streams over the subtropical SAO, around 40°S, is reinforced by

a stationary Rossby waves pattern originating in the Pacific. This strengthening facilitates a south-to-north Ekman transport in the underlying ocean, generating the characteristic dipole pattern of SSH anomalies in the SAO (LOPEZ *et al.*, 2016). Interestingly, the SSH dipole pattern also exhibits a significant correlation with the Atlantic Meridional Overturning Circulation (AMOC) at 30°S, suggesting the modulation of the AMOC by the IPO. Additionally, both the findings of Lopez *et al.* (2016) and Rodrigues, Campos and Haarsma (2015) indicate a pronounced remote influence of the Pacific region on the anomalous patterns observed in the SAO during the southern hemisphere summer. This influence is attributed to a weaker subtropical jet stream, which facilitates the propagation of wave energy flux during this time of the year.

In the context of anthropogenic global warming, there is growing interest in understanding the potential changes occurring in the SAO and their implications for the climate system. Recent observations have indicated modifications in the AMOC within the SAO, attributable to factors such as Agulhas Leakage reinforcement and increased melting of continental ice in Greenland (BEAL *et al.*, 2011). Furthermore, the SASH, which has a great interplay with both the AMOC and the SAD, has exhibited a poleward shift in recent decades (GILLILAND; KEIM, 2018). Climate projections for the future also suggest a similar trend of poleward displacement for the SASH in the coming century (REBOITA *et al.*, 2019). Still regarding to observed changes over the SAO, Vizy and Cook (2016) identified a cooling trend in SST over the subtropical SAO (18°S to 28°S) during the period of 1982-2013. This trend is due to the SASH poleward shifting according to the authors, which generate stronger winds and increased latent heat loss in this region of the SAO. These observed changes, combined with other atmospheric and oceanic factors associated with global warming, have the potential to influence the patterns of SST anomalies across the SAO, including the SAD. Consequently, these alterations may have implications for the complex interactions between the ocean and atmosphere in this region.

Given the evidence of changes in the SAO due to global warming in recent decades, there is a growing interest in understanding the behavior of this region under future climate scenarios. The international scientific community, through the Coupled Model Intercomparison Project (CMIP), plays a pivotal role in addressing these questions. The CMIP involves collaboration among numerous climate modeling centers worldwide, working together to develop sophisticated coupled general circulation models (GCMs) capable of

projecting future climate conditions (EYRING *et al.*, 2016). Currently, the project is in its sixth phase, known as CMIP6. Regarding the SAO, several studies have assessed the performance of models associated with the CMIP across its different phases. These evaluations have revealed a consistent issue in GCMs, wherein sea surface temperature (SST) over the Atlantic and Benguela Niños region tends to be overestimated (DAI, 2006; RICHTER; TOKINAGA, 2020). This overestimation of SST anomalies is often linked to the challenges faced by models in accurately representing upwelling areas. Specifically, over the Atlantic Niño region, a bias in westerly surface winds has been identified, which weakens the typical easterly winds and reduces upwelling, thereby leading to an overestimation of SST. Additionally, it has been suggested that this bias in westerly winds may be associated with excessive precipitation in the Atlantic ITCZ, which is also displaced southward during the austral autumn in GCMs (RICHTER; TOKINAGA, 2020). With regard to SAD, Bombardi and Carvalho (2011) carried out a study with ten CMIP3 models that showed that GCMs are able to reproduce general characteristics such as spatial pattern and periodicity of oscillation.

Considering all this context, it is essential to investigate whether there have been any alterations in the SAD, as the first mode of variability between the ocean and atmosphere in the SAO, in recent decades and under future global warming scenarios. Understanding the potential impact of these possible changes on the regional climate, specifically over South American continent in the case of present study, is of utmost importance. This thesis aims to address these questions by following the outlined structure:

- Material and Methods: Offers a concise description of the datasets and methodologies employed in the study.
- Results: It seeks to provide a comprehensive description of the findings concerning the SAD, encompassing both historical and future climate perspectives.
- Conclusions: Summarizes the main findings of the study and draws conclusive remarks.

By following this structured approach, this thesis aims to shed light on any potential changes in the SAD, the ocean-atmosphere interaction, and their subsequent impacts on the climate of the South American continent.

1.1 Objectives

1.1.1 General objectives

The primary aim of this study was to examine potential changes in the main mode of variability in the South Atlantic Ocean (SAO), known as the South Atlantic Dipole (SAD), and its impacts on South America climate. The investigation should encompass the historical period from the post-industrial revolution to the present day, as well as future projections under various global warming scenarios throughout the 21st century.

1.1.2 Specific objectives

- Determine potential changes in the SAD pattern over the last century and a half and under different future climate scenarios.
- Explore the atmospheric dynamics and precipitation patterns associated with the SAD over South America during the same time periods.
- Differentiate the influence of the SAD from other modes of variability on the climate of South America.
- Investigate potential connections between the SAD and the Interdecadal Pacific Oscillation (IPO) during the analyzed historical period.

Chapter 2

Material and methods

2.1 Observational data

2.1.1 Reanalysis datasets

This study utilizes monthly data from three reanalysis datasets to facilitate comparison and validation of the findings. The reanalysis datasets employed are NOAA-CIRES 20th Century V2c (COMPO *et al.*, 2011), ERA-20C (POLI *et al.*, 2016), and ERA5 (HERSBACH *et al.*, 2020). The NOAA-CIRES 20th Century V2c (hereinafter abbreviated as NOAA-CIRES) reanalysis provide data with a resolution of 2° for atmospheric variables and 1° for SST, spanning the period from 1851 to 2014. The ERA-20C reanalysis have a horizontal resolution of 125 km (T159) and cover the time range of 1911 to 2010. The ERA5 reanalysis dataset, with an approximate resolution of 30 km, covers the period from 1950 to 2020. In addition to the reanalysis data, monthly precipitation data from the Global Precipitation Climatology Center (GPCC) (SCHNEIDER *et al.*, 2011), with a resolution of 1°, were utilized for rainfall analysis. This precipitation dataset cover the period from 1901 to 2020.

2.1.2 El Niño - Southern Oscillation (ENSO)

The Oceanic Niño Index (ONI), obtained from the Climate Prediction Center (CPC) website (https://origin.cpc.ncep.noaa.gov/products/analysis_monitoring/ensostuff/ONI_v5.php), was utilized to identify ENSO events. The index is characterized by the three-month running mean of SST anomaly at Nino 3.4 (5°N-5°S, 120°W-170°W). An El Niño (La Niña) event is defined as the moment when 5 consecutive months exceed (fall below) 0.5°C (-0.5°C) in the ONI index. The CPC utilizes the ERSST.v5 dataset for the

computation of ONI index. The index span the period from 1950 to 2020, so ENSO events in ths work are considered only within this timeframe. In Figure 2.1, the graph illustrates the ONI values from 1950 to 2020. The red line represents the positive phase of ENSO oscillation (El Niño), while the blue line corresponds to the negative phase (La Niña). The black line indicates neutral ENSO conditions.

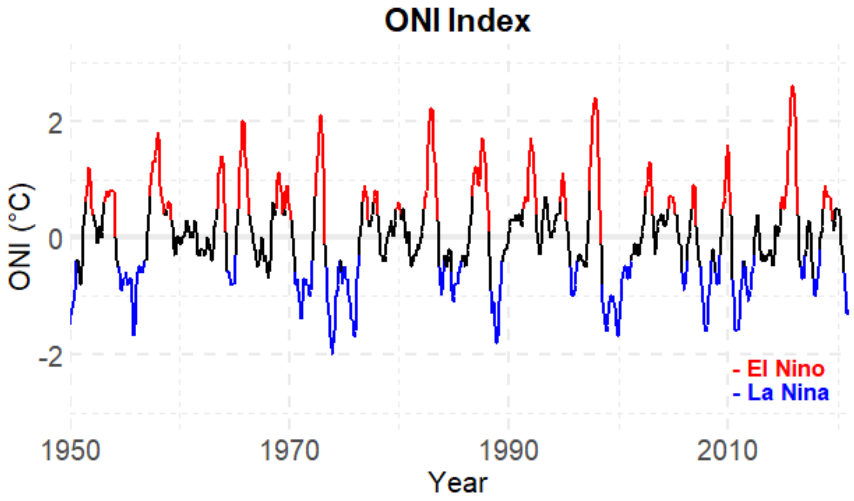

Figure 2.1: Monthly Oceanic Niño Index (ONI) between 1950 and 2020. Blue line denotes a negative ENSO phase (La Niña) and red line indicates a positive ENSO phase (El Niño).

2.1.3 *Interdecadal Pacific Oscillation (IPO)*

To consider the IPO, the Tripole Index (TPI) (HENLEY *et al.*, 2015) was used. The index data was obtained from the Physical Sciences Laboratory (PSL/NOAA) website (https://psl.noaa.gov/data/timeseries/IPOTPI/) and was calculated with the COBE-SST dataset (ISHII *et al.*, 2005). The TPI is defined as follows:

$$TPI = SST2_{anom} - \frac{SST1_{anom} + SST3_{anom}}{2} \tag{2.1}$$

Where, $SST1_{anom}$ is the mean SST anomaly over the northwest Pacific (25°N-45°N, 140°E-145°W), $SST2_{anom}$ is the mean SST anomaly over the central-equatorial Pacific east (10°S-10°N, 170°E-90°W) and the $SST2_{anom}$ is the mean SST anomaly over the southwest Pacific (50°S-15°S, 150°E-160°W). The SST data undergoes a preprocessing step where the seasonal cycle is first eliminated. After the TPI calculation, a 13-year Chebyshev low-pass filter is applied to derive the filtered version of the index.

Figure 2.2 displays the TPI Index, both unfiltered (represented by the dark line) and filtered (indicated by the blue and red lines based on the IPO phase), spanning from 1891

to 2020. Positive values signify the positive phase of the IPO (IPO+), while negative values indicate the negative phase (IPO-). In our analysis, we utilize the IPO phases identified by the filtered TPI as temporal markers. In this fashion, the time periods 08/1916-08/1923, 01/1943-03/1978, and 06/1997-12/2020 correspond to the IPO- phases, while the intervals 01/1891-07/1916, 09/1923-12/1942, and 04/1978-05/1997 represent the IPO+ phase. For the ease of reference, these time ranges are named as "IPO intervals" and will be henceforth denoted as: 1891-1916, 1916-1923, 1923-1942, 1943-1978, 1978-1997, and 1997-2020.

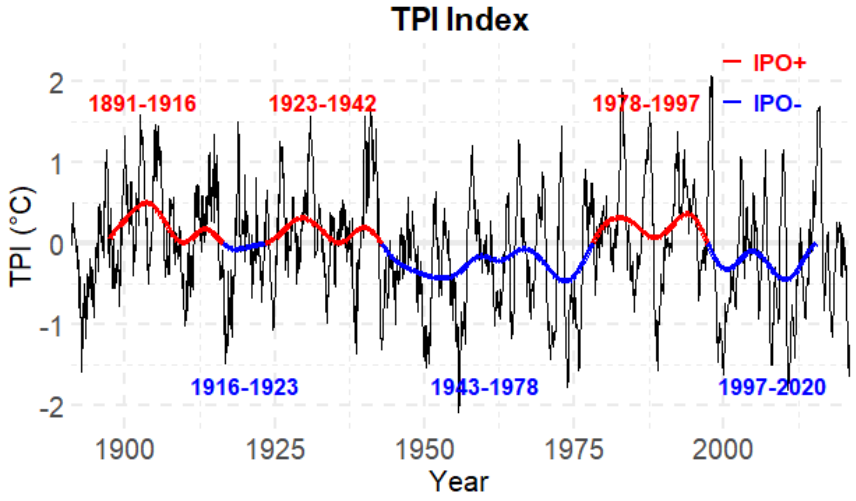

Figure 2.2: Unfiltered Tripole (TPI) index (dark line) and filtered TPI (blue and red line according to Interdecadal Pacific Oscillation [IPO] phase).

2.2 *Coupled Model Intercomparison Project phase 6 (CMIP6)*

The CMIP6 represents a globally coordinated endeavor in climate science, that aims to enhance our comprehension of climate system and project its future (EYRING *et al.*, 2016). The project is a central component in international assessments on climate change, such as the Intergovernmental Panel on Climate Change (IPCC) reports, and it is under the supervision of World Climate Research Programme (WCRP). One of the key objectives of the project is to make the multi-model output accessible to the broader climate community and users, presented in a standardized format that promotes comprehensive analysis.

In our study it was utilized outputs from 42 coupled GCMs within the CMIP6 framework, which are briefly described in Tables 2.1 and 2.2. Two sets of experiments were employed: CMIP6 historical simulations (CMIP6-HS), covering the data period from 1850 to 2014, and simulations representing distinct future climate scenarios (2015 to 2100), ba-

sed on different socioeconomic narratives, named Shared Socioeconomic Pathways (SSPs), and expected radiative forcings by the end of 21st century. The CMIP6-HS model outputs were utilized to assess the performance of the models in the study region (SAO and South America) and their ability to reproduce the SAD and its characteristics, which are the main focus of this study. In turn, CMIP6 future climate scenarios experiments were used to give us projections, based on different socioeconomic scenarios, of how the mode will behave and influence the climate throughout the 21st century.

2.2.1 CMIP6 Historical Simulations (CMIP6-HS)

According to Eyring *et al.* (2016), the CMIP6-HS comprises a set of model experiments requested from all participating models in the CMIP6. It spans a period from 1850 to 2014 and it builds upon pre-industrial control simulations, which serve as a baseline within the CMIP6. These simulations are forced by observed data and incorporate various external factors such as solar variability, volcanic aerosols, and changes in atmospheric composition (including greenhouse gases and aerosols) resulting from human activities. By utilizing the CMIP6-HS, we gain valuable insights into the capabilities of models to accurately simulate climate, encompassing both short-term variability and long-term trends spanning a long period of time. This, in turn, enables us to validate CMIP6 models for the use of future climate scenarios outputs generated by corresponding GCMs.

2.2.2 Future climate scenarios

The Scenario Model Intercomparison Project (ScenarioMIP) (O'NEILL *et al.*, 2016) is an important component within the broader scope of CMIP6, comprising 21 endorsed projects. Its main objective is to develop a range of scenarios depicting the future global climate. These scenarios are generated using integrated assessment models (IAMs) and based on different narratives of future emissions and land use changes, the SSPs. These are a set of plausible socioeconomic narratives for the course of the 21st century, formulated by the international climate change research community (O'NEILL *et al.*, 2017).

According to Böttinger and Kasang (2020), there are five distinct narratives which are used as basis for the construction of these scenarios, each one containing alternative socio-economic developments. These narratives encompass themes such as sustainable development, regional competition, inequality, fossil-fueled growth and moderate develop-

Table 2.1 - The 42 CMIP6 Coupled General Circulation Models (GCMs) utilized in this work.

Model name	Country	Atmospheric model (AM)	AM approx. horizontal res.	AM vert. levels	Oceanic model (OM)	OM approx. horizontal res.	OM Vertical levels
ACCESS-CM2	Australia	MetUM-HadGEM3-GA7.1	250 km	85	ACCESS-OM2 GFDL-MOM5	100 km	50
ACCESS-ESM1-5	Australia	HadGAM2 r1.1	250 km	38	ACCESS-OM2 MOM5	100 km	50
BCC-CSM2-MR	China	BCC_AGCM3_MR	100 km	46	MOM4	50 km	40
BCC-ESM1	China	BCC_AGCM3_LR	250 km	26	MOM4	50 km	40
CAMS-CSM1-0	China	ECHAM5_CAMS	100 km	31	MOM4	100 km	50
CanESM5	Canada	CanAM5	500 km	49	NEMO3.4.1 ORCA1	100 km	45
CESM2	USA	CAM6	100 km	32	POP2	100 km	60
CESM2-FV2	USA	CAM6	250 km	32	POP2	100 km	60
CESM2-WACCM	USA	WACCM6	100 km	70	POP2	100 km	60
CESM2-WACCM-FV2	USA	WACCM6	250 km	70	POP2	100 km	60
CIESM	China	CIESM-AM FV/FD	100 km	30	CIESM-OM FD	50 km	46
CMCC-CM2-SR5	Italy	CAM5.3	100 km	30	NEMO3.6 ORCA1	100 km	50
CMCC-ESM2	Italy	CAM5.3	100 km	30	NEMO3.6 ORCA1	100 km	50
E3SM-1-0	USA	EAM v1.0	100 km	72	MPAS-Ocean v6.0	50 km	60
E3SM-1-1	USA	EAM v1.1	100 km	72	MPAS-Ocean v6.0	50 km	60
E3SM-1-1-ECA	USA	EAM v1.1	100 km	72	MPAS-Ocean v6.0	50 km	60
EC-Earth3	European countries	IFS cy36r4	100 km	91	NEMO3.6 ORCA1	100 km	75
EC-Earth3-AerChem	European countries	IFS cy36r4	100 km	91	NEMO3.6 ORCA1	100 km	75
EC-Earth3-CC	European countries	IFS cy36r4	100 km	91	NEMO3.6 ORCA1	100 km	75
EC-Earth3-Veg	European countries	IFS cy36r4	100 km	91	NEMO3.6 ORCA1	100 km	75
EC-Earth3-Veg-LR	European countries	IFS cy36r4	250 km	62	NEMO3.6 ORCA1	100 km	75
FGOALS-f3-L	China	FAMIL2.2	100 km	32	LICOM3.0	100 km	30
FGOALS-g3	China	GAMIL3	250 km	26	LICOM3.0	100 km	30
FIO-ESM-2-0	China	CAM4	100 km	26	POP2-W	100 km	60
GFDL-ESM4	USA	GFDL-AM4.1	100 km	49	GFDL-OM4p5 GFDL-MOM6	50 km	75

Table 2.2 - Continuation of table 2.1.

Model name	Country	Atmospheric model	AM approx. horizontal res.	AM vert. levels	Oceanic models	OM approx. horizontal res.	OM Vertical levels
GISS-E2-1-G	USA	GISS-E2.1	250 km	40	GISS Ocean GO1	100 km	40
GISS-E2-1-H	USA	GISS-E2.1	250 km	40	HYCOM Ocean	100 km	32
INM-CM4-8	Russia	INM-AM4-8	100 km	21	INM-OM5	100 km	40
INM-CM5-0	Russia	INM-AM5-0	100 km	73	INM-OM5	50 km	40
IPSL-CM5A2-INCA	France	LMDZ APv5	500 km	39	NEMO-OPA v3.6	250 km	31
IPSL-CM6A-LR	France	LMDZ NPv6	250 km	79	NEMO-OPA eORCA1.3	100 km	75
IPSL-CM6A-LR-INCA	France	LMDZ NPv6	250 km	79	NEMO-OPA eORCA1.3	100 km	75
KACE-1-0-G	South Korea	MetUM-HadGEM3 -GA7.1	250 km	85	MOM4p1	100 km	50
KIOST-ESM	South Korea	GFDL-AM2.0	250 km	32	GFDL-MOM5.0	100 km	52
MCM-UA-1-0	USA	R30L14	250 km	14	MOM1.0	250 km	18
MIROC6	Japan	CCSR AGCM	250 km	81	COCO4.9	100 km	63
MPI-ESM-1-2-HAM	Germany	ECHAM6.3	250 km	47	MPIOM1.63	250 km	40
MPI-ESM1-2-HR	Germany	ECHAM6.3	100 km	95	MPIOM1.63	50 km	40
MPI-ESM1-2-LR	Germany	ECHAM6.3	250 km	47	MPIOM1.63	250 km	40
MRI-ESM2-0	Japan	MRI-AGCM3.5	100 km	80	MRI.COM4.4	100 km	61
NESM3	China	ECHAM6.3	250 km	47	NEMO v3.4	100 km	46
TaiESM1	Taiwan	TaiAM1	100 km	30	POP2	100 km	60

ment. However, the long-term demographic and economic projections associated with the SSPs exhibit a broad range of uncertainty. Complete description on how theses scenarios were developed can be found in (O'NEILL *et al.*, 2017). Here, they are briefly summarized as follows:

- SSP1: Sustainability - The humanity gradually becomes more sustainable, respecting environmental boundaries. The demographic transition is accelerated due investments in education and health, which contribute to a lower worldwide population. The economic focus gradually shifts from growth to human well-being. Inequality is reduced across and within countries, aided by environmental technology and changes in tax structures. Renewable energy becomes more attractive, and material and

resource comsumption is reduced. All this results in manageable challenges for mitigation and adaptation, while improving human well-being.

- SSP2: Middle of the Road - The world's trajectory remains largely consistent with historical patterns in terms of social, economic, and technological trends.

- SSP3: Regional Rivalry - Countries increasingly focus on domestic or regional issues due to the resurgence of nationalism. Concerns relate to competitiveness, security and ongoing regional conflicts.

- SSP4: Inequality - Uneven allocation of resources towards human capital development, together with growing gaps in economic opportunities and political influence, result in escalating inequalities and stratification, affecting both national and individual levels.

- SSP5: Fossil-fueled Development - Motivated by the economic achievements of both industrialized nations and emerging economies, this global landscape places growing trust in competitive markets, innovation, and inclusive societies. It believes that these factors will foster swift technological advancements and human capital development, ultimately paving the way for sustainable development. Simultaneously, the pursuit of economic and social progress is accompanied by the utilization of abundant fossil fuel reserves and the adoption of resource and energy-intensive lifestyles worldwide. Although local environmental issues are effectively tackled through technological advancements, there is a notable lack of emphasis on mitigating potential global environmental impacts. This is attributed to a perceived tradeoff between economic development progress and the need to address these global concerns.

Subsequently, these narratives underwent a transformation from qualitative descriptions to quantitative projections. This was implemented through the use of quantitative models to consider demographic and economic drivers, and through the use of IAMs to elaborate the developments in the energy system, land use and greenhouse emissions. By doing so, it was found that in the absence of supplementary climate protection measures, the SSP1 and SSP2 would result in an additional radiative forcing ranging from $5W/m^2$ and $6.5W/m^2$ for the year 2100 (RIAHI *et al.*, 2017). In this way, pathways outlined in the CMIP5 Representative Concentration Pathways (RCP) scenarios (VAN VUUREN *et al.*,

2011) could not be reproduced by the SSPs scenarios and the climate target of $2.6W/m^2$, that corresponds to stipulated temperature change limit of 2°C for the end of 21st century (SCHELLNHUBER; RAHMSTORF; WINKELMANN, 2016), could not be reached. At first, the SSPs lacked climate policies that went beyond the existing measures and did not consider the requirement to implement adaptation strategies in light of the ongoing climate change. To address this, Shared Climate Policy Assumptions (SPAs) (KRIEGLER *et al.*, 2014) were developed. These SPAs outline varying levels of political endeavors aimed at mitigating and adapting to climate change.

To build the SSP scenarios (future climate scenarios), three different conditions were considered. These conditions include the level of climate change (represented by the intensity of additional radiative forcing resulting from human-induced greenhouse gas effects at the end of century), the different socioeconomic pathways (SSP1-SSP5) and, if necessary, SPAs were taken into account. The level of climate change factor, measured in terms of radiative forcings, was relatively aligned with the RCP scenarios (RCP2.6, RCP4.5, RCP6.0, and RCP8.5), with other additional classes included according to specific interests of climate science community.

Unlike the RCP scenarios, the new scenarios based on SSPs provide economic and social justifications for the assumed emission pathways and changes in land use. Moreover, they incorporate updated historical emissions of greenhouse gases and aerosols, as well as changes in land use, while employing improved IAMs.

As part of the ScenarioMIP initiative, a consensus was reached on four standard scenarios globally. Thus, the scenarios are named SSPi-$x.x$, where SSPi corresponds to each of the five different SSPs narratives described above, and $x.x$ is the radioactive forcing in watts per square meter by the year 2100. This way, the four scenarios are described as follow:

- SSP1-2.6: This scenario, aiming to match the 2°C target, represents a revised version of the optimistic RCP2.6 scenario. It projects a radiative forcing of $2.6W/m^2$ by the end of 21st century. Similar to its predecessor, this scenario assumes the implementation of climate protection measures (SPAs are attributed).

- SSP2-4.5: As a revision of the RCP4.5 scenario, SSP2-4.5 represents a moderate course for future greenhouse gas emissions, projecting an additional radiative forcing

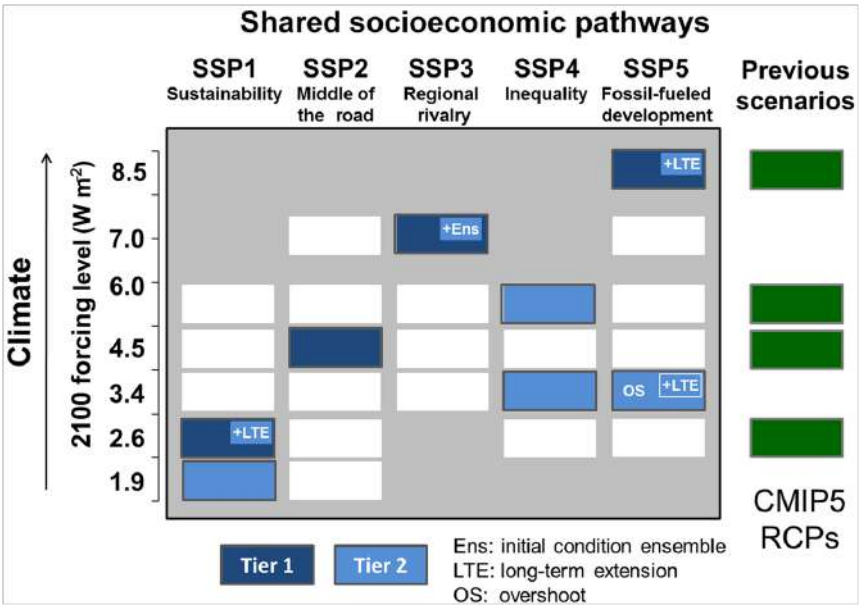

Figure 2.3: SSP-RCP scenario matrix, illustrating the various combinations of socioeconomic development pathways (SSPs) and climate outcomes based on feasible forcing pathways. Each cell within the matrix represents a specific scenario, with dark blue cells denoting the Tier 1 SSPs utilized in this study. Light blue cells represent Tier 2 scenarios (not employed here). Source: O'Neill *et al.* (2016).

of $4.5W/m^2$ by the year 2100. This scenario assumes the implementation of SPAs.

- SSP3-7.0: This scenario, projecting a radiative forcing of $7W/m^2$, falls within the upper-middle segment of the spectrum of scenarios. It was introduced during the CMIP6, aiming to fill a gap between CMIP5 RCP6.0 and RCP8.5 scenarios.

- SSP5-8.5: With an additional radiative forcing of $8.5W/m^2$ by the year 2100, this scenario represents the upper boundary of the range of scenarios described in the literature. It can be understood as an update of the CMIP5 scenario RCP8.5, now combined with socioeconomic reasons.

These five scenarios are referred to as "Tier 1" experiments in the matrix depicted in Figure 2.3, retrieved from O'Neill *et al.* (2016), which combines the five pathways with the varying climate forcings.

Figure 2.4 illustrates the temporal progression (1960-2100) of CO_2 emissions and concentration, anthropogenic radiative forcing and the temperature change. The observed data spans from 1960 to the present, while the projections from 2015 onwards are derived from various SSPs of ScenarioMIP, including the specific scenarios employed in this work (SSP1-2.6, SSP2-4.5, SSP3-7.0, and SSP4-8.5). When compared to the preindustrial le-

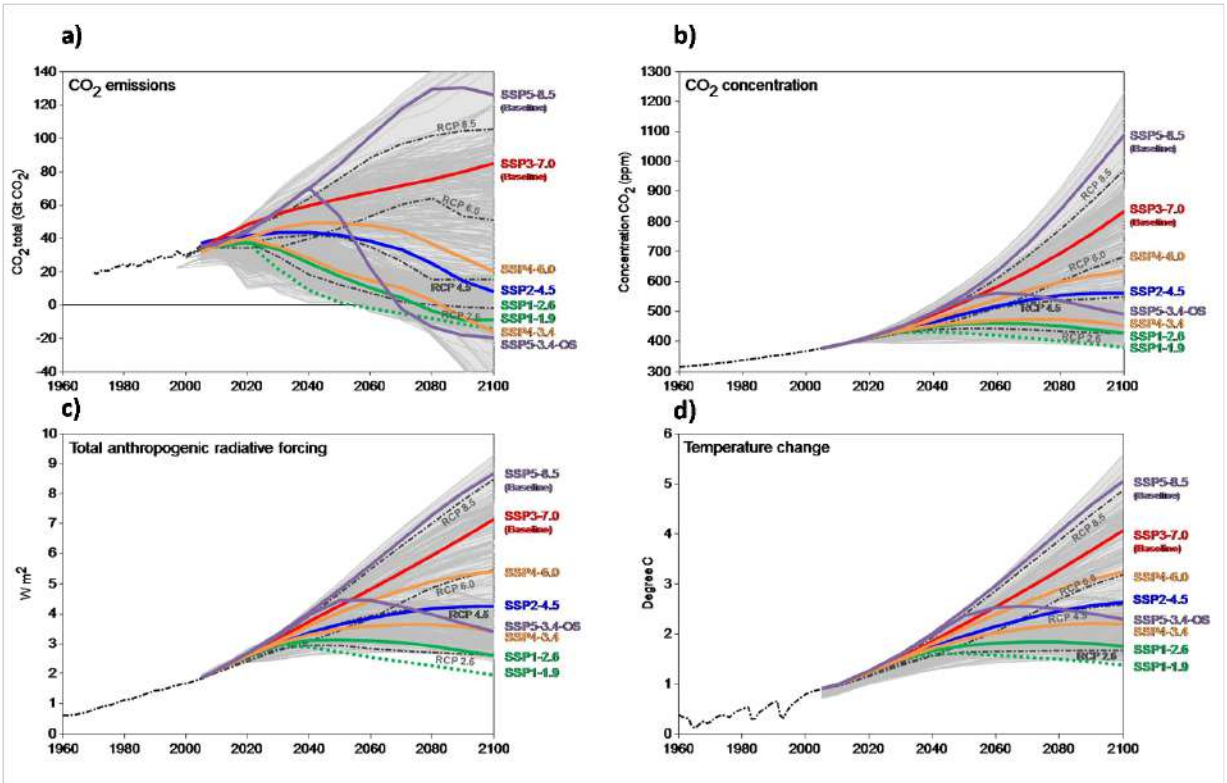

Figure 2.4: Trends of CO_2 a) emissions, b) CO_2 concentrations, c) anthropogenic radiative forcing and d) global mean temperature for the different SSPs over the 21st century. The shaded areas indicate the range of scenarios encompassed within the scenarios database for the IPCC Fifth Assessment Report. Source: O'Neill *et al.* (2016).

vel, the current radiative forcing has increased by approximately $2.5W/m^2$ (Figure 2.4c). The SSPs scenarios assume that these values will range from $2.6W/m^2$ (increase of only $0.1W/m^2$) to $8.5W/m^2$ (increase of $6W/m^2$) at the end of the century.

Analyzing the global CO_2 emission trajectories across various SSPs (Figure 2.4a), it is noticeable that achieving a temperature increase limit of 2°C by the end of the century, as verified in the SSP1-2.6 scenario, necessitates immediate and substantial reductions in emissions. Plus, to meet this objective, a global average that includes negative emissions must be achieved no later than 2075.

2.3 Methods

2.3.1 Singular value decomposition (SVD)

The coupled oscillation pattern of the SAD is obtained using the singular value decomposition (SVD) method applied to the SST and MSLP data. The SVD method, as

described by Björnsson *et al.* (2011), is employed to identify covariability patterns between two variables. This method is commonly used in climate science to analyze the relationship between MSLP and SST (e.g. BOMBARDI *et al.*, 2014; HAARSMA; CAMPOS; MOLTENI, 2003; STERL; HAZELEGER, 2003; VENEGAS; MYSAK; STRAUB, 1997). Through the utilization of SVD, this analysis identifies pairs of spatial patterns that exhibit coupled variability and their corresponding temporal variations. Prior to the SVD calculation, the SST and MSLP data series are preprocessed by removing their annual cycles and employing LOESS regression (CLEVELAND; GROSSE; SHYU, 1992) to eliminate long-term nonlinear trends.

To exemplify the SVD method, let's consider a space-time matrix for the variables under study. We have a matrix $[S]$ representing the SST data and another matrix $[M]$ representing the MSLP data. The $[S]$ matrix has t rows and s columns, where each column represents a SST time series (ranging from 1 to t) at a particular grid point (ranging from 1 to s). Similarly, the matrix $[M]$ consists of t rows representing the time series of MSLP data, and m columns corresponding to different grid points. Both the $[S]$ and $[M]$ matrices are time-centered, meaning that they contain anomalies relative to the temporal average at each grid point.

This analysis can be done with the variables covering different areas ($m \neq s$ or $m = s$ is accepted), but necessarily they need to cover the same period of time t. The first step is to calculate the covariance matrix $[C]$ between the two variables:

$$[C]_{(s\times m)} = [S]^T_{(s\times t)}\,[M]_{(t\times m)} \tag{2.2}$$

Unlike the principal component analysis (PCA) method, the covariance matrix can be rectangular, since the $[S]$ and $[M]$ data can cover different areas with different amounts of grid points. At this point, it is worth noting that in some cases it is preferable to divide each time series by its standard deviation, which turns the covariance matrix $[C]$ into a correlation matrix $[R]$. Some researchers choose to use the matrix $[R]$ instead of $[C]$, because one variable may show greater temporal variation in relation to the other, causing the variability in a given field to dominate the covariance structure between the matrices.

The process of SVD involves determining the matrices $[U]$, $[V]$, and the diagonal matrix $[L]$, which satisfy the following relationship:

$$[C]_{(s\times m)} = [U]_{(s\times s)}\,[L]_{(s\times m)}\,[V]^T_{(m\times m)} \tag{2.3}$$

Where the matrix $[U]$ is formed by the singular vectors of $[S]$ (representing SST data), while the matrix $[V]$ comprises the singular vectors of [M] (representing MSLP data), which are equivalent to the eigenvectors in PCA. In the matrices $[U]$ and $[V]$, every row among the s (m) rows corresponds to a distinct grid point, while each column represents a singular vector u_i (v_i). In simpler terms, these columns signify s (m) modes of variability, capturing different patterns of variability within the dataset. Each pair of singular vectors represents a mode of covariability between the spatiotemporal matrices of $[S]$ and $[M]$. The diagonal matrix $[L]$ consists of the singular values (comparable to the eigenvalues in PCA). The total squared covariance of the matrix $[C]$ is determined by summing the diagonal values of $[L]$.

The matrices of expansion coefficients of $[S]$ and $[M]$ (SST and MSLP anomaly matrices) are obtained by projecting the singular vectors onto the original field of the corresponding variable. For the matrix $[S]$ is given:

$$[A]_{(t\times s)} = [S]_{(t\times s)}\,[U]_{(s\times s)} \tag{2.4}$$

For the $[M]$ (MSLP anomaly matrix) we have:

$$[B]_{(t\times m)} = [M]_{(t\times m)}\,[V]_{(m\times m)} \tag{2.5}$$

The columns of $[A]$ and $[B]$ contain the expansion coefficients (a_i and b_i) of each mode, which show the temporal behavior of each of the s singular vectors (or modes of variability) associated with $[S]$ matrix, and each of the m singular vectors related with $[M]$ matrix. Since we apply this method to SST ($[S]$) and MSLP ($[M]$) data, for convenience these coefficients are called $\mathrm{SVDi}_{\mathrm{SST}}$ (a_i) $\mathrm{SVDi}_{\mathrm{MSLP}}$ (b_i) from now on, according to its i covariability mode. The total squared covariance in the matrix $[C]$ is also given by the sum of the elements l_i of the diagonal of the matrix $[L]$. In this way, the squared covariance fraction (SCF) that explains each i mode is performed as follows:

$$SCF_i = \frac{{l_i}^2}{\sum {l_i}^2} \tag{2.6}$$

Each squared covariance fraction (SCF_i) corresponds to a pair of singular vectors u_i and v_i. The first covariability mode ($\mathrm{SVD1}_{\mathrm{SST}}$ and $\mathrm{SVD1}_{\mathrm{MSLP}}$) is the one with the highest SCF value, followed by the second ($\mathrm{SVD2}_{\mathrm{SST}}$ and $\mathrm{SVD2}_{\mathrm{MSLP}}$), third ($\mathrm{SVD3}_{\mathrm{SST}}$ and $\mathrm{SVD3}_{\mathrm{MSLP}}$) and so on. For each mode, we can plot the pair of singular vectors on a map in order to

verify which is the coupled pattern of variability of the two variables in question. As well as we can evaluate the expansion coefficients SVDi_{SST} (for SST) and $\text{SVDi}_{\text{MSLP}}$ (for MSLP) to verify how these patterns behave in time. Wavelet analysis (TORRENCE; COMPO, 1998) is eventually utilized to examine the time series of expansion coefficients (SVDi_{SST} and $\text{SVDi}_{\text{MSLP}}$), providing insights into the periodicity and temporal variations of the mode of covariability.

There are other ways to plot the spatial patterns corresponding to the SVD besides plotting the singular vectors by themselves. Björnsson *et al.* (2011) mention that the amplitudes of the plots, in the case of singular vectors, are not easy to interpret. A widely used option is the homogeneous correlation between the coefficient of expansion (SVDi_{SST} and $\text{SVDi}_{\text{MSLP}}$) of the ith variability mode and the time series at each grid point of the field of variables (matrices $[M]$ and $[S]$).

The SVD analysis is conducted within a spatial domain spanning from 5°N–45°S and 20°E–60°W (Figure 2.5), encompassing a important portion of the SAO situated north of the Subantarctic Front. This specific domain, as recommended by Nnamchi, Li and Anyadike (2011), is chosen due to its relevance. The northern boundary of the domain extends into the northern hemisphere, as the meteorological equator, marked by the position of the maximum SST and the minimum MSLP, resides north of the geographical equator. When considering interacting oceanic and atmospheric variables, such as SST and MSLP, the first mode of covariability within the designated domain is the SAD.

2.3.2 South Atlantic Dipole phases

To identify the positive and negative phases of the SAD, thresholds based on percentiles were applied to the expansion coefficient time series associated with the SST anomalies (referred to as SVD1_{SST}) obtained from the SVD analysis (e.g. BOMBARDI *et al.*, 2014). Specifically, values falling below the 25th percentile of the time series are classified as the SAD negative phase (SAD-), while values surpassing the 75th percentile are categorized as the SAD positive phase (SAD+).

2.3.3 Analysis intervals

In order to explore potential changes in the SAD over time, it was necessary to conduct analyses within specific time intervals. These intervals should be sufficiently wide to

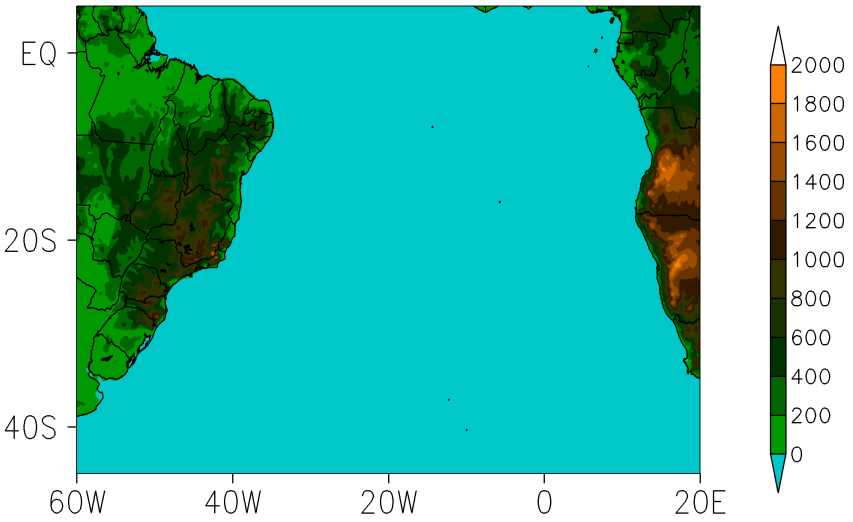

Figure 2.5: Spatial domain used to identify the covariability modes with the Singular Value Decomposition (SVD). The figure shows the relief, with altitude described in meters.

capture the periods of oscillation, while also allowing for the detection of any important variations. Previous studies, such as Lopez *et al.* (2016), have highlighted the significant influence of the IPO on the AMOC at interdecadal timescales. As discussed earlier in the introduction, the IPO affects the SASH circulation, which subsequently impacts the AMOC through teleconnections. This suggests a plausible connection between the IPO and the SAD, given the inherent relationship between the SAD and SASH on interdecadal timescales. Furthermore, findings from Kayano, Andreoli and Ferreira de Souza (2013) also suggest a potential relationship between the SAD and the IPO.

Given that the IPO exhibits periods that coincide with the spectral peaks of the SAD and may share a relationship with it, it is appropriate to utilize time intervals associated with each phase of the IPO for conducting analyses related to the SAD. In this context, the phase intervals derived from the filtered TPI index (Figure 2.2), that is 1891-1916, 1916-1923, 1923-1942, 1943-1978, 1978-1997 and 1997-2020 were employed in our analyses. These intervals are adequated to assess the temporal evolution of the SAD and its associated atmospheric and oceanic dynamics. This approach also enables us to evaluate potential links between the IPO and the SAD while considering their respective phase intervals. It is important to note that due to variations in the available datasets and their respective time coverage, these intervals have been chosen to align with the limitations of the data's

full periods.

In order to examine the future period using data from CMIP6 future climate scenarios (2015-2100), specific time intervals were utilized: 2015-2040, 2041-2070, and 2071-2100. These intervals were chosen to serve a similar purpose as the "IPO intervals", but without any direct association with the IPO. Hence, they are referred to as the "SSPs intervals" in reference to SSPs scenarios (2.2.2).

2.3.4 Composites

To elucidate the ocean-atmosphere interaction linked to the SAD oscillation, anomalous fields of various climatic variables were computed for different SAD phases. The objective was to understand the specific dynamics associated with this oscillation. In some cases, to isolate the influence of external factors, analyses were conducted excluding ENSO events (considering only months with neutral conditions as depicted in Figure 2.1). In these cases, only post-1950 data are considered, since there is no ONI index for previous periods. Considering a grid point within a spatial field, composite calculations were employed following the approach outlined below:

$$\bar{V}_i = \frac{1}{n} \sum_{t=1}^{n} v_{t,i} \tag{2.7}$$

Where, $\bar{V}i$ represents the temporal average of a variable at a specific grid point(i) within a defined phase of the SAD. The total number of months where the designated condition (either SAD positive or negative phase in this context) was observed over time is denoted by n. Each $v_{t,i}$ signifies a temporal value associated with the specified condition at the given grid point. Notably, the $v_{t,i}$ values for a particular variable are time-centered, indicating that they represent anomalies relative to the temporal average at each grid point. Thus, $\bar{V}_i$ represents the average of anomalies under a specific condition (SAD phase). To assess the statistical significance of the anomalies, all $\bar{V}_i$ undergo the Student's-T test at a 95% confidence level.

2.3.5 Forecast skill

For a better computation of the analyses with CMIP6 models (Tables 2.1 and 2.2), a selection of the best models was performed. This happened through root mean square

error (RMSE). According to Déqué (2007), the RMSE is described as follows:

$$RMSE = \sqrt{\frac{1}{N}\sum_{n=1}^{N}\left(V_{est_{i,j}} - V_{obs_{i,j}}\right)} \tag{2.8}$$

Where N is the number of data observations, V_{est_i} is the estimated value and V_{obs_i} is the observational value.

In our calculations the observational values (V_{est_i}) were derived from the SST and MSLP data obtained from reanalyses (NOAA-CIRES, ERA-20C and ERA5), while the estimated values were obtained from corresponding variables of the CMIP6-HS experiment derived from each CMIP6 model. A specific spatial domain was chosen, which corresponds to a rectangle between 90°W-30°E and 60°S-25°N, which encompasses South America, the SAO and surroundings. It is important to note that this spatial domain differs from the SVD domain described in subsection 2.3.1. The period considered here is from 1979 to 2010, known as the "satellite era". This period was chosen because reanalysis data during this time offer a closer representation of reality compared to previous periods. The availability of concurrent data in the three reanalysis datasets considered in this study further supports the selection of this specific time frame. The aim was to identify the top three CMIP6 models that best replicate the two key variables (SST and MSLP) within our study area. This selection would enable us to conduct further analyses using outputs from these models for the SSPs scenarios. An arithmetic mean of all RMSE in relation to each specific CMIP6 model was used to made this selection.

In addition, the RMSE was calculated at each individual grid point to create maps that provide a detailed analysis of the region of interest. Bias maps were also generated, which serve as quantitative measures to evaluate whether the estimated data consistently overestimates or underestimates the observed values on average. Bias is defined as follows:

$$Bias = \frac{1}{N}\sum_{n=1}^{N}\left(V_{est_i} - V_{obs_i}\right) \tag{2.9}$$

With the same definitions of equation 2.8.

Chapter 3

Results

3.1 *The South Atlantic Dipole: after the industrial revolution to the present day*

3.1.1 General characterization

In order to visualize a mode of coupled variability identified using the SVD technique, a common approach is to plot the homogeneous correlation between the expansion coefficients and their corresponding spatiotemporal anomaly arrays. Figure 3.1 illustrates the homogeneous correlation between the SST and MSLP expansion coefficients (SVD1_{SST} and $\text{SVD1}_{\text{MSLP}}$, respectively) and their respective anomaly arrays ($[S]$ and $[M]$) for each of the three reanalysis datasets utilized in this study. Note that the domain shown in Figure 3.1 is larger than the SVD calculation domain (Figure 2.5), as it encompasses areas of interest such as the entire SAO and South America. It is also important to mention that each dataset encompasses distinct analysis periods. Nonetheless, all three datasets distinctly exhibit the SAD configuration, characterized by a dipole of SST anomalies spanning from the tropics to the extratropics, overlapped with a monopole of MSLP anomalies. Values greater than the 95% statistical confidence level are highlighted by green and brown dots for the SST and MSLP anomalies, respectively. Significant values are observed over the entire SAO domain for both variables. The squared covariance fraction for this first mode (SCF_1), which represents the extent to which the mode explains the total covariability in the SAO, shows values around 60-65%, highlighting the importance of this oscillation.

To gain insights into the temporal variability of SST and MSLP anomalies associated with the SAD, we can analyze the time series of the expansion coefficients corresponding to SST (SVD1_{SST}) and MSLP ($\text{SVD1}_{\text{MSLP}}$). Figures 3.2, 3.3 and 3.4 present the series of

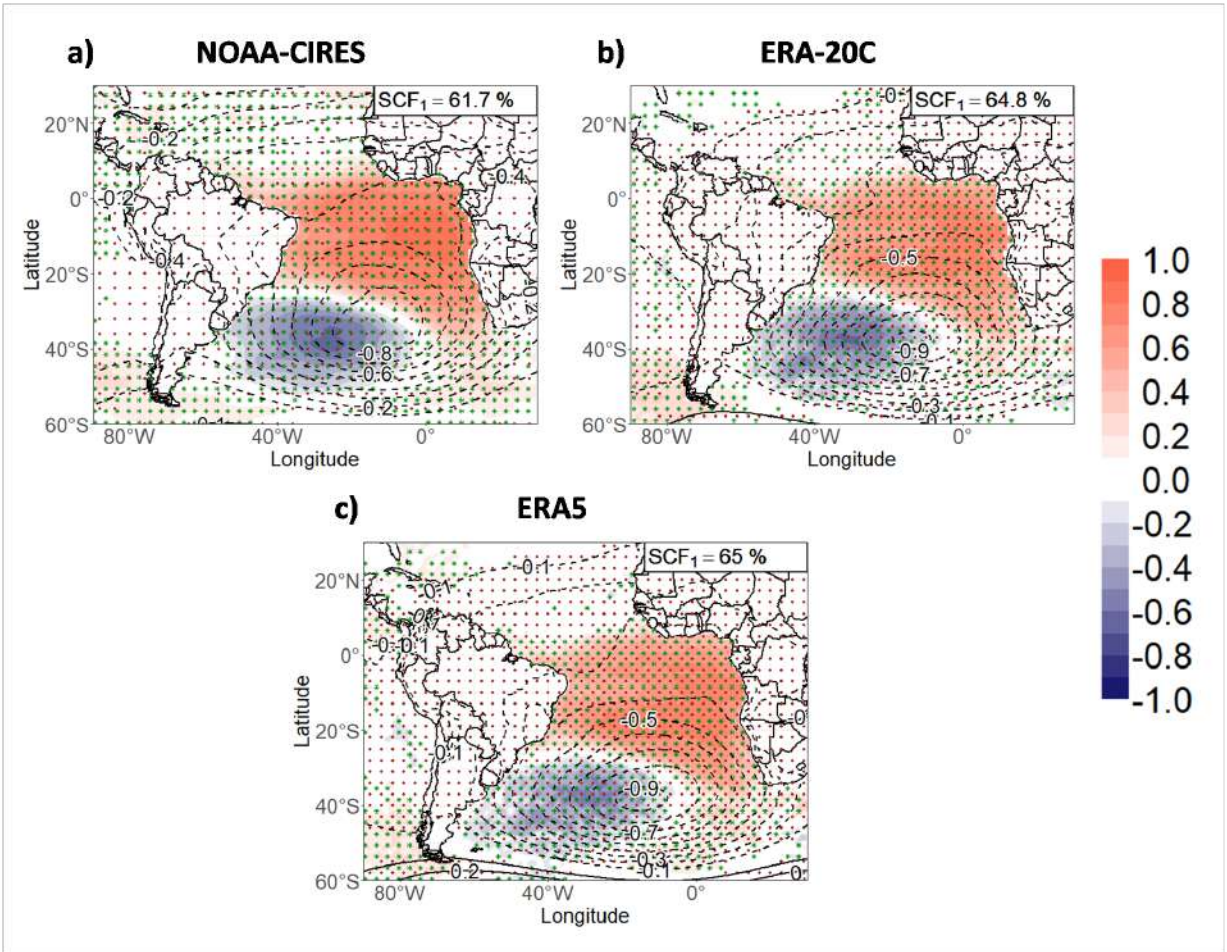

Figure 3.1: Homogeneous correlation between $SVD1_{SST}$ and SST anomalies (shaded) and between $SVD1_{MSLP}$ and MSLP anomalies (contours) identified for the full periods of a) NOAA-CIRES 20th Century V2c (1851-2014), b) ERA-20C (1901-2010) and c) ERA5 (1950-2020) reanalyses. Correlations with a statistical confidence level above 95% are shown as green (brown) dots for SST (MSLP) anomalies.

these coefficients (upper portion) and their corresponding wavelet power spectra (bottom) for the NOAA-CIRES, ERA-20C and ERA5 reanalyses, respectively. The $SVD1_{SST}$ time series are on the left, and $SVD1_{MSLP}$ are on the rigt part of the figures. In the $SVD1_{SST}$ graphs, the $P(25)$ and $P(75)$ percentiles of the series are depicted as blue and red dotted lines, respectively, serving as thresholds to distinguish the negative ($values < P(25)$) and positive ($values > P(75)$) phases of the SAD. In the wavelet analysis of the expansion coefficients (bottom part of Figures 3.2, 3.3 and 3.4), it verifies the periods of oscillations and how they vary over time.

Upon examining the $SVD1_{SST}$ graphs across all datasets (bottom part of Figures 3.2a, 3.3a and 3.4a), it becomes evident that the oceanic component, which best characterizes the SAD, exhibits prominent peaks on the interannual (16-128 months) and interdecadal

(128-512 months) scales, agreeing with previous studies (e.g. BOMBARDI *et al.*, 2014; STERL; HAZELEGER, 2003; VENEGAS; MYSAK; STRAUB, 1997). In all three datasets, a consistent peak at around 128 months is observed throughout the entire time span. Notably, in the NOAA-CIRES, there is an additional peak at 256 months, specifically between the late 19th century and the early 20th century (bottom part of 3.2a). Within the interannual band (16-128 months) of this same dataset, an apparent alternation of oscillation peaks between 32 and 64 months is observed. During the approximate periods of 1851-1880, 1910-1960, and 2000 onwards, a higher occurrence of peaks is observed closer to the 32-month scale. Conversely, for the periods of 1880-1910 and 1960-2000, there is a predominance of peaks around the 64-month scale. This interchange in the oscillation peaks is also observed in the other two sets of reanalysis (bottom part of Figures 3.3a and 3.4a), although partially, as the two datasets are more recent. The reason for these alternations can either be the result of internal variability or be related to other low-frequency oscillations, but the analysis of this is beyond the scope of the current work.

Regarding the MSLP anomalies (Figures 3.2b, 3.3b and 3.4b), notable peaks are observed across the intraseasonal to interannual scale (2 to 32 months), presenting a discontinuous pattern. However, significant peaks are also evident in the interannual and interdecadal timescales (32 to 256 months), which aligns with the observed patterns for SST anomalies.

The Pearson linear correlation between the $SVD1_{SST}$ and $SVD1_{MSLP}$ indexes across different reanalysis for the period 1950-2010, which corresponds to the consistent range across all reanalysis datasets, is displayed in Table A.1 in the Appendix A. Notably, for the same reanalysis, the $SVD1_{SST}$ and $SVD1_{MSLP}$ indexes exhibit statistically significant correlations ranging arround 0.3 to 0.4. This, added to a certain spectral alignment of the $SVD1_{SST}$ and $SVD1_{MSLP}$ (as indicated in Figures 3.2 to 3.4), reinforces that there is indeed a coupling between the oceanic and atmospheric components in the SAD oscillation. Additionally, the SVD1 index for a same variable (SST or MSLP) across the different reanalysis datasets demonstrates a strong correlation, exceeding 0.870 in all the cases, indicating a high level of agreement among the different reanalysis in representing the oscillation for the specified period.

SST and MSLP anomalies for the positive (SAD+) and negative (SAD-) phases of the SAD are shown in Figure 3.5, across the different reanalysis datasets and their respective

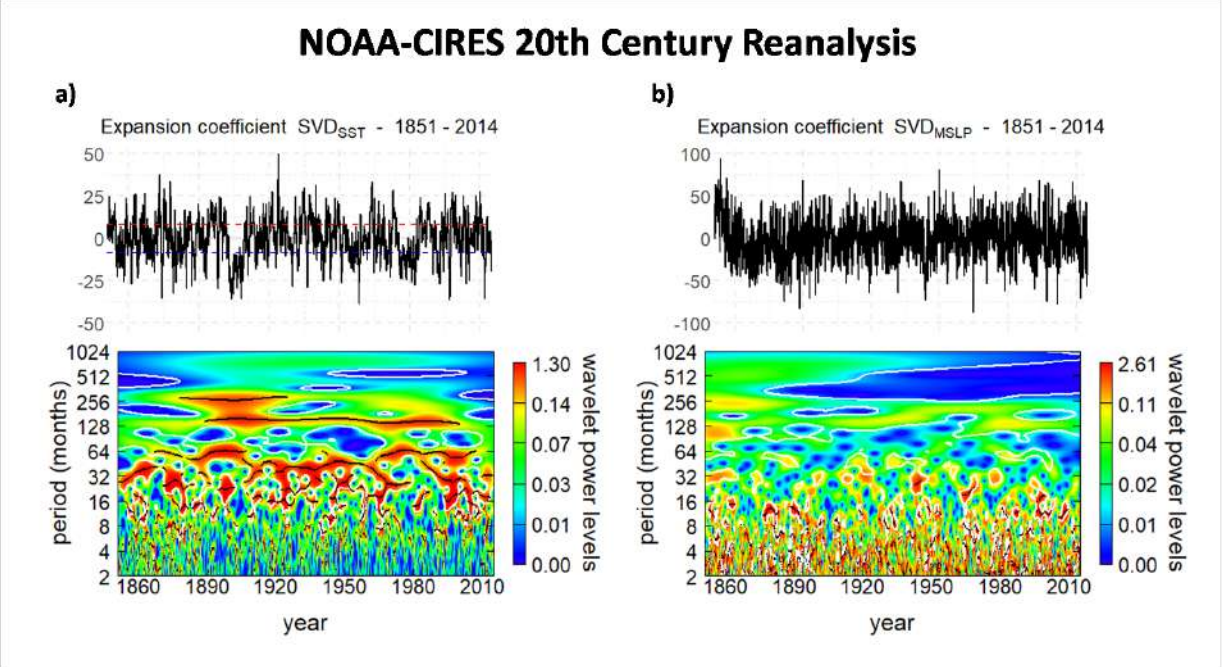

Figure 3.2: Time series of the expansion coefficients a) of the SST ($SVD1_{SST}$) and b) of the MSLP ($SVD1_{MSLP}$) with their respective power spectrum obtained by wavelet analysis obtained from the NOAA-CIRES reanalysis, calculated for the SVD area (5°N–45°S and 20°E–60°W - Figure 2.5) for the period from 1851 to 2014. Red (blue) dotted lines in the $SVD1_{SST}$ series, in Figure a - top, indicate the 75th (25th) percentile which is used as the threshold for the positive (negative) phase of the SAD. Values with 95% statistical confidence level in the Power spectrum are delimited by a white contour.

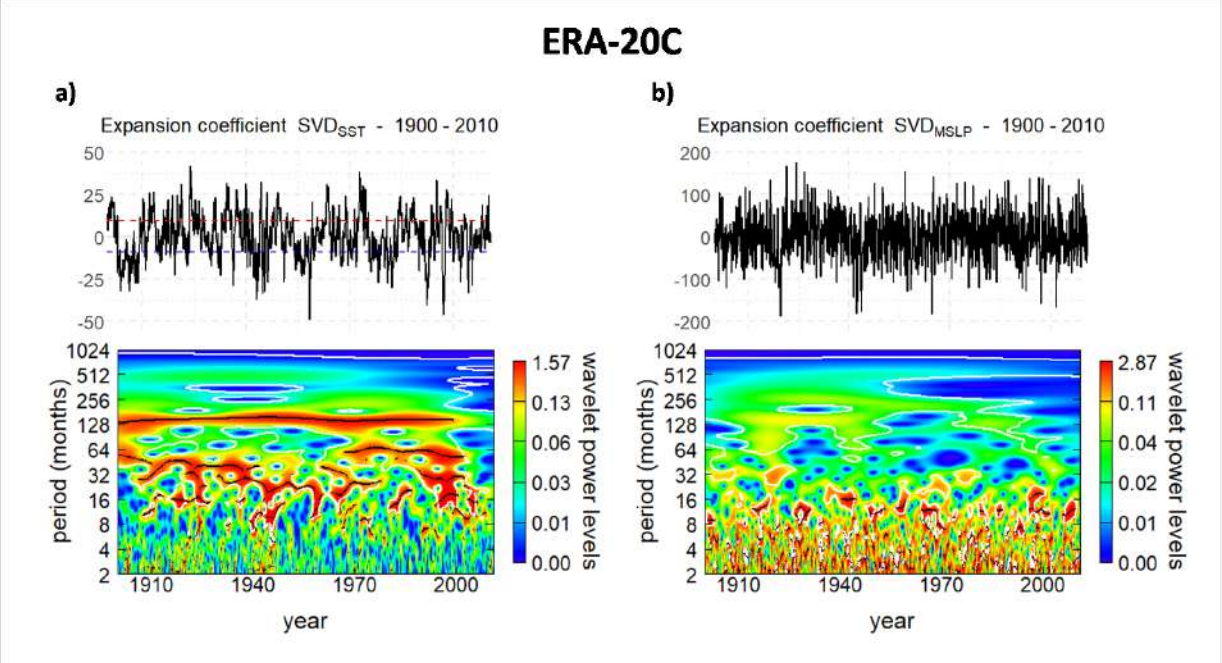

Figure 3.3: The same as in Figure 3.2 with data obtained from the ERA-20C reanalysis, for the period from 1901 to 2010.

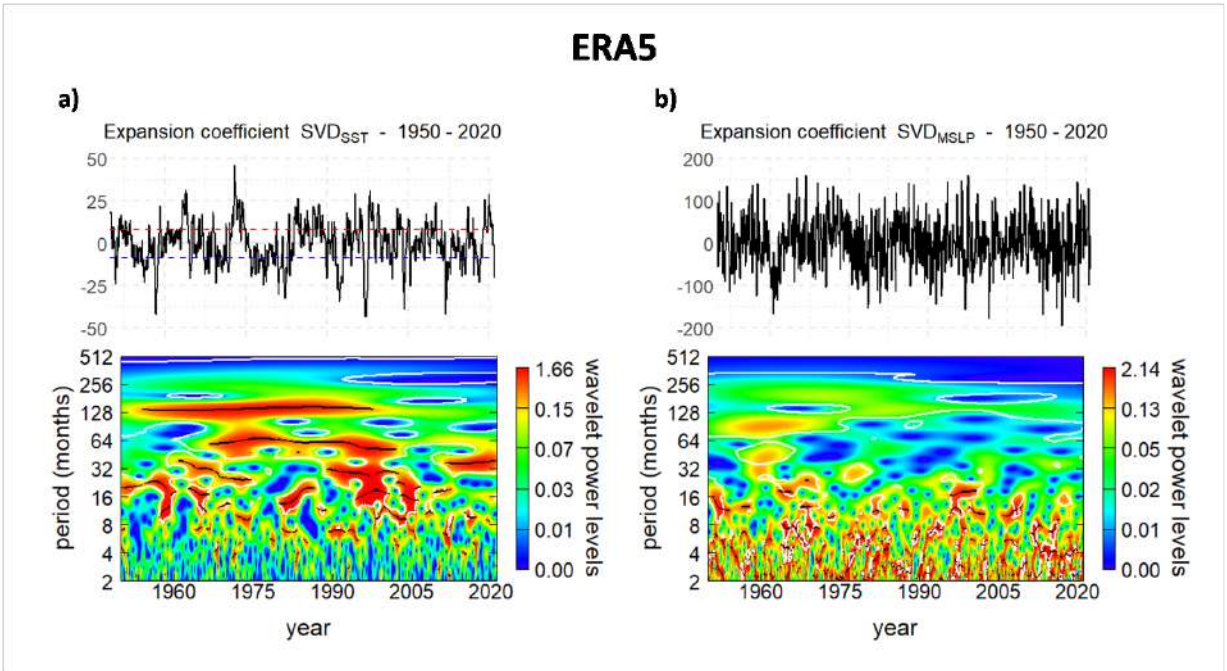

Figure 3.4: The same as in Figure 3.2 with data obtained from the ERA5 reanalysis, for the period from 1950 to 2020.

analysis periods. These phases were identified based on the above-mentioned percentile thresholds derived from the SST coefficient time series (Figures 3.2a, 3.3a and 3.4a). For all datasets, despite having different data periods, and as expected from the SVD analysis (Figure 3.1), during the positive (negative) phase of the SAD, positive (negative) SST anomalies are observed over tropical regions, while extratropical areas exhibit negative (positive) anomalies. At the same time, negative (positive) MSLP anomalies are observed in an overlapped way. The tropical pole of SST anomalies associated with the SAD can be divided into two distinct sectors, which will be useful for the analyses conducted in this study: the Atlantic Niño region off the coast of Guinea (approximately 10°S-0° and 15°W-15°E) and the Benguela Current sector ($\sim$ 35°S-10°S and 20°W-15°E).

Precipitation anomalies associated with each SAD phase identified for each reanalysis dataset are presented in Figure 3.6. These fields are computed using the GPCC precipitation dataset, and to mitigate the influence of external factors on regional precipitation, the calculation of composites excludes ENSO events. Considering that ENSO event data (Figure 2.1) is not used prior to 1950, the composites are calculated for periods after this year. For the three reanalyses, in the positive phase of the SAD (Figures 3.6a, 3.6c and 3.6e), we observe positive precipitation anomalies in the northern portion of Northeast Brazil (NNE) and southeastern South America (SESA), while central-eastern Brazil (CEBR)

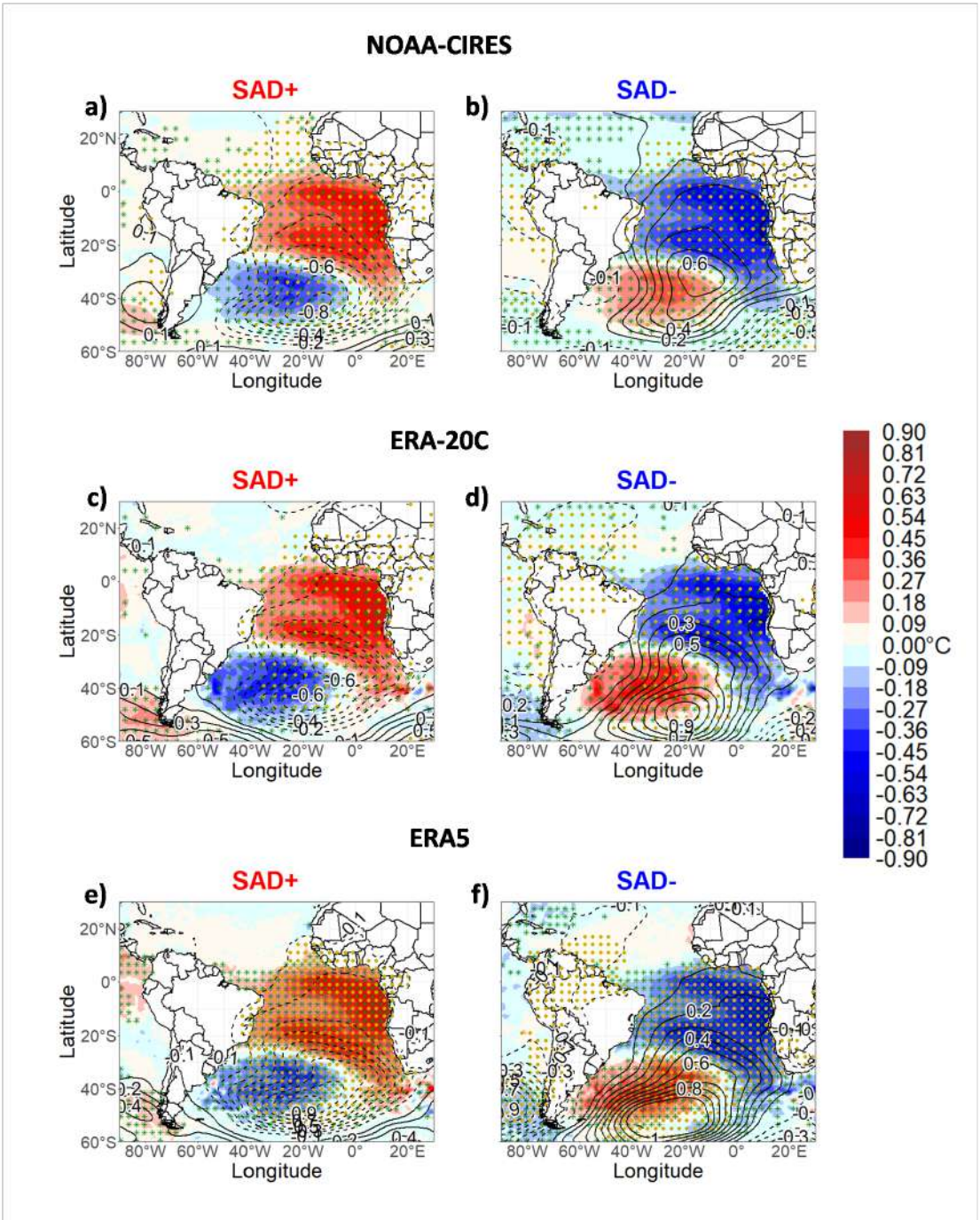

Figure 3.5: Composites with SST anomalies (in colors) and MSLP anomalies (contours) for the positive (SAD+) and negative (SAD-) phases of the South Atlantic Dipole determined for the full periods of NOAA-CIRES 20th Century V2c (a) SAD+, b) SAD- - period: 1851-2014), ERA-20C (c) SAD+, d) SAD- - period: 1901-2010) and ERA5 (e) SAD+, f) SAD- - period: 1950-2020) reanalysis. Values with a statistical confidence level above 95% are shown in green (yellow) dots for SST (MSLP) anomalies.

and the Guyanas region (GYR) exhibit negative anomalies. Conversely, during negative SAD phases (Figures 3.6b, 3.6d and 3.6f), the opposite pattern emerges, with negative rainfall anomalies observed in NNE and SESA, and positive ones over CEBR and GYR.

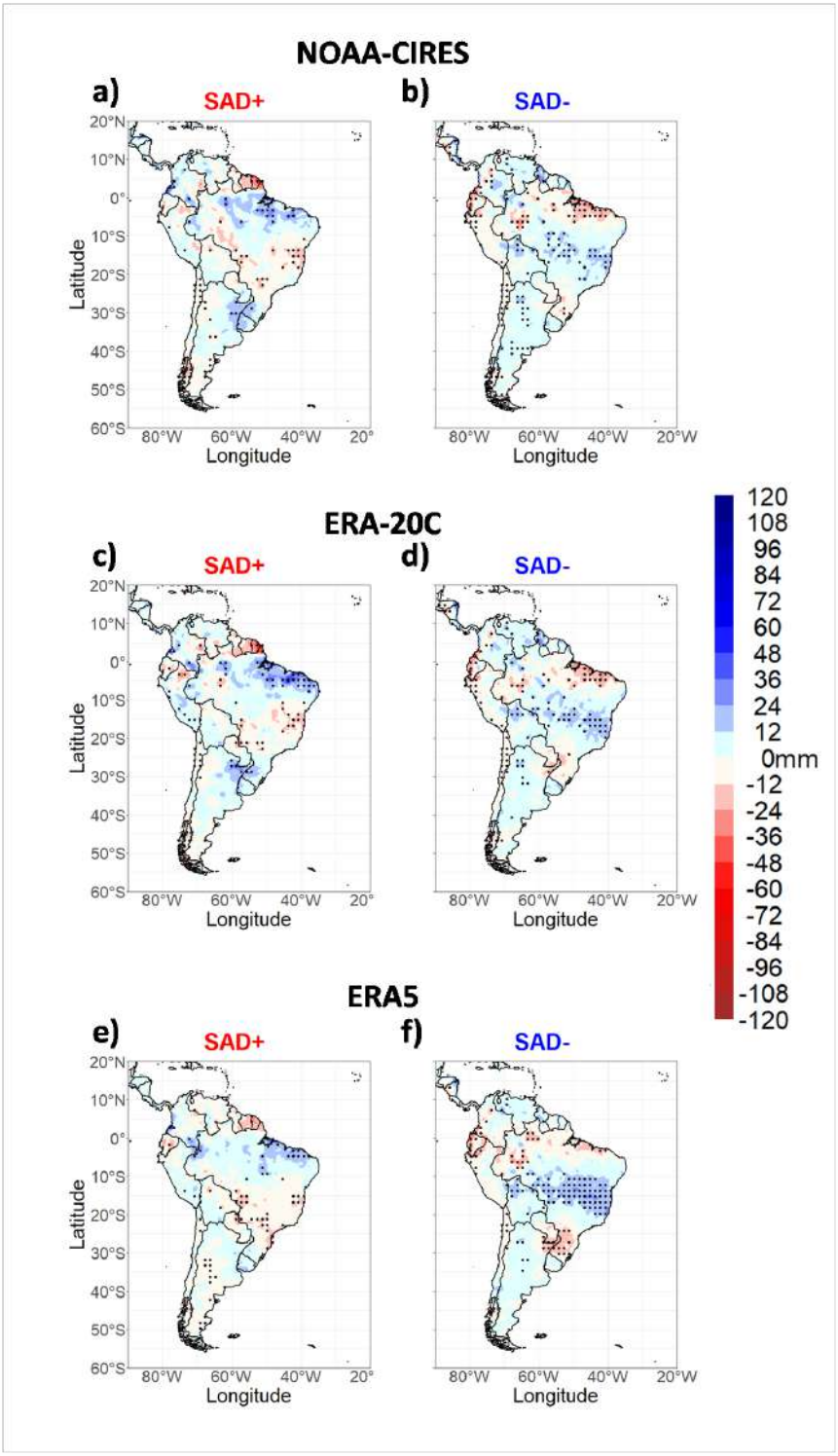

Figure 3.6: Composites with precipitation anomalies (in color) for the positive (SAD+) and negative (SAD-) phases of the South Atlantic Dipole. Calculated with GPCC precipitation dataset. Determined for the full periods of NOAA-CIRES 20th Century V2c (a) SAD+, b) SAD- - period: 1950-2014), ERA-20C (c) SAD+, d) SAD- - period: 1950-2010) and ERA5 (e) SAD+, f) SAD- - period: 1950-2020) reanalysis. ENSO periods are disregarded in this analysis. Dots are values with a statistical confidence level above 95%.

3.1.2 Seasonal variability

This subsection provides a broader overview of the SAD in each season of the year. The seasons considered here are defined as December-February (DJF), March-May (MAM), June-August (JJA), and September-November (SON) quarters. In the main body of this subsection, we present analyses conducted using the ERA5 reanalysis. This choice is based on the fact that ERA5 not only captures the results found in other reanalysis datasets but also provides the most up-to-date data, representing the current state of the art in reanalysis (HERSBACH *et al.*, 2020). However, for the purpose of comparison, the composites created with the NOAA-CIRES and ERA-20C reanalysis datasets can be accessed and viewed in Appendix B.

Previous research has highlighted the presence of seasonal variability in the SAD configuration and its associated atmospheric circulation (e.g. KAYANO; ANDREOLI; FERREIRA DE SOUZA, 2013; NNAMCHI *et al.*, 2017). This variability is evident for the different seasonal SAD configuration, as depicted in Figure 3.7 for the ERA5 reanalysis, where the first mode of coupled variability between SST and MSLP over SAO is shown for DJF, MAM, JJA and SON seasons. Similar patterns of variability are observed in the NOAA-CIRES (Figure B.1) and ERA-20C (Figure B.8) datasets. To identify these specific patterns for each season, separate SVD analyses were conducted.

During the JJA months (austral winter) (Figures 3.7c, B.1c and B.8c), the SAD is situated in its northernmost position, while the southernmost one happens in DJF (austral summer) (Figure 3.7a, B.1a and B.8a). This meridional shift of the SAD configuration throughout the year is also verified in the SASH (REBOITA *et al.*, 2019), further highlighting the coupling between these systems.

The SCF_1 for each season vary across the reanalysis datasets, as well as the season importance. In the ERA5 reanalysis, the SCF_1 ranges from 55.5% for the MAM quarter to 67.8% for the SON months (Figures 3.7b and 3.7d respectively). In the NOAA-CIRES dataset (Figure B.1), SCF_1 values range from 51.7% in JJA to 73.7% in SON, and for the ERA-20C dataset (Figure B.1) shows SCF_1 values ranging from 56.2% in SON to 65% in DJF months.

The anomalous patterns of SST and MSLP for each SAD phase during different seasons across the Pacific and Atlantic ocean basins are verified in Figures 3.8 (DJF and MAM)

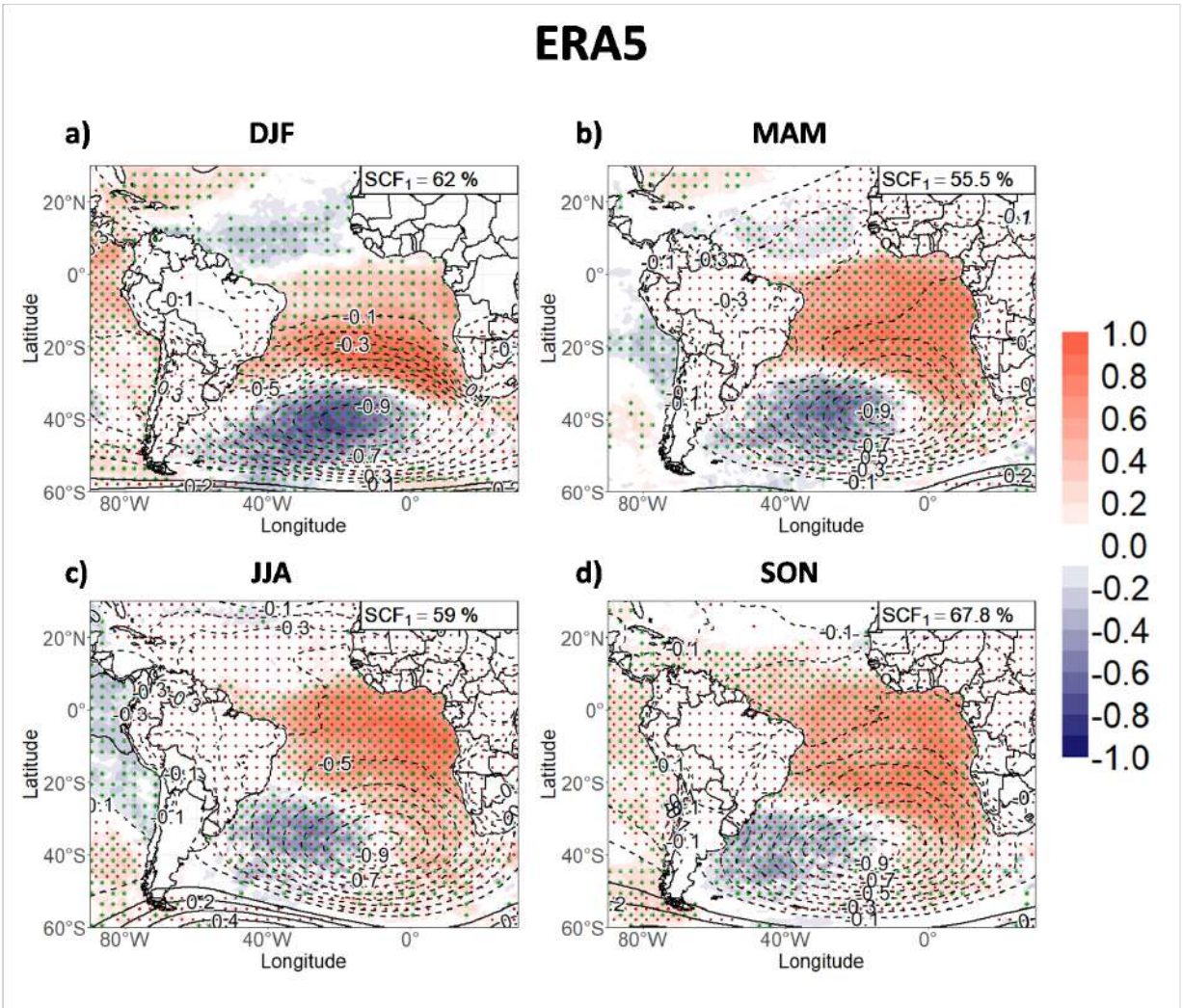

Figure 3.7: Homogeneous correlation between $SVD1_{SST}$ and SST anomalies (in shaded) and between $SVD1_{MSLP}$ and MSLP anomalies (contours) identified for the a) December-February (DJF), b) March-May (MAM), c) June-August (JJA) and d) September-November (SON). Calculated for the ERA5 reanalysis, period 1950-2020. Correlations with a statistical confidence level above 95% are shown in green (yellow) dots for SST (MSLP) anomalies.

and 3.9 (JJA and SON). Corresponding NOAA-CIRES schemes are found in Figures B.2 and B.3, and for ERA-20C in Figures B.9 and B.10. Note that during the southernmost configuration of the SAD, which occurs in the summer months (Figure 3.8a-b for ERA5, B.2a-b for NOAA-CIRES and B.9a-b for ERA-20C), positive (negative) SST anomalies in the Pacific Niño region are associated with the positive (negative) phase of SAD. Conversely, during the northernmost SAD pattern observed in the JJA season (Figures 3.9a-b for ERA5, B.3a-b for NOAA-CIRES and B.10a-b for ERA-20C), the positive (negative) SST anomalies in the Pacific Niño align with the negative (positive) phase of the SAD. Particularly over the Pacific, the anomalies are more intense and significant in the ERA5

(Figures 3.8 and 3.9) and ERA-20C datasets (Figures B.9 and B.10).

It is known that central Pacific El Niño (La Niña) events are linked with positive (negative) SAD phases, through a teleconnection of stationary atmospheric Rossby waves between the two ocean basins (KAYANO; ANDREOLI, 2006; RORDIGUES; CAMPOS; HAARSMA, 2015), specifically a PSA2 pattern (MO; PAEGLE, 2001). Here, this pattern appears to be particularly associated with the southernmost patterns of the SAD, which occurs in the warmer seasons, namely DJF and SON months. Otherwise, the presence of opposite signs in SST anomalies between the equatorial Atlantic and Pacific basins indicates a potential relationship between the northernmost SAD pattern and the induction of ENSO events by SAD through the Walker circulation, as suggested by Kayano, Andreoli and Ferreira de Souza (2013).

Figures 3.10, B.4 and B.11 illustrates the precipitation anomalies observed in each of the four quarters of the year for the ERA5, NOAA-CIRES and ERA-20C reanalyses, respectively. Similar to the overall annual pattern (for example the Figure 3.6 for the ERA5 dataset), a quadripole pattern of anomalies can be observed between GYR-NNE-CEBR-SESA during the MAM season (Figures 3.10c-d, B.4c-d and B.11c-d). During this time of the year, the anomalies are particularly pronounced in the GYR-NNE dipole.

However, in the DJF and SON months (Figures 3.10a-b, 3.10g-h, B.4a-b, B.4g-h, B.11a-b and B.11g-h), the GYR pole vanishes, with the NNE-CEBR-SESA tripole left and with more intense anomalies observed between CEBR and SESA. The DJF months, in general, has more intense anomalies. During the negative SAD phase of the SON season (Figures 3.10l, B.4l and B.11l), it is also observed a fourth pole over central-north Argentina, with significant positive precipitation anomalies. In comparison, a similar tripole pattern of precipitation between NNE-CEBR-SESA, associated with SAD during the summer season, was also identified by Bombardi *et al.* (2014).

On the other hand, during the JJA months (Figures 3.10e-f, B.4e-f and B.11e-f), there is a singular concentration of precipitation anomalies over the far northern region of the continent, that is characterized by positive (negative) precipitation anomalies during the SAD+ (SAD-) phase.

It is worth noting that the rainfall anomalies linked to the SAD annual pattern (Figure 3.6), that is the quadripole GYR-NNE-CEBR-SESA, can be explained as a combination of distinct seasonal patterns. For instance, the precipitation dipole between CEBR and

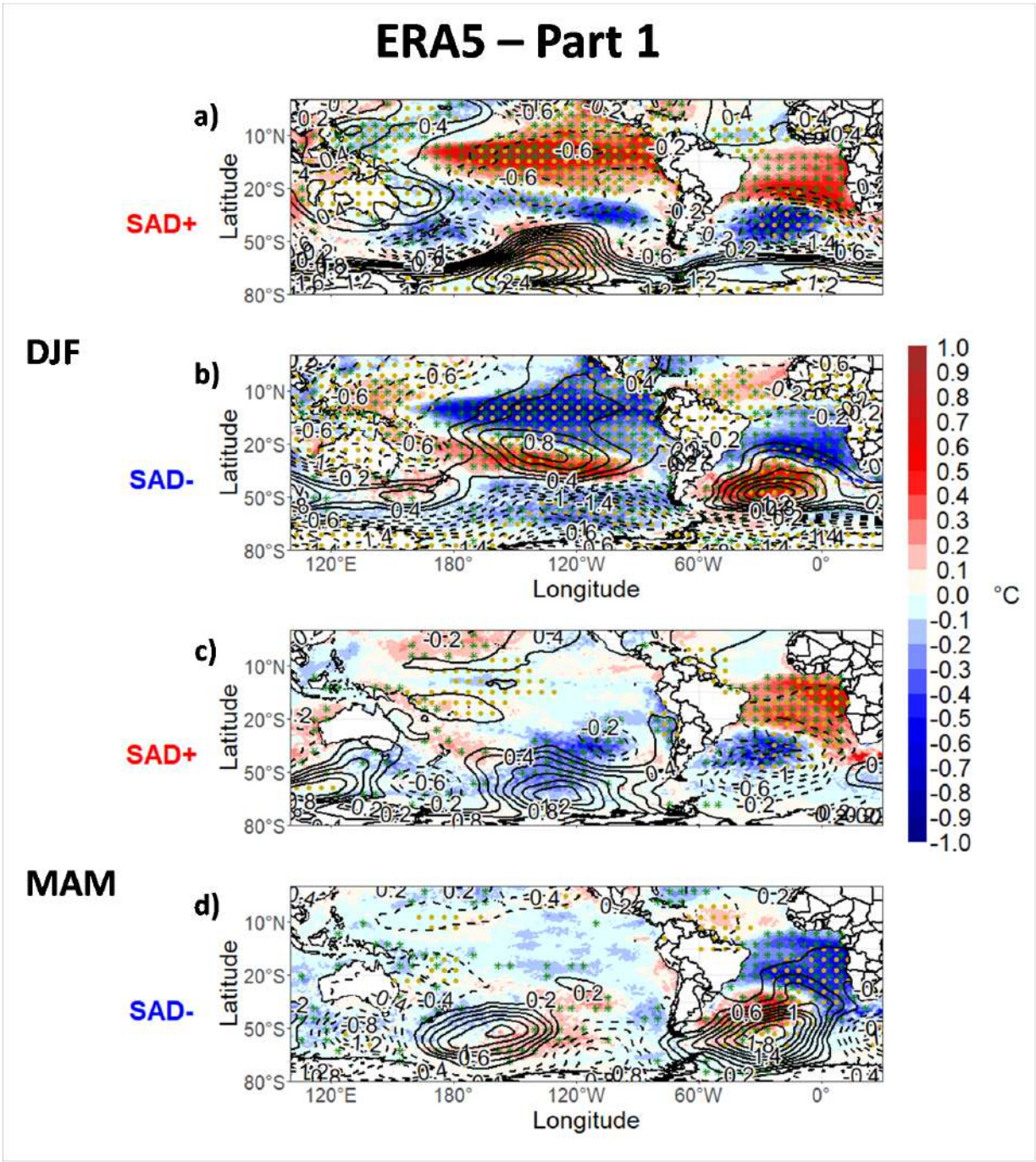

Figure 3.8: Composites with SST anomalies (in colors) and MSLP anomalies (contours) for the positive (SAD+) and negative (SAD-) phases of the South Atlantic Dipole for the DJF (itens a and b) and MAM (itens c and d) over the South Pacific and Atlantic basins domain. Calculated for the ERA5 reanalysis, period 1950-2020. Values with a statistical confidence level above 95% are shown in green (yellow) dots for SST (MSLP) anomalies.

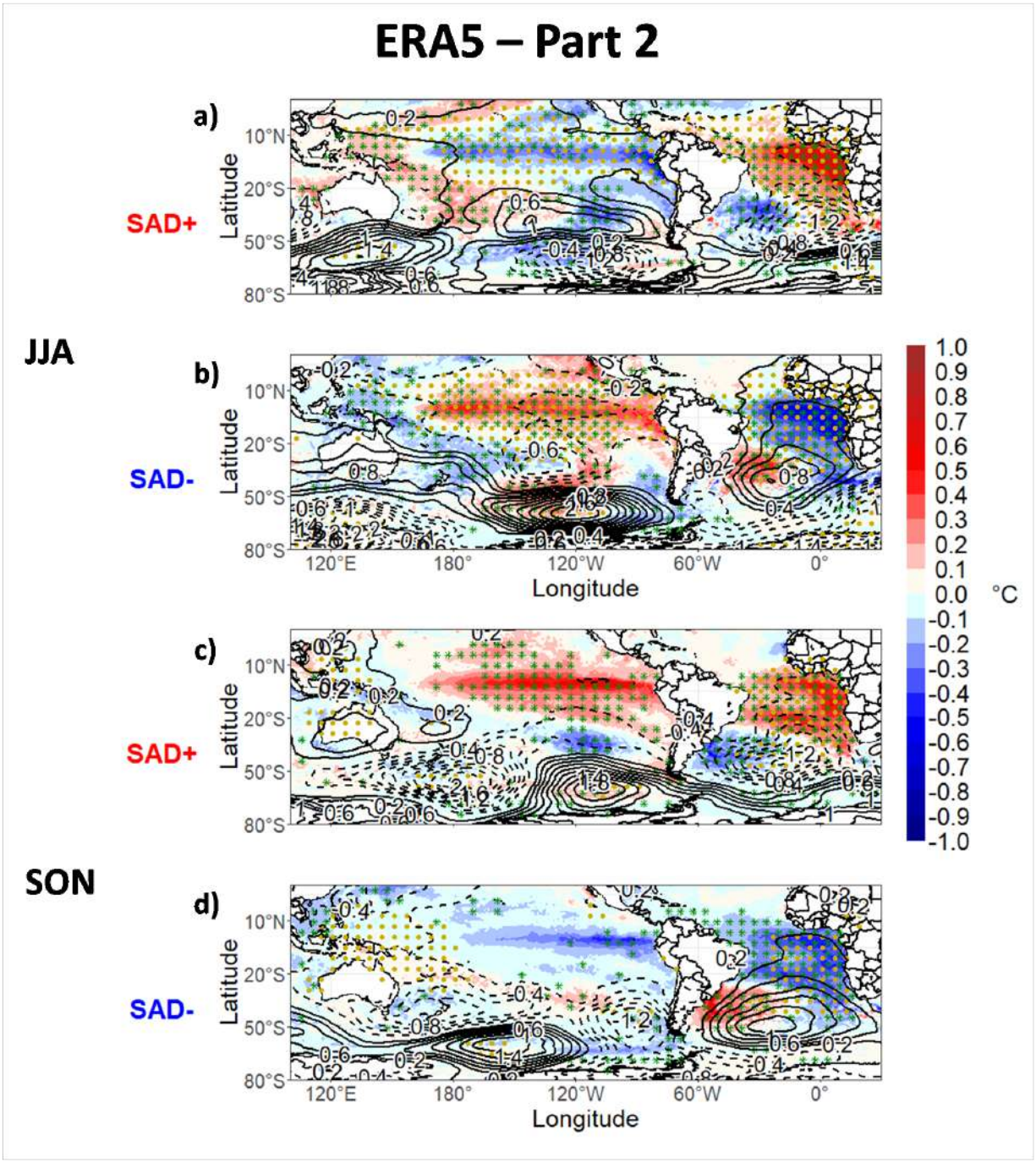

Figure 3.9: The same as in Figure 3.8 except for JJA and SON months. Values with a statistical confidence level above 95% are shown in green (yellow) dots for SST (MSLP) anomalies.

SESA, identified in the annual pattern, is predominantly prominent during the summer months (Figures 3.10a-b, B.4a-b and B.11a-b), while the dipole of precipitation anomalies between GYR and NNE becomes more apparent in MAM (Figures 3.10c-d, B.4c-d and B.11c-d). A similar seasonal variation in precipitation for the tropical South America was also reported by Kayano, Andreoli and Ferreira de Souza (2013).

Figures 3.11-3.13 for ERA5, B.5-B.7 for NOAA-CIRES and B.12-B.14 for ERA-20C provide a mean description of the atmosphere for each of the seasons described in this work. To minimize the influence of external factors on the relationship between the SAD and the surrounding atmospheric circulation in the SAO, these composites excluded ENSO events in their calculations.

The SST and MSLP anomalies for each season is shown in Figures 3.11, B.5 and B.12. The same meridional shift of the SAD configuration across the different seasons, also observed in Figures 3.7-3.9, B.1-B.3 and B.8-B.10 can be noticed here, although SAD is not as well configured as we consider ENSO events. When focusing on the northern pole of the SAD's SST anomaly, the presence of the Atlantico Niño (Benguela Current) sector becomes less apparent in DJF (JJA), as the SAD shifts further north (south).

The circulation and specific moisture anomalies at 850 mb (low atmospheric levels) during each quarter can be seen in Figures 3.12, B.6 and B.13. Over the SAO, positive (negative) specific moisture anomalies overlap positive (negative) SST anomalies (compare Figures 3.11 with B.6, B.5 with B.6 and B.12 with B.13). This occurs mainly over tropical latitudes and during warmer months. It suggests an ocean-to-atmosphere (atmosphere-to-ocean) moisture flux in cases of positive (negative) SST anomalies and approximately reflects the SAD signature over the area. Additionally, the wind anomalies closely correspond to the anomalies in MSLP (Figures 3.11, B.5 and B.12), with cyclonic (anti-cyclonic) wind anomalies aligning with negative (positive) MSLP anomalies.

During the MAM to the SON seasons (Figures 3.12c-h, B.6c-h and B.13c-h), there is a distinct meridional dipole of specific moisture anomalies across the equatorial Atlantic Ocean, that is more evident for the ERA5 and ERA-20C datasets. That dictates the average movement of the ITCZ that converges towards the region with higher humidity. In these months, with the tropical pole of the SAD positioned farther north, positive (negative) SST anomalies, as shown in Figures 3.11c-h, B.5c-h and B.12c-h, promote the southward (northward) convergence of moisture. So, the ITCZ tend to act anomalously

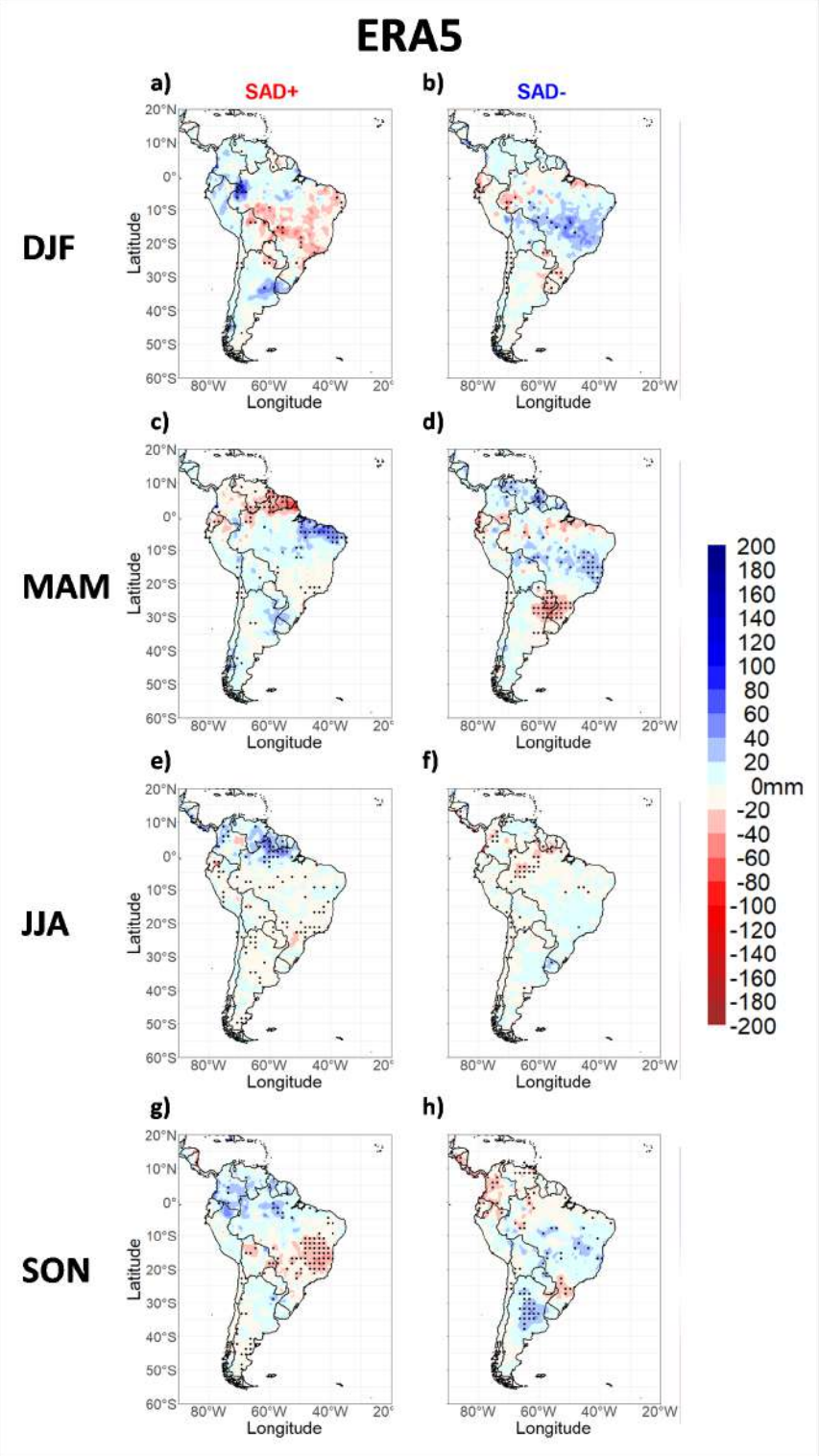

Figure 3.10: Composites with precipitation anomalies (in color) for the SAD positive (SAD+) and negative (SAD-) phases identified for the DJF (itens a and b), b) MAM (itens c and d), c) JJA (itens e and f) and SON (itens g and h). Calculated for the ERA5 reanalysis, period 1950-2020. ENSO periods are disregarded in this analysis. Dots are values with a statistical confidence level above 95%.

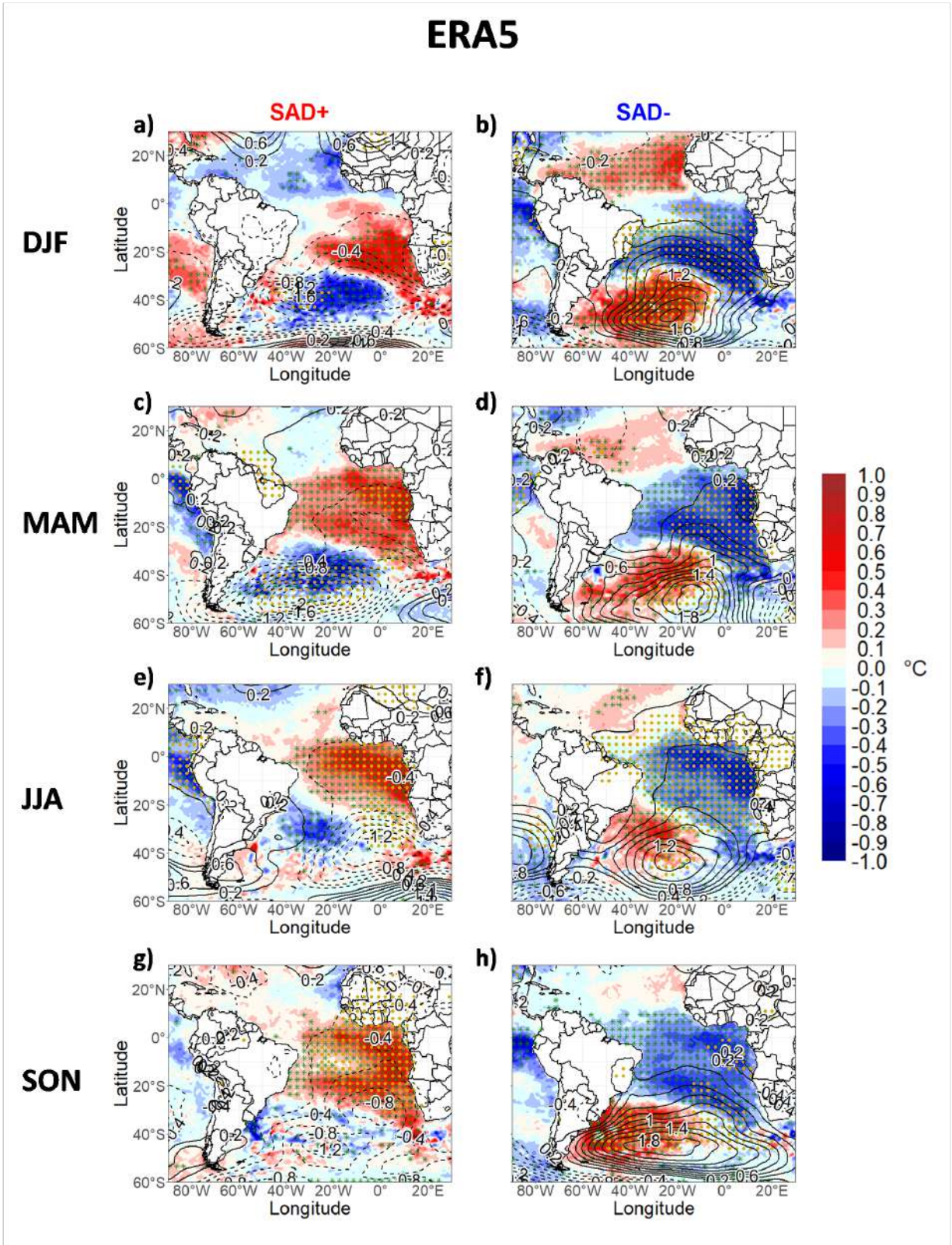

Figure 3.11: Composites with SST anomalies (in colors) and MSLP anomalies (contours) for the positive (SAD+) and negative (SAD-) phases of the South Atlantic Dipole for the DJF (itens a and b), MAM (itens c and d), JJA (itens e and f) and SON (itens g and h). Calculated for the ERA5 reanalysis, period 1950-2020. ENSO periods are disregarded in this analysis. Values with a statistical confidence level above 95% are shown in green (yellow) dots for SST (MSLP) anomalies.

further south (north) during SAD+ (SAD-).

For the DJF season (Figures 3.12a-b, B.6a-b and B.13a-b), the characteristic ITCZ pattern is no longer observed, as the SST anomalies associated with the northern pole of the SAD shift southward (Figures 3.11a-b, B.5a-b and B.12a-b). However, the ERA5 reanalysis fields give interisting insights for the austral summer and autumn precipitation anomalies verified between CEBR and SESA (Figures 3.10a-d, B.4a-d and B.11a-d). During SAD+ (SAD-) phases, an anticyclonic (cyclonic) circulation anomaly is observed between CEBR and southern Brazil in these composites (Figures 3.12a-d). This atmospheric configuration favors the transport of moisture from the Amazon region towards SESA (CEBR) during the positive (negative) phase of the oscillation. Although, these anomalous circulation patterns are not reported for the NOAA-CIRES and ERA-20C reanalyses (Figures B.6a-d and B.13a-d).

For the upper troposphere, the circulation and divergence anomalies associated with each phase of the SAD in each of the seasons can be verified in Figures 3.13, B.7 and B.14. Regions experiencing positive (negative) upper-level divergence anomalies tend to exhibit positive precipitation anomalies, which is mainly verifiable for ERA5 and ERA-20C reanalyses (compare Figures 3.13 with 3.10 and B.14 with B.11). This relationship arises from the atmospheric instability in such areas, which results from the forced upward movement and subsequent adiabatic cooling of the upper tropospheric layers (BLUESTEIN, 1993). At extratropical latitudes, it is observed a comparable circulation pattern to what was identified at the 850 mb level (compare Figures 3.13 with 3.12, B.7 with B.6 and B.14 with B.13), indicating barotropic anomalies. Otherwise, within the tropical latitudes, it is observed baroclinic anomalies, which originate from convection processes.

For the ERA5 and ERA-20C datasets, it is noticed that the SAD configuration, further south during the austral summer, favors (disfavors) storm tracks at mid-latitudes by 40°S during the positive (negative) phase of the SAD (Figures 3.13a[b] and B.14a[b]). As a result of this, cyclogenesis conditions are favored near the La Plata river mouth (southeastern coast of Brazil) (BOMBARDI *et al.*, 2014).

The quadripole observed in the annual precipitation anomalies pattern (GYR-NNE-CEBR-SESA) depicted in Figure 3.6 can be dissected into two distinct dipoles, namely GYR-NNE and CEBR-SESA. These dipoles exhibit independent origins in their relationship with the SAD and their characteristics become more evident when observed in the

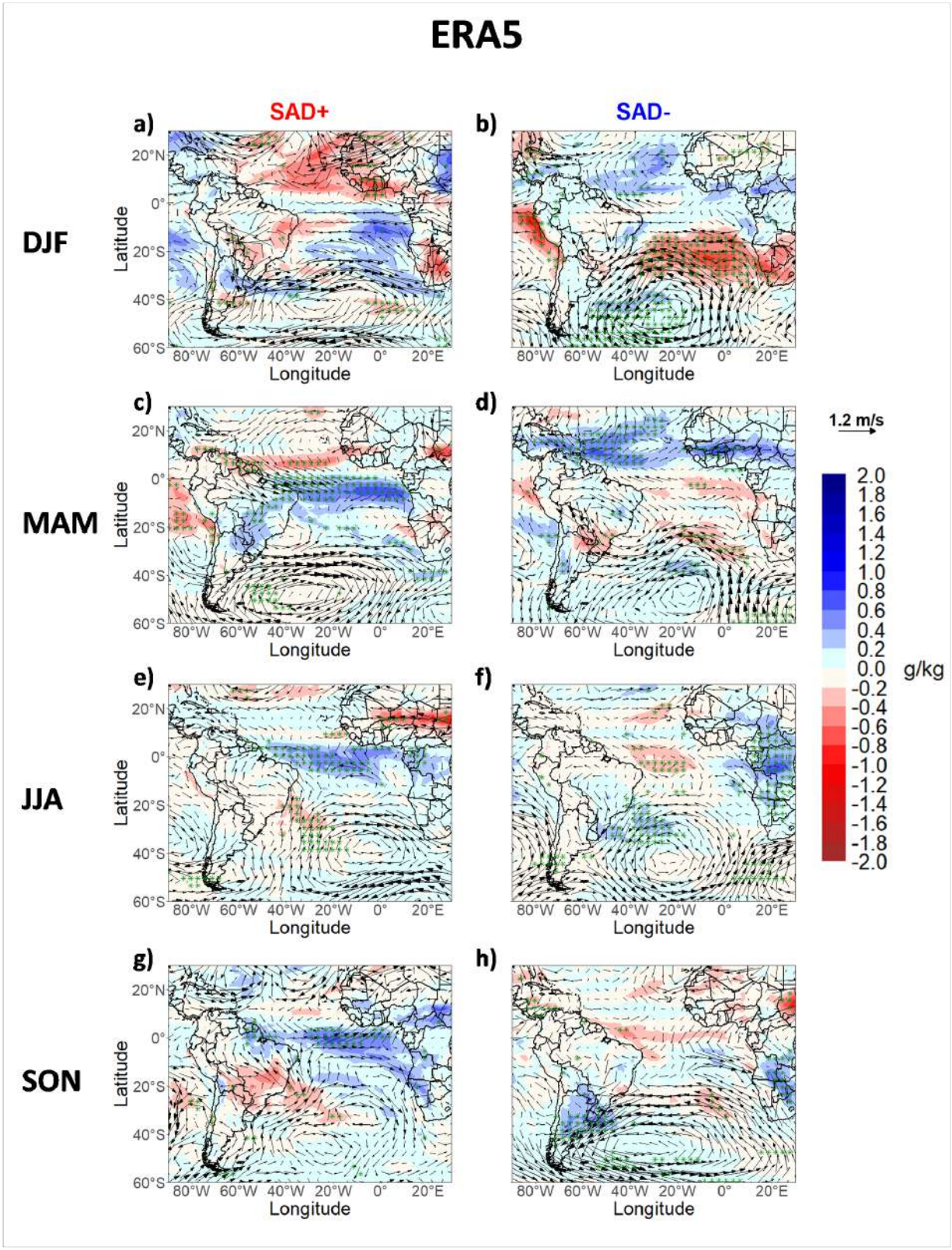

Figure 3.12: Composites with specific moisture anomalies (in colors) and wind anomalies (vectors) in 850 mb for the positive (SAD+) and negative (SAD-) phases of the South Atlantic Dipole for the DJF (itens a and b), MAM (itens c and d), JJA (itens e and f) and SON (itens g and h). Calculated for the ERA5 reanalysis, period 1950-2020. ENSO periods are disregarded in this analysis. Values with a statistical confidence level above 95% are shown in green dots for the specific moisture anomalies.

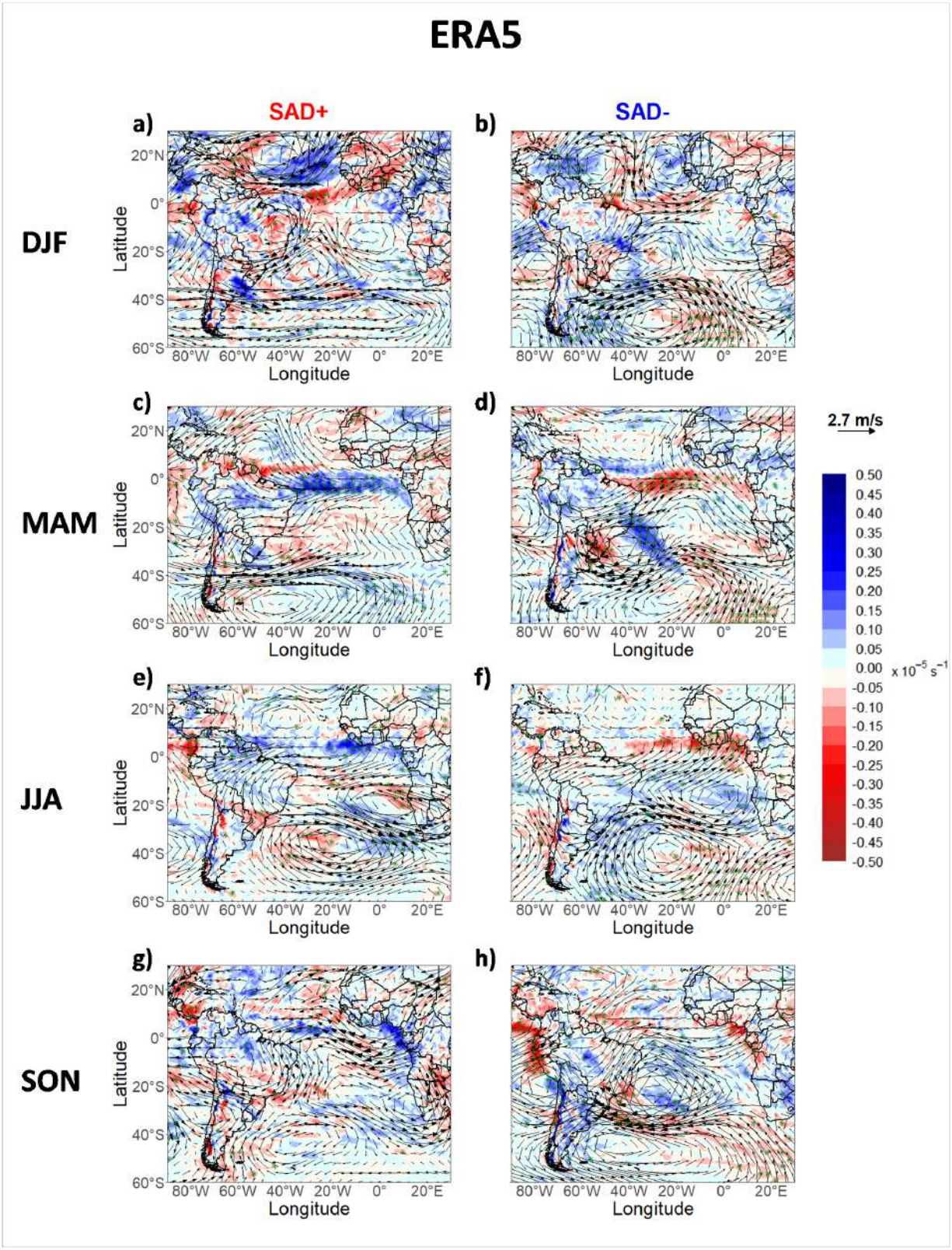

Figure 3.13: Composites with divergence anomalies (in colors) and wind anomalies (vectors) in 200 mb for the positive (SAD+) and negative (SAD-) phases of the South Atlantic Dipole for the DJF (itens a and b), MAM (itens c and d), JJA (itens e and f) and SON (itens g and h). Calculated for the ERA5 reanalysis, period 1950-2020. ENSO periods are disregarded in this analysis. Values with a statistical confidence level above 95% are shown in green dots for the divergence anomalies.

seasonal fields. The enhanced cyclonic activity over SESA (CEBR), during the positive (negative) phase of the SAD, is apparent through the presence of cyclonic anomalies over these regions at lower levels during the DJF and MAM months, as illustrated in Figures 3.12a-d. In turn, this leads to increased precipitation over SESA (CEBR) during the positive (negative) phase of the SAD, as shown in Figures 3.10a-d.

The dipole of precipitation anomalies between GYR and NNE is predominantly influenced by the SAD's tropical pole and its association with the average position of the ITCZ. This system reaches its peak activity near NNE during the southern autumn season (CHIANG; KUSHNIR; GIANNINI, 2002; SCHNEIDER; BISCHOFF; HAUG, 2014). This can be verified in Figures 3.12c-d, B.6c-d and B.13c-d, when the moisture associated with ITCZ converges southernmost. It also corresponds to the time of year when the tropical part of South America experiences a notable precipitation response to the SAD, as evident in Figures 3.10c-d, B.4c-d and B.11c-d. Positive (negative) SST anomalies coincide with increased (decreased) ITCZ activity over NNE during this season, consequently resulting in positive (negative) precipitation anomalies. During the JJA period, this precipitation response of the ITCZ shifts further northward. Positive (negative) SST anomalies over the tropical Atlantic are associated with positive (negative) precipitation anomalies over the northern regions of South America (Figures 3.10e-f, B.4e-f and B.11e-f).

3.1.3 Evolution over time based on the Interdecadal Pacific Oscillation

To investigate the progression of the SAD and its associated atmospheric patterns, we employ the intervals defined by each phase of the IPO (see Figure 2.2). The SAD annual configurations associated with each interval of the IPO phases are displayed in Figures 3.14, 3.15 and 3.16 for the NOAA-CIRES, ERA-20C, and ERA5 reanalyses, respectively. In each dataset, the left side corresponds to the positive IPO periods (IPO+), while the right side represents the negative IPO periods (IPO-). It should be noticed that only the NOAA-CIRES dataset provides data starting from the beginning of the IPO series (1891). In the last interval analyzed, based on the IPO phases, it is important to acknowledge the varying lengths of available data for each reanalysis. Specifically, the NOAA-CIRES (1997-2014), ERA-20C (1997-2010), and ERA5 (1997-2020) reanalyses cover 17, 14, and 24 years, respectively. Upon examining the images for the NOAA-CIRES (Figure 3.14) and ERA-20c (Figure 3.15) reanalyses, discordant configurations of the first mode of coupled variability in the SAO are observed in the first three intervals (1891[1900]-1916, 1916-1923, and 1923-1942). Additionally, the SAD is not well defined during these periods in the ERA-20C analysis (Figures 3.15a-c). These findings suggest a low reliability in conducting analyses for these time intervals. On the other hand, in the last three time periods (1943[1950]-1978, 1978-1997, and 1997-2010[14 and 20]), consistent patterns are identified across all three datasets. This is a natural outcome considering the advancements in measurement technology over the past few decades and the advent of the "satellite era" (1979-present) (MINNETT *et al.*, 2019).

Thus, when examining the last three intervals (post-1943) in Figures 3.14, 3.15 and 3.16, an important observation becomes evident. Over time, a noticeable trend has emerged, indicating a southward shift of the entire SAD pattern. This shift is likely influenced by the expanding Hadley cell and the southward movement of the SASH, as documented in recent studies (HU; FU, 2007; HU; HUAN; ZHOU, 2018; REBOITA *et al.*, 2019). As a result, the shifting SASH leads to corresponding southward displacement of SST anomaly patterns. The expansion of the Hadley cell and the southward shift of the SASH are likely linked to global warming caused by increased greenhouse gas emissions and stratospheric ozone depletion (HU; HUAN; ZHOU, 2018). These findings strongly support the notion that the observed changes in the SAD over the past few decades are indeed associated with

climate change.

Since the periods prior to 1943 data exhibit low reliability, we give a concise examination of SCF_1 focusing on the subsequent time intervals. Examining the NOAA-CIRES dataset (Figure 3.14), the SCF_1 values suggest a diminishing significance of the SAD as a mode of covariability over the SAO over time. The values decrease from 73.7% in the 1943-1978 to 56.6% in the 1997-2014 interval. Conversely, for the ERA-20C and ERA5 reanalyses (Figures 3.15 and 3.16, respectively), the SCF_1 demonstrates a fluctuation with values around 50% during the periods 1942(50)-1978 and 1997-2010(20), with a peak reaching approximately 66% in the 1978-1997 interval.

SAD configurations found by the SVD analysis in interval periods based on the IPO itervals, are now presented for the previously examined seasonal periods (DJF, MAM, JJA, and SON). These analyses are depicted in Figure 3.17 for the ERA5 reanalysis. In the appendix C, Figures C.1 to C.4 present the the same analysis for the NOAA-CIRES, and similarly, Figures C.11 to C.14 display the results for the ERA-20C reanalysis. It is noteworthy that, if we consider periods post 1943 across all three datasets, the poleward shift of the SAD pattern identified in the annual configuration of the mode is more pronounced during DJF and SON (Figures 3.17a-c and 3.17j-l for the ERA5 reanalysis, Figures C.1 and C.4 for the NOAA-CIRES, and Figures C.11 and C.14 for the ERA-20C), representing austral summer and spring, respectively. Similar to the findings for the annual analysis (Figure 3.15), there is a discrepancy in representing the SAD configuration in periods before 1943, particularly prominent in the ERA-20C dataset across all seasons (Figures C.11 to C.14).

In relation to SCF_1 for the different seasons and IPO intervals, considering post-1943 periods, two trends were identified across the three utilized reanalyses: an increasing importance of SAD over time and a greater values of SCF_1 during negative IPO phases in some cases. For the DJF season (Figures 3.17a-c, C.1 and C.11), higher SCF_1 values were observed for IPO- periods compared to the IPO+ period. There were slight enhancements in importance of the SAD for ERA5 and NOAA-CIRES reanalyses (Figures 3.17d-f and C.2), while ERA-20C exhibited a substantial increase in importance (Figure C.12) during the MAM. In the JJA quarter (Figures 3.17g-i, C.3 and C.13), there was an increase in SCF_1 values for ERA5 and ERA-20C reanalyses, whereas NOAA-CIRES showed higher values during IPO- intervals. For the SON season (Figures 3.17j-l, C.4 and C.14), an eleva-

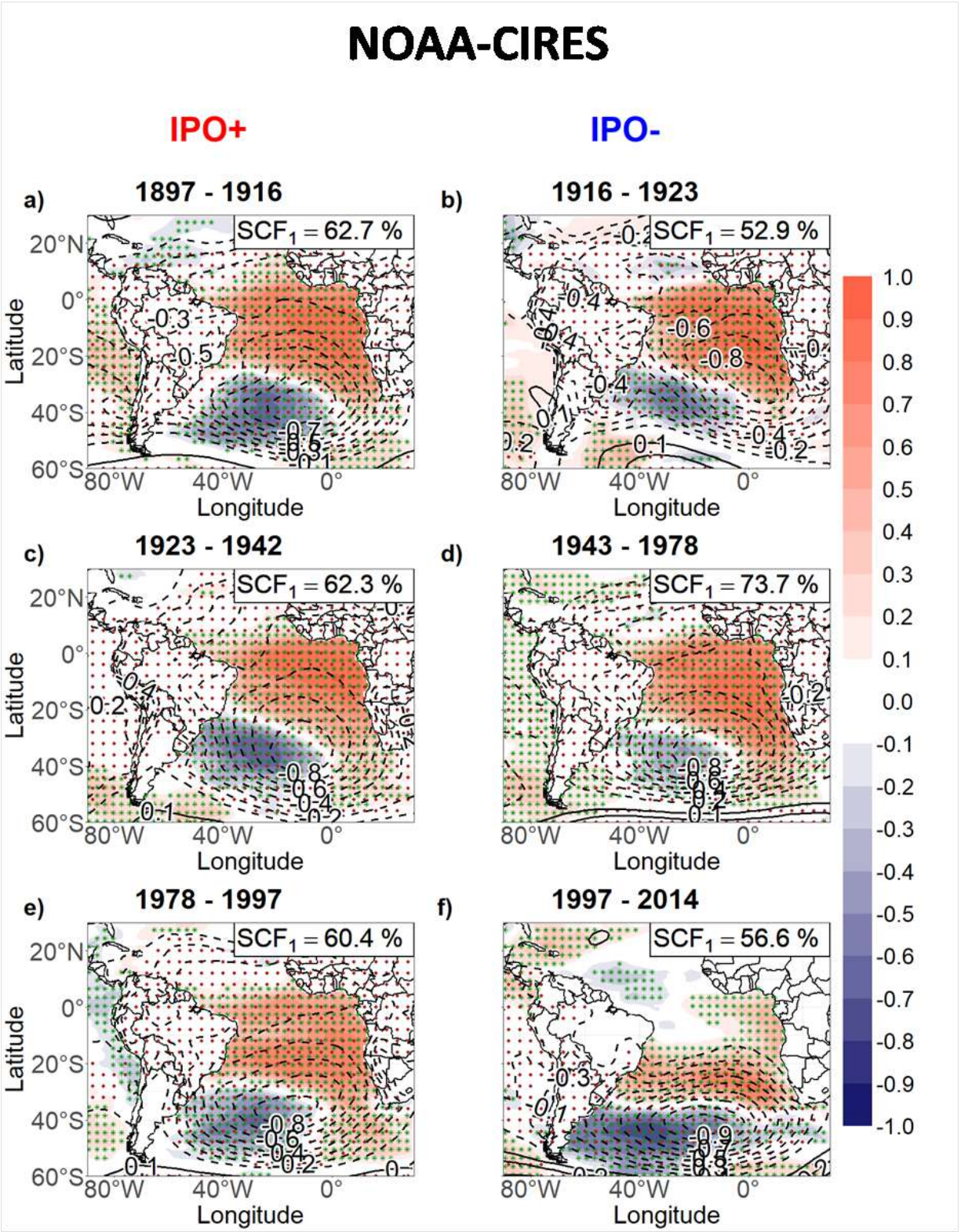

Figure 3.14: Same as in Figure 3.1, except for the periods a) 1950-1978, b) 1978-1997 and c) 1997-2020, which are associated with the phases of the Interdecadal Pacific Oscillation (IPO). On the left side, there are fields corresponding to the positive IPO periods (IPO+) and to the right side the negative periods of the IPO (IPO-). Analyzes made with NOAA-CIRES 20th Century V2c reanalysis. Correlations with a statistical confidence level above 95% are shown in green (yellow) dots for SST (MSLP) anomalies.

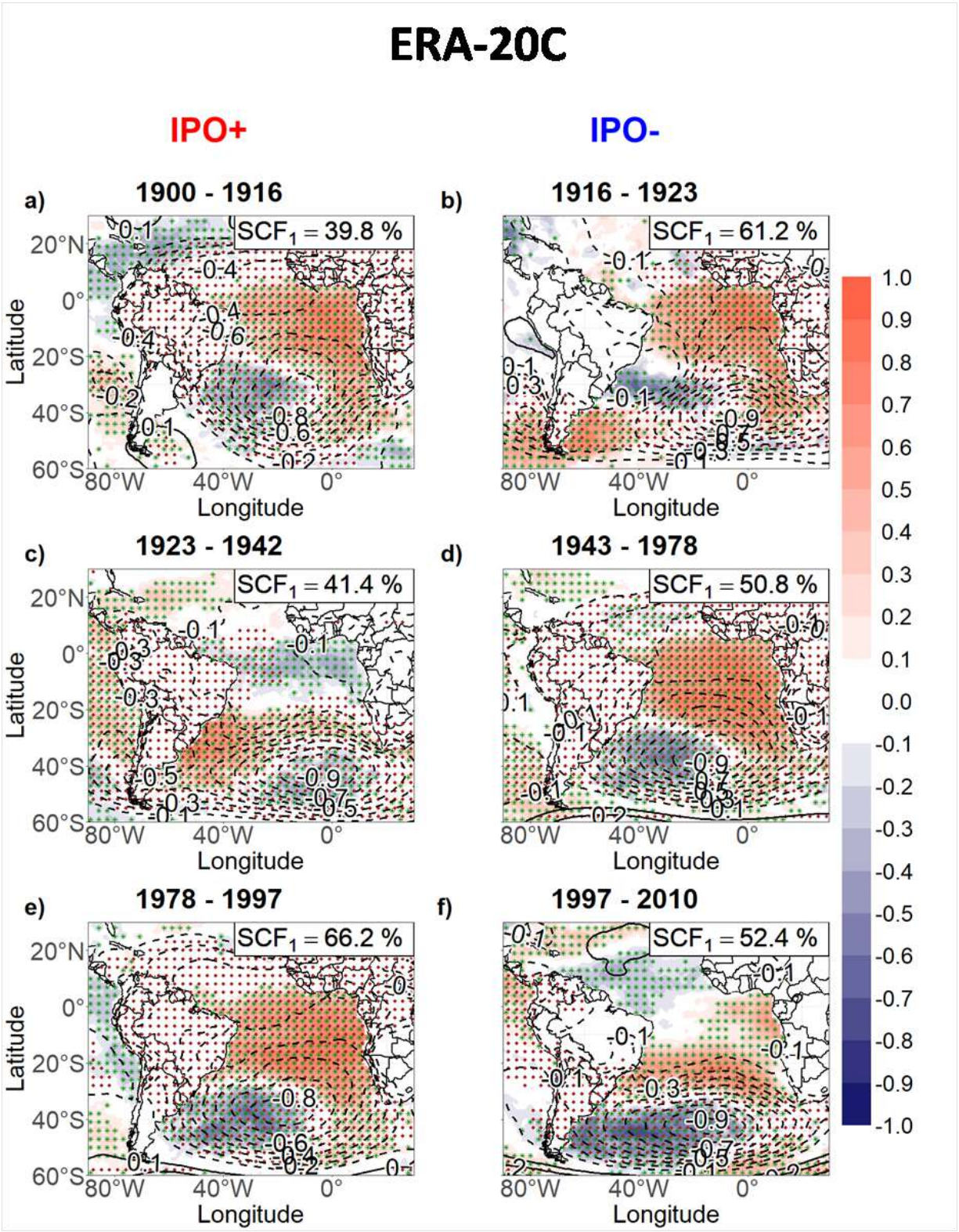

Figure 3.15: Same as in Figure 3.14, except for the ERA-20C reanalysis

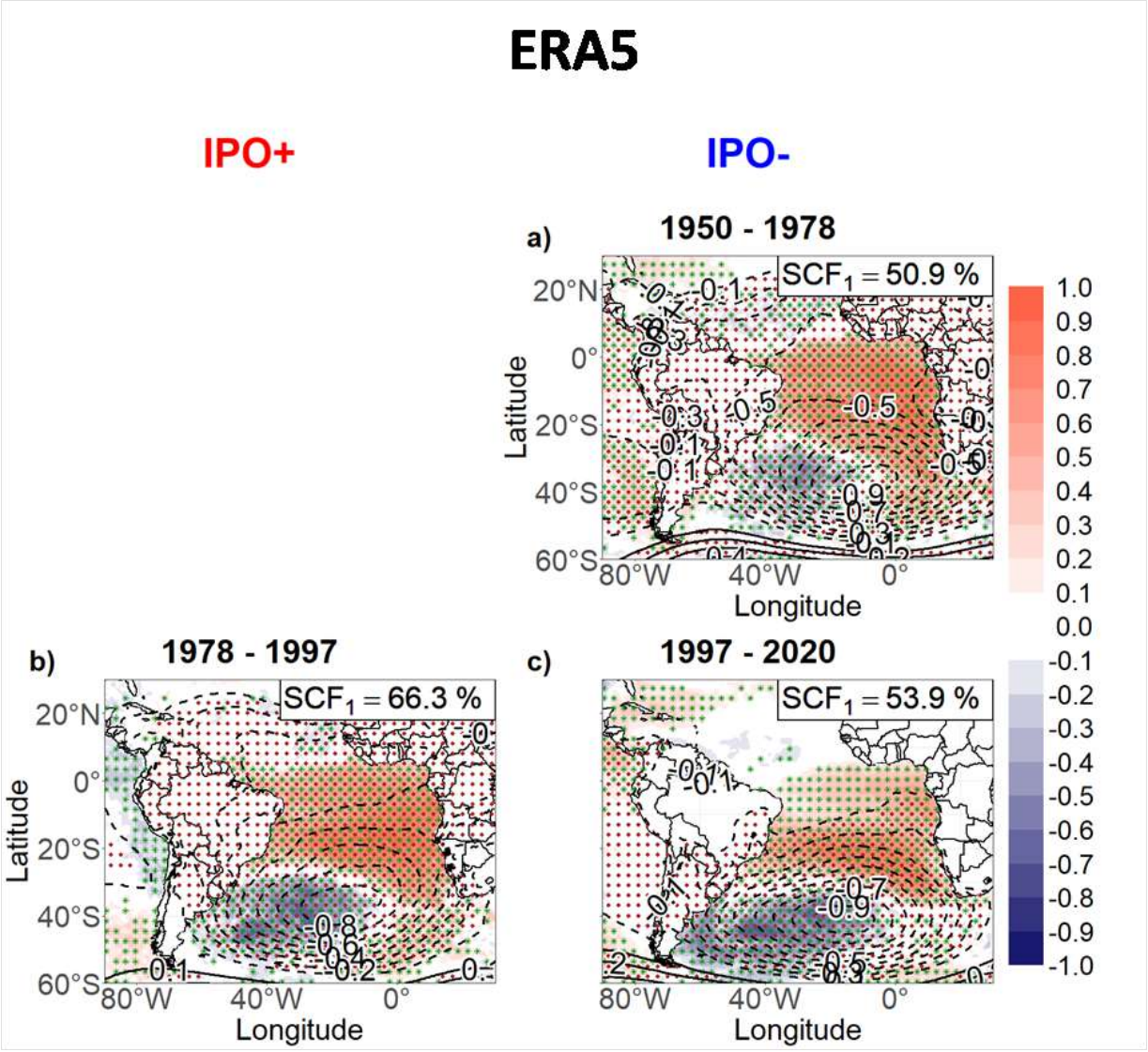

Figure 3.16: Same as in Figure 3.14, except for the ERA5 reanalysis

tion in SCF_1 values was observed for ERA5 and ERA-20C reanalyses, with NOAA-CIRES exhibiting higher values during the IPO- intervals.

The annual anomalies in SST and MSLP over the Pacific and Atlantic ocean basins, corresponding to each SAD phase within the IPO-associated intervals are illustrated in Figure 3.18 for the ERA5 reanalysis, in Figure C.5 for the NOAA-CIRES and in Figure C.15 for the ERA-20C. Two key observations stand out for the three most recent intervals in this analysis and for all datasets. First, there is a clear southward shift in the SAD pattern over the SAO, as previously observed in other analyses. Second, there exists an interchange relationship between the SAD and the equatorial Pacific SST anomalies according to the IPO phase. During the IPO- periods (1943[50]-1978 and 1997-2010[14

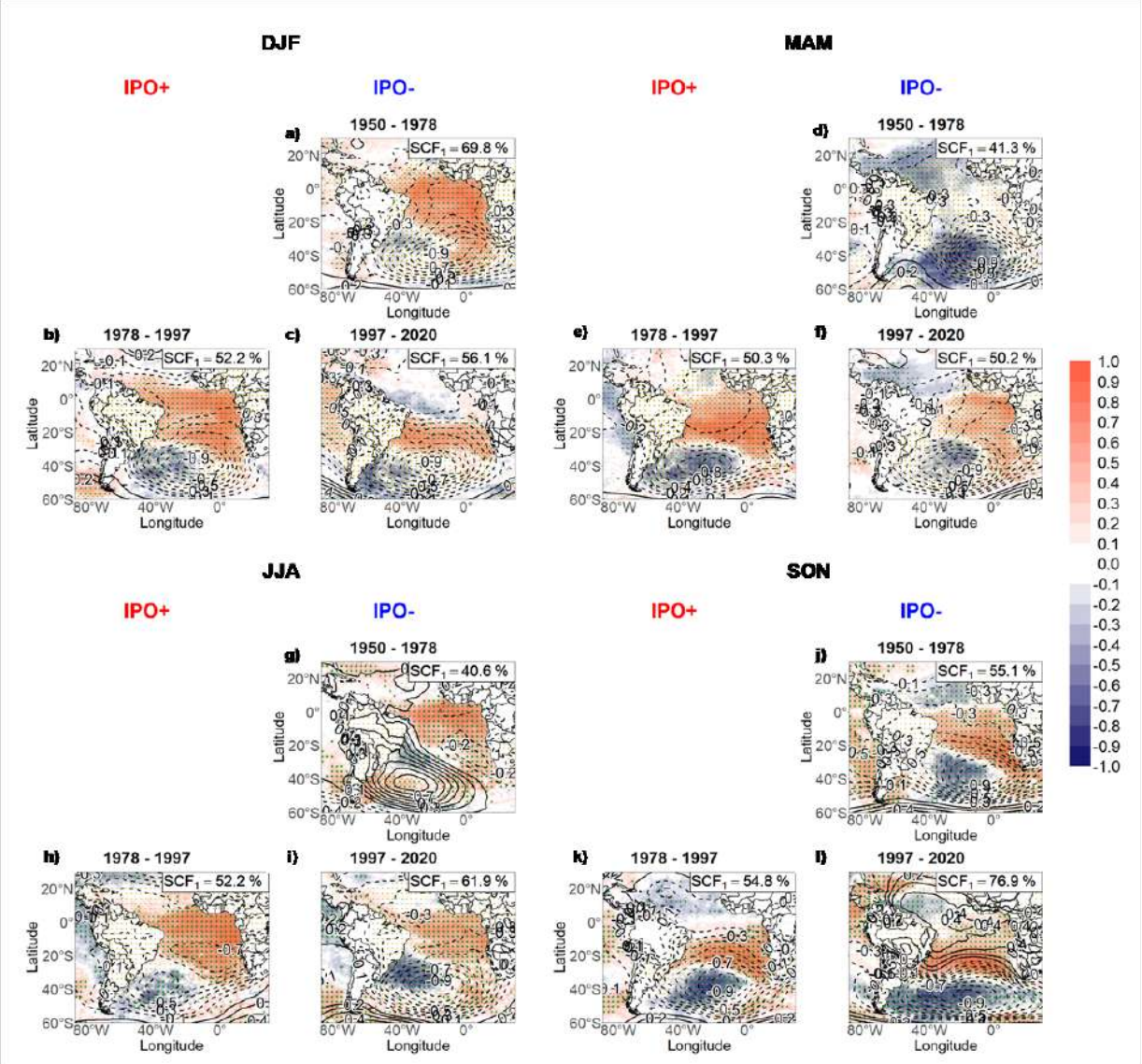

Figure 3.17: Same as Figure 3.16 except for December-February (DJF), March-May (MAM), June-August (JJA) and September-November (SON) quarters. For each item, the fields corresponding to the positive periods of the IPO (IPO+) are positioned on the left side, and on the right side the negative periods of the IPO (IPO-). Correlations with a statistical confidence level above 95% are shown in green (yellow) dots for SST (MSLP) anomalies.

and 20] intervals), positive (negative) SST anomalies are observed in the Pacific Niño region simultaneously with a SAD+ (SAD-) phase (Figures 3.18a-b and 3.18e-f for the ERA5 reanalysis, Figures C.5g-h and C.5k-l for the NOAA-CIRES, and Figures C.15g-h and C.15k-l for the ERA-20C). For the interval 1978-1997 (IPO+ phase), only the SAD negative phase (Figure 3.18d, C.5j and C.15j) displayed a significant relationship with the Pacific Niño SST anomalies. Intriguingly, positive SST anomalies were observed in the Pacific Niño region during this period, the opposite to what was verified in the periods 1943[50]-1978 and 1997-2010[14 and 20] (IPO- phase).

Moreover, two noteworthy trends have been identified in the Pacific Niño SST anomalies during the latest period, indicating an increase in intensity and a westward shift (Figures C.5e-f, C.15k-l and 3.18k-l). These alterations may be a factor to cause the changes in the atmospheric circulation patterns between the two ocean basins, as well as the modifications observed in SAD during these specific negative IPO intervals.

The observed interchange in the relationship between SAD and Pacific Niño, as revealed in this study, bears resemblance to the findings documented by Kayano, Andreoli and Ferreira de Souza (2013). Their research unveiled a similar alternating pattern between these two modes during specific time periods in the previous century. There, a positive (negative) lag-correlation between the SAD and ENSO was identified for the 1940-1980 (1975-2000) period, in which ENSO events tended to precede (follow) SAD events by 6 months (one year). However, it is worth noting that Kayano, Andreoli and Ferreira de Souza (2013) directly correlated the SAD and ENSO without considering the IPO, which is an important point to consider in our analysis.

SST and MSLP anomalies over the Pacific and Atlantic ocean basins, in each SAD phase and for the IPO intervals, but now specifically for seasons DJF and MAM are presented in Figure 3.19, and for the JJA and SON is shown in Figure 3.20. The corresponding fields for the NOAA-CIRES dataset can be found in Figures C.6 to C.9, while for ERA-20C, they are displayed between Figures C.16 and C.19, with a separate representation for each season. Despite the alternating Pacific Niño-SAD relationship observed in the annual analysis, a consistent positive association between Pacific Niño and SAD is evident in the DJF and SON quarters (Figures 3.19a-f and 3.20g-l for ERA5, C.6g-l and C.9g-l for NOAA-CIRES [post-1943], and C.16g-l and C.19g-l for ERA-20C [post-1943]). This positive relationship holds true for all IPO intervals, as indicated by positive (negative)

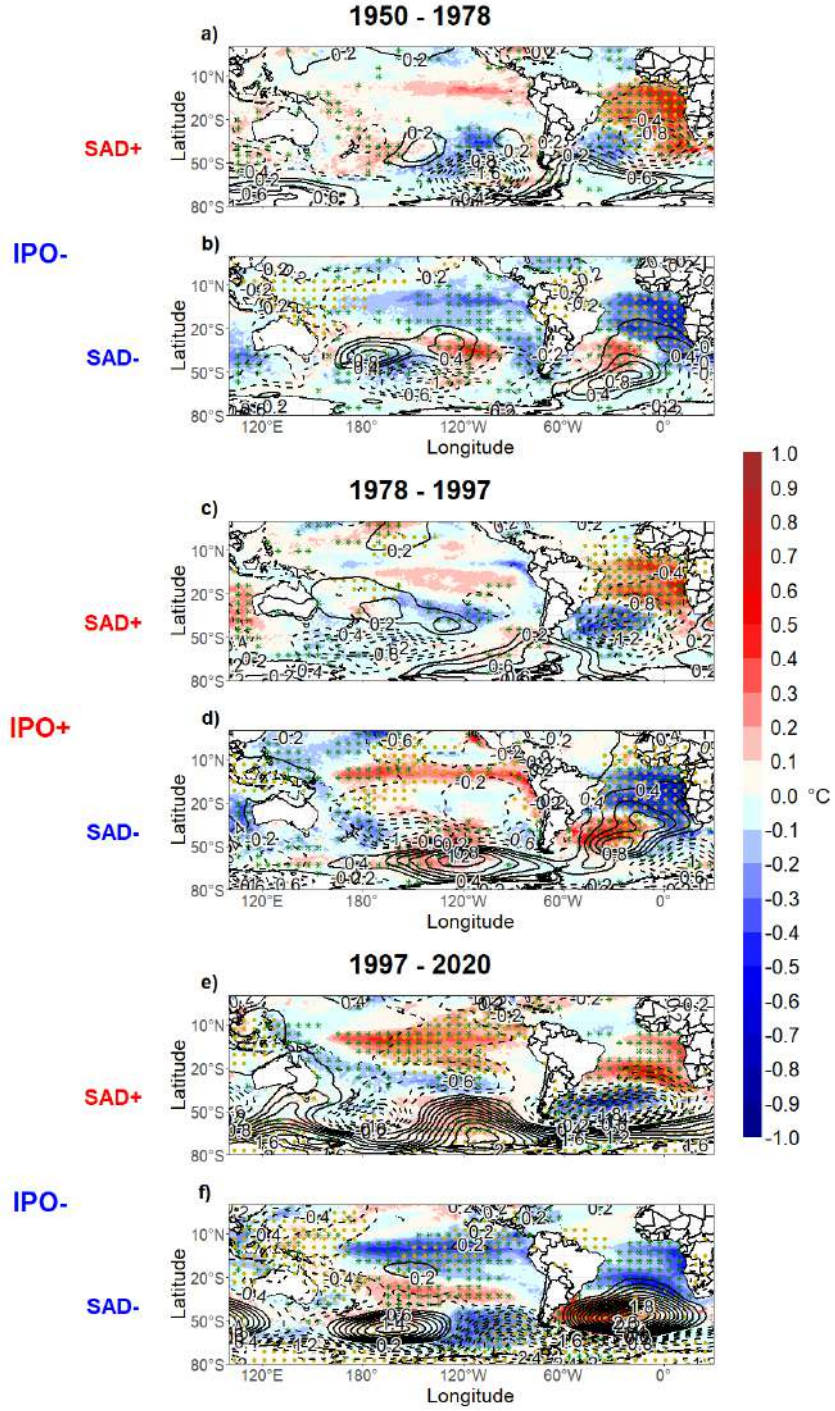

Figure 3.18: Composites with SST anomalies (in colors) and MSLP anomalies (contours) for the positive (SAD+) and negative (SAD-) phases of the South Atlantic Dipole for the periods 1950-1978 (itens a) SAD+ and b) SAD-), 1978-1997 (itens c) SAD+ and d) SAD-) and 1997-2020 (itens e) SAD+ and f) SAD-), which are associated with the phases of the Interdecadal Pacific Oscillation (IPO). IPO+ (IPO-) indicates a positive (negative) phase of IPO. The domain displayed is over the South Pacific and Atlantic basins. Calculated for the ERA5 reanalysis. Values with a statistical confidence level above 95% are shown in green (yellow) dots for SST (MSLP) anomalies.

SST anomalies over the Pacific Niño region corresponding with the positive (negative) phase of SAD over SAO. However, it is worth noting that the intensity of Pacific Niño anomalies during the 1978-1997 (IPO+ interval) is relatively lower compared to the 1950-1978 and 1997-2020 (IPO- intervals). Additionally, notable intense anomalies are observed in both ocean basins during the last interval, accompanied by the southward displacement of the SAD pattern (Figures 3.19e-f, 3.20k-l, C.6k-l, C.9k-l, C.16k-l and C.19k-l).

Regarding the JJA quarter, Figures 3.20a-f for ERA5, C.8 for NOAA-CIRES, and C.18 for ERA-20C demonstrate that negative (positive) SST anomalies in the Pacific Niño region are associated with positive (negative) SAD phases. Over time, there appears to be a subtle increase in the significance of this association for all datasets in the post-1943 period. Otherwise, when examining the MAM quarter (Figures 3.19g-l for ERA5, C.7 for NOAA-CIRES, and C.17 for ERA-20C), establishing a clear Pacific Niño-SAD relationship becomes challenging due to the discrepancies among the different datasets.

In Figures 3.21 for ERA5 dataset, C.10 for NOAA-CIRES, and C.20 for ERA-20C, the analysis explores the association between the SAD phases and the IPO intervals for the different ENSO conditions (El Niño, Neutral and La Niña). These statistics are disposed for the year as a whole and for the different seasons of the year. For the annual statistics (Figures 3.21a-c, C.10a-c and C.20a-c), one main feature is notable. Comparing the positive and negative phases of the SAD, an alternation in the SAD-ENOS relationship is verified according to the different IPO intervals. A greater number of positive (negative) phases of the SAD are found associated with El Niño (La Niña) events during the negative phases of the IPO. During the positive phase of the IPO, this relationship is inverted, that is, there is a greater number of negative (positive) phases of the SAD associated with El Niños (La Niñas).

During the DJF and SON seasons, there is a prevalence in the number of months in the SAD positive phase, compared to the SAD negative phase, associated with El Niño events in all IPO intervals (Figures 3.21d, 3.21m, C.10d, C.10m, C.20d and C.20m). Although the occurrence of SAD+ is relatively lower during the IPO+ interval (1978-1997), they still outweigh the SAD- phases in terms of month count. For La Niñas in the DJF and SON quarters (Figures 3.21f, 3.21o, C.10f, C.10o, C.20f and C.20o), the prevalence of negative SAD phases is verified only for the IPO- intervals (1950-1978 and 1997-2020). It is worth remembering here that works such as Kayano and Andreoli (2006)

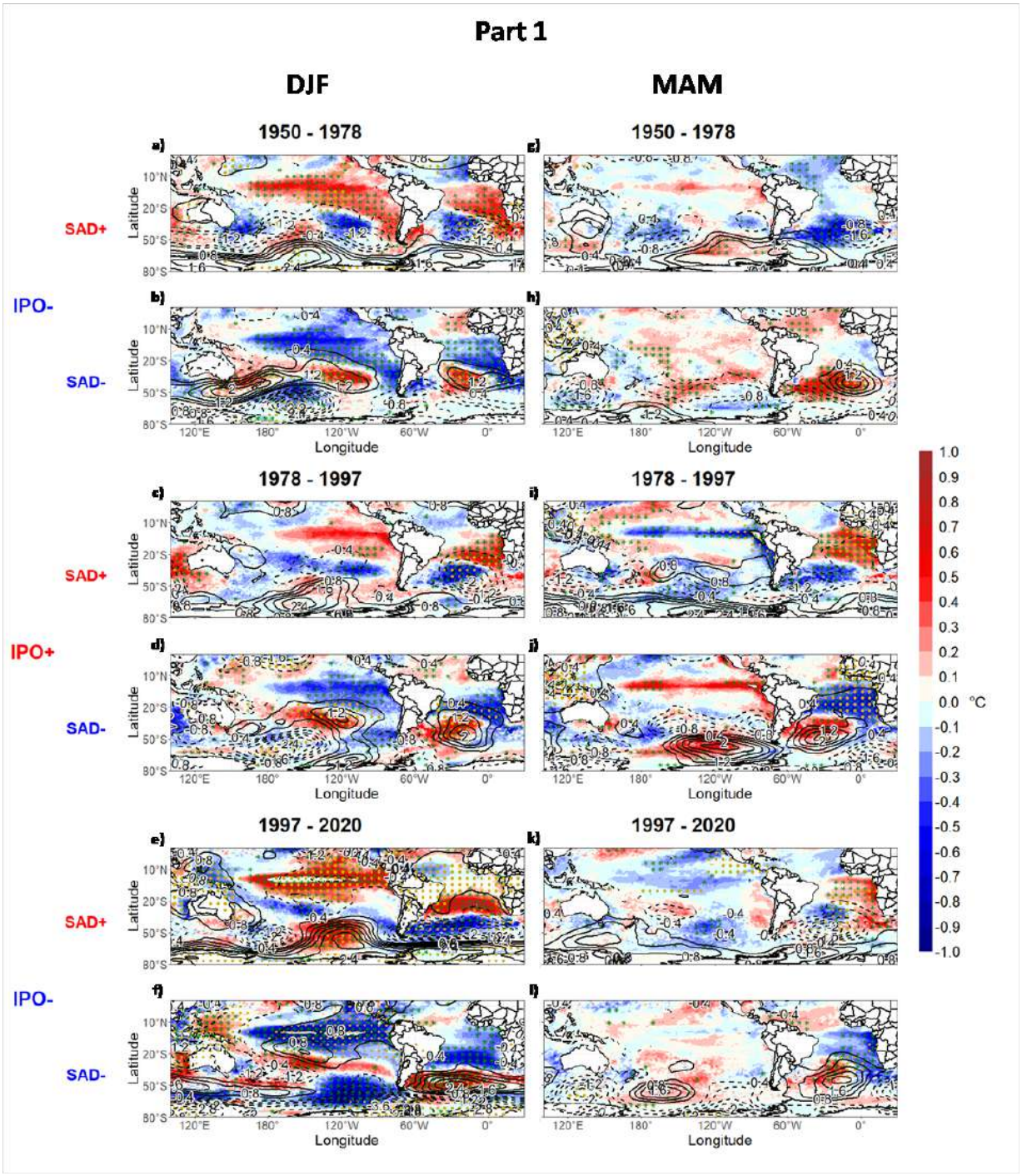

Figure 3.19: The same as in Figure 3.18 but for the DJF (itens a-f) and MAM (itens g-l) seasons. Values with a statistical confidence level above 95% are shown in green (yellow) dots for SST (MSLP) anomalies.

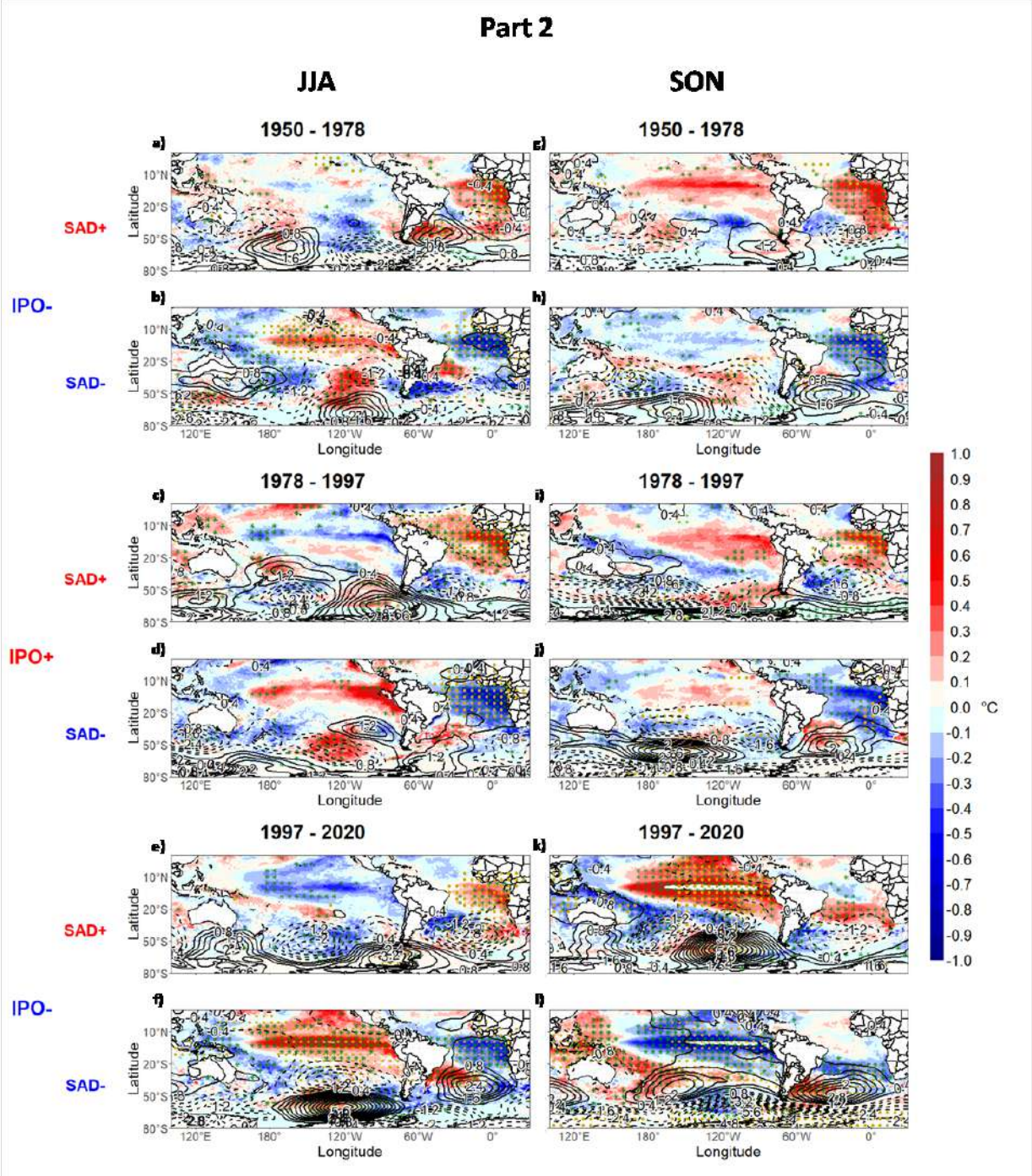

Figure 3.20: The same as in Figure 3.18 but for the JJA (itens a-f) and SON (itens g-l) seasons. Values with a statistical confidence level above 95% are shown in green (yellow) dots for SST (MSLP) anomalies.

and Rodrigues *et al.* (2011) indicate a modulation of the SAD by the central Pacific ENSO via teleconnections. Based on these findings, along with the observed positive relationship between the Pacific Niño and the SAD during DJF and SON (Figures 3.19a-f, 3.20g-l, C.6, C.9, C.16 and C.19), and the progressive increase in SCF_1 during DJF months coinciding with the southward expansion of the SAD (Figures 3.17a-c, C.1 and C.11), it can be hypothesized that an important factor influencing the more southerly positioning of the SAD, which is commonly observed during these seasons, is the central ENSO conditions. However, further investigation is required to explore this hypothesis in a more robust manner. On the other hand, the results obtained here suggest that the hypothesis of ENSO modulation by the SAD, as suggested by Kayano, Andreoli and Ferreira de Souza (2013), is associated with the northernmost configuration of the SAD, typically observed in the JJA months. In this configuration, more significant SST anomalies are observed over the most equatorial portion of the Atlantic, generating the necessary conditions for such a hypothesis.

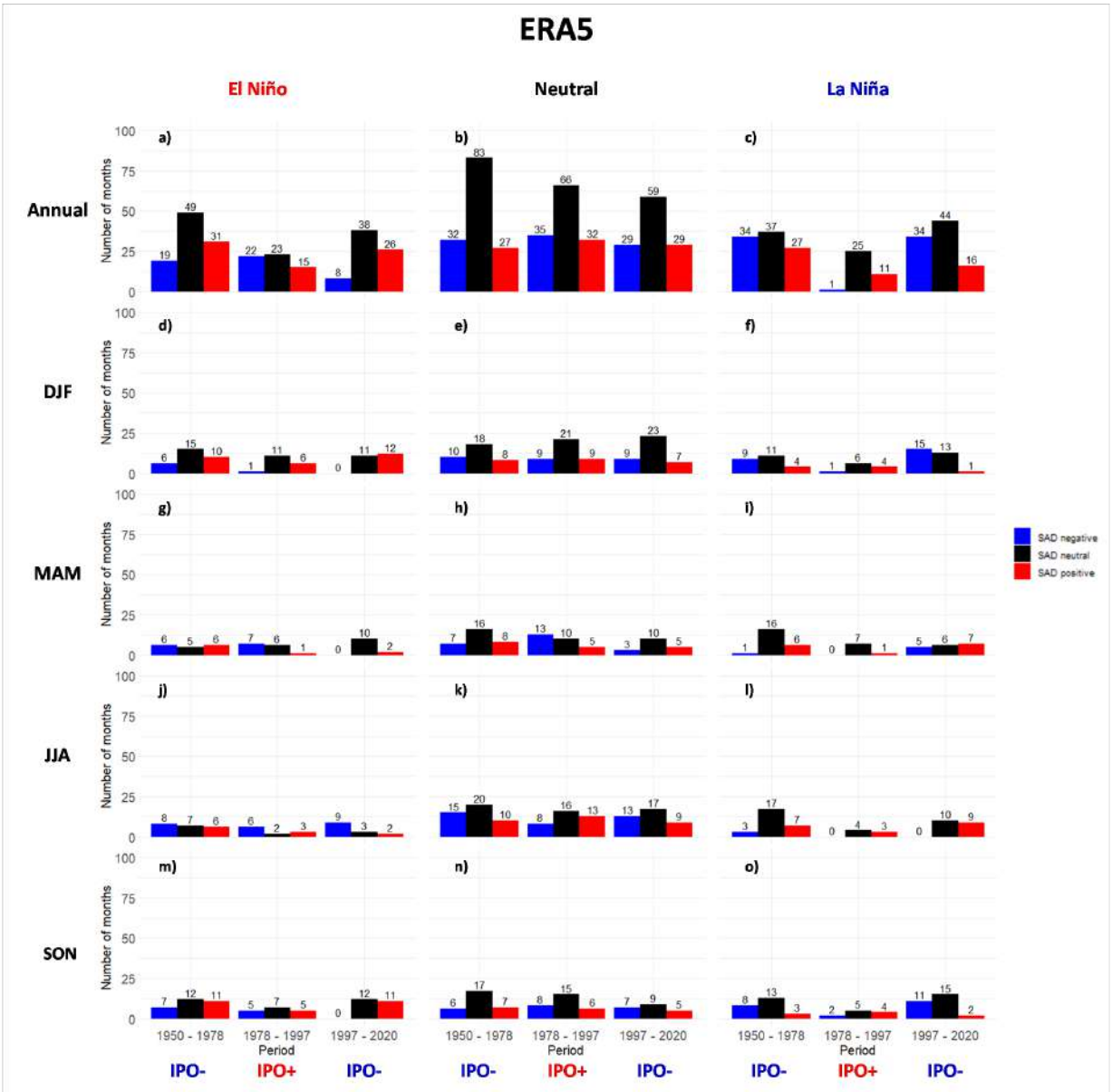

Figure 3.21: Number of months in the negative (blue bars), neutral (black bars) and positive (red bars) phase of SAD, for each IPO intervals during El Niõs (figures on the left side), Neutral ENSO (central figures) and La Niãs (figures on the right side) events. The Figures are disposed according to the annual (itens a-c), DJF (itens d-f), MAM (itens g-i), JJA (itens j-l) and SON (itens m-o).

3.1.4 *Evolution of atmospheric characteristics of the South Atlantic Dipole in austral summer*

During the summer months, there is a particularly interisting interplay between the SAD and precipitation patterns over South America, exhibiting significant changes throughout the study period. Hence, the DJF season was selected to highlight the principal alterations in oceanic and atmospheric patterns associated with the SAD during the analyzed IPO intervals. In order to minimize the impact of external factors on the relationship between the SAD and the climate of South America, the composites calculations in this subsection exclude ENSO periods. The results obtained from ERA5 reanalysis are shown within this subsection, while the NOAA-CIRES and ERA-20C are presented in the Appendix D.1 for comparison. There is no field for the SAD+ period 1997-2010 associated with the ERA-20C reanalysis (Figures D.5e, D.6e, D.6e, D.7, D.8e) due to the non-identification of this phase for this dataset during DJF months in this interval, as can be noticed in the graph of Figure C.20e.

Figure 3.22 presents the DJF precipitation anomalies associated with each phase of the SAD and for different periods of the IPO for the ERA5 reanalysis. The same fields are shown in the Figures D.1 and D.5 for the NOAA-CIRES and ERA-20C respectively. For all the datasets, a tripole pattern of rainfall anomalies between NNE-CEBR-SESA is observed for the SAD- in the interval 1950-1978 (Figures 3.22b, D.1b and D.5b) and the SAD+ of the period 1978-1997 (Figures 3.22c, D.1c and D.5c). This pattern is similar with the observed rainfall anomalies for DJF across the period 1950-2020 (Figures 3.10a-b, B.4a-b and B.11a-b).

In contrast, the anomalous patterns observed during the SAD+ period from 1950 to 1978 (Figures 3.22a, D.1a and D.5a) displays a tripole pattern NNE-CEBR-SESA with the same sign as SAD- for the same interval, except for the western Amazonian region where contrasting anomalies are observed between the two cases. In a different manner, for the SAD- period from 1978 to 1997 (Figures 3.22d, D.1d and D.5d), a well-defined configuration is not observed, with only a few points exhibiting significant anomalies across the study area.

The latest and southernmost arrangement of the SAD during the southern summer (shown in Figures 3.17c, C.1f and C.11f) exhibits a broader contrast in precipitation ano-

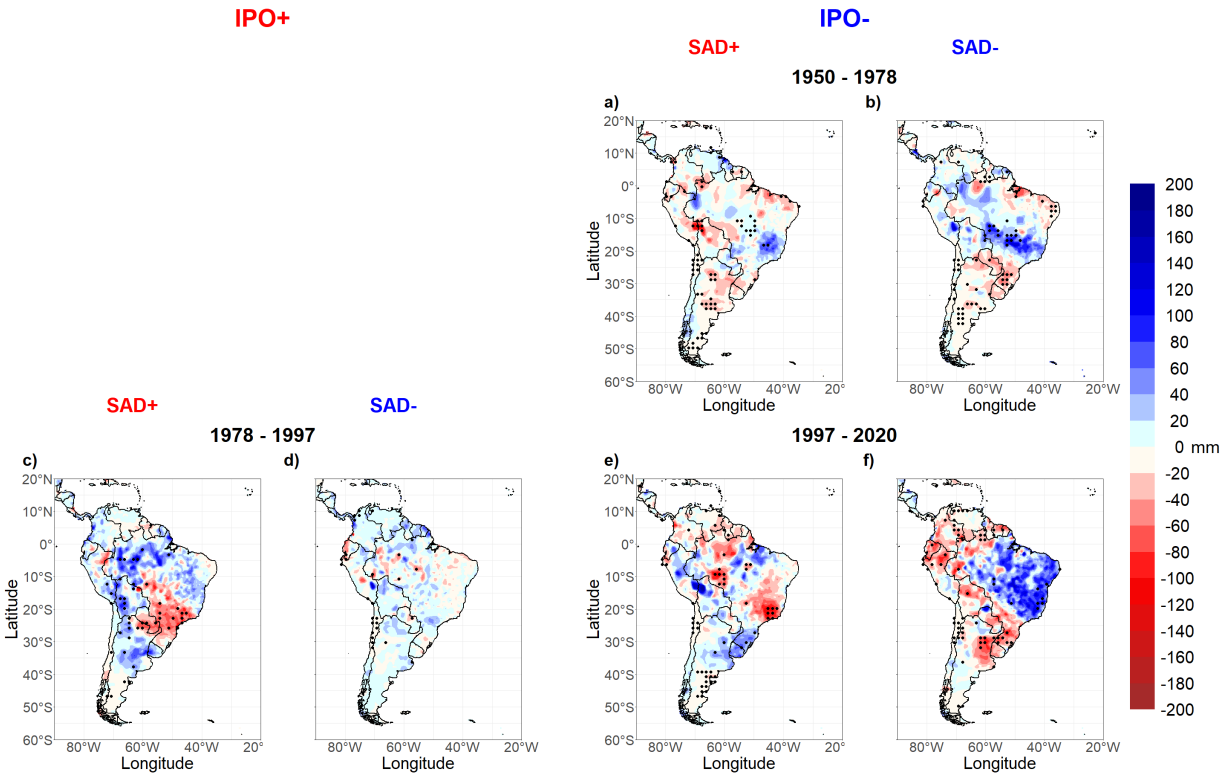

Figure 3.22: Composites with precipitation anomalies (in color) for the positive (SAD+) and negative (SAD-) phases of the South Atlantic Dipole, determined from the ERA5 reanalysis dataset and for the December-February quarter (DJF) season. Calculated with GPCC precipitation dataset. Determined for the IPO intervals a-b) 1950-1978, c-d) 1978-1997 and e-f) 1997-2020. ENSO periods are disregarded in this analysis. Values with a statistical confidence level above 95% are shown in dotted lines.

malies between the CEBR and the SESA (Figures 3.22e-f, D.1e-f and D.5f). In the initial period under analysis (Figures 3.22b, D.1b and D.5b), the positive phase of the SAD was associated with increased precipitation anomalies in the NNE, but these anomalies disappeared entirely in the final interval (Figures 3.22f, D.1f and D.5f). Therefore, while it is true that some instances lacked identifiable patterns, the prevailing trend undeniably demonstrates a shift from the tripole pattern (NNE-CLBR-SESA) observed in previous periods to a clear dipole between the CEBR and SESA regions in the final period of analysis.

Composite maps of SST and MSLP anomalies for the DJF months and different time intervals of the IPO are presented in Figures 3.23 for the ERA5, D.2 for the NOAA-CIRES and D.6 for the ERA-20C. It is important to note that the exclusion of ENSO events in these analyses leads to significant differences between the observed patterns in these composites and the disposition found by the first SVD mode over the SAO (as depicted in Figures

3.17a-c, C.1d-f and C.11d-f). However, when we consider the influence of ENSO events, it is found a SAD configuration that closely resembles the SVD patterns (for example, compare Figures 3.19a-f, specifically over the SAO, with Figures 3.17a-c).

In light of this, for all the different reanalysis, the MSLP and SST anomaly maps presented in Figures 3.23, D.2 and D.6 reveal two primary SAD configurations. The first pattern closely resembles the typical SAD structure, characterized by a dipole of SST anomalies spanning from the tropical to extratropical regions of the SAO, accompanied by a superimposed monopole of MSLP anomalies. This disposition is evident during the intervals of 1950-1978 for both SAD phases (Figures 3.23a-b, D.2a-b and D.6a-b) and for the SAD negative phase in the 1978-1997 interval (Figures 3.23d), D.2d and D.6d). Otherwise, the second pattern is distinguished by a southward shift in the dipole of SST anomalies, without a clearly defined monopole of MSLP anomalies over the SAO. Instead, this configuration exhibits fragmented MSLP anomalies with the same sign as the anticipated monopole, dispersed across the SAO. Plus, a dipole of small anomalous MSLP centers can be observed between the southeastern coast of Brazil and the coast of Argentina. This arrangement is observed during the 1978-1997 interval (SAD+ phase) (Figures 3.23c, D.2c and D.6c) and for both SAD phases in the most recent period under examination (Figures 3.23e-f, D.2e-f and D.6f). An increased (decreased) cyclonic activity along the coast of Argentina and reduced (enhanced) cyclone formation near the southeastern coast of Brazil are suggested by these regional dipole of MSLP anomalies during the positive (negative) phases of the SAD, agreeing with the results of Bombardi *et al.* (2014). Consequently, the positive (negative) rainfall anomalies in the CEBR region during the SAD- (SAD+) can be associated with more (less) cyclonegenesis near the southeastern coast of Brazil. It is noteworthy that this pattern becomes more prevalent in the last intervals.

Figures 3.24, D.3 and D.7 displays wind and specific moisture anomalies at 850 mb (low troposphere levels). During the positive phase of the SAD in the 1978-1997 and 1997-2020 intervals (Figures 3.24c, 3.24e, D.3c, D.3e and D.7c), cyclonic anomalies are observed along the Argentine coast, while near the southeastern coast of Brazil it is verified an anticyclonic anomaly, aligning with the dipole of MSLP anomalies between these two regions (Figures 3.23c, 3.23e, D.2c, D.2e and D.6c). This arrangement promotes a wet flow from the Amazon region towards the SESA, while inhibiting the same airflow over the CEBR. In the case of the SAD negative phase, during the most recent interval (Figures 3.24f, D.3f

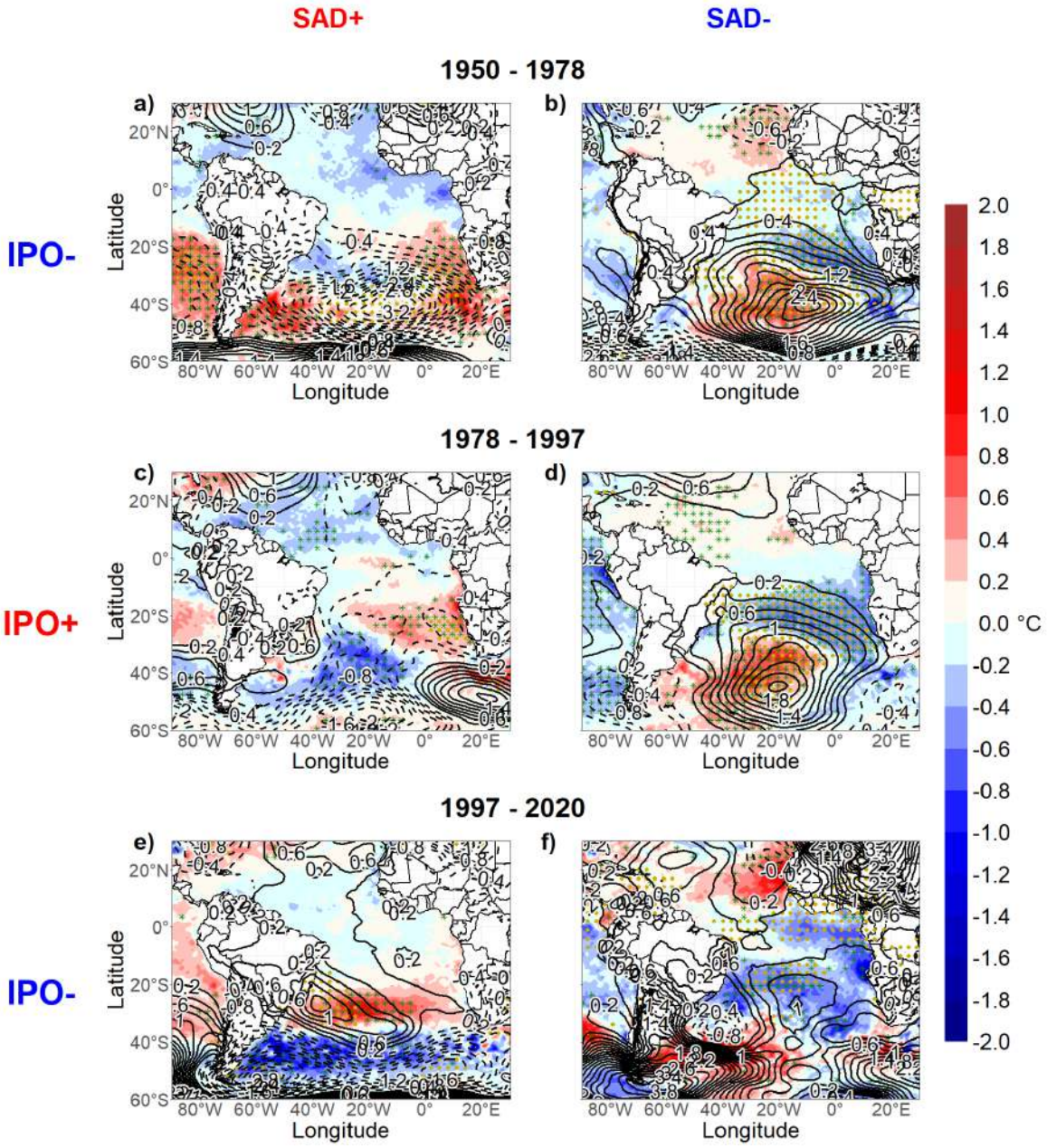

Figure 3.23: Composites with SST anomalies (in colors) and MSLP anomalies (contours) for the positive (SAD+) and negative (SAD-) phases of the South Atlantic Dipole for the December-February quarter (DJF) and for the periods a-b) 1950-1978, c-d) 1978-1997 and e-f) 1997-2020. ENSO periods are disregarded in this analysis. Values with a statistical confidence level above 95% are shown in green (yellow) dots for SST (MSLP) anomalies.

and D.7f), the cyclonic anomaly observed along the southeastern coast of Brazil favors a moist airflow over the CEBR.

Over NNE region, where negative precipitation anomalies were detected during both SAD phases of the 1950-1978 interval (Figures 3.22a-b, D.1a-b and D.5a-b), a negative moisture anomalies can be detected over the region (as shown in Figure 3.24a-b, D.3a-b and D.7a-b). On the other hand, the positive precipitation anomalies over the NNE during the SAD positive phase in the 1978-1997 period (Figures 3.22c, D.1c and D.5c) show little evidence of being associated with moisture anomalies over the region (Figures 3.24c, D.3c and D.7c). In the most recent interval (1997-2020), where no anomalous precipitation signals are present over the NNE in either SAD phase (Figures 3.22e-f, D.1e-f and D.5f), no significant anomalies can be seen in the moisture flow across the region (Figures 3.24e-f, D.3e-f and D.7f).

Wind and divergence anomalies at 200mb (upper troposphere) are shown in Figures 3.25, D.4 and D.8. For the SAD positive phases of 1978-1997 and 1997-2020 periods (Figures 3.25c, 3.25e, D.4c, D.4e and D.8c), the presence of anticyclonic anomalies close to the southern coast of Brazil enhances the strength of the subtropical jet around 40°S. As the region where the jet entrance is conducive to convection, this atmospheric circulation pattern facilitates precipitation over the SESA. On the other hand, a cyclonic circulation anomaly is observed over the same region during the SAD- in the 1997-2020 interval (Figures 3.25f, D.4f and D.8f). This feature also promotes the formation of the SACZ trough and provides dynamic support for positive precipitation anomalies over the CEBR region.

In the NNE region, during the SAD positive phase in the period of 1978-1997, besides moisture at low levels does not present a clear relationshipt with the occurrence of positive precipitation anomalies in the area (Figures 3.22c, D.1c and D.5c), positive divergence anomalies contribute to convection and create favorable dynamic conditions for positive rainfall anomalies (Figures 3.25c, D.4c and D.8c).

The merging of the precipitation anomaly poles of the CEBR with those of the NNE region across the three examined periods (depicted in Figures 3.22, D.1 and D.5), while still preserving the signal from the CEBR pole in this updated configuration, is specifically linked to the southward displacement of SST anomalies from the tropical pole of the SAD (Figures 3.23, D.2 and D.6). The convergence of moisture at low troposhphere is favored by the SST anomaly southward shift during the SAD positive (negative) phase on the

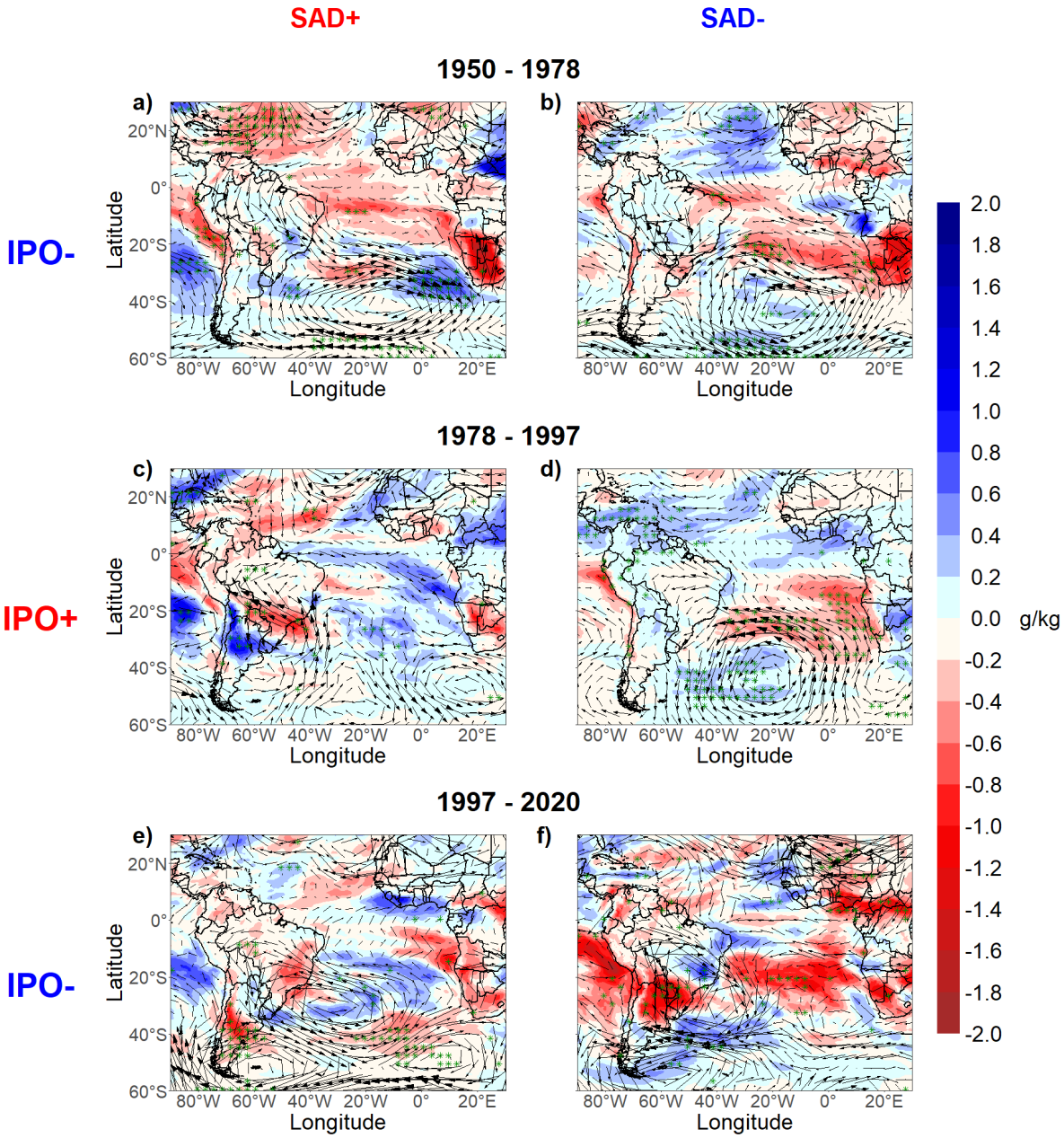

Figure 3.24: Composites with specific moisture anomalies (in colors) and wind anomalies (vectors) in 850 mb for the positive (SAD+) and negative (SAD-) phases of the South Atlantic Dipole, for the DJF quarter and for the IPO periods a-b) 1950-1978, c-d) 1978-1997 and e-f) 1997-2020. ENSO periods are disregarded in this analysis. Values with a statistical confidence level above 95% are shown in green dots for the specific moisture anomalies.

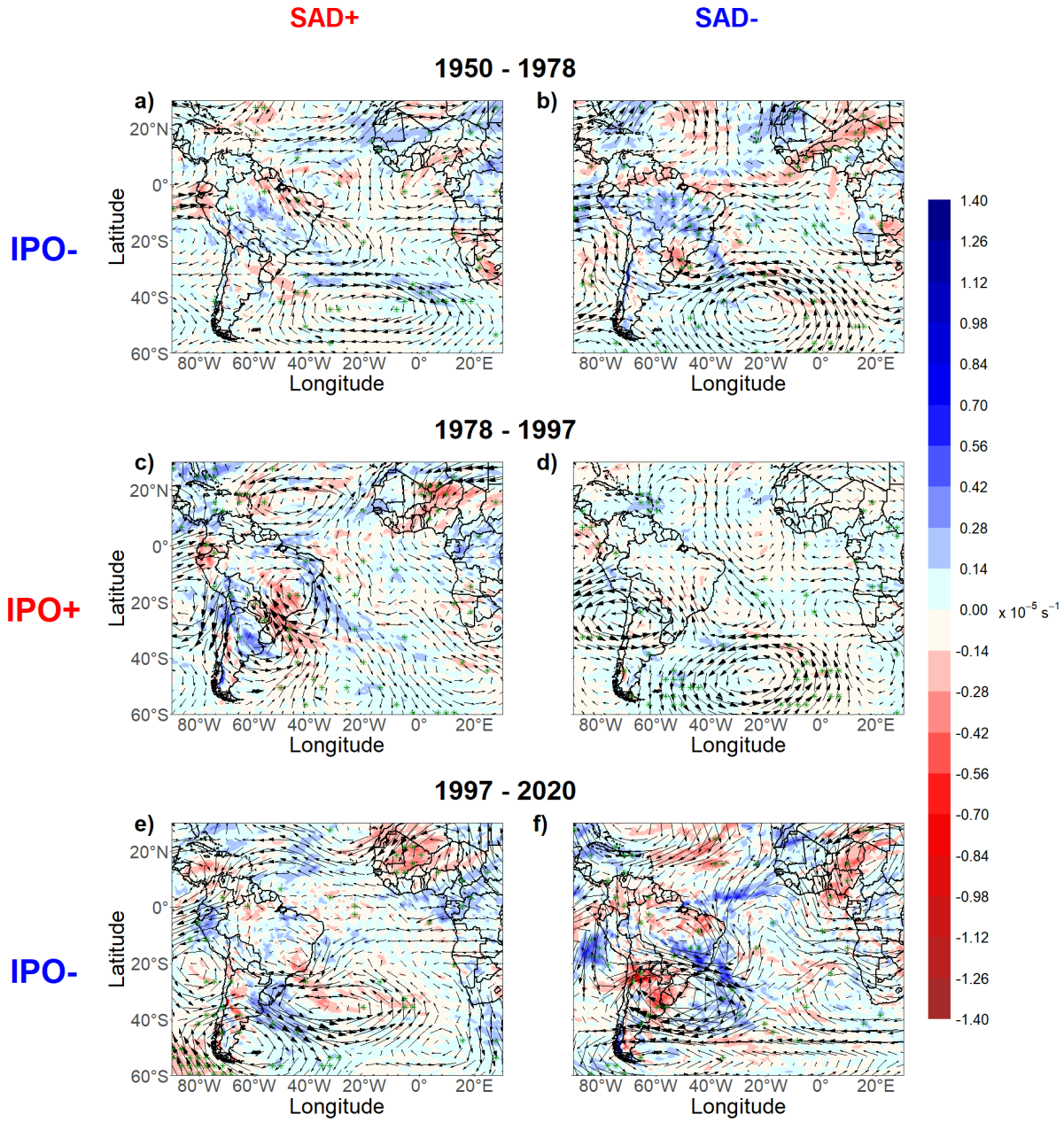

Figure 3.25: Composites with divergence anomalies (in colors) and wind anomalies (vectors) in 200 mb for the positive (SAD+) and negative (SAD-) phases of the South Atlantic Dipole, for the DJF quarter and for the IPO periods from a-b) 1950-1978, c-d) 1978-1997 and e-f) 1997-2020. ENSO periods are disregarded in this analysis. Values with a statistical confidence level above 95% are shown in green dots for the divergence anomalies.

NNE over time (Figures 3.24, D.3 and D.7). The intensification of the dipole of precipitation anomalies CEBR-SESA in the most recent period (Figures 3.22e-f, D.1e-f and D.5f), in comparison to the earlier periods (Figures 3.22a-b, D.1a-b and D.5a-b), appears to be associated with the overall southward shift of the SAD as a whole (Figures 3.17a-c, C.1 and C.11). The alteration in the summer pattern of the SAD has led to a shift in the anomalies of maximum westerlies (easterlies) in the upper-level airflow along the eastern coastline of South America (as evidenced in Figures 3.25, D.4 and D.8). During the SAD positive (negative) phase, this maximum has relocated from 30°S to 40°S, resulting in the strengthening (weakening) of storm tracks near 40°S. Consequently, this modification may have created dynamic conditions that amplify the frequency and/or intensity of cyclones over the La Plata river mouth (southeast coast of Brazil) during the SAD positive (negative) phase over time. This observation is corroborated by the dipole of MSLP and circulation anomalies between the southeastern coast of Brazil and the coast of Argentina in the later IPO intervals (Figures 3.23e-f, 3.24e-f, 3.25e-f, D.2e-f, D.3e-f, D.4e-f, D.6e-f, D.7e-f, D.8e-f).

3.2 CMIP6 Historical Simulations

In this section, it is shown the process of selecting the three most promising CMIP6 models (see Tables 2.1 and 2.2) for the analysis of SAD in the different future climate scenarios (next section), focusing on their hindcast skills. Subsequently, we evaluate the performance of these chosen models in simulating the SAD during the historical period. The discussion on projections from ScenarioMIP will be presented in the next section.

3.2.1 Evaluation and Selection of CMIP6 Models

The CMIP6 data validation involves a comparison between the CMIP6-HS outputs of multiple CMIP6 models and the reanalysis data utilized in this study (NOAA-CIRES, ERA-20C, and ERA5). As previously explained in subsection 2.3.5, the RMSE was calculated for each of the 42 CMIP6 models (estimated data) in relation to each reanalysis (observational data). This performance analysis covers the period from 1979 to 2010. The choice of the starting year (1979) marks the beginning of the "satellite era", indicating the increased reliability of the reanalysis data used as observational data in calculating the RMSE. The selection of the final year ensures temporal alignment among all datasets (as the ERA-20C reanalysis concludes in 2010), facilitating accurate comparisons. The spatial domain considered for the calculation of the RMSE is an area that encompasses the SAO and the South America (60°S-30°N and 90°W-30°E), an area that is of greatest interest to our study. The overall average RMSE among the three reanalyses and two variables ($RMSE_{all}$) was used to select the top three models. Table 3.1 displays the ranked overall average RMSE values for each of the 42 CMIP6 models. The RMSE values for each variable in each reanalysis dataset are also provided for comparison. Based on this overall average RMSE ranking, the three best models identified were FIO-ESM-2-0, CMCC-ESM2, and CMCC-CM2-SR5. These models were chosen to conduct further analysis on the SAD for the SSPs 21st century scenarios.

To enhance our understanding of the capabilities and performance of the 42 models utilized in this study, visual assessments of the CMIP6-HS are conducted over the for the same area analyzed for the RMSE. These assessments provide valuable insights into the models' performance and enhance our comprehension of their varying strengths. Within this subsection, we focus on the evaluations conducted in comparison to the ERA5 rea-

Table 3.1 - Root mean square error for the SST series of CMIP6 models in relation to NOAA-CIRES 20th Century V2c ($RMSE_{SST,NOAA}$), to ERA-20C ($RMSE_{SST,ERA20}$) and to ERA5 ($RMSE_{SST,ERA5}$) SST series. Root mean square error for the MSLP series of CMIP6 models in relation to NOAA-CIRES 20th Century V2c ($RMSE_{MSLP,NOAA}$), to ERA-20C ($RMSE_{MSLP,ERA20}$) and to ERA5 ($RMSE_{MSLP,ERA5}$) MSLP series. $RMSE_{SST}$ and $RMSE_{MSLP}$ are the mean root mean square error across the three reanalyses and their respective variables. The ranking of CMIP6 models is according to the overall Root Mean Squared Error ($RMSE_{all}$). The period considered is between 1979-2010 and the domain used in the calculations is 60°S-30°N and 90°W-30°E.

	Model	RMSE SST, NOAA	RMSE SST, ERA20	RMSE SST, ERA5	RMSE SST	RMSE MSLP, NOAA	RMSE MSLP, ERA20	RMSE MSLP, ERA5	RMSE MSLP	**RMSE all**
1°	FIO-ESM-2-0	1.385	1.299	1.393	1.359	3.295	3.415	3.321	3.344	**2.351**
2°	CMCC-ESM2	1.385	1.321	1.402	1.369	3.367	3.478	3.368	3.404	**2.387**
3°	CMCC-CM2-SR5	1.441	1.382	1.457	1.427	3.390	3.512	3.392	3.431	**2.429**
4°	MPI-ESM1-2-HR	1.467	1.415	1.482	1.455	3.376	3.500	3.364	3.414	**2.434**
5°	IPSL-CM6A-LR	1.446	1.409	1.445	1.434	3.497	3.653	3.517	3.555	**2.495**
6°	GFDL-ESM4	1.399	1.359	1.404	1.387	3.571	3.656	3.630	3.619	**2.503**
7°	IPSL-CM6A-LR-INCA	1.454	1.414	1.451	1.440	3.516	3.660	3.524	3.567	**2.503**
8°	TaiESM1	1.685	1.589	1.690	1.655	3.314	3.449	3.336	3.366	**2.511**
9°	MRI-ESM2-0	1.327	1.272	1.330	1.310	3.602	3.970	3.628	3.733	**2.522**
10°	CIESM	1.802	1.697	1.817	1.772	3.313	3.487	3.397	3.399	**2.585**
11°	MPI-ESM1-2-LR	1.625	1.555	1.626	1.602	3.523	3.692	3.568	3.594	**2.598**
12°	CanESM5	1.664	1.640	1.662	1.655	3.633	3.600	3.556	3.596	**2.626**
13°	CESM2	1.588	1.517	1.600	1.568	3.570	3.853	3.676	3.700	**2.634**
14°	BCC-CSM2-MR	1.595	1.509	1.606	1.570	3.580	3.858	3.671	3.703	**2.636**
15°	FGOALS-g3	1.584	1.504	1.597	1.561	3.579	3.872	3.707	3.719	**2.640**
16°	MCM-UA-1-0	1.401	1.304	1.432	1.379	3.861	4.119	3.923	3.968	**2.673**
17°	CESM2-WACCM	1.583	1.514	1.592	1.563	3.676	3.939	3.745	3.787	**2.675**
18°	MPI-ESM-1-2-HAM	1.938	1.862	1.936	1.912	3.427	3.493	3.421	3.447	**2.680**
19°	ACCESS-ESM1-5	1.868	1.788	1.889	1.849	3.493	3.581	3.481	3.519	**2.684**
20°	CAMS-CSM1-0	1.852	1.777	1.864	1.831	3.515	3.666	3.567	3.583	**2.707**
21°	BCC-ESM1	1.950	1.876	1.966	1.931	3.493	3.581	3.481	3.519	**2.725**
22°	ACCESS-CM2	1.930	1.861	1.945	1.912	3.613	3.558	3.480	3.550	**2.731**
23°	EC-Earth3	2.178	2.093	2.194	2.155	3.352	3.496	3.379	3.409	**2.782**
24°	EC-Earth3-Veg	2.194	2.106	2.207	2.169	3.335	3.500	3.373	3.403	**2.786**
25°	EC-Earth3-AerChem	2.156	2.063	2.168	2.129	3.385	3.555	3.439	3.460	**2.794**
26°	INM-CM5-0	1.938	1.909	1.939	1.929	3.758	3.601	3.639	3.666	**2.798**
27°	KIOST-ESM	1.839	1.780	1.856	1.825	3.700	3.909	3.751	3.787	**2.806**
28°	EC-Earth3-Veg-LR	2.263	2.178	2.276	2.239	3.390	3.489	3.365	3.415	**2.827**
29°	CESM2-WACCM-FV2	1.990	1.921	2.008	1.973	3.682	3.901	3.738	3.774	**2.873**
30°	FGOALS-f3-L	1.584	1.500	1.588	1.557	4.228	4.187	4.215	4.210	**2.884**
31°	CESM2-FV2	1.975	1.905	1.990	1.957	3.749	3.939	3.766	3.818	**2.888**
32°	NESM3	1.915	1.866	1.915	1.898	3.870	3.980	3.804	3.885	**2.892**
33°	INM-CM4-8	2.143	2.085	2.152	2.127	3.841	3.669	3.753	3.754	**2.940**
34°	E3SM-1-1-ECA	1.661	1.602	1.663	1.642	4.052	4.465	4.222	4.246	**2.944**
35°	E3SM-1-0	1.797	1.548	1.661	1.669	4.060	4.475	4.224	4.253	**2.961**
36°	E3SM-1-1	1.580	1.523	1.579	1.561	4.250	4.679	4.433	4.454	**3.007**
37°	GISS-E2-1-G	2.035	1.961	2.042	2.013	4.162	3.881	3.998	4.013	**3.013**
38°	IPSL-CM5A2-INCA	2.064	2.055	2.060	2.060	3.939	4.136	4.007	4.027	**3.044**
39°	EC-Earth3-CC	2.969	2.914	3.065	2.983	3.300	3.462	3.324	3.362	**3.172**
40°	MIROC6	2.199	2.100	2.218	2.173	5.081	4.734	4.912	4.909	**3.541**
41°	GISS-E2-1-H	2.341	2.271	2.341	2.318	6.378	5.951	6.146	6.158	**4.238**
42°	KACE-1-0-G	7.569	7.457	7.579	7.535	3.592	3.443	3.447	3.494	**5.514**

nalysis, as the results were generally consistent across all three reanalyses. Detailed results pertaining to the NOAA-CIRES and ERA-20C reanalyses can be found in Appendix E.

In Figures 3.26 and 3.27 it is shown the Taylor Diagrams of the SST and MSLP variables, respectively, which condense several useful information for evaluating models in relation to observational data. To reduce visual pollution, each diagram features up to ten models. The observational dataset (indicated by the circle on the base axis of the standard deviation graph) is confronted with data from different models (other colored points on the graph). From the graph it is possible to extract information such as the correlation and the RMSE of each model in relation to observed data (reanalysis dataset), as well as the standard deviation of each specific dataset. For example, it is observable in Figures 3.26c that the correlation of the SST data of the FIO-ESM-2-0 model with respect to the ERA5 reanalysis is around 0.99, the standard deviations of all models dataset in this figure are slightly below the reference set (ERA5 reanalysis), while SST RMSE is 1.393 (verifiable in both Table 3.1 and Figures 3.26c, open green triangle). Overall, it can be seen how the chosen models FIO-ESM-2-0 (open green triangle in Figures 3.26c and 3.27c), CMCC-ESM2 and CMCC-CM2-SR5 (the last two, the pink triangle and the open pink circle, reciprocally, in Figures 3.26b and 3.27b) perform well for both variables.

Between Figures 3.28 and 3.31 are presented the spatial arrangement of the RMSE for the SST, for each of the 42 CMIP6-HS models in relation to the ERA5 reanalysis and over the study region domain (South America and the SAO). The analysis made in relation to the NOAA-CIRES reanalysis can be seen in Figures E.3-E.6, and for the ERA-20C in Figures E.21-E.24, both in Appendix E. Again, the good performance of the three chosen models, in relation to the other models, is noteworthy (Figures 3.28l, E.3l andE.21l for the CMCC-CM2-SR5, 3.29a, E.4a and E.22a for the CMCC-ESM2, and 3.29l, E.4l and E.22l for the FIO-ESM-2-0). In general, in very few points the models presented values that exceeded 1.6°C of RMSE for SST for the entire study area. Such spots still correspond to places with complex oceanic dynamics such as the Angola-Benguela Upwelling region and the Brazil-Malvinas Confluence.

Likewise, the SST bias of CMIP6 models is illustrated in Figures 3.32 to 3.35 for ERA5, E.7 to E.10 for NOAA-CIRES, and E.25 to E.28 for ERA-20C. Overall, the biases are generally small; however, certain regions exhibit important biases. Notably, the Angola-Benguela region displays consistently pronounced warm biases across all models, attributed

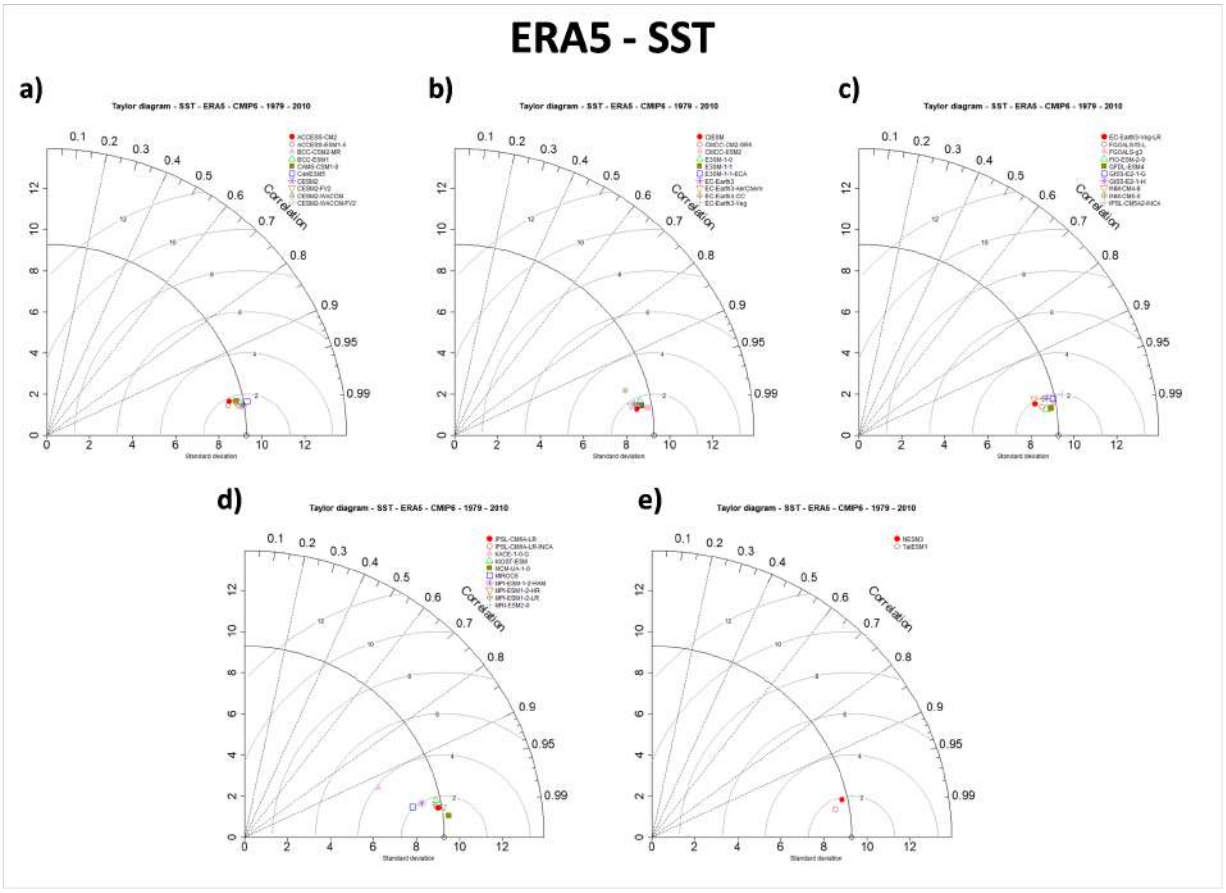

Figure 3.26: Taylor diagrams comparing observational data from ERA5 and different CMIP6 models, for the SST variable over the study region and during the period 1979 to 2010.

to inadequate representation of wind-driven coastal upwelling, which plays a crucial role in the cooling processes in the area (RICHTER; TOKINAGA, 2020). The Brazil-Malvinas confluence region also exhibits a north-south dipole with substantial opposite sign biases in all models. Additionally, regions with robust oceanic dynamics, such as the extratropics of the SAO and Agulhas Leakage, display notable positive and negative bias values in several models, although the selected models exhibit low biases in these areas. These important biases are primarily associated with the challenge faced by GCMs in accurately reproducing the complex ocean dynamics in such regions, with limitations in resolution to capture mesoscale processes as the main contributing factor (BROGGIO; GARCIA; SILVA, 2021). Specifically, among the chosen models, CMCC-CM2-SR5 (Figures 3.32l, E.7l and E.25l) and CMCC-ESM2 (Figures 3.33a, E.8a and E.26a) demonstrate slightly positive biases over the SAO, while FIO-ESM-2-0 (Figures 3.33l, E.8l and E.26l) exhibits slightly negative bias values for the same region.

For the MSLP, the RMSE schemes are presented between Figures 3.36 and 3.39 in

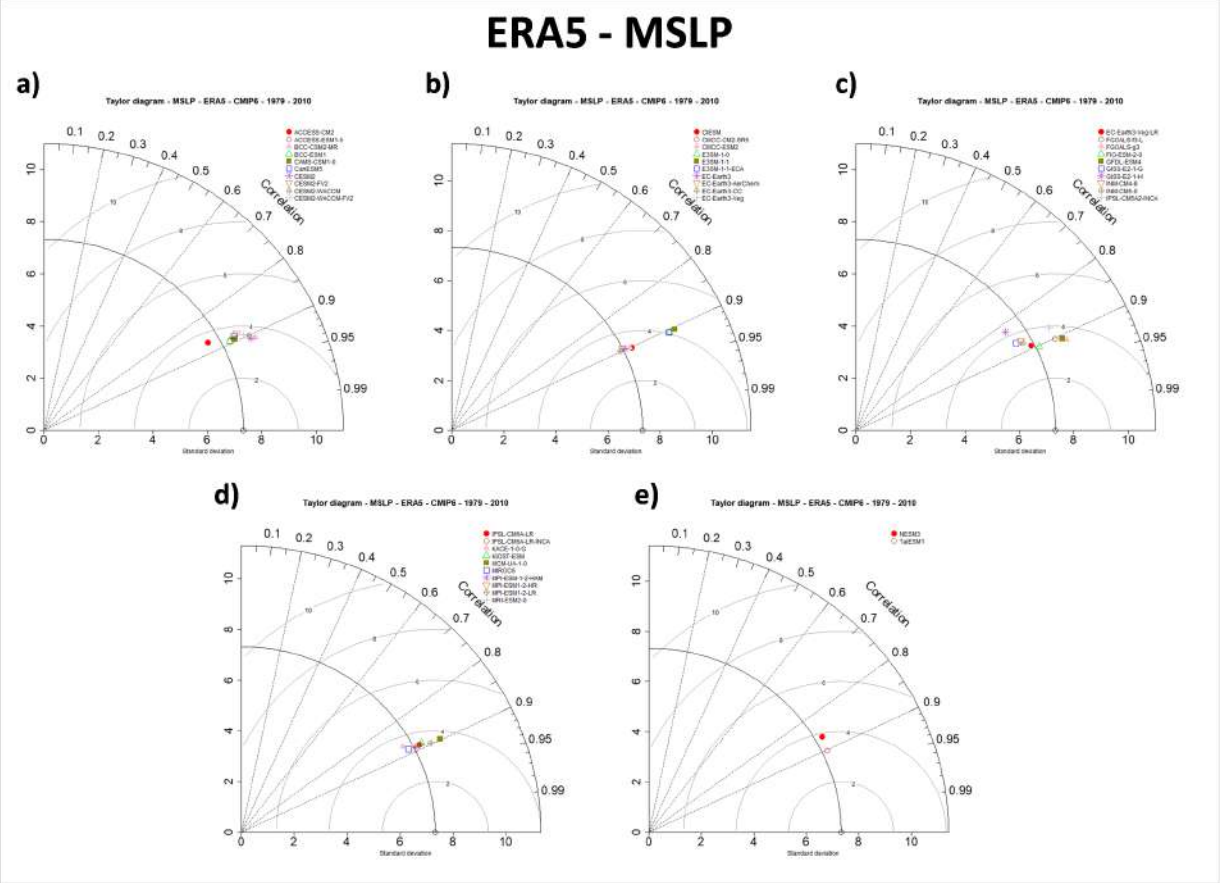

Figure 3.27: The same as in Figure 3.26 except for the MSLP variable.

reference to ERA5 reanalysis. The MSLP RMSE in relation to NOAA-CIRES and ERA-20C are shown in Figures E.11-E.14 and E.29-E.32, respectively. For all models, there is a pattern of lower RMSE in tropical areas, with values below 5 mb and higher values in extratropics, exceeding that value. The selected models (Figures 3.36l for the CMCC-CM2-SR5, 3.37a for the CMCC-ESM2 and 3.37l for the FIO-ESM-2-0) perform particularly well in comparison to the other models.

The bias in MSLP is depicted in Figures 3.40 to 3.43 for ERA5 reanalysis, E.15 to E.18 for NOAA-CIRES reanalysis and E.33 to E.36 for ERA-20C reanalysis. Among the selected models (CMCC-CM2-SR5, CMCC-ESM2, and FIO-ESM-2-0), a consistent pattern emerges. In the extratropics, there is a prevalent positive bias, while in the tropics, the bias ranges from neutral to slightly negative (Figures 3.40l, E.15l and E.33l for the CMCC-CM2-SR5; 3.41a, E.16a and E.34a for the CMCC-ESM2; and 3.41l, E.16l and E.34l for the FIO-ESM-2-0). The higher occurrence of pronounced biases in extratropical latitudes can likely be attributed to the presence of transient systems that induce greater

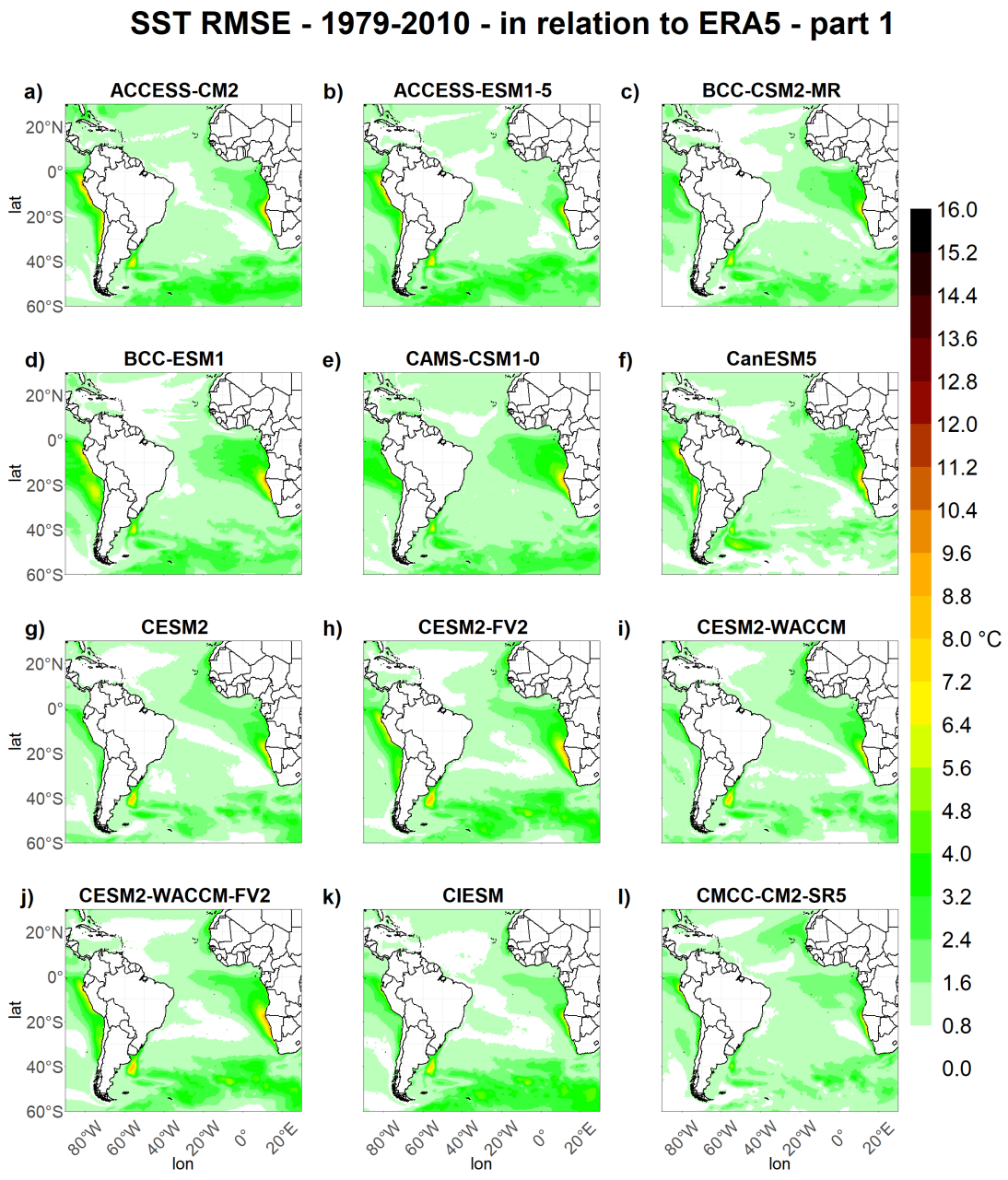

Figure 3.28: Root mean square error (RMSE) of the SST variable over the study area, for the period 1979-2010, for different CMIP6 models with respect to ERA5 reanalyses. Part 1.

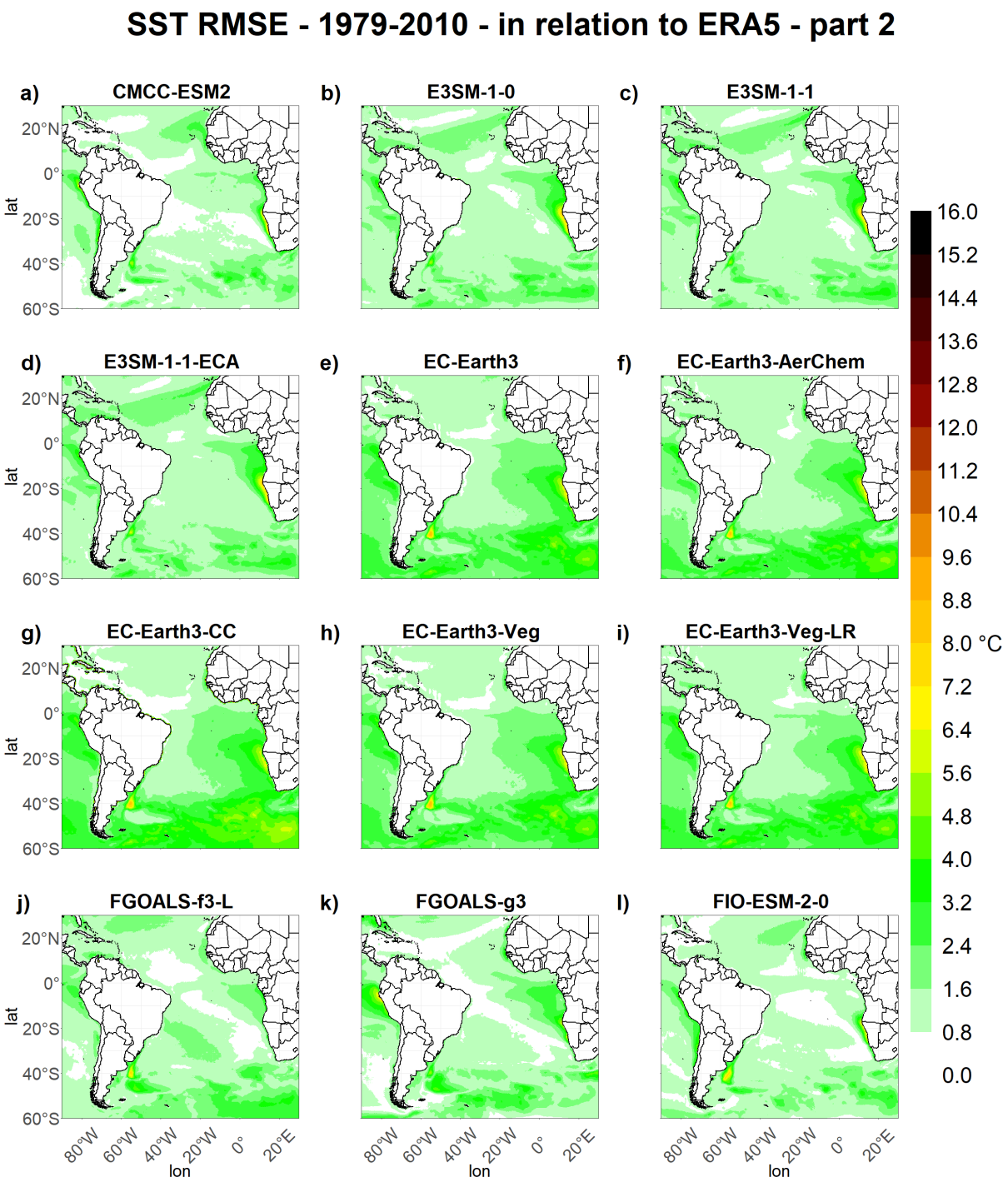

Figure 3.29: The same as in 3.28 part 2.

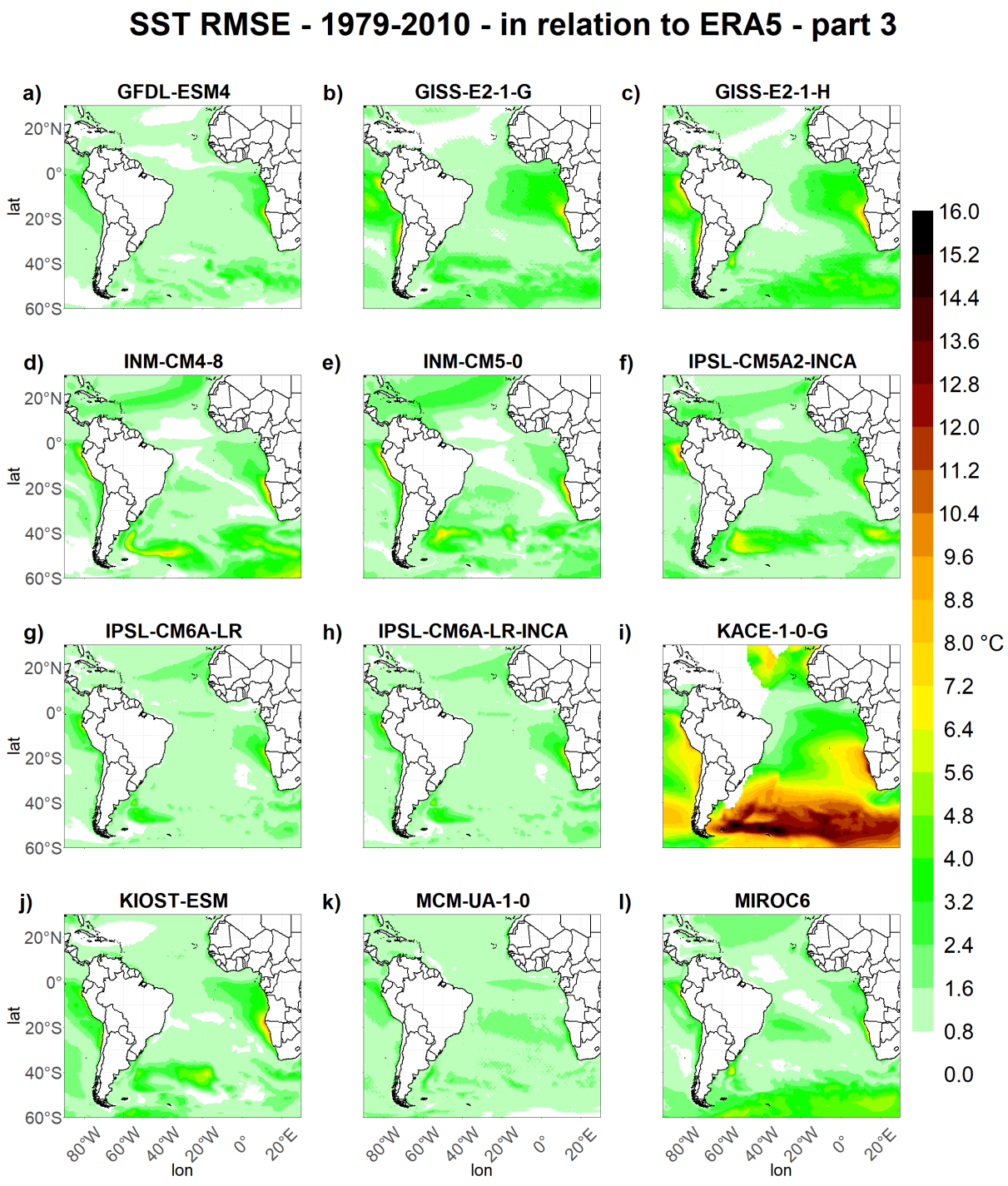

Figure 3.30: The same as in 3.28 part 3.

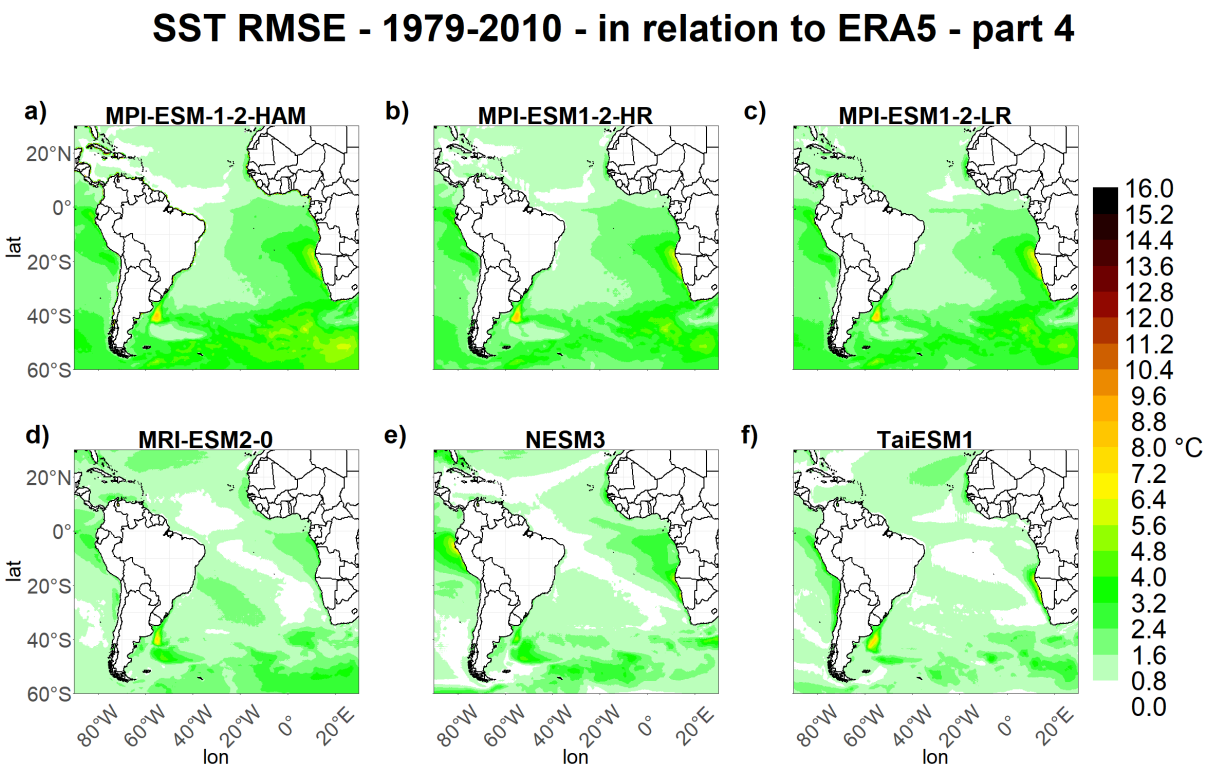

Figure 3.31: The same as in 3.28 part 4.

variations in MSLP in those regions, thus making them more susceptible to biases.

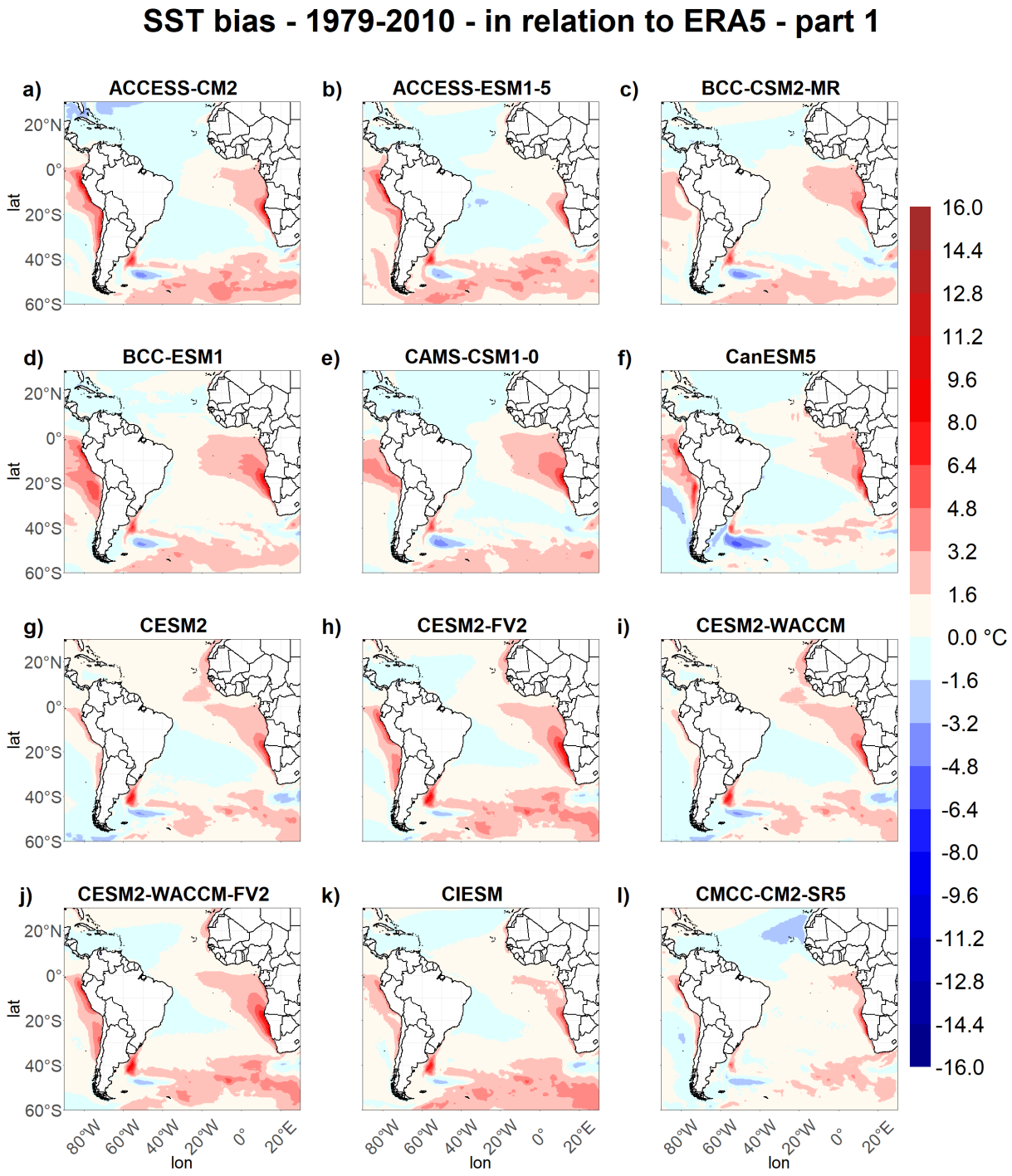

Figure 3.32: Bias of the SST variable over the study area, for the period 1979-2010, for different CMIP6 models with respect to ERA5 reanalyses. Part 1.

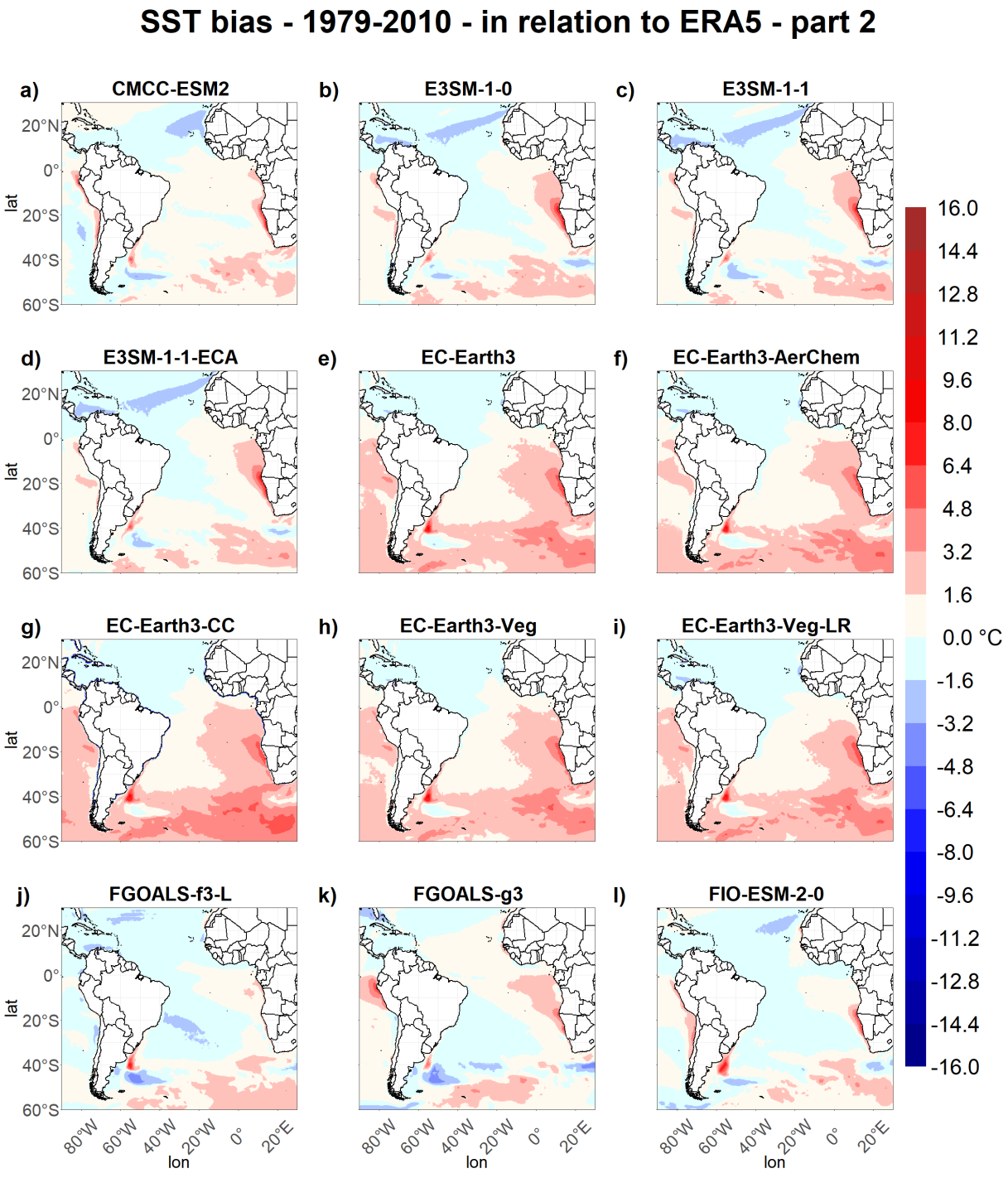

Figure 3.33: The same as in 3.32 part 2.

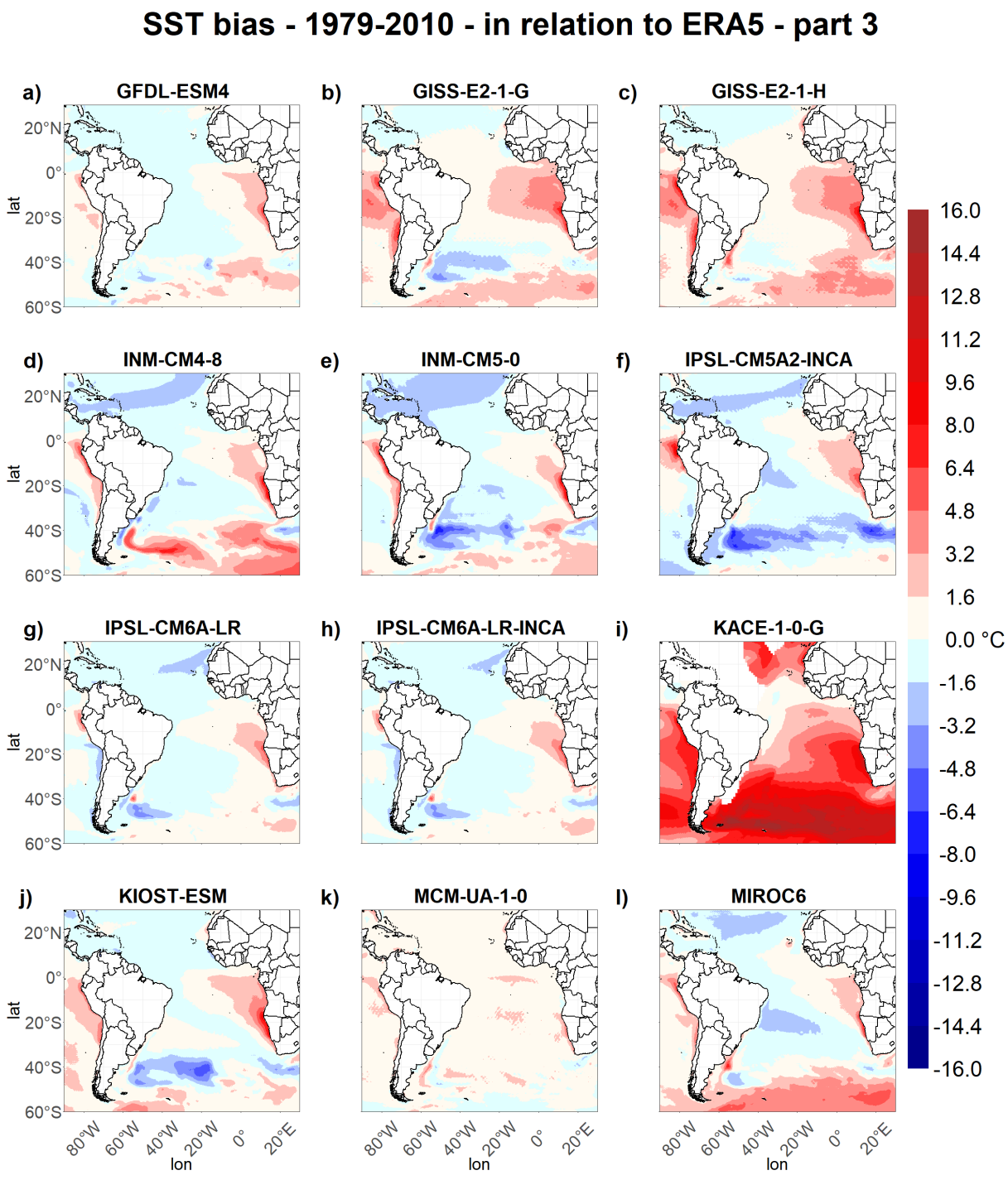

Figure 3.34: The same as in 3.32 part 3.

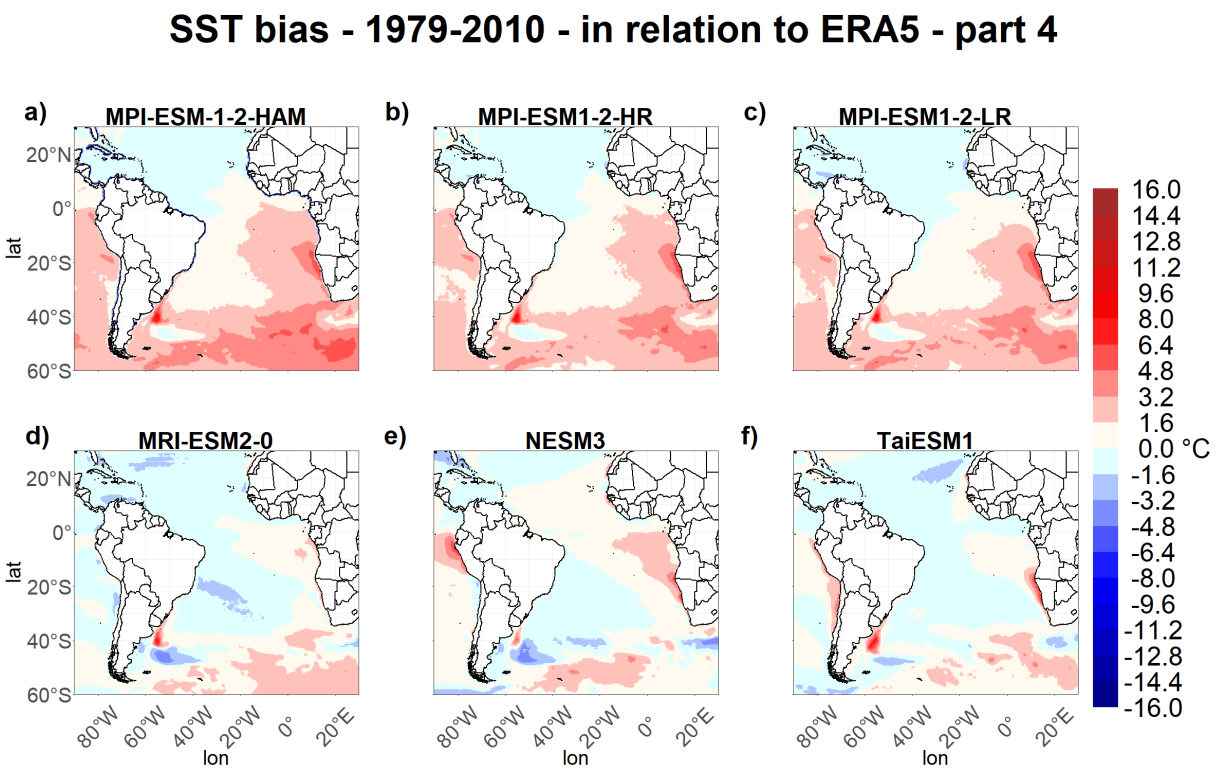

Figure 3.35: The same as in 3.32 part 4.

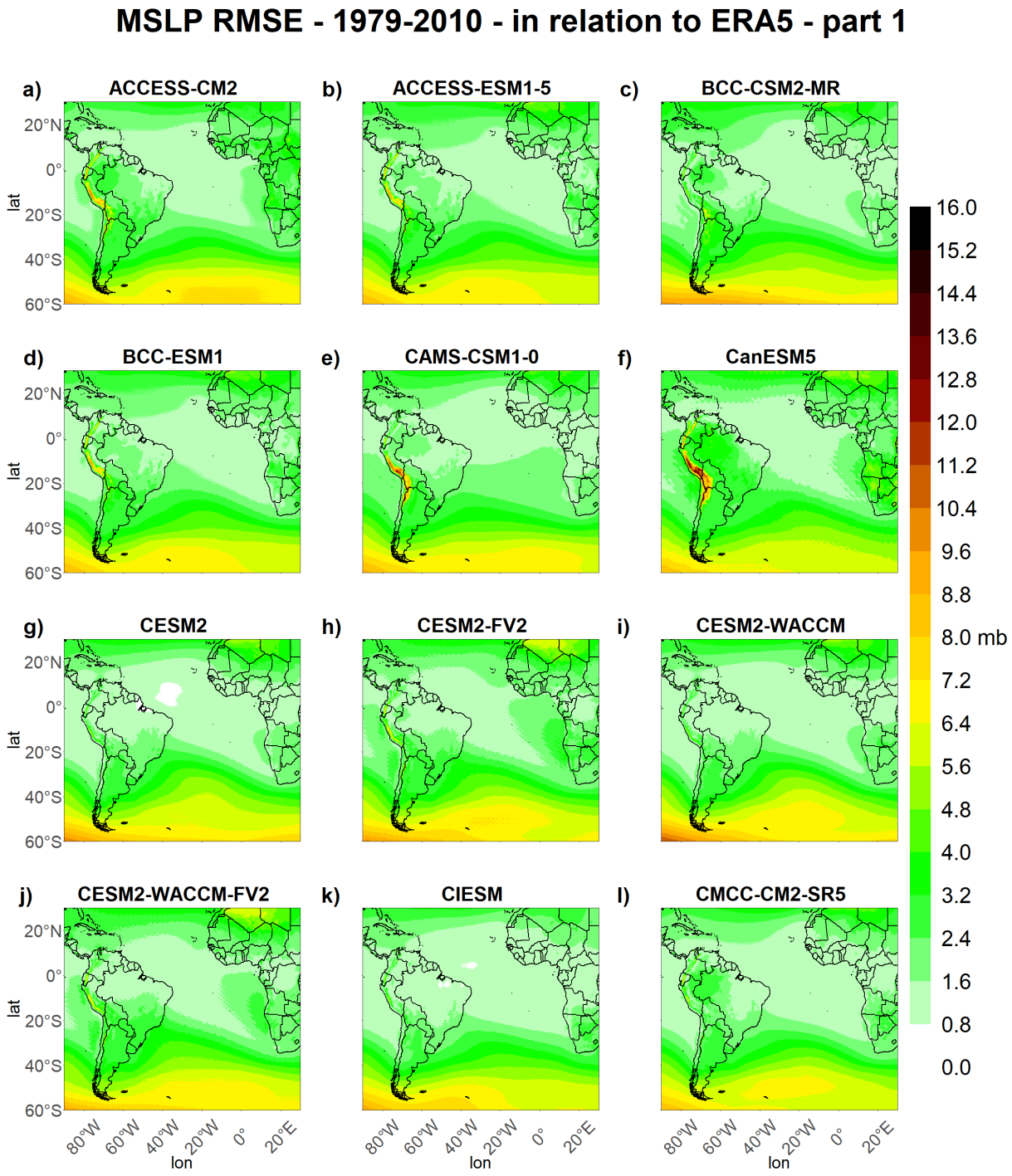

Figure 3.36: Root mean square error (RMSE) of the MSLP variable over the study area, for the period 1979-2010, for different CMIP6 models with respect to ERA5 reanalyses. Part 1.

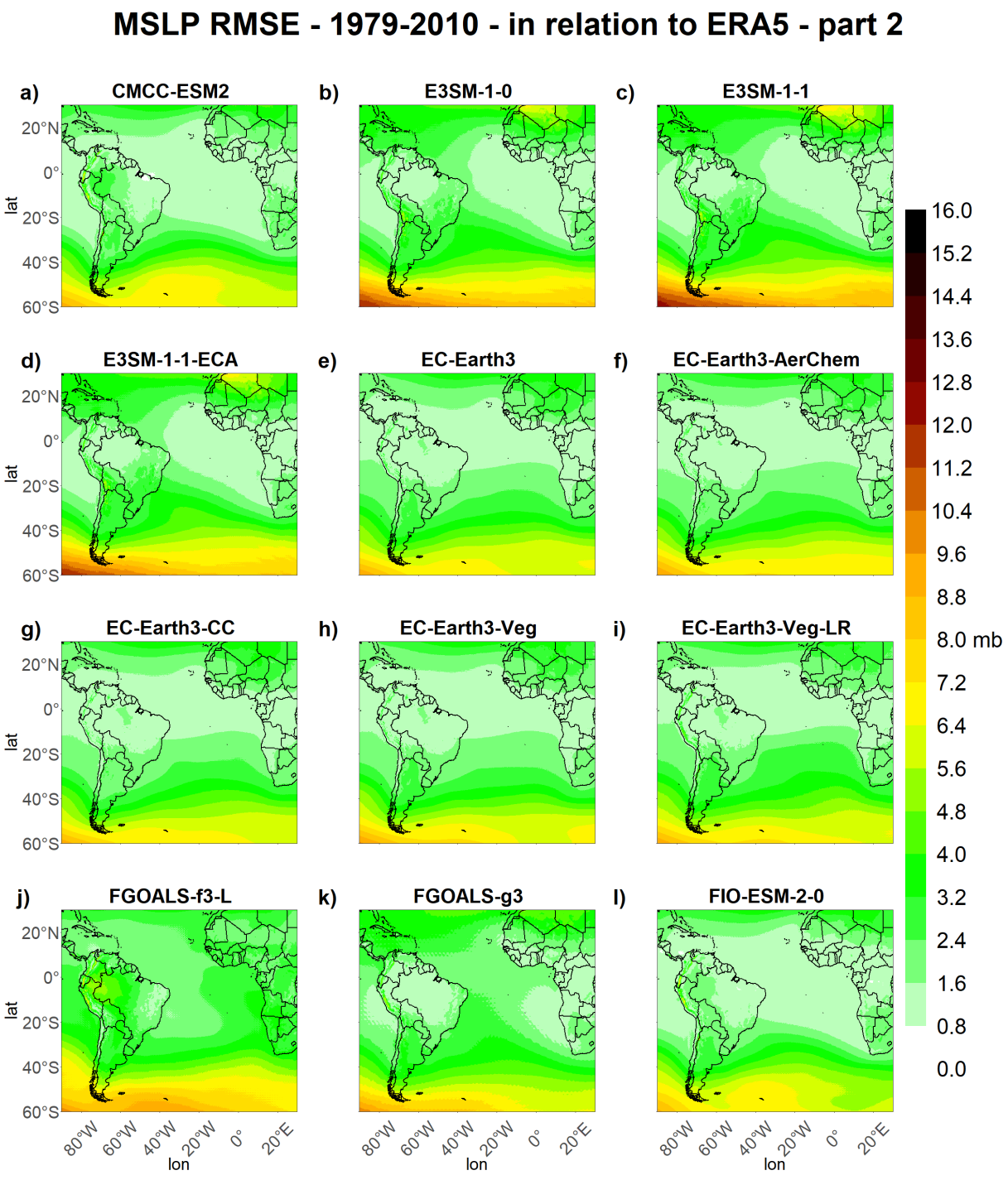

Figure 3.37: The same as in 3.36 part 2.

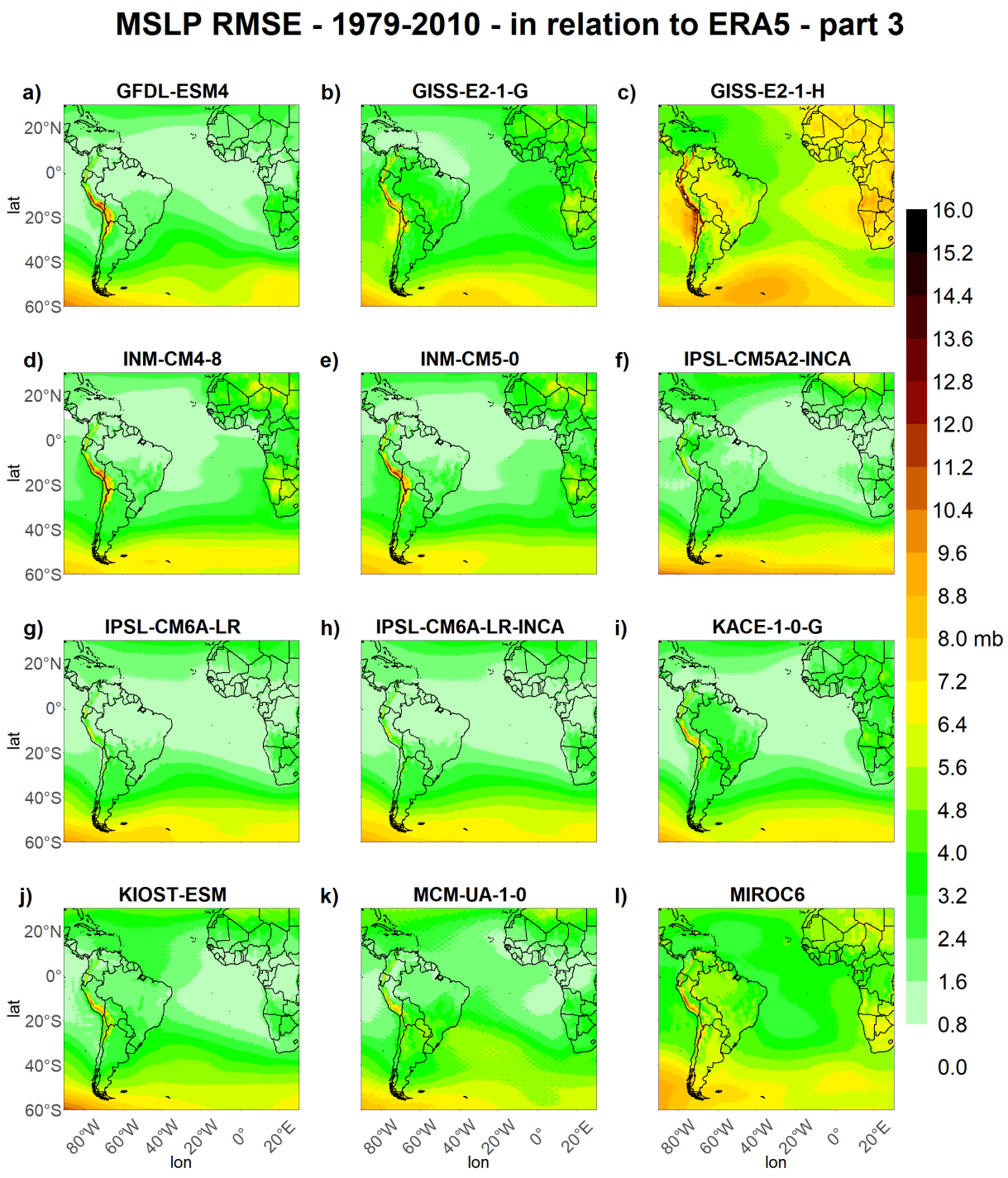

Figure 3.38: The same as in 3.36 part 3.

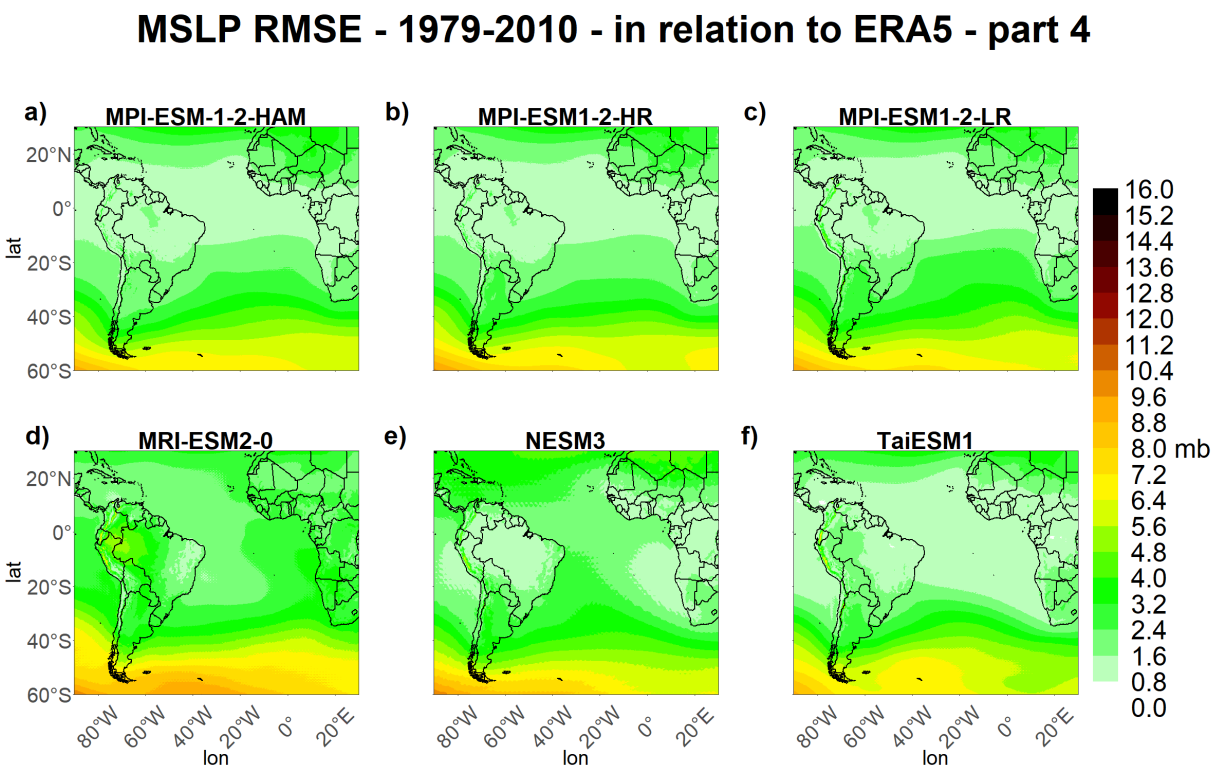

Figure 3.39: The same as in 3.36 part 4.

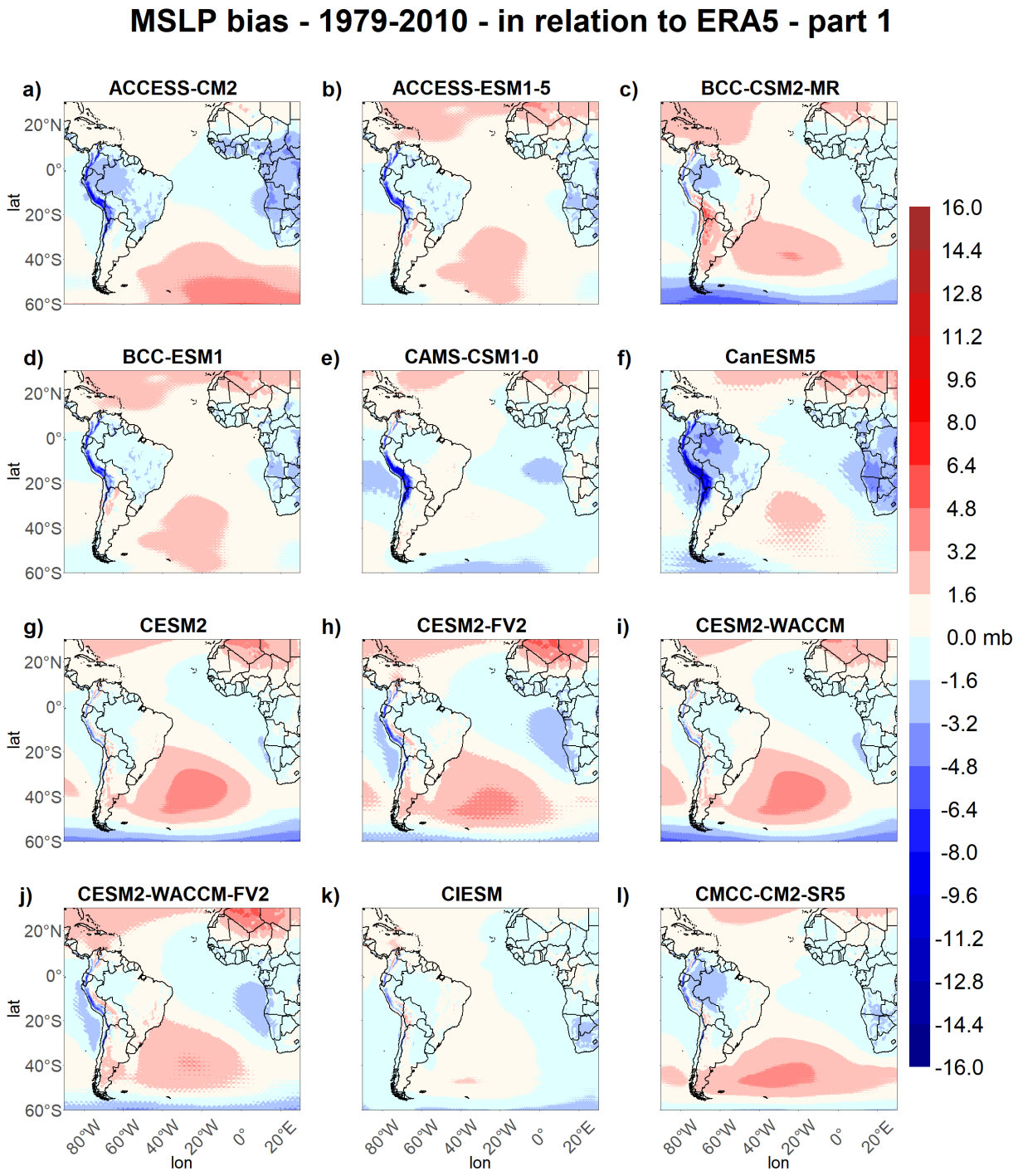

Figure 3.40: Bias of the MSLP variable over the study area, for the period 1979-2010, for different CMIP6 models with respect to ERA5 reanalyses. Part 1.

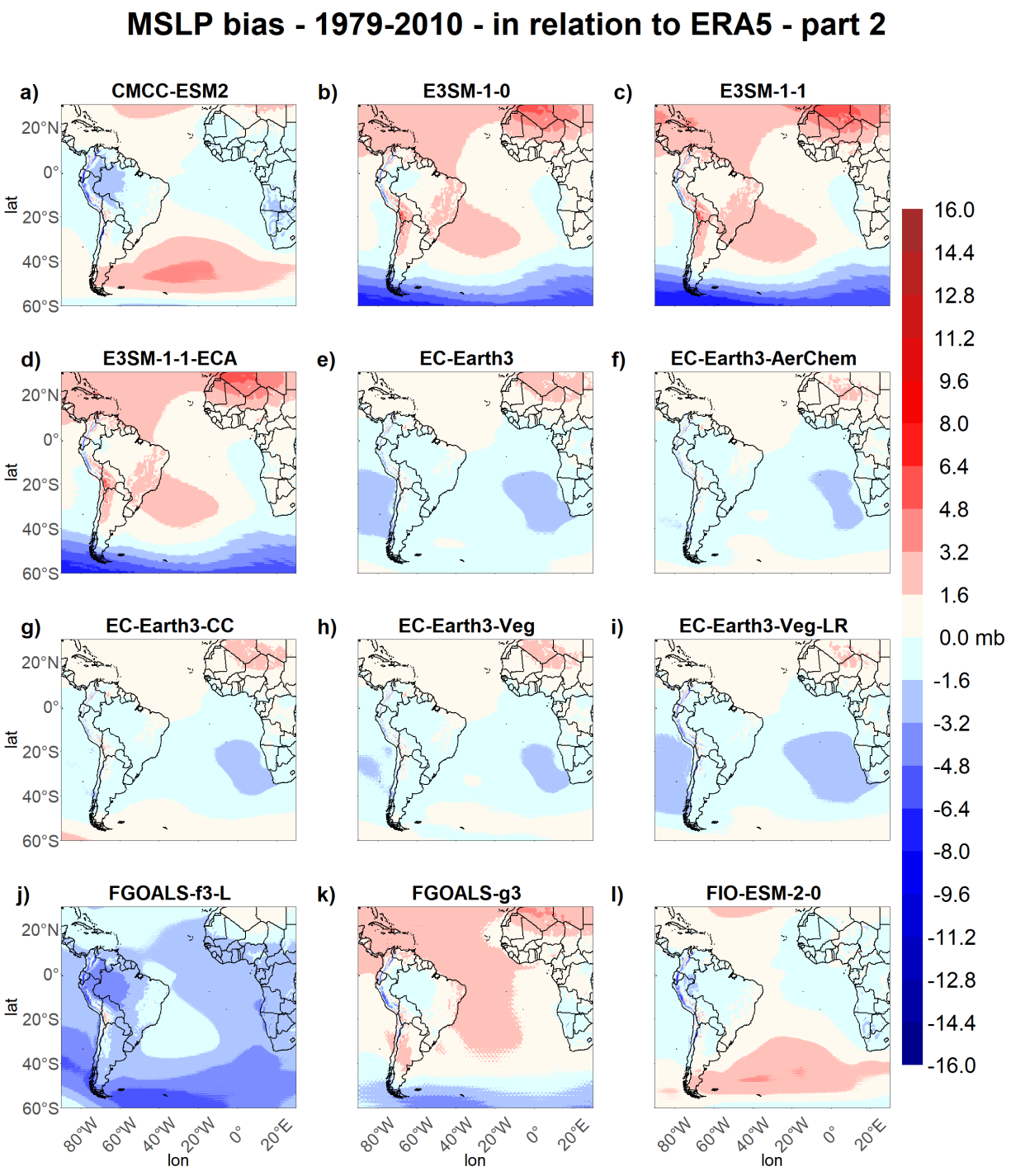

Figure 3.41: The same as in 3.40 part 2.

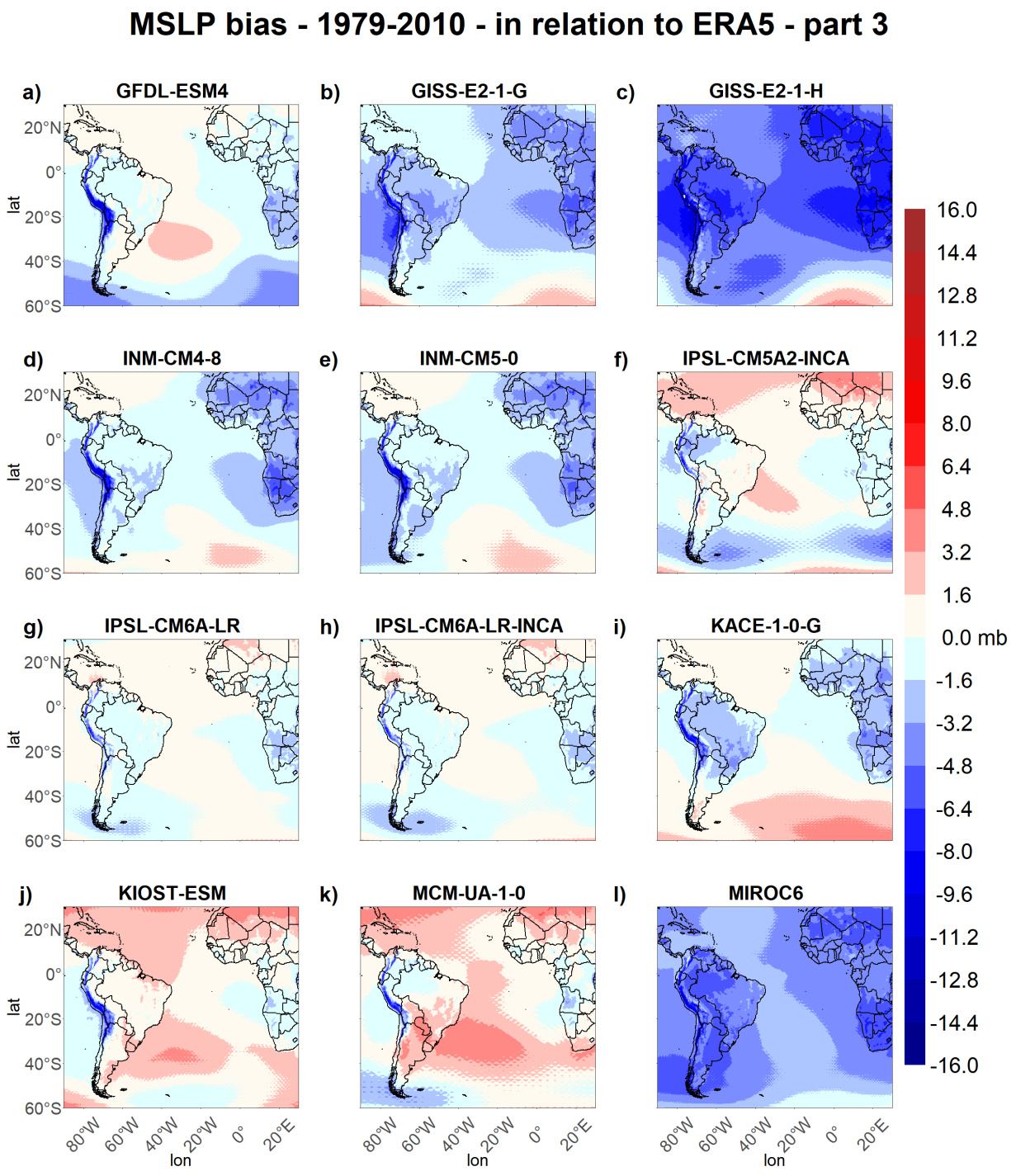

Figure 3.42: The same as in 3.40 part 3.

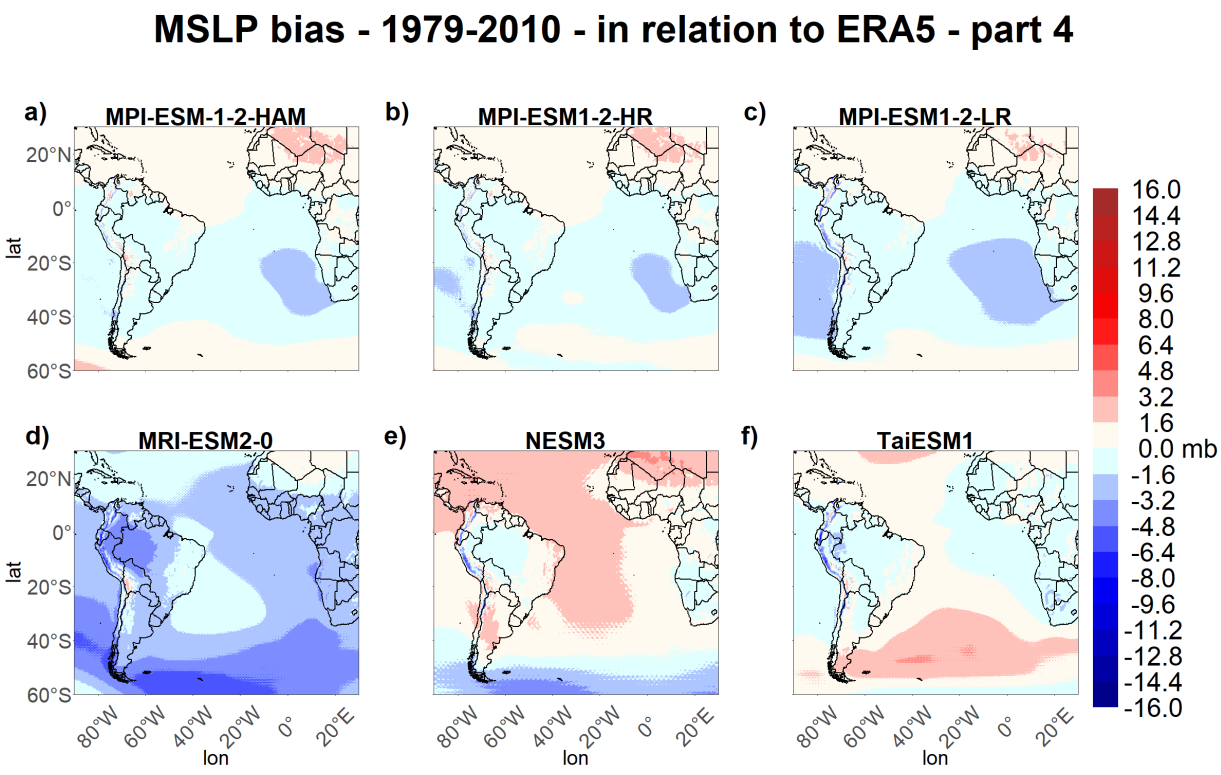

Figure 3.43: The same as in 3.40 part 4.

3.2.2 *The South Atlantic Dipole representation by the CMIP6 Historical Simulations of the selected models*

Previously, in this study, we conducted analyses to examine the behavior and interactions of the SAD in relation to the climate over South America, as well as its connections with the IPO, within a post-industrial climate context spanning from 1851 to the present day. To accomplish this, we utilized reanalysis datasets from NOAA-CIRES 20th Century V2c, ERA-20C, and ERA5. The main findings were the low concordance of datasets in the pre-1950 period, a southerly shift of the entire SAD climate pattern over the last few decades, possibly connected to anthropogenic global warming (HU; HUAN; ZHOU, 2018), and also a alternation in the SAD-Pacific Niño relationship according to the IPO phase over the last century. These same analyses, carried out with observational data, were carried with the CMIP6-HS of the three chosen CMIP6 models (FIO-ESM-2-0, CMCC-ESM2 and CMCC-CM2-SR5) to evaluate how well they represent the SAD features.

In Figure 3.44 is depicted the homogeneous correlation between the series of expansion coefficients from the first covariability mode, derived through SVD, and the corresponding SST anomalies (shaded) and MSLP anomalies (contours) for each of the aforementioned models, covering the entire CMIP6-HS period from 1850 to 2010. The main configuration of the SAD, characterized by a dipole of SST anomalies between the tropics and extratropics along with a superimposed monopole of MSLP anomalies, is clearly evident in all models. Correlations with good statistical significance are verified for both SST and MSLP over the entire SAO, corroborating the description of the mode by the models. However, the presence of the Atlantic Niño sector, typically observed in annual SVD analyses as shown in Figure 3.1, is not observed in this context. One potential reason for the absence of representation in this sector could be attributed to SST biases of the models observed in this specific region, as discussed in the last subsection (see Figures 3.32-3.35, E.7-E.10 and E.25-E.28). For the 20th century climate scenario (20C3M) of CMIP3, Bombardi and Carvalho (2011) found comparable SAD patterns in various GCMs outputs with a spanning period from 1971 to 2000. However, it is important to mention that models such as CSIRO and GFDL2.0 demonstrated the presence of an Atlantic Niño signature at that time.

The SCF_1 value ranges from 64% in the CMMCC-ESM2 model (Figure 3.44b) to 71.7%

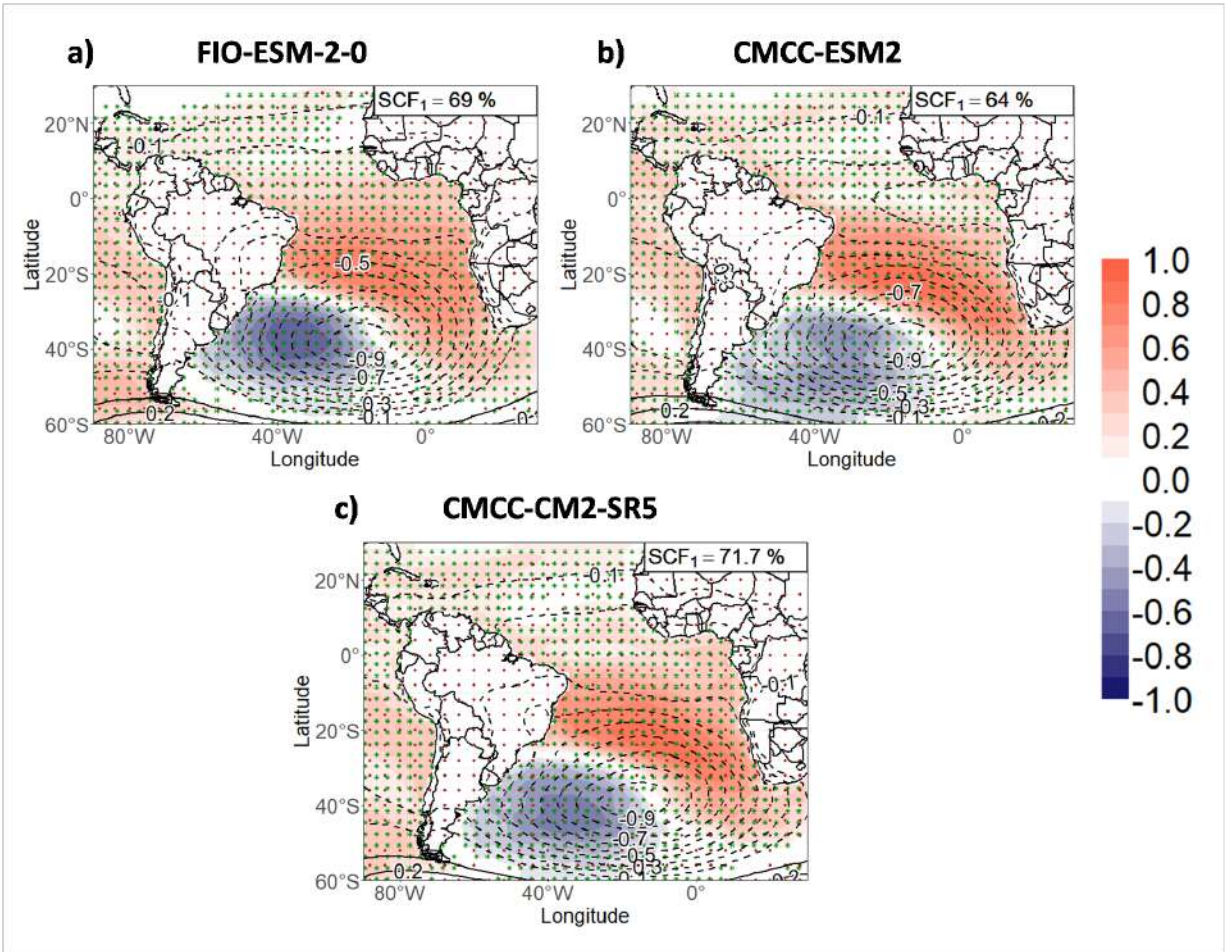

Figure 3.44: Homogeneous correlation between $SVD1_{SST}$ and SST anomalies (in shaded) and between $SVD1_{MSLP}$ and MSLP anomalies (contours) identified for the CMIP6 Historical Simulations (period between 1851-2010) of models a) FIO-ESM-2-0, b) CMCC-ESM2 and b) CMCC-CM2-SR5. Correlations with a statistical confidence level above 95% are shown in green (yellow) dots for SST (MSLP) anomalies.

in the CMCC-CM2-SR5 model (Figure 3.44c), compared with reanalysis values varying from 61.7% to 65% (Figure 3.1). This indicates that both the CMIP6 models and the reanalyses used in this study attribute comparable importance to the SAD as a covariability mode between the ocean and atmosphere over the SAO.

In order to enhance clarity and due to the absence of significant deviations, this subsection exclusively presents figures derived from the analyses conducted using the outputs of the FIO-ESM-2-0 model, since this model exhibited the highest level of accuracy in comparison to the observed data. For reference, the analyses involving CMCC-ESM2 and CMCC-CM2-SR5 can be found in Appendix F.

The expansion coefficients of the MSLP and SST anomalies and their respective wavelet analysis for the FIO-ESM-2-0, CMCC-ESM2 and CMCC-CM2-SR5 models are shown in

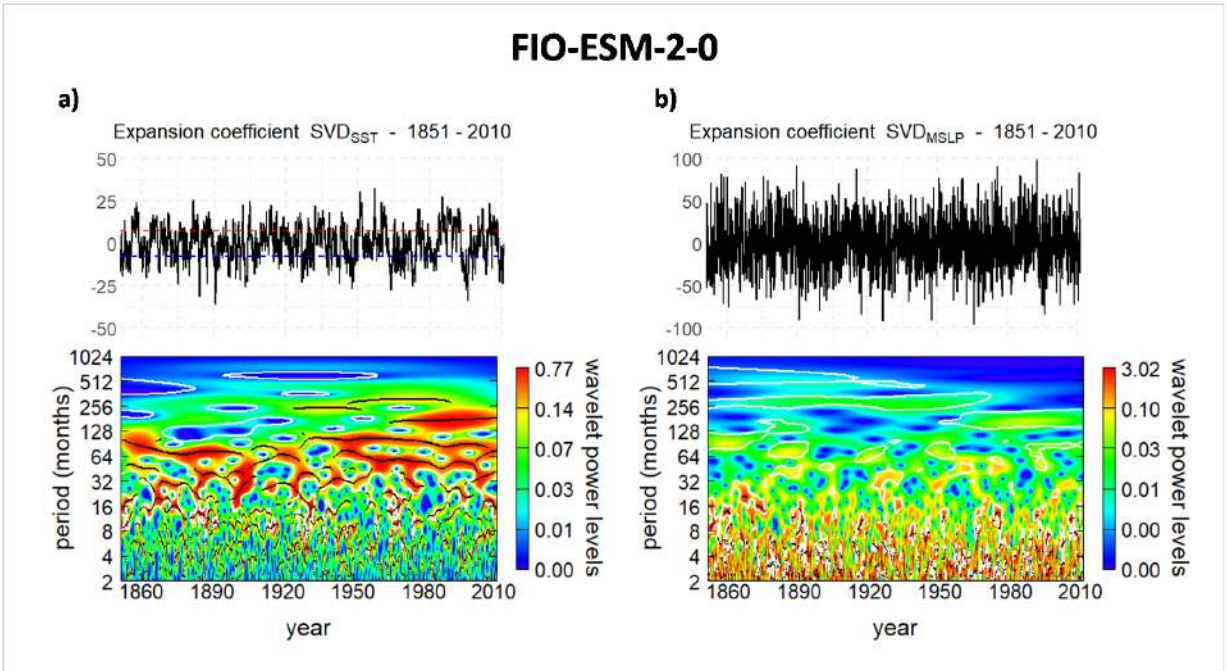

Figure 3.45: Time series of the expansion coefficients a) of the SST ($SVD1_{SST}$) and b) of the MSLP ($SVD1_{MSLP}$) with their respective power spectrum obtained by wavelet analysis obtained from CMIP6 Historical Simulations of the FIO-ESM-2-0, for the period from 1851 to 2010. Red (blue) dotted lines in the $SVD1_{SST}$ series, in Figure a - top, indicate the 75th (25th) percentile which is used as the threshold for the positive (negative) phase of the SAD. Values with 95% statistical confidence level in the Power spectrum are delimited by a white contour.

Figures 3.45, F.1 and F.4, respectively. Remebering that it is a way of examining the temporal behavior of these variables in relation to the SAD. It is not expected to observe concurrent variability in the SAD across models that align with the observations, however it can be noticed that the models simulate well the characteristic of the oceanic component of the SAD to present a lower frequency (with peaks in the interannual and interdecadal scales), while the atmospheric component presents a high frequency with peaks in the intraseasonal to interannual timescales (comparing Figures 3.45, F.1 and F.4 with Figures 3.2, 3.3 and 3.4).

The correlations between the coefficients obtained from the reanalyses and the models are shown in Table A.1. Statistically significant values (in bold) are verified between the SST and MSLP coefficients between the different reanalyses. For CMIP6-HS, significant correlations are found between the SST and MSLP coefficients of the same model, indicating a coupled ocean-atmosphere interaction within the simulation. However, as anticipated, there is no correlation between the reanalyses and CMIP6-HS, or when comparing different models.

Figures 3.46, F.2, and F.5 illustrate the representation of the seasonal variation of the SAD in the CMIP6-HS for the FIO-ESM-2-0, CMCC-ESM2, and CMCC-CM2-SR5 models, respectively. Overall, these models exhibit a less pronounced meridional migration of the SAD compared to the observed data (Figures 3.7, B.1, and B.8). Although CMCC-ESM2 and CMCC-CM2-SR5 show slightly better representation, they still do not capture the full range of variability. The Atlantic Niño sector remains consistently underrepresented in all simulations throughout the year. Notably, in the JJA quarter, the CMCC-ESM2 model (Figure F.2) exhibits such poor representation of the Atlantic Niño sector that it produces signals contrary to the specific characteristics observed in this region during this time of the year.

No clear pattern of variability in the SCF_1 was observed in the observational datasets (Figures 3.7, B.1 and B.8), and this pattern was similarly absent in the models. When considering the overall SCF_1 variability, the observational datasets exhibited extreme values ranging from 51.7% in JJA to 73.7% in SON, both based on the NOAA-CIRES reanalysis. Likewise, the models demonstrated comparable SCF_1 values, with a range of 48% in JJA for the CMCC-ESM2 model (Figure F.2) to 73.3% in SON for the FIO-ESM-2-0 model (Figure 3.46).

The first covariability mode, the SAD, for each of the intervals associated with the IPO (1897-1916, 1916-1923, 1923-1942, 1943-1978, 1978-1997 and 1997-2010) for the CMIP6-HS is shown in Figure 3.47 for the FIO-ESM-2-0, F.3 for the CMMC-ESM2 and F.6 for the CMMC-CM2-SR5. Considering periods after 1943, where it was observed a south displacemente of SAD in observational datasets (Figures 3.14, 3.15 and 3.16), the same characteristic is not observable for the GCMs. What can be observed in all three models is an increase in the significance of the SAD tropical (extratropical) pole of SST anomalies during the positive (negative) phase of the IPO, which is not verifiable in the observational data.

In terms of the SCF_1, ERA5 and ERA-20C reanalyses exhibited a declining trend in the importance of the first mode of variability over the SAO starting from 1943 (Figures 3.16 and 3.15). Similarly, the FIO-ESM-2-0 and CMCC-ESM2 models demonstrate a comparable pattern, with SCF_1 values decreasing from 69.8% to 48.2% and from 65.6% to 55.5%, respectively. In contrast, the CMCC-CM2-SR5 model exhibits an opposite trend during the same period, with SCF_1 values increasing from 67.4% to 76.7%.

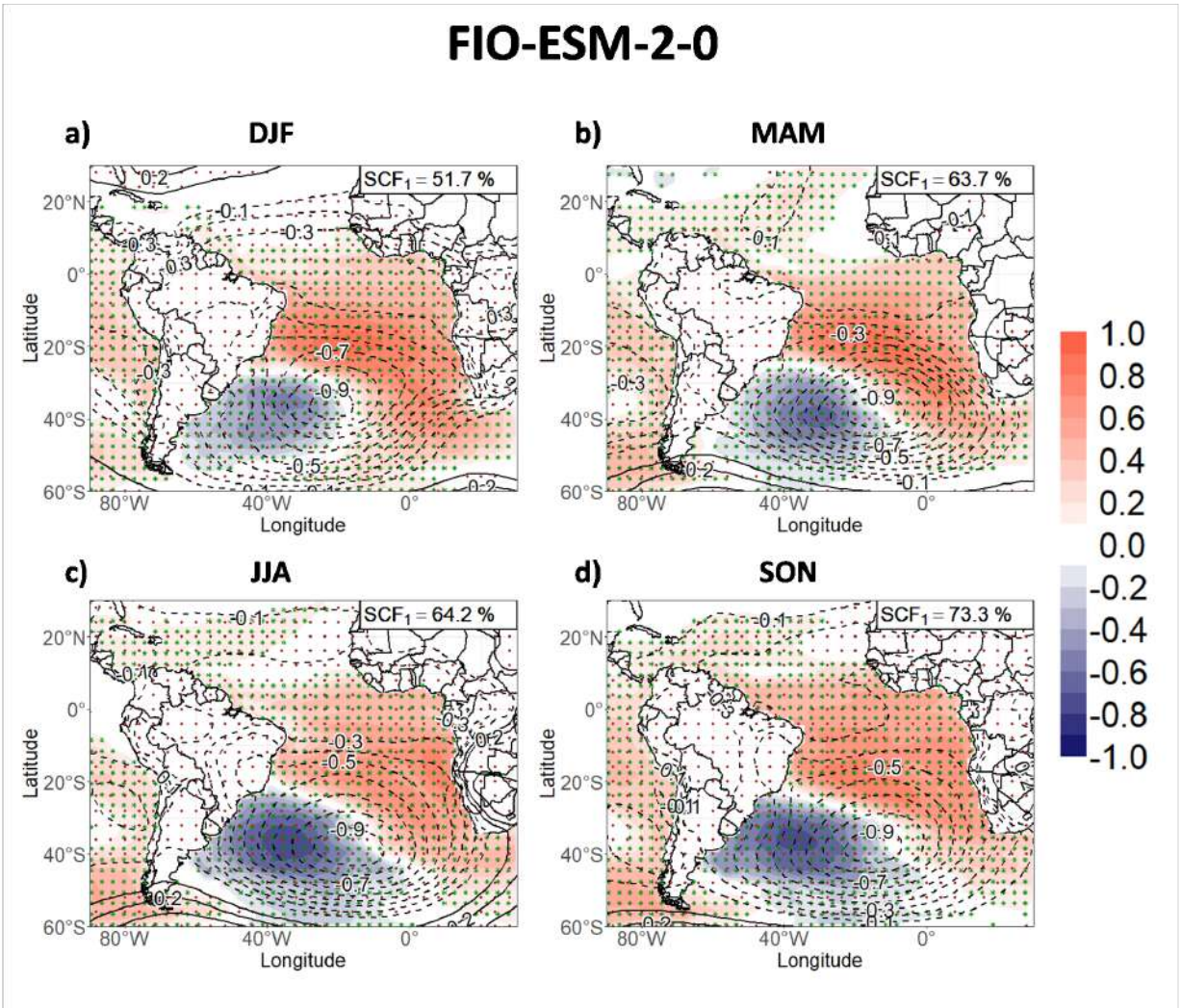

Figure 3.46: The same as in Figure 3.7 except for the FIO-ESM-2-0 model CMIP6 Historical Simulations.

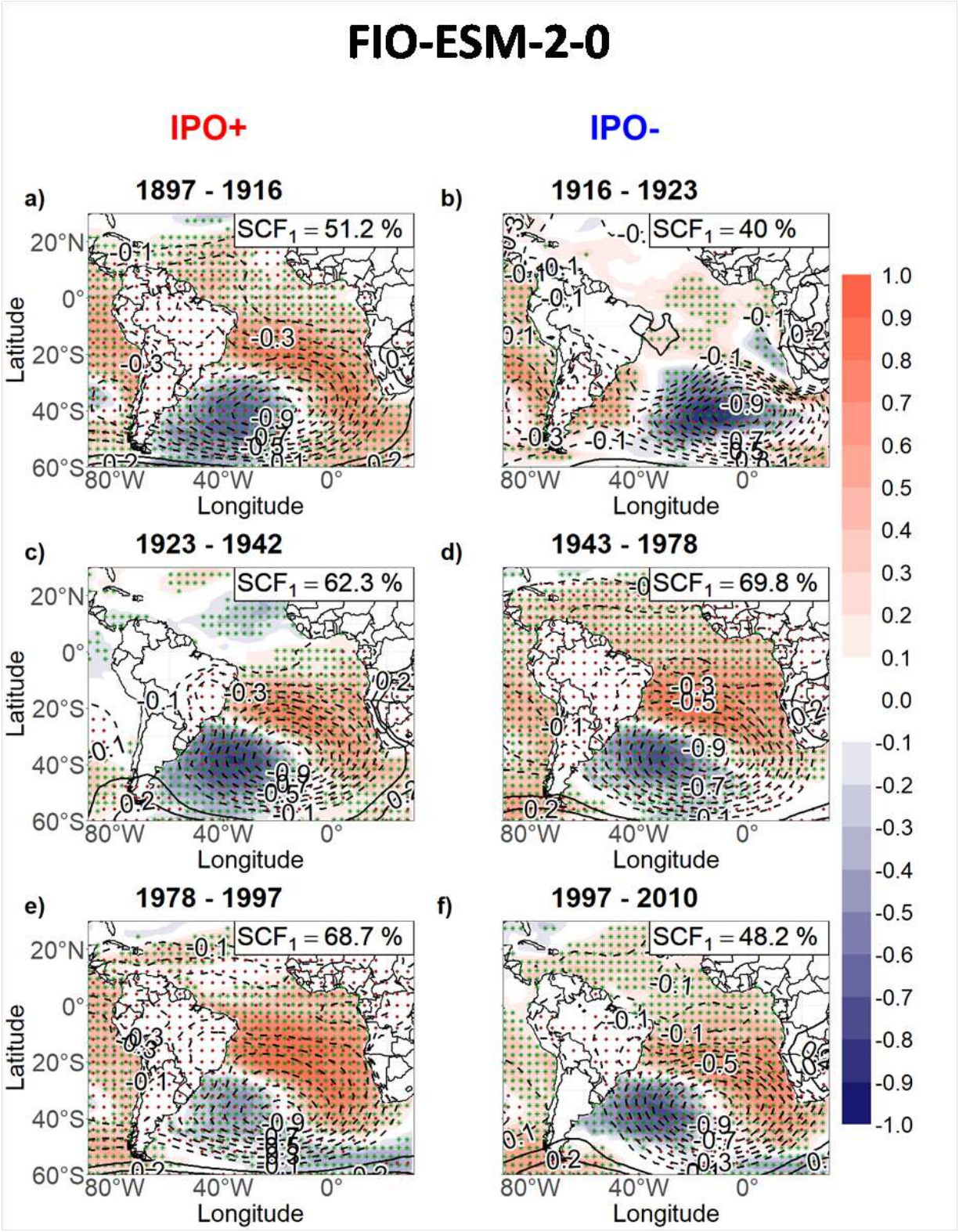

Figure 3.47: The same as in Figure 3.14 except for the FIO-ESM-2-0 model CMIP6 Historical Simulations.

3.3 The South Atlantic Dipole: Throughout the 21st century

In this section, we examine the SAD across the 21st century, for the three chosen models (FIO-ESM-2-0, CMCC-ESM2 and CMCC-CM2-SR5) considering the various SSPs scenarios (SSP1-2.6, SSP2-4.5, SSP3-7.0 and SSP5-8.5) described in subsection 2.2.2. These analyses encompass the entire period from 2015 to 2100, as well as three distinct intervals: 2015-2040, 2041-2070, and 2071-2100. These intervals, as well as the previously utilized IPO intervals, are chosen to capture the spectral peaks of the SAD while enabling us to assess potential changes in the mode over the entire duration. Priority is given to showing the figures associated with the FIO-ESM-2-0 model in the body of the section text to avoid visual pollution. Anyway, the Figures of the analyses performed with the CMCC-ESM2 and CMCC-CM2-SR5 models are found in Appendix G.

3.3.1 SSP1-2.6

SSP1-2.6 represents the "sustainability"scenario, as discussed in subsection 2.2.2. It is characterized by maintaining radiative forcing at levels comparable to the present day, while striving to limit the global warming to a maximum of 2°C by the end of the century (as illustrated in Figure 2.4d).

Figure 3.48 displays composites of SST and MSLP anomalies representing the positive and negative phases of the SAD for the three selected models throughout the entire SSPs period (2015-2100). The simulations for the 21st century appear to capture the SAD pattern well, characterized by a dipole of SST anomalies and the associated monopole MSLP anomalies. However, the lack of coupling between the Atlantic Niño sector and the SAD is also observed. This discrepancy can be attributed to two possible explanations: Firstly, it may be attributed to the inadequate representation of the Atlantic Niño sector in the models, as discussed in the previous section; Alternatively, it could be a natural outcome of a plausible southern configuration of the SAD. This trend, observed in the last analyzed intervals using observational data and corresponding to the last IPO interval configuration of the SAD (see Figures 3.14f, 3.15f and 3.16c), suggests that the Atlantic Niño naturally appears to be weakly coupled or even uncoupled under such circumstances.

The projected patterns of rainfall anomalies for the SSP1-2.5 covering the period 2015-2100 is shown in Figure 3.49, as predicted by each model. These patterns exhibit resem-

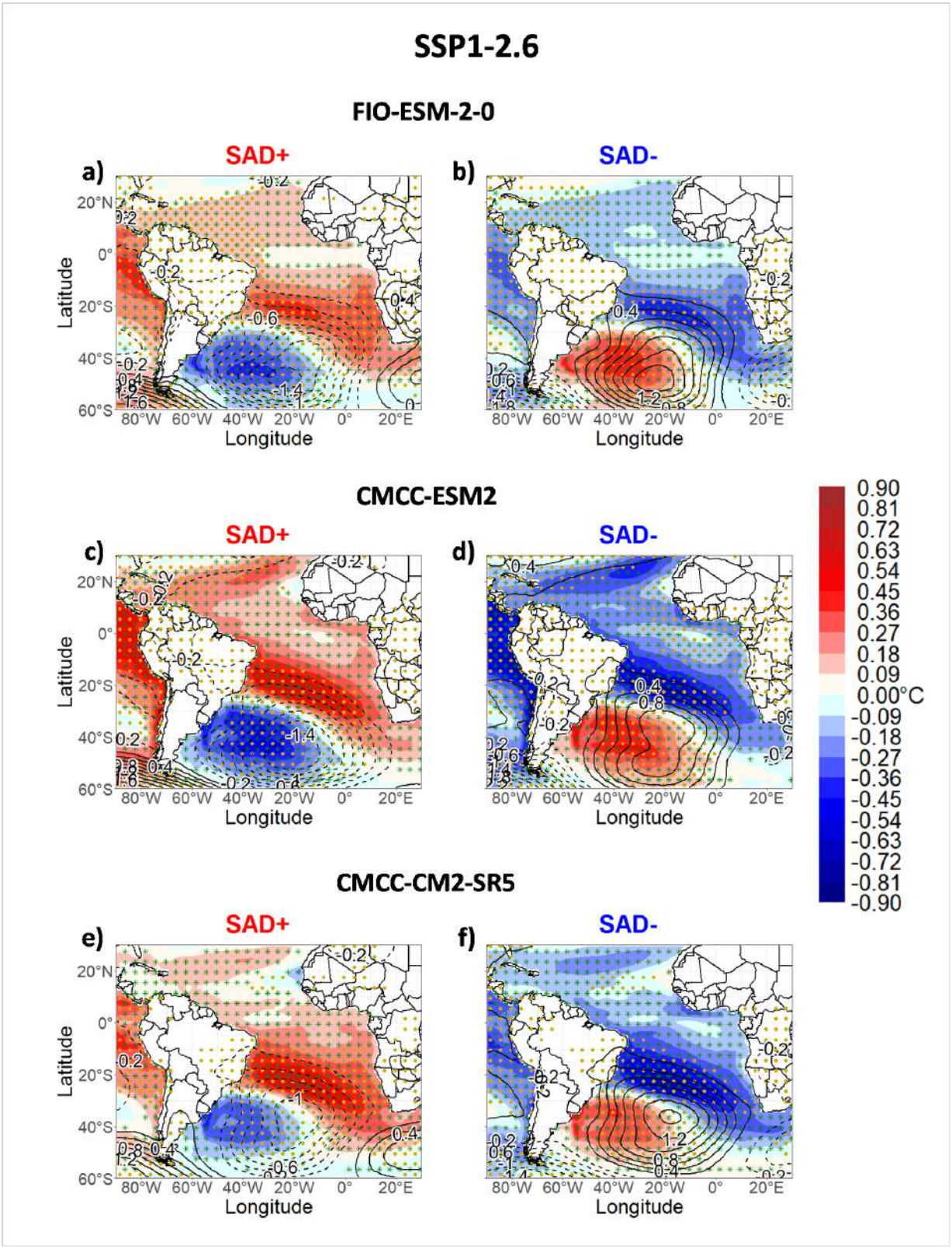

Figure 3.48: Composites with SST anomalies (in colors) and MSLP anomalies (contours) for the positive (SAD+) and negative (SAD-) phases of the South Atlantic Dipole determined for the full period (2015-2100) of the outputs of SSP1-2.6 scenario for the models FIO-ESM-2-0 (a) SAD+, b) SAD-), CMCC-ESM2 (c) SAD+, d) SAD-) and CMCC-CM2-SR5 (e) SAD+, f) SAD-). Values with a statistical confidence level above 95% are shown in green (yellow) dots for SST (MSLP) anomalies.

blances to the wider dipole pattern observed between a merged sector of NNE-CEBR and SESA during the last IPO interval (1997-present) for the DJF months in the reanalysis datsets (Figures 3.22e-f, D.1e-f and D.5f). This dipole pattern is closely linked to the southernmost configuration of the SAD.

The SST and MSLP anomalies associated with each phase of the SAD for the SSPs intervals (2015-2040, 2041-2070 and 2071-2100) are shown in Figures 3.50, G.1, and G.7 illustrate. The dipole of SST anomalies presents a subtle southward shift throughout the intervals for the FIO-ESM-2-0 and CMCC-ESM2 models (Figures 3.50 and G.1, respectively). However, no significant changes are observed in MSLP anomalies across all three models. In terms of anomaly intensity, a decreasing trend is noticeable for both SST and MSLP anomalies in all cases.

For each of the three models, Figures 3.51, G.2, and G.8 depict the precipitation anomalies during each phase of the SAD across the corresponding SSPs intervals. Overall, the models consistently exhibit a dipole pattern of precipitation anomalies between the northern region of South America and SESA, which aligns with the anomalies observed throughout the entire SSPs period (Figure 3.49).

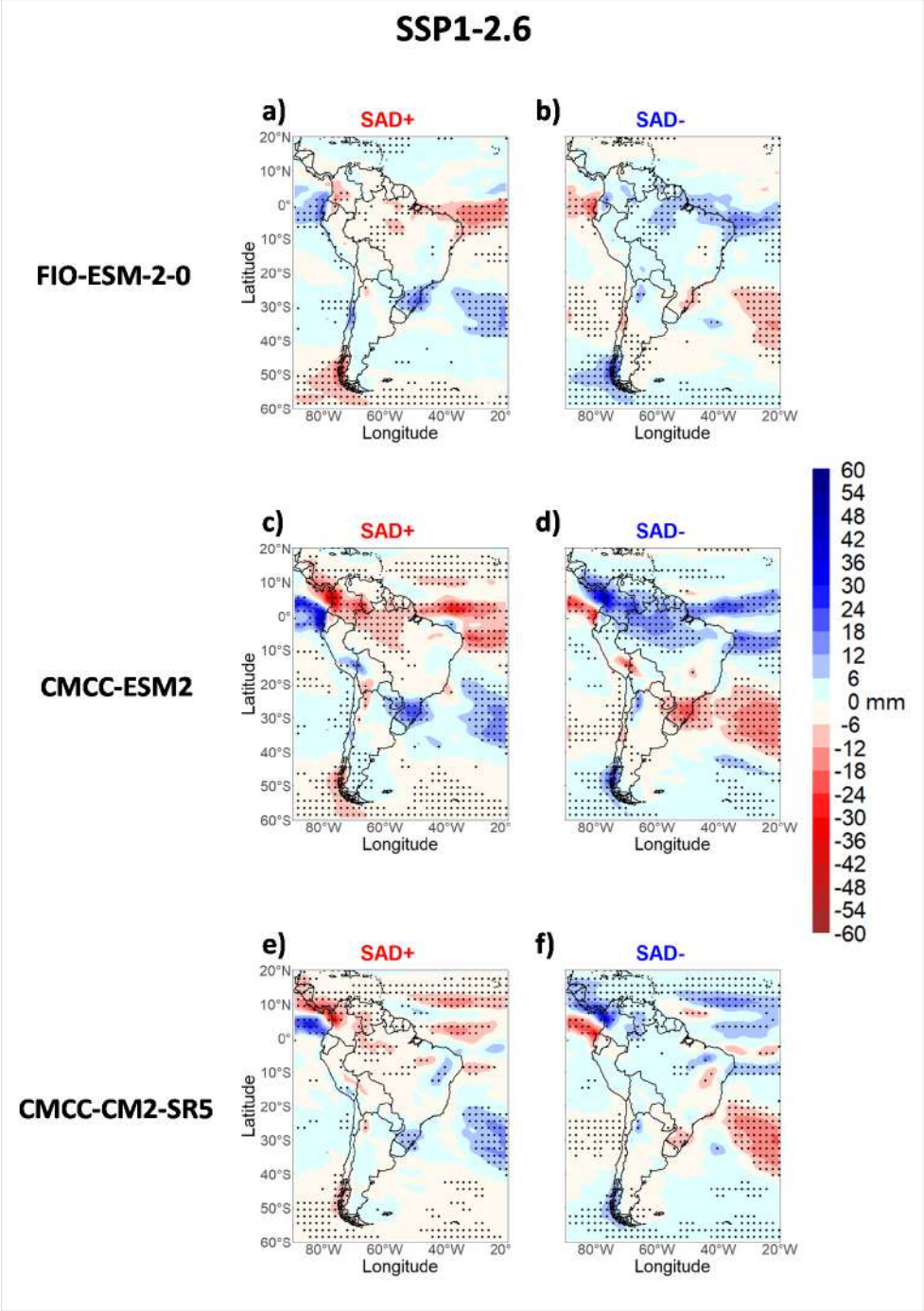

Figure 3.49: Composites with precipitation anomalies (in color) for the positive (SAD+) and negative (SAD-) phases of the South Atlantic Dipole determined for the full period (2015-2100) of the outputs of SSP1-2.6 scenario for the models FIO-ESM-2-0 (a) SAD+, b) SAD-), CMCC-ESM2 (c) SAD+, d) SAD-) and CMCC-CM2-SR5 (e) SAD+, f) SAD-). Dots are values with a statistical confidence level above 95%.

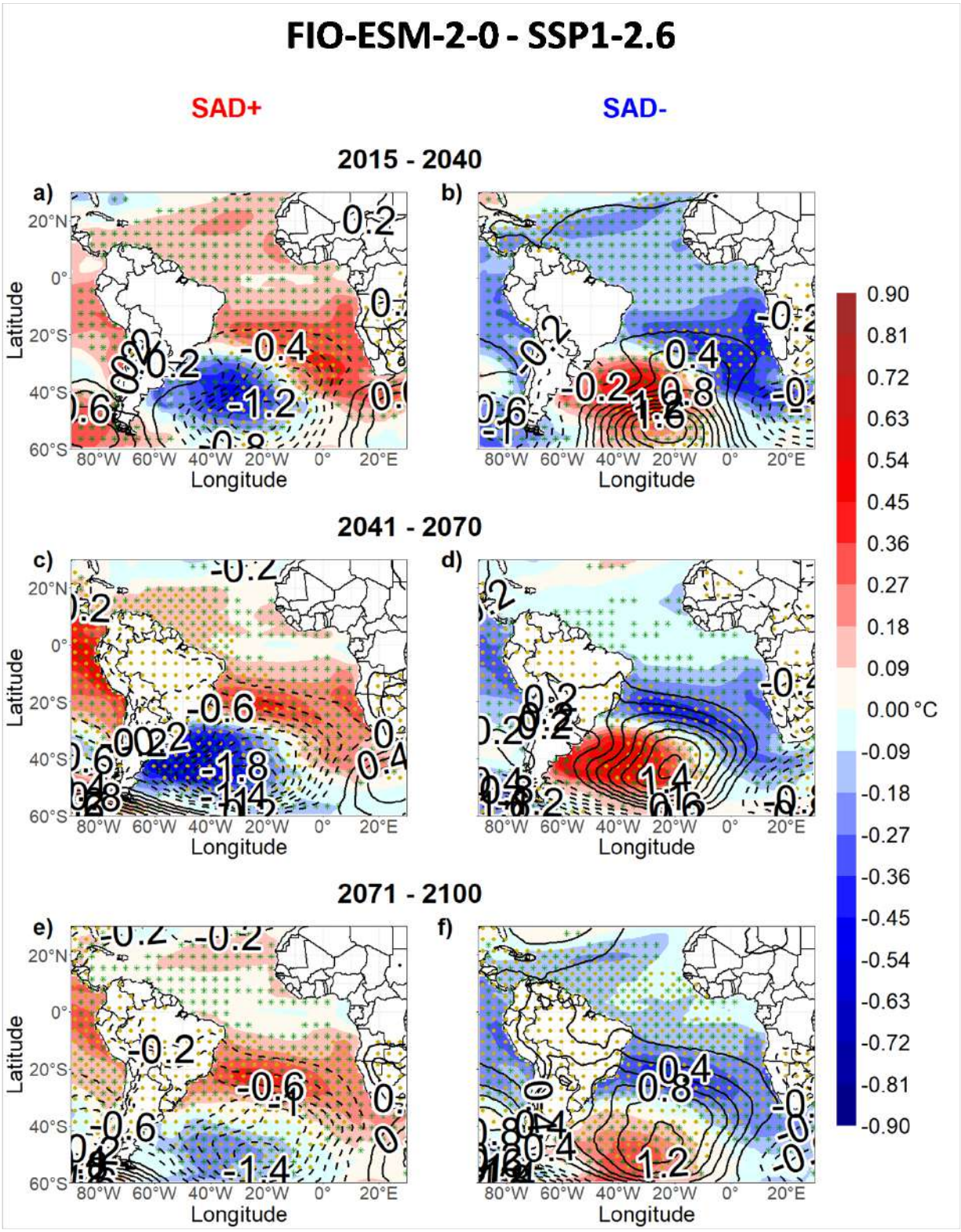

Figure 3.50: Composites with SST anomalies (in colors) and MSLP anomalies (contours) for the positive (SAD+) and negative (SAD-) phases of the South Atlantic Dipole for the periods 2015-2040 (itens a) SAD+ and b) SAD-), 2041-2070 (itens c) SAD+ and d) SAD-) and 2071-2100 (itens e) SAD+ and f) SAD-). Computed using the outputs of the FIO-ESM-2-0 model for the SSP1-2.6 scenario. Values with a statistical confidence level above 95% are shown in green (yellow) dots for SST (MSLP) anomalies.

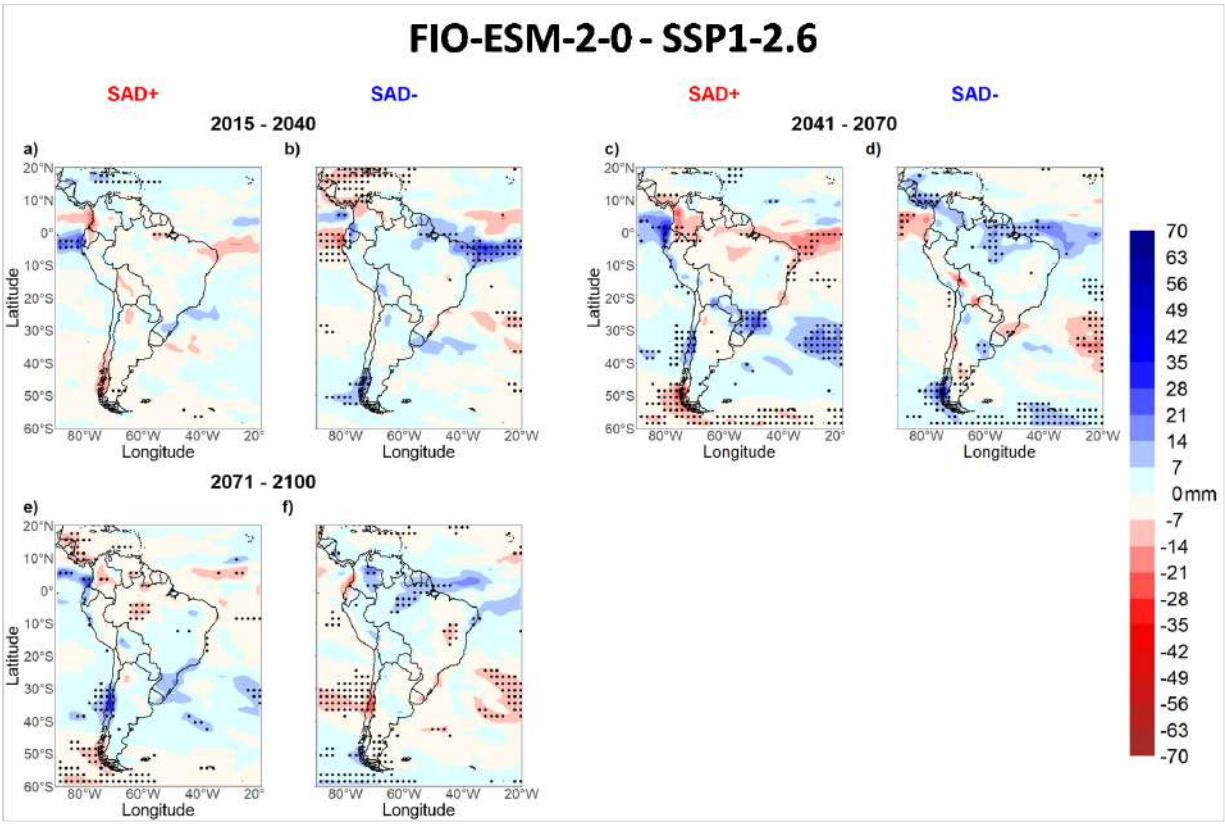

Figure 3.51: Composites with precipitation anomalies (in color) for the positive (SAD+) and negative (SAD-) phases of the South Atlantic Dipole, determined from the ERA5 reanalysis dataset and for the December-February quarter (DJF) season. Calculated with GPCC precipitation dataset. Determined for the IPO intervals a-b) 1950-1978, c-d) 1978-1997 and e-f) 1997-2020. ENSO periods are disregarded in this analysis. Values with a statistical confidence level above 95% are shown in dotted lines.

3.3.2 SSP2-4.5

Referred to as the "middle of the road" scenario, SSP2-4.5 offers a moderate outlook for the future of climate and socioeconomic conditions. This scenario predicts a warming of approximately 2.5°C by the year 2100 (Figure 2.4d), compared to pre-industrial levels.

The SAD maintains a consistent configuration from 2015 to 2100, as evident in the analysis of all three models (Figure 3.52). When compared to SSP1-2.6 (Figure 3.48), both the SST and MSLP anomalies exhibit slightly higher intensity across all models, with the FIO-ESM-2-0 model specifically showing a more northerly positioning (Figure 3.52a-b).

The precipitation anomalies associated with each SAD phase throughout the entire SSPs period for each model are demonstrated in Figure 3.53. As well as to SSP1-2.6, a distinct dipole pattern of precipitation is observed between northern South America and SESA. However, the anomalies exhibit greater intensity during the SAD positive phase for all three models when comparing to SSP1-2.6 (Figures 3.53a, 3.53c, and 3.53e). In contrast, during the negative phase of the SAD, the anomalies are less pronounced for the FIO-ESM-2-0 and CMCC-ESM2 models (Figures 3.53b and 3.53d, respectively), while the CMCC-CM2-SR5 model shows heightened intensity (Figure 3.53f).

The SST and MSLP anomalies for each SAD phase within each SSPs interval is displayed in Figures 3.54 for FIO-ESM-2-0, G.3 for CMCC-ESM2 and G.9 for CMCC-CM2-SR5. When examining the evolution of these anomalies throughout the 21st century, it becomes evident that the configuration of the SAD remains relatively stable with minimal or no considerable changes.

Figures 3.55, G.4, and G.10 depict the precipitation anomalies during each phase of the SAD for each SSPs interval and GCMs. In the case of the FIO-ESM-2-0 model (Figure 3.55), the dipole of anomalies between northern South America and SESA exhibit an increasing intensity throughout the SSPs intervals. For the CMCC-ESM2 model (Figure G.4), the dipole pattern persists, but with diminishing anomaly intensity over time. Additionally, there is a slight expansion of precipitation anomalies associated with SESA towards CEBR across the intervals. As for the CMCC-CM2-SR5 model (Figure G.10), a noteworthy change occurs in the CEBR pole, which roughly separates from the NEBR pole and eventually merges with the SESA pole by the end of the 21st century. However,

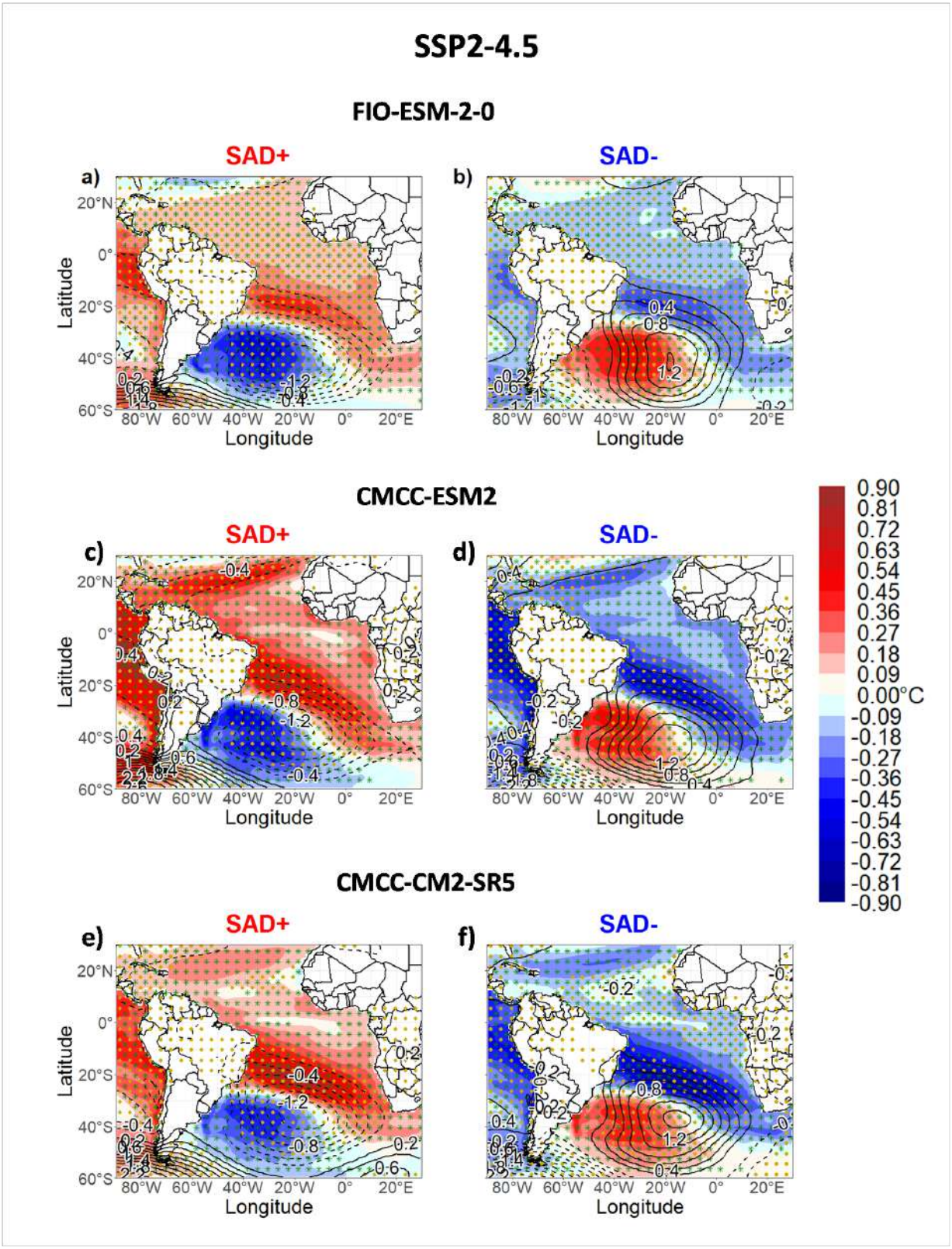

Figure 3.52: The same as in Figure 3.48 except for the SSP2-4.5 scenario.

it is worth noting that the characterization of anomalies for SAD+ is less defined in the first two intervals (Figures G.10a and G.10c).

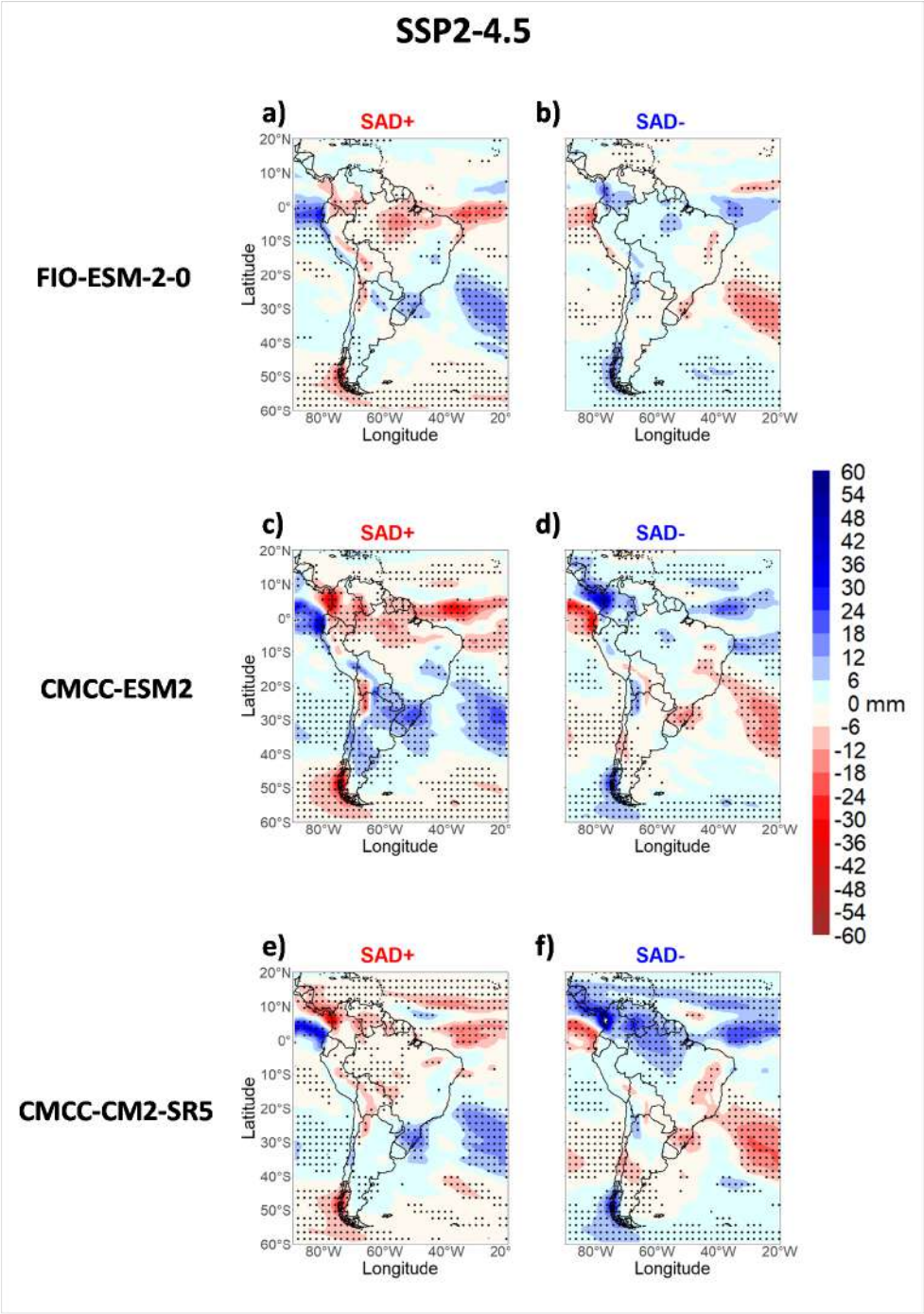

Figure 3.53: The same as in Figure 3.49 except for the SSP2-4.5 scenario.

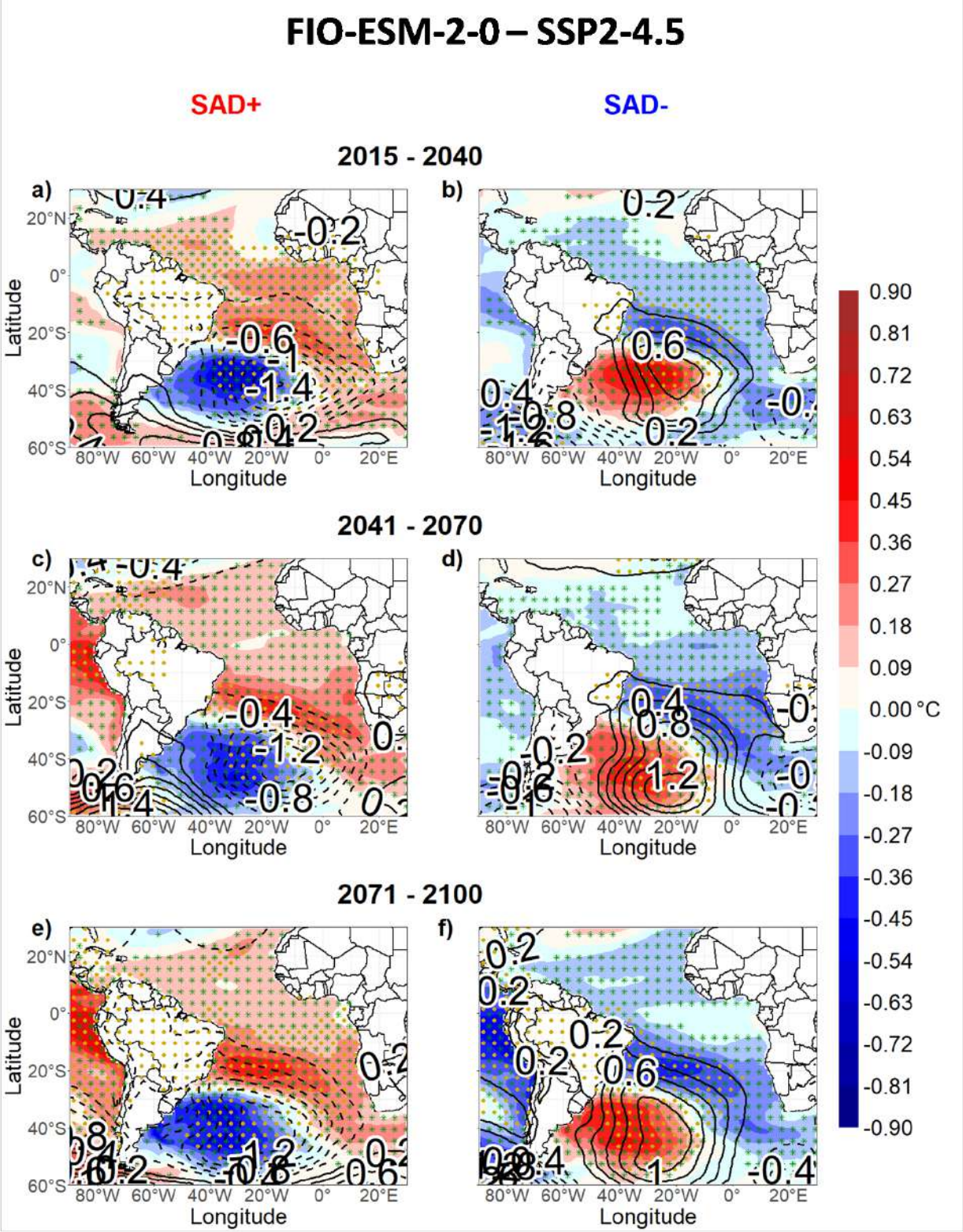

Figure 3.54: The same as in Figure 3.50 except for the SSP2-4.5 scenario.

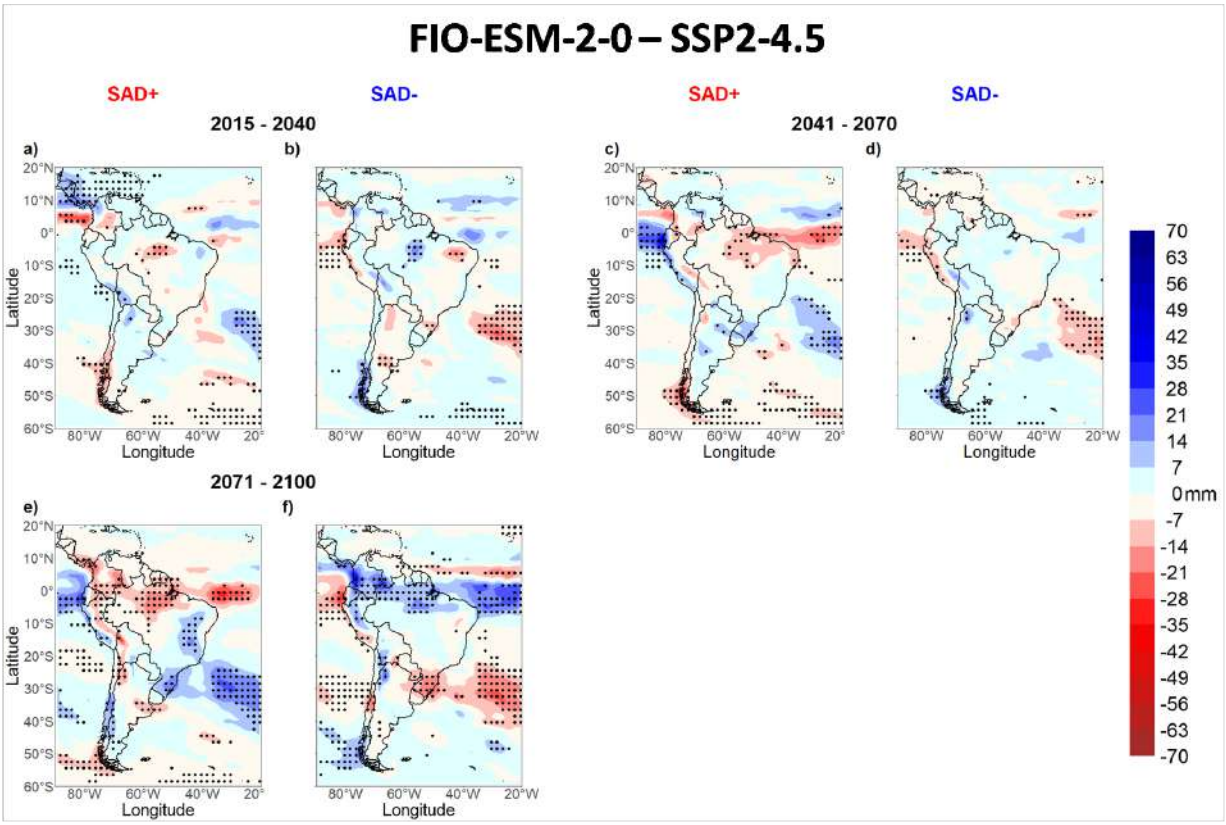

Figure 3.55: The same as in Figure 3.51 except for the SSP2-4.5 scenario.

3.3.3 SSP3-7.0

SP3-7.0 represents a "regional rivalry" scenario, where global cooperation on environmental preservation policies is very limited. In this scenario, the projected CO_2 concentration reaches 830ppm, and the average global temperature is estimated to increase by 4°C compared to pre-industrial levels by the end of the 21 st century (as depicted in Figures 2.4b and 2.4d, respectively).

In this particular scenario, we only have data available from the CMCC-EMS2 and CMCC-CM2-SR5 models. The SST and MSLP anomalies for the period 2015-2100 are illustrated in Figure 3.56. Notably, this scenario exhibits the most pronounced anomalies compared to all other SSPs. Otherwise, when it comes to the configuration of the SAD, no significant variations are observed in comparison to the other SSPs.

Figure 3.57 displays the precipitation anomalies throughout the entire SSPs period for the CMCC-ESM2 and CMCC-CM2-SR5 models. The anomaly pattern aligns with the dipole pattern observed between the northern region of South America and SESA, already observed in other SSPs. Notably, the precipitation anomalies exhibit greater intensity compared to all other analyzed SSPs. Moreover, these anomalies exhibit a wider spatial extent around the previously observed nuclei.

Figures 3.58 and 3.59 illustrate the SST and MSLP anomalies within the SSPs intervals for the CMCC-ESM2 and CMCC-CM-SR5 models, respectively. Overall, these figures reveal the presence of more pronounced anomalies. The SST anomaly dipole does not show important changes, while the MSLP anomalies exhibit a slight northwestward shift across the intervals in both models.

The dipole pattern of precipitation anomalies, characterized by contrasting anomalies between the tropical region of South America and SESA, is consistently well-defined across all intervals and for both models (Figures 3.60 and 3.61). These anomalies exhibit the highest intensity among all the analyzed SSPs, particularly in the case of CMCC-ESM2 (Figure 3.60).

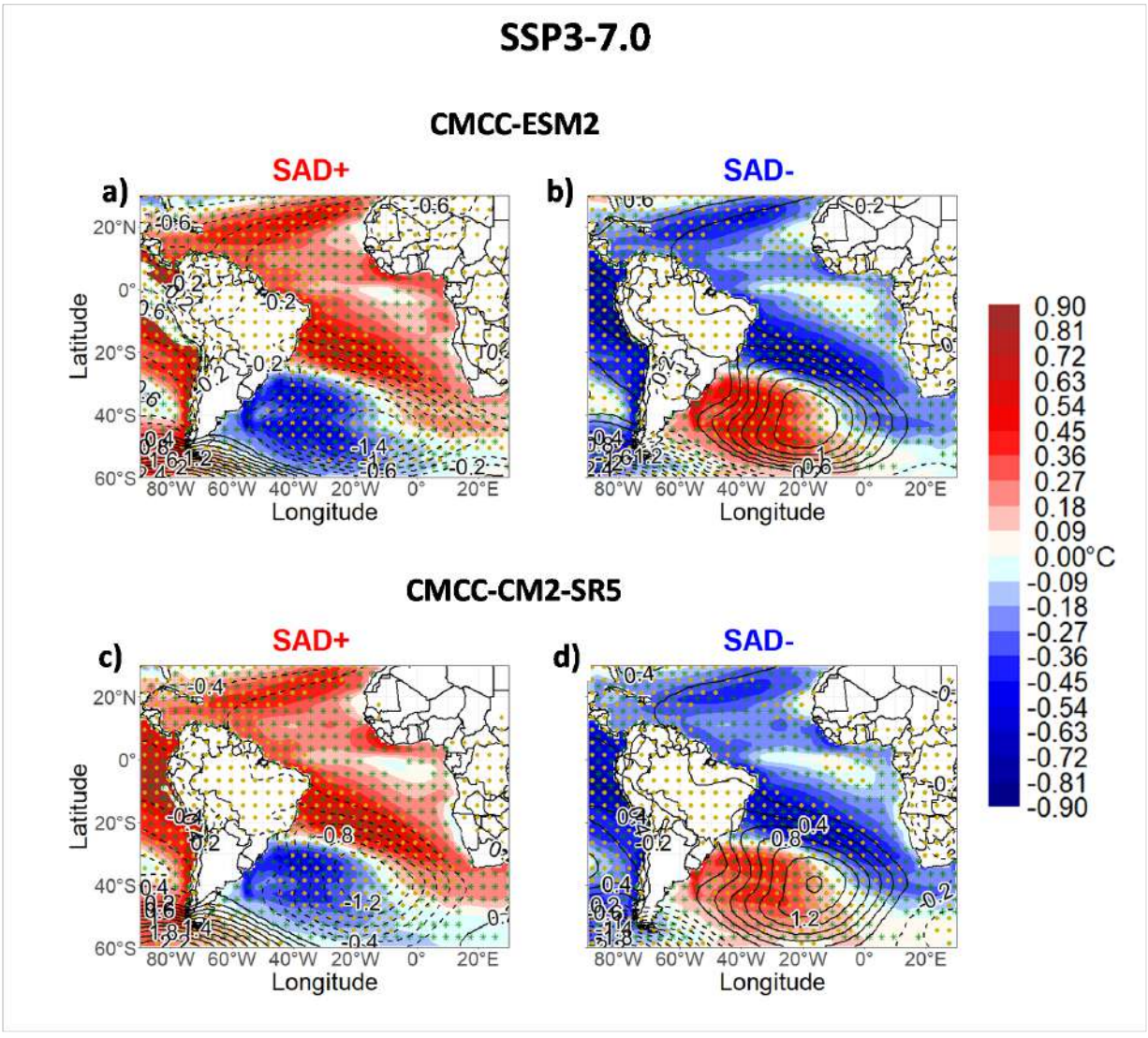

Figure 3.56: The same as in Figure 3.48 except for the SSP3-7.0 scenario.

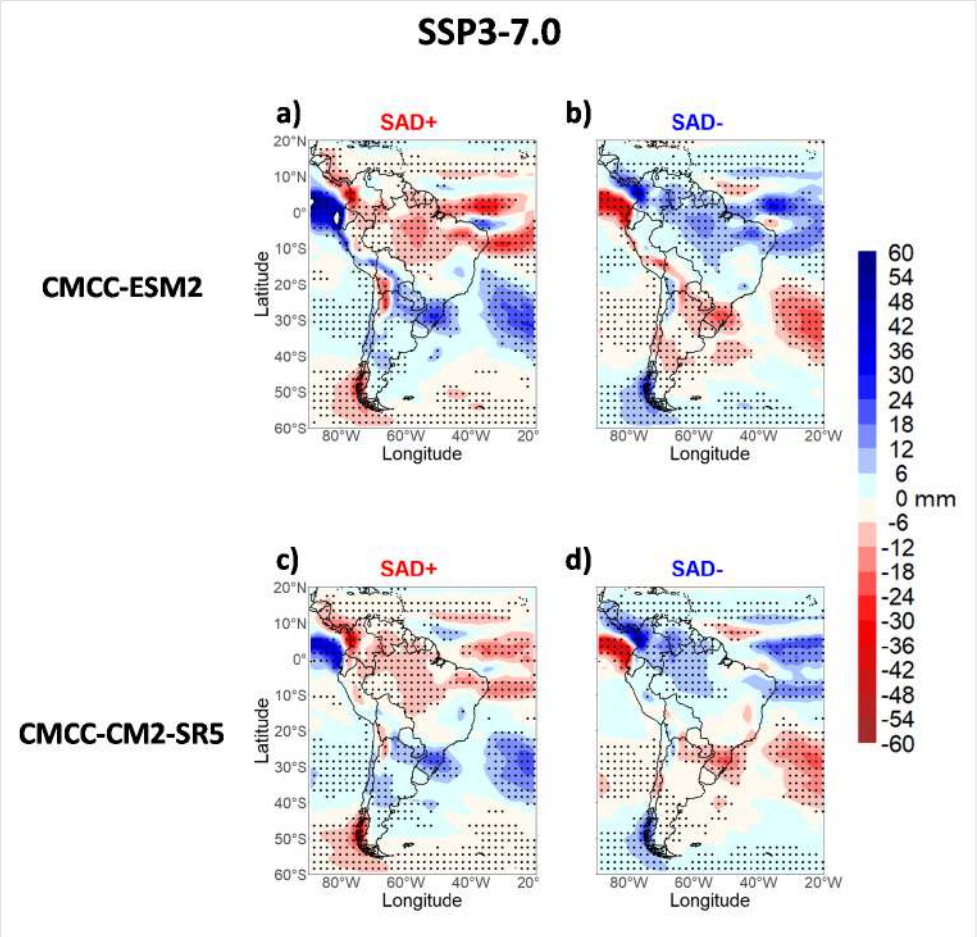

Figure 3.57: The same as in Figure 3.49 except for the SSP3-7.0 scenario.

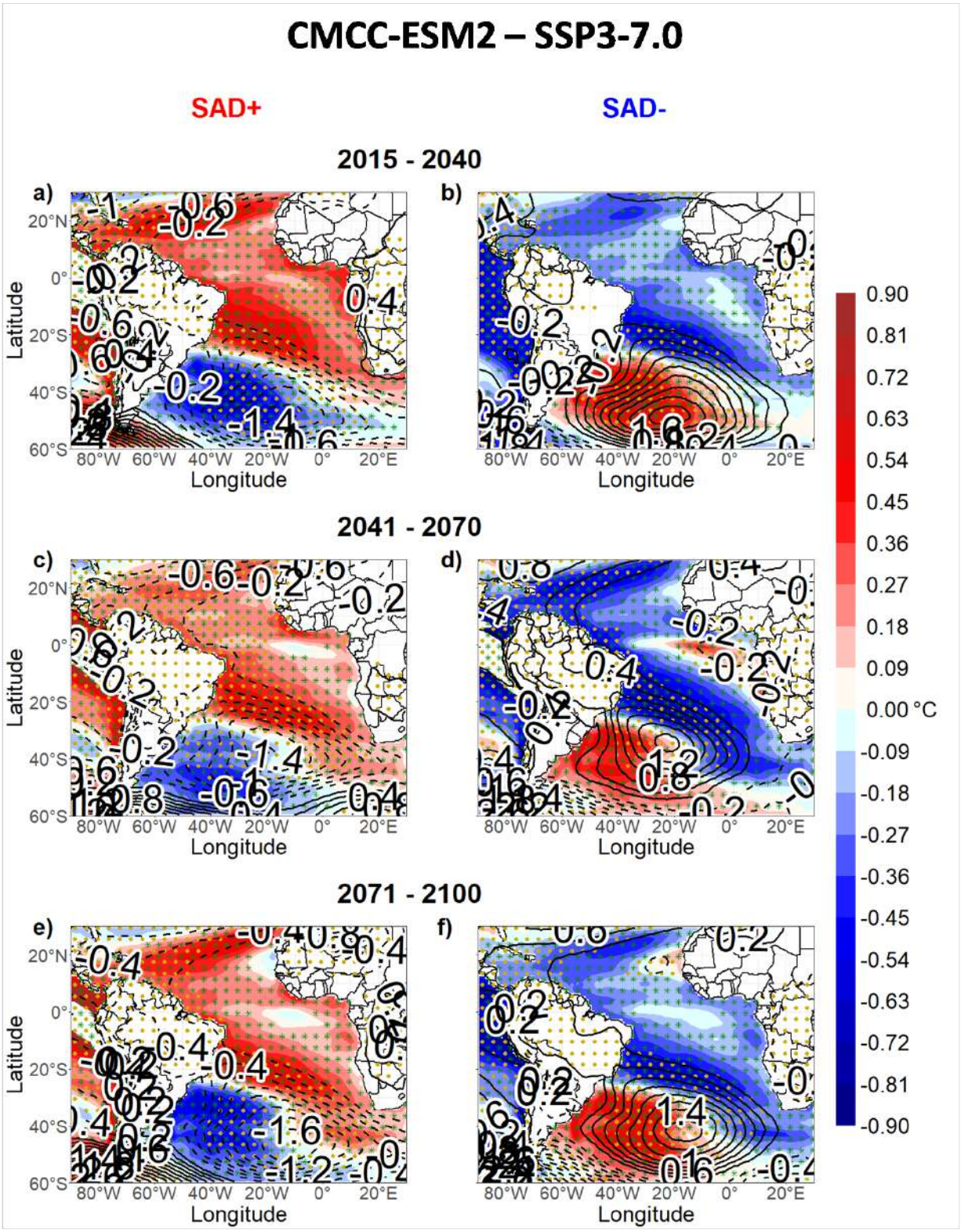

Figure 3.58: The same as in Figure G.1 except for the SSP3-7.0 scenario.

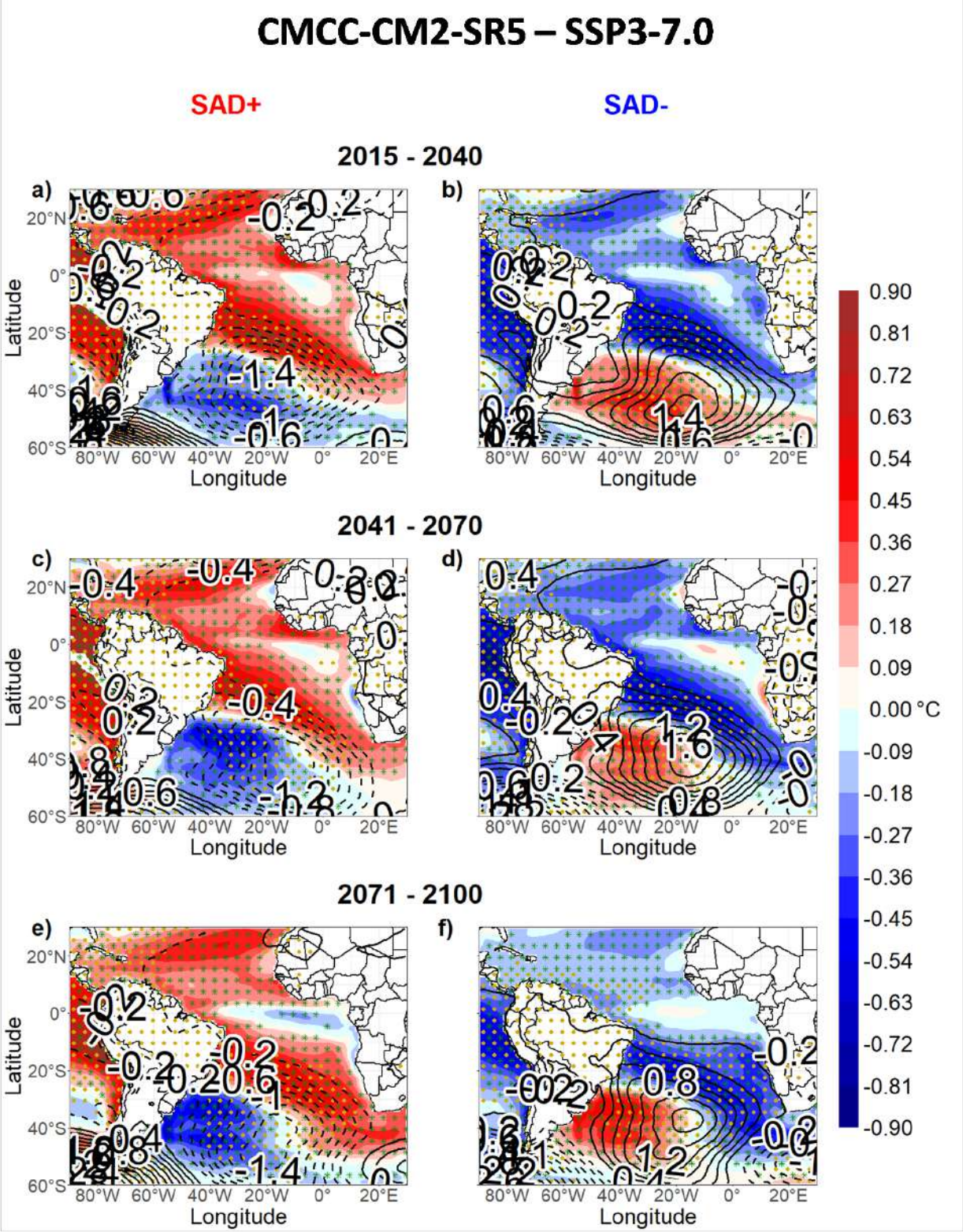

Figure 3.59: The same as in Figure G.7 except for the SSP3-7.0 scenario.

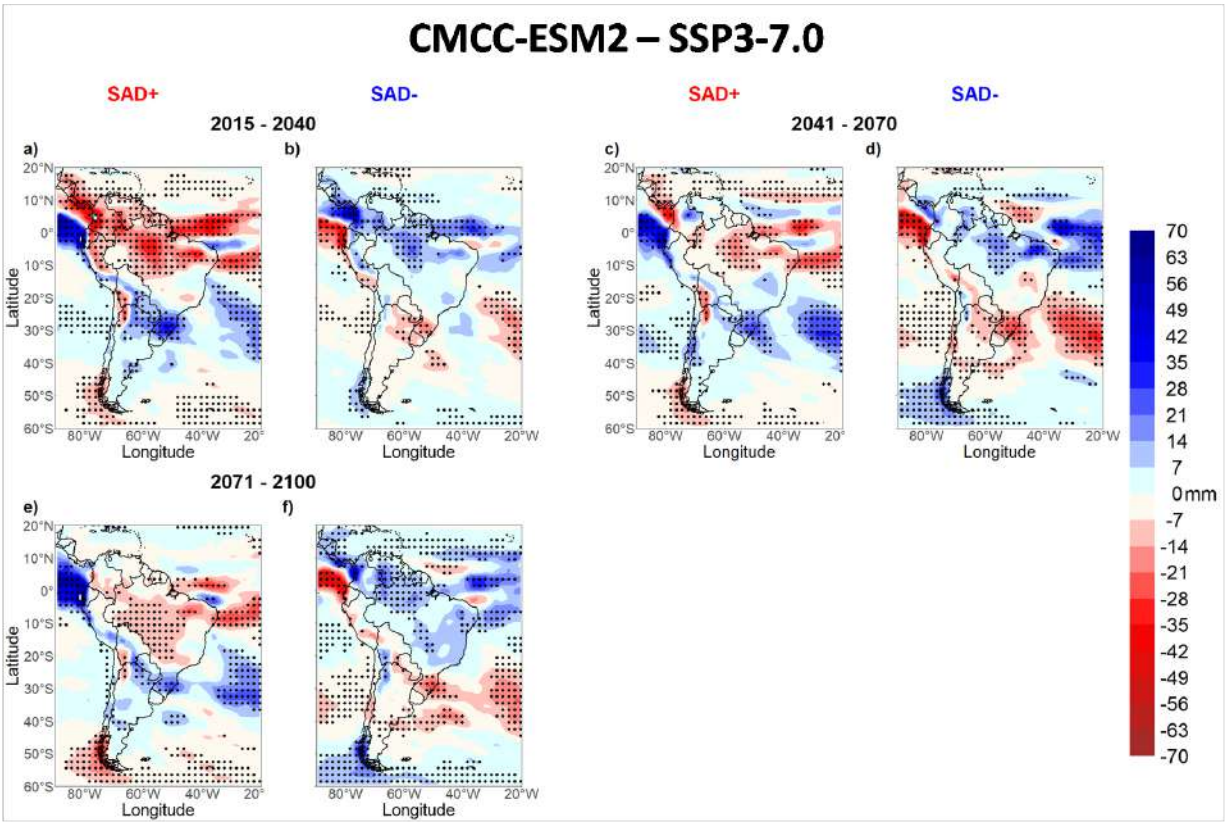

Figure 3.60: The same as in Figure G.2 except for the SSP3-7.0 scenario.

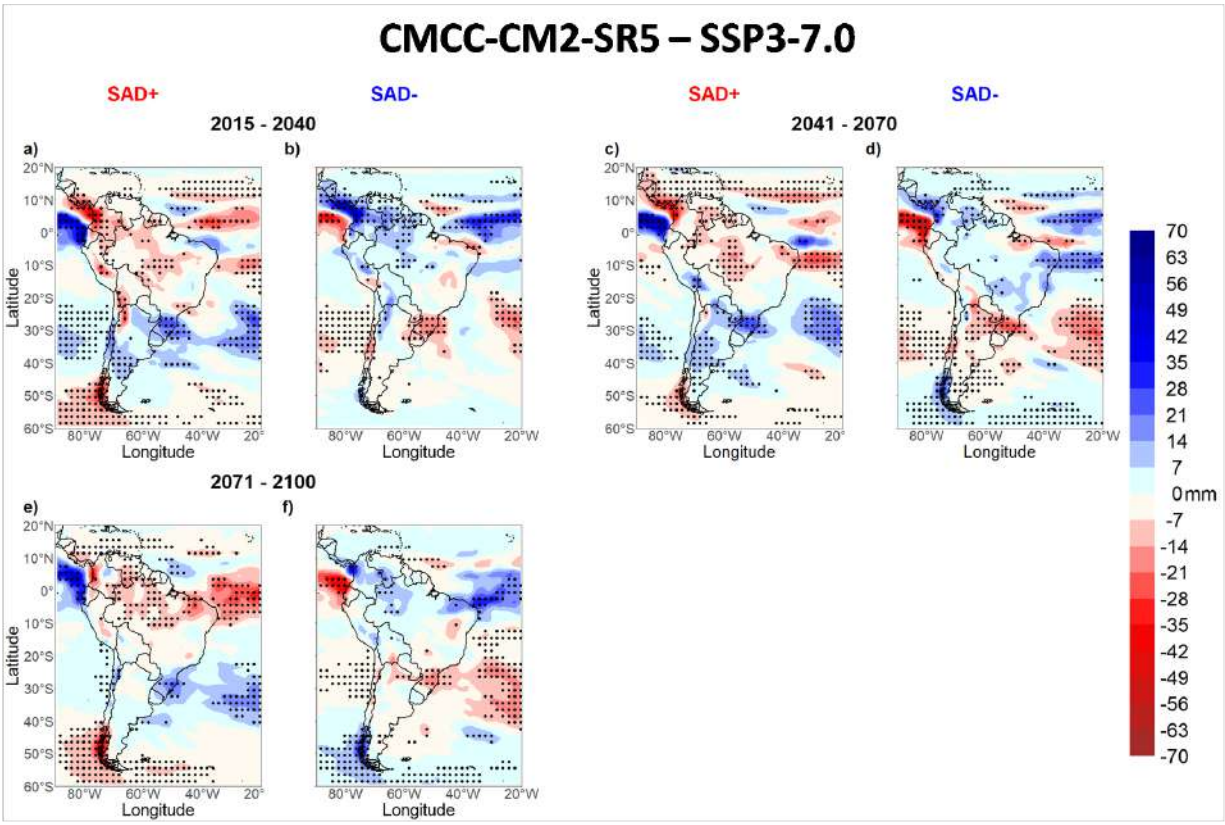

Figure 3.61: The same as in Figure G.8 except for the SSP3-7.0 scenario.

3.3.4 SSP5-8.5

A future dominated by "fossil-fueled development,"prioritizing strong economic and social advancement with limited regard for environmental factors, it is what is represented by the SSP5-8.5 scenario. This scenario predicts the highest levels of CO_2 concentration (1100ppm) and a substantial increase in global average temperature (5°C) by the end of the 21st century (Figures 2.4b and 2.4d).

In terms of the SAD, the SSP5-8.5 exhibits similar patterns to the other SSPs, with slightly less intense anomalies compared to SSP3-7.0, which is characterized by the highest intensity. This observation holds true when considering the entire SSPs period (Figure 3.62). The same trend can be observed for precipitation anomalies (Figure 3.49). Specifically for the FIO-ESM-2-0 model, which lacks data for SSP3-7.0, both the SST and MSLP anomalies (Figures 3.62a-b) as well as the precipitation anomalies (Figures 3.49a-b) are shown to be the most intense, considering the period 2015-2100 as a whole and among the available scenarios.

Figures 3.64, G.5, and G.11 depict the SST and MSLP anomalies for each SSPs interval in each SAD phase. In the case of the FIO-ESM-2-0 model (Figure 3.64), a slight northward shift of the SST anomaly dipole is observed during the middle interval (2041-2070), accompanied by an Atlantic Niño signal (Figures 3.64c-d). This is notable for being an isolated case within the analyses we performed with the CMIP6 GCMs, considering that the SAD is typically shown to be coupled with the Atlantic Niño in analyses with long-term observational data. However, in the other two intervals (2015-2040 and 2071-2100) (Figures 3.64a-b and 3.64e-f), the SST anomaly dipole remains further south, consistent with previous situations. For the CMCC-ESM2 model (Figure G.5), a minor southward shift in the SAD pattern and a reduction in associated anomalies are noticed in the last interval (2071-2100) (Figures G.5e-f) compared to the previous intervals (Figures G.5a-d). In the CMCC-CM2-SR5 model (Figure G.11), an Atlantic Niño signature is observed in the first interval (Figures G.11a-b), but it vanishes in the subsequent intervals. Over time, there is a strengthening of the associated anomalies.

Precipitation anomalies in each phase of the SAD for each SSPs interval and model are presented in Figures 3.65, G.6, and G.12. In the case of the FIO-ESM-2-0 model, the dipole of precipitation anomalies between northern South America and a merged CEBR-

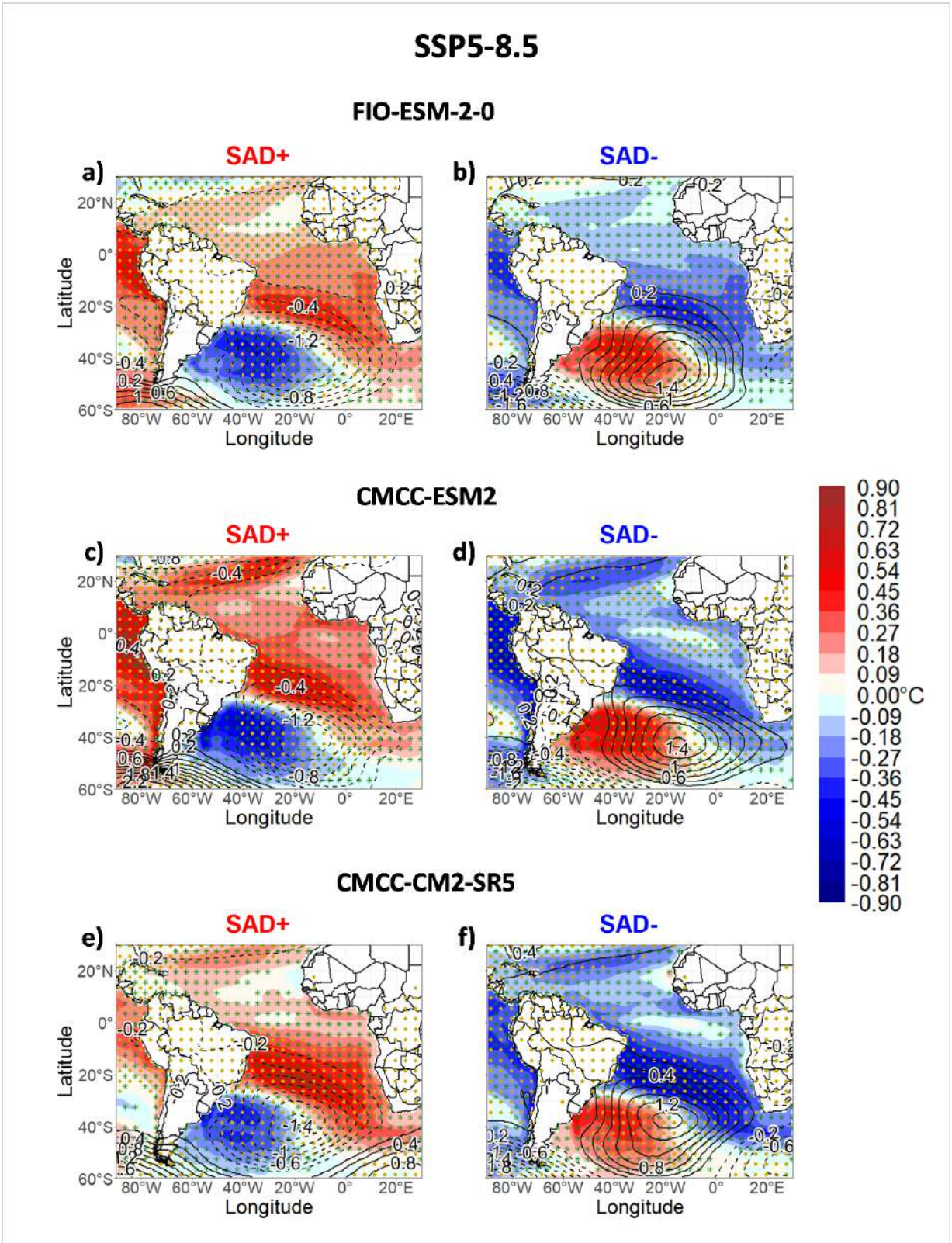

Figure 3.62: The same as in Figure 3.48 except for the SSP5-8.5 scenario.

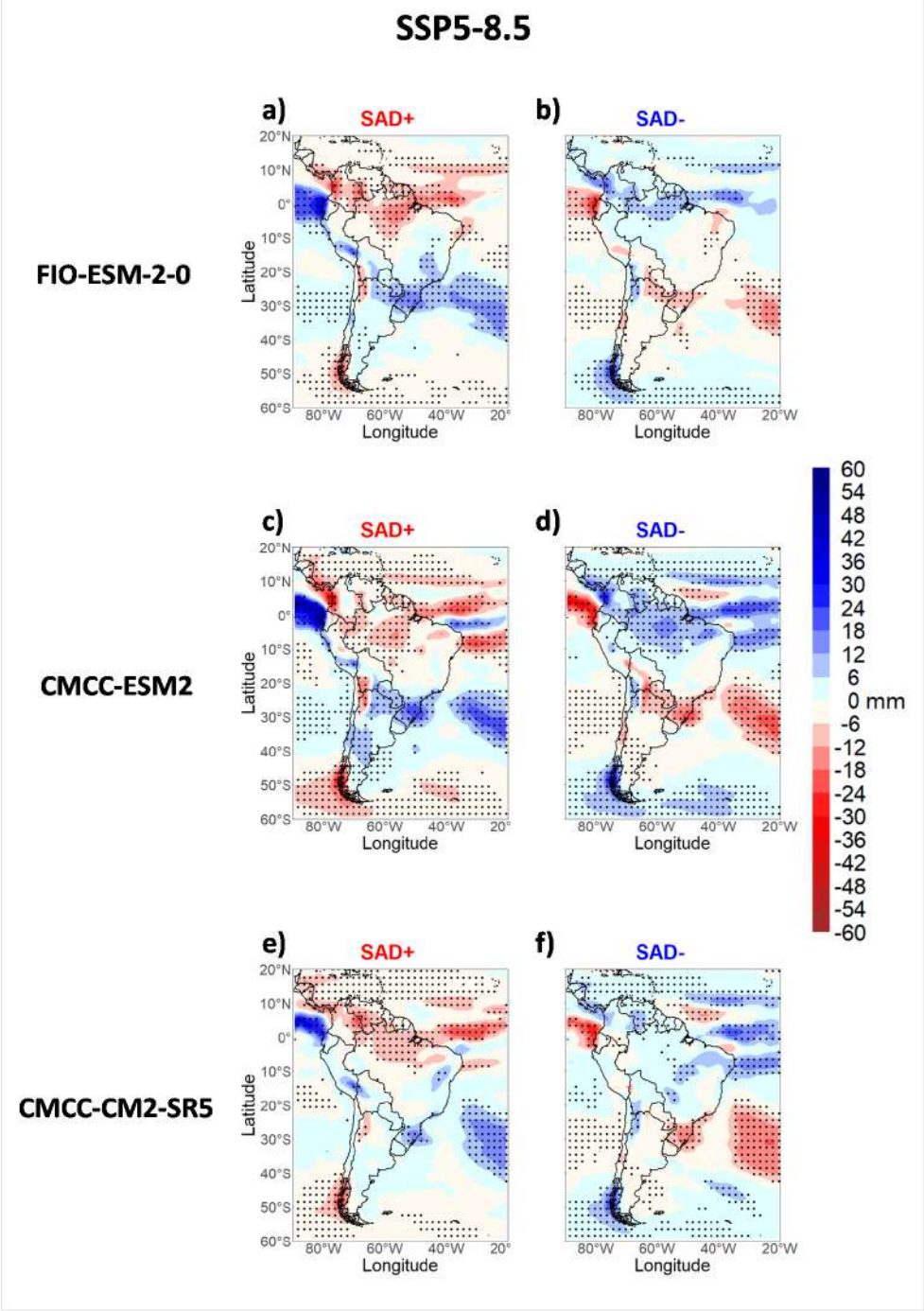

Figure 3.63: The same as in Figure 3.49 except for the SSP5-8.5 scenario.

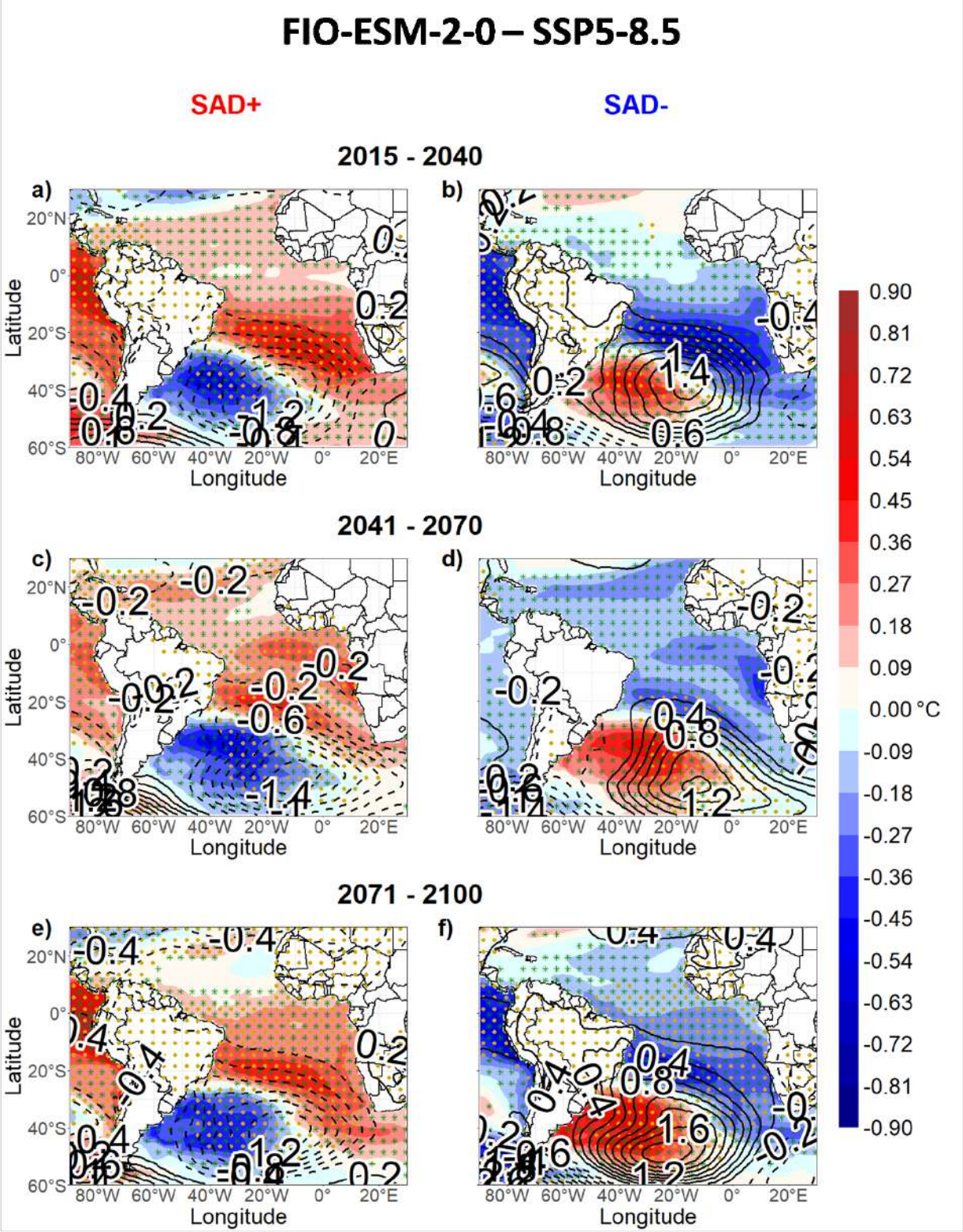

Figure 3.64: The same as in Figure 3.50 except for the SSP5-8.5 scenario.

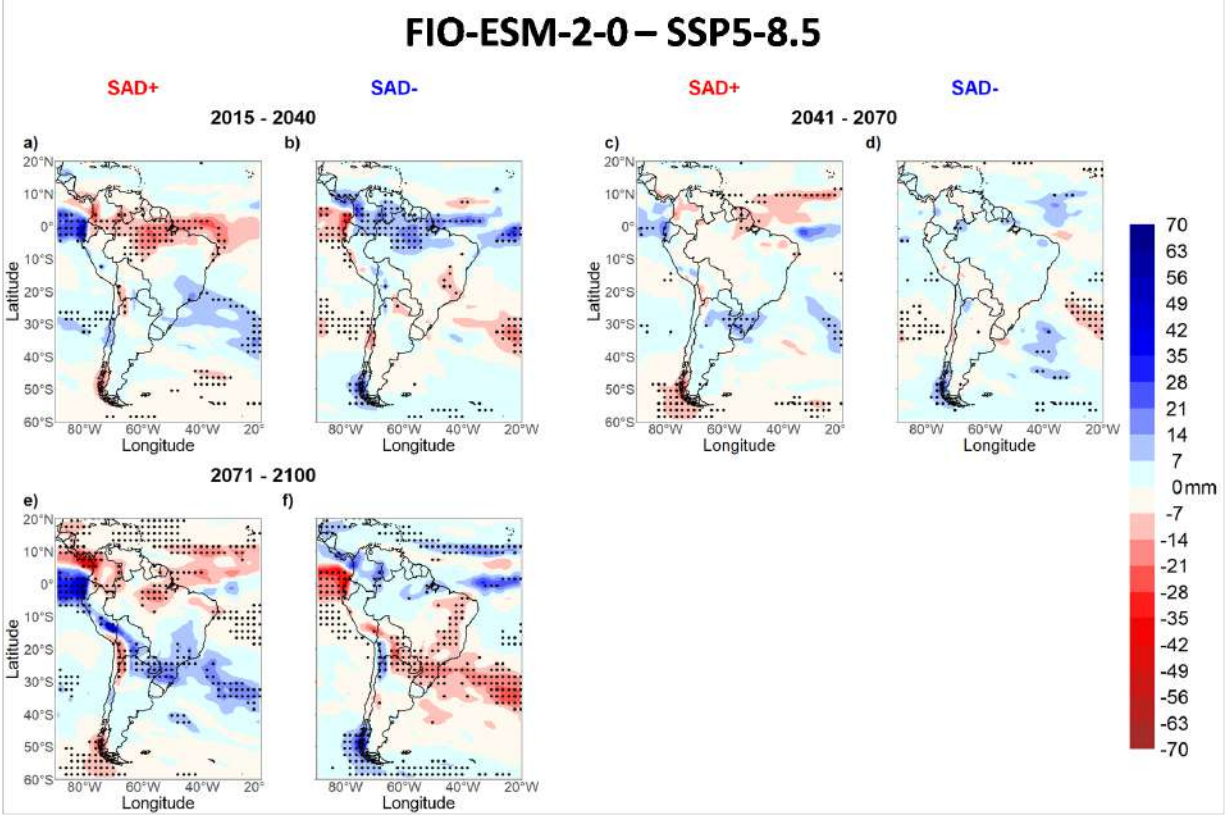

Figure 3.65: The same as in Figure 3.51 except for the SSP5-8.5 scenario.

SESA is verified in the first and last intervals (Figures 3.65a-b and 3.65e-f). However, during the middle interval (Figures 3.65c-d), there are fewer significant anomalies over the whole study area. For the CMCC-ESM2 model (Figure G.6), the dipole of precipitation anomalies between northern South America and SESA is consistently and clearly observed in all intervals. The pattern is significant and well-defined. Regarding the CMCC-CM2-SR5 model (Figure G.12), the dipole between northern South America and a merged CEBR-SESA is more pronounced in the last interval (Figures G.12e-f). Notwithstanding, in the other intervals, there is also a trend indicating the dipole, but the anomalies appear fragmented over the South American continent, lacking a coherent pattern.

Chapter 4

Conclusions

The objective of this study was to investigate the spatio-temporal variability of SAD from the post-industrial revolution to the end of the 21st century (1850s-2100) and its influence on the climate of South America. To put it concisely, the study was divided into three main parts: 1) examining the SAD through the historical period (1850-2020) with observational data; 2) assessing the ability of CMIP6 models to replicate the historical SAD and its regional climate impacts; 3) analyzing the future evolution of the SAD (2015-2100) under different CMIP6 future climate scenarios.

In the first part of the study, we conducted a set of analyses mainly derived from SVD and composites, using data from reanalysis and precipitation datasets (observational data). Through SVD analysis, we identified the first coupled mode between ocean and atmosphere over the SAO, known as the SAD, and explored its characteristics, importance, and spatio-temporal variations. The SAD was analyzed from different temporal points of view, from the annual to the seasonal variability. It was given a special insight for the austral summer since is a special season for the mode in its interaction with the South America climate. Furthermore, we investigated the interactions between this oscillation and the climate of South America by analyzing composites of various variables. To detect changes in the behavior of the SAD and its associated climate over time, we employed the framework of IPO phases. These phases are directly connected to the SAD and encompass the dominant spectral peaks of the oscillation. Thus, they provided us with a valuable tool for our analyses, allowing us to assess any temporal shifts in the mode's characteristics and their impact on the climate of the study area. This approach allowed us to examine the coupled interactions between the ocean and atmosphere, providing a comprehensive understanding of the dynamics at play.

This first part of analyses have some findings, which have been previously identified in earlier studies and further supported in this research:

- The SAD is an oscillation with more concise spectral peaks on the interannual and interdecadal scales.
- The SAD is in the southernmost (northernmost) position during the Austral summer (winter).
- A positive relationship between the SAD and ENSO was observed during the IPO negative phase periods, namely 1950-1978 and 1997-2020. Conversely, a negative relationship was found between the negative phase of SAD and ENSO during the IPO positive phase period spanning from 1978 to 1997. This is reinforced by a higher occurrence of SAD+ (SAD-) during El Niño (La Niña) events within the IPO- periods. Inversely, a greater number of SAD- (SAD+) events are associated with El Niño (La Niña) during the IPO+.
- The precipitation anomaly patterns associated with the SAD exhibit seasonal variations. During the MAM season, a quadripole of anomalies (GYR-NNE-CEBR-SESA) is observed, while during DJF and SON months, a tripole (NNE-CEBR-SESA) pattern emerges. In JJA months, a monopole is observed over northern South America.
- Strong agreement is found among different reanalysis datasets for periods after 1943.

Overall, these findings provide valuable insights into the characteristics and relationships of the SAD, its connection with ENSO and IPO, and the associated precipitation anomaly patterns throughout different seasons. Furthermore, the consistency across various reanalysis datasets adds robustness to the results obtained from this study.

The remarkable outcomes from this first part of study can be summarized as follows:

- The most notable finding of this research is the southward displacement of the entire SAD pattern in recent decades (post 1943). This shift towards the south was particularly prominent during the Austral spring (SON) and summer (DJF) seasons.
- Within the South American continent, specifically during the summer season, there has been a notable alteration in the precipitation anomaly pattern associated with the SAD. The previously observed tripole pattern, characterized by anomalies in

the northern-northeastern (NNE), central-eastern Brazil (CEBR), and southeastern South America (SESA) regions, has transformed into a dipole pattern. This new pattern exhibits intensified anomalies between the CEBR and SESA regions.

- Regarding the SCF_1 across different seasons and IPO intervals, considering post-1943 periods, two trends have emerged consistently across the three reanalysis datasets used in this study. Firstly, there is an increasing importance of the SAD over time. Secondly, higher values of SCF_1 were found during negative IPO phases in certain cases, highlighting the relationship between IPO and the SAD.

These findings are consistent with the expansion of the Hadley cell and the southward shift of westerlies, which are phenomena linked to anthropogenic global warming. The observed changes in the SAD pattern and its associated precipitation anomalies provide further evidence of the evolving climate dynamics in the region. The transition from a tripole to a dipole pattern of precipitation anomalies, characterized by stronger signals between CEBR and SESA, can be attributed to two distinct factors. Firstly, the disappearance of precipitation anomalies over the NNE region can be attributed to the southward movement of the SAD's tropical pole of SST anomalies. Secondly, the intensified dipole of precipitation anomalies between CEBR and SESA are associated with the itensified cyclonic activity observed along the southeastern coast of Brazil and the coast of Argentina. This shift in precipitation patterns may arise from the southward displacement of the SAD or the SASH, in addition to other contributing factors such as anomalous wave train conditions. However, further investigation is needed in order to fully understand these dynamics and their implications for future studies.

The second part of this research focused on the selection of the top three CMIP6 models within the studied region, as well as to assess their ability to replicate the distinctive characteristics of the historical SAD. This evaluation involved conducting analogous analyses to those performed on the observational data, as described earlier, but this time for the CMIP6-HS data and period spanning from 1850 to 2010. The three best CMIP6 models were chosen based on an overall RMSE ranking evaluated on the preferred region of study (which encompasses SAO and the continent of South America approximately). These models, namely FIO-ESM-2-0, CMCC-ESM2, and CMCC-CM2-SR5, demonstrated superior performance and were identified as the top choices based on this criterion.

The main findings for this part are:

- The main configuration of the SAD, characterized by a dipole pattern of SST anomalies between the tropical and extratropical SAO, accompanied by an overlaid monopole of MSLP anomalies, is accurately represented by the models when the entire analysis period is considered.

- The Atlantic Niño sector, which is typically coupled to the SAD in methods for identifying variability modes, does not exhibit the same coupling in the models. This discrepancy can likely be attributed to the SST biases commonly observed in the model simulations within the region.

- Both CMIP6 models and observational data attribute similar importance, as indicated by comparable SCF[1] values, to the SAD, further validating the representation of this phenomenon in the models.

- CMIP6 models effectively capture the low-frequency characteristics of the oceanic component of the SAD, as well as the higher-frequency variability associated with the atmospheric component.

- CMIP6 models perform partially the seasonal variability of SAD. Specifically, CMCC-ESM2 and CMCC-CM2-SR5 show slightly better representation, but they still do not capture the full range of variability.

- In contrast to observational datasets where a southward displacement of the SAD has been observed after 1943, this characteristic is not evident in the CMIP6 GCMs evaluated in this study.

These findings provide insights into the models' abilities to replicate various aspects of the SAD, including its configuration, temporal representation of the oceanic and atmospheric components, coupling with the Atlantic Niño sector and the seasonal variability. They also highlight differences between the models and observational datasets, particularly regarding the southward displacement of the SAD in recent years.

The third and final phase of this study involved conducting SAD analyses for future climate scenarios within the CMIP6 framework. These scenarios took into account socioeconomic narratives projected for the 21st century, ranging from environmentally sustainable practices (SSP1) to the extreme case of continued reliance on fossil fuels (SSP5).

Additionally, the scenarios incorporated plausible radiative forcing levels expected by the end of the century. Within this context, the selected models (FIO-ESM-2-0, CMCC-ESM2, and CMCC-CM2-SR5) were utilized to examine the configuration of the SAD and assess patterns of future precipitation anomalies. Specifically, the focus was on the following scenarios: SSP1-2.6, SSP2-4.5, SSP3-7.0, and SSP4-8.5.

Summarizing the key findings for this third part, we have:

- The simulations for the 21st century adequately capture the SAD pattern across different scenarios and throughout the analysis intervals.

- Atlantic Niño sector is also not represented in the most part of future scenarios. However, exceptions include the FIO-ESM-2-0 model for the 2041-2070 interval in the SSP5-8.5 scenario and the CMCC-CM2-SR5 model for the 2015-2040 interval in the SSP5-8.5 scenario, where a slight Atlantic Niño signature was observed within the SAD configuration.

- Considering annual analyses of the CMIP6 models, all scenarios tend to exhibit similarities to the broader dipole pattern of precipitation anomalies observed between the merged sectors of NNE-CEBR and SESA during the last IPO interval for the DJF months in the reanalysis datasets. This dipole pattern is closely linked to the southernmost configuration of the SAD.

- There are no significant changes in the SAD spatial configuration throughout the 21st century across all scenarios and models studied.

- The greatest SST, MSLP and precipitation anomalies associated with the SAD are observed in the SSP3-7.0 scenario for the CMCC-ESM2 and CMCC-CM2-SR5 models.

- Specifically for the FIO-ESM-2-0 model, the SSP5-8.5 scenario exhibits the highest SST, MSLP, and precipitation anomalies associated with the SAD. However, it is important to note that the FIO-ESM-2-0 model does not present data for the SSP3-7.0.

These findings provide valuable insights into the projected behavior of the SAD under diverse future climate scenarios. While it is noteworthy that significant changes in the

SAD configuration were not observed in the analyzed projections, the results indicate a concerning trend. Specifically, more pronounced anomalies are associated with future climate scenarios characterized by limited measures to mitigate global warming, such as SSP3-7.0 and SSP5-8.5. These intensified anomalies suggest an increased likelihood of extreme events, particularly over the South American continent, which are linked to the studied mode of variability. This finding reinforces the potential impacts of climate change on the region, emphasizing the importance of implementing effective measures to mitigate and adapt to these projected changes.

4.1 Future works

Based on the identified gaps in this study, we propose the following suggestions for future research on the SAD:

- Investigate the underlying factors contributing to the variable periods of the SAD within the interannual timescale. Exploring potential relationships with the IPO, which exhibits similar periodicity and some association with the SAD, could serve as a valuable proxy.

- Assess the specific role of central ENSO events as a factor influencing the occurrence of the southernmost patterns of the SAD.

- In this same sense, northernmost SAD is the preferable configuration to modulate ENSO events through the Walker circulation?

- Determine the predominant factor in modulating the SAD further south: ENSO or the expansion of the Hadley cell in the southern hemisphere associated with global warming. Unraveling the relative contributions of these factors can help clarify the mechanisms driving the SAD's behavior.

- Extend the analysis of the SAD to include additional CMIP6-HS models. Evaluate these models based on seasonality criteria and their ability to reproduce the observed southward shift of the SAD over time in historical and future periods. This broader assessment would enhance our confidence in the representation of the SAD across different models.

Bibliography

BEAL, L. M.; DE RUIJTER, W. P.; BIASTOCH, A.; ZAHN, R. On the role of the Agulhas system in ocean circulation and climate. **Nature**, v. 472, n. 7344, p. 429-436, 2011. DOI https://doi.org/10.1038/nature09983.

BJÖRNSSON, H.; VENEGAS, S. A manual for EOF and SVD analyses of climatic data. **CCGCR Report**, v. 97, n. 1, p. 112-134, 1997.

BLUESTEIN, H. B. **Synoptic-dynamic Meteorology in Midlatitudes: Observations and theory of weather systems**. New York: Oxford University Press, 1993. v. 2.

BOMBARDI, R. J.; CARVALHO, L. M. The South Atlantic dipole and variations in the characteristics of the South American Monsoon in the WCRP-CMIP3 multi-model simulations. **Climate Dynamics**, v. 36, p. 2091-2102, 2011. DOI https://doi.org/10.1007/s00382-010-0836-9.

BOMBARDI, R. J.; CARVALHO, L. M.; JONES, C.; REBOITA, M. S. Precipitation over eastern South America and the South Atlantic Sea surface temperature during neutral ENSO periods. **Climate Dynamics**, v. 42, p. 1553-1568, 2014. DOI https://doi.org/10.1007/s00382-013-1832-7.

BÖTTINGER, M.; KASANG, D. The SSP Scenarios, 2020. Disponível em: https://www.dkrz.de/en/communication/climate-simulations/cmip6-en/the-

sspscenarios. Acesso em: 03 mai. 2023.

BROGGIO, M. F.; GARCIA, C. A. E.; SILVA, R. R. d. Evaluation of South Atlantic Thermohaline Properties from BESM-OA2. 5 and Three Additional Global Climate Models. **Ocean and Coastal Research**, v. 69, p. e21029, 2021. DOI https://doi.org/10.1590/2675-2824069.21012mfb.

CHIANG, J. C.; KUSHNIR, Y.; GIANNINI, A. Deconstructing Atlantic Intertropical Convergence Zone variability: Influence of the local cross-equatorial sea surface temperature gradient and remote forcing from the eastern equatorial Pacific. **Journal of Geophysical Research: Atmospheres**, v. 107, n. D1, p. ACL-3, 2002. DOI https://doi.org/10.1029/2000JD000307.

CLEVELAND, W.; GROSSE, E.; SHYU, W. Local regression models. *In:* CHAMBERS, J.; HASTIE, T. (eds.). **Statistical Models**. Pacific Grove: Wadsworth & Brooks/Cole, 1992, cap. 8, p. 608.

COMPO, G. P. et al. The twentieth century reanalysis project. **Quarterly Journal of the Royal Meteorological Society**, v. 137, n. 654, p. 1-28, 2011. DOI https://doi.org/10.1002/qj.776.

DAI, A. Precipitation characteristics in eighteen coupled climate models. **Journal of Climate**, v. 19, n. 18, p. 4605-4630, 2006. DOI https://doi.org/10.1175/JCLI3884.1.

DÉQUÉ, M. Continuous variables. *In:* JOLLIFE, I. T.; STEPHENSON, D. B. (eds.). **Forecast Verification: A Practitioner's Guide in Atmospheric Science**. West Sussex: Willey, 2007, cap. 7, p. 97-199.

EYRING, V.; BONY, S.; MEEHL, G. A.; SENIOR, C. A.; STEVENS, B.; STOUFFER, R. J.; TAYLOR, K. E. Overview of the Coupled Model Intercomparison Project Phase 6 (CMIP6) experimental design and organization. **Geoscientific Model Development**, v. 9, n. 5, p. 1937-1958, 2016. DOI https://doi.org/10.5194/gmd-9-1937-2016.

FAUCHEREAU, N.; TRZASKA, S.; RICHARD, Y.; ROUCOU, P.; CAMBERLIN, P. Sea surface temperature co-variability in the Southern Atlantic and Indian Oceans and its connections with the atmospheric circulation in the Southern Hemisphere. **International Journal of Climatology: A Journal of the Royal Meteorological Society**, v. 23, n. 6, p. 663-677, 2003. DOI https://doi.org/10.1002/joc.905.

GILLILAND, J. M.; KEIM, B. D. Position of the South Atlantic Anticyclone and its impact on surface conditions across Brazil. **Journal of Applied Meteorology and Climatology**, v. 57, n. 3, p. 535-553, 2018. DOI https://doi.org/10.1175/JAMC-D-17-0178.1.

HAARSMA, R. J.; CAMPOS, E. J.; MOLTENI, F. Atmospheric response to South Atlantic SST dipole. **Geophysical Research Letters**, v. 30, n. 16, 2003. DOI https://doi.org/10.1029/2003GL017829.

HENLEY, B. J.; GERGIS, J.; KAROLY, D. J.; POWER, S.; KENNEDY, J.; FOLLAND, C. K. A tripole index for the interdecadal Pacific oscillation. **Climate Dynamics**, v. 45, p. 3077-3090, 2015. DOI https://doi.org/10.1007/s00382-015-2525-1.

HERSBACH, H. et al. The ERA5 global reanalysis. **Quarterly Journal of the Royal Meteorological Society**, v. 146, n. 730, p. 1999-2049, 2020. DOI https://doi.org/10.1002/qj.3803.

HU, Y.; FU, Q. Observed poleward expansion of the Hadley circulation since 1979. **Atmospheric Chemistry and Physics**, v. 7, n. 19, p. 5229-5236, 2007. DOI https://doi.org/10.5194/acp-7-5229-2007.

HU, Y.; HUANG, H.; ZHOU, C. Widening and weakening of the Hadley circulation under global warming. **Science Bulletin**, v. 63, n. 10, p. 640-644, 2018. DOI https://doi.org/10.1016/j.scib.2018.04.020.

ISHII, M.; SHOUJI, A.; SUGIMOTO, S.; MATSUMOTO, T. Objective analyses of seasurface temperature and marine meteorological variables for the 20th century using ICOADS and the Kobe collection. **International Journal of Climatology: A Journal of the Royal Meteorological Society**, v. 25, n. 7, p. 865-879, 2005. DOI https://doi.org/10.1002/joc.1169.

KAYANO, M. T.; ANDREOLI, R. V. Relationships between rainfall anomalies over northeastern Brazil and the El Niño-Southern Oscillation. **Journal of Geophysical Research: Atmospheres**, v. 111, n. D13, 2006. DOI https://doi.org/10.1029/2005JD006142.

KAYANO, M. T.; ANDREOLI, R. V.; FERREIRA DE SOUZA, R. A. Relations between ENSO and the South Atlantic SST modes and their effects on the South American rainfall. **International Journal of Climatology**, v. 33, n. 8, p. 2008-2023, 2013. DOI https://doi.org/10.1002/joc.3569.

KRIEGLER, E.; EDMONDS, J.; HALLEGATTE, S.; EBI, K. L.; KRAM, T.; RIAHI, K.; WINKLER, H.; VAN VUUREN, D. P. A new scenario framework for climate change research: the concept of shared climate policy assumptions. **Climatic Change**, v. 122, p. 401-414, 2014. DOI https://doi.org/10.1007/s10584-013-0971-5.

LOPEZ, H.; DONG, S.; LEE, S.-K.; CAMPOS, E. Remote influence of Interdecadal Pacific Oscillation on the South Atlantic meridional overturning circulation variability. **Geophysical Research Letters**, v. 43, n. 15, p. 8250-8258, 2016. DOI https://doi.org/10.1002/2016GL069067.

MINNETT, P. et al. Half a century of satellite remote sensing of sea-surface temperature. **Remote Sensing of Environment**, v. 233, p. 111366, 2019. DOI https://doi.org/10.1016/j.rse.2019.111366.

MO, K. C.; PAEGLE, J. N. The Pacific-South American modes and their downstream effects. **International Journal of Climatology: A Journal of the Royal Meteoro-**

logical Society, v. 21, n. 10, p. 1211-1229, 2001. DOI https://doi.org/10.1002/joc.685.

MORIOKA, Y.; TOZUKA, T.; YAMAGATA, T. On the growth and decay of the subtropical dipole mode in the South Atlantic. **Journal of Climate**, v. 24, n. 21, p. 5538-5554, 2011. DOI https://doi.org/10.1175/2011JCLI4010.1.

NNAMCHI, H. C.; KUCHARSKI, F.; KEENLYSIDE, N. S.; FARNETI, R. Analogous seasonal evolution of the South Atlantic SST dipole indices. **Atmospheric Science Letters**, v. 18, n. 10, p. 396-402, 2017. DOI https://doi.org/10.1002/asl.781.

NNAMCHI, H. C.; LI, J. Influence of the South Atlantic Ocean dipole on West African summer precipitation. **Journal of Climate**, v. 24, n. 4, p. 1184-1197, 2011. DOI https://doi.org/10.1175/2010JCLI3668.1.

NNAMCHI, H. C.; LI, J.; ANYADIKE, R. N. Does a dipole mode really exist in the South Atlantic Ocean?. **Journal of Geophysical Research: Atmospheres**, v. 116, n. D15, 2011. DOI https://doi.org/10.1029/2010JD015579.

NNAMCHI, H. C.; LI, J.; KUCHARSKI, F.; KANG, I.-S.; KEENLYSIDE, N. S.; CHANG, P.; FARNETI, R. An equatorial-extratropical dipole structure of the Atlantic Niño. **Journal of Climate**, v. 29, n. 20, p. 7295-7311, 2016. DOI https://doi.org/10.1175/JCLI-D-15-0894.1.

NUNES, L. H.; VICENTE, A. K.; CANDIDO, D. H. Clima da Região Sudeste do Brasil. *In:* CAVALCANTI, I.; FERREIRA, N.; SILVA, M.; DIAS, M. (eds.). **Tempo e clima no Brasil**. São Paulo: Oficina de Textos, 2009, cap. 16, p. 243-258.

O'NEILL, B. C. et al. The roads ahead: Narratives for shared socioeconomic pathways describing world futures in the 21st century. **Global Environmental Change**, v. 42, p. 169-180, 2017. DOI https://doi.org/10.1016/j.gloenvcha.2015.01.004.

O'NEILL, B. C. et al. The scenario model intercomparison project (Scenario-

MIP) for CMIP6. **Geoscientific Model Development**, v. 9, n. 9, p. 3461-3482, 2016. DOI https://doi.org/10.5194/gmd-9-3461-2016.

PETERSON, R. G.; STRAMMA, L. Upper-level circulation in the South Atlantic Ocean. **Progress in Oceanography**, v. 26, n. 1, p. 1-73, 1991. DOI https://doi.org/10.1016/0079-6611(91)90006-8.

POLI, P. et al. ERA-20C: An atmospheric reanalysis of the twentieth century. **Journal of Climate**, v. 29, n. 11, p. 4083-4097, 2016. DOI https://doi.org/10.1175/JCLI-D-15-0556.1.

REBOITA, M. S.; AMBRIZZI, T.; SILVA, B. A.; PINHEIRO, R. F.; DA ROCHA, R. P. The South Atlantic subtropical anticyclone: present and future climate. **Frontiers in Earth Science**, v. 7, p. 8, 2019. DOI https://doi.org/10.3389/feart.2019.00008.

RIAHI, K. et al. The Shared Socioeconomic Pathways and their energy, land use, and greenhouse gas emissions implications: An overview. **Global Environmental Change**, v. 42, p. 153-168, 2017. DOI https://doi.org/10.1016/j.gloenvcha.2016.05.009.

RICHTER, I.; TOKINAGA, H. An overview of the performance of CMIP6 models in the tropical Atlantic: mean state, variability, and remote impacts. **Climate Dynamics**, v. 55, n. 9-10, p. 2579-2601, 2020. DOI https://doi.org/10.1007/s00382-020-05409-w.

RODRIGUES, R. R.; CAMPOS, E. J.; HAARSMA, R. The impact of ENSO on the South Atlantic subtropical dipole mode. **Journal of Climate**, v. 28, n.7, p. 2691-2705, 2015. DOI https://doi.org/10.1175/JCLI-D-14-00483.1.

RODRIGUES, R. R.; HAARSMA, R. J.; CAMPOS, E. J.; AMBRIZZI, T. The impacts of inter-El Niño variability on the tropical Atlantic and Northeast Brazil climate. **Journal of Climate**, v. 24, n. 13, p. 3402-3422, 2011. DOI https://doi.org/10.1175/2011JCLI3983.1.

SCHELLNHUBER, H. J.; RAHMSTORF, S.; WINKELMANN, R. Why the right climate target was agreed in Paris. **Nature Climate Change**, v. 6, n. 7, p. 649-653, 2016. DOI https://doi.org/10.1038/nclimate3013.

SCHNEIDER, T.; BISCHOFF, T.; HAUG, G. H. Migrations and dynamics of the intertropical convergence zone. **Nature** v. 513, n. 7516, p. 45-53, 2014. DOI https://doi.org/10.1038/nature13636.

SCHNEIDER, U.; BECKER, A.; FINGER, P.; MEYER-CHRISTOFFER, A.; RUDOLF, B.; ZIESE, M. GPCC full data reanalysis version 6.0 at 0.5: Monthly land-surface precipitation from rain-gauges built on GTS-based and historic data. **GPCC Data Report**, v. 10, p. 585, 2011. DOI https://doi.org/10.5676/DWD_GPCC/FD_M_V6_100.

STERL, A.; HAZELEGER, W. Coupled variability and air-sea interaction in the South Atlantic Ocean. **Climate Dynamics**, v. 21, p. 559-571, 2003. DOI https://doi.org/10.1007/s00382-003-0348-y.

STRAMMA, L.; ENGLAND, M. On the water masses and mean circulation of the South Atlantic Ocean. **Journal of Geophysical Research: Oceans**, v. 104, n. C9, p. 20863-20883, 1999. DOI https://doi.org/10.1029/1999JC900139.

TORRENCE, C.; COMPO, G. P. A practical guide to wavelet analysis. **Bulletin of the American Meteorological Society**, v. 79, n. 1, p. 61-78, 1998. DOI https://doi.org/10.1175/1520-0477(1998)079¡0061:APGTWA¿2.0.CO;2.

VAN VUUREN, D. P. et al. The representative concentration pathways: an overview. **Climatic Change**, v. 109, p. 5-31, 2011. DOI https://doi.org/10.1007/s10584-011-0148-z.

VENEGAS, S.; MYSAK, L.; STRAUB, D. Atmosphere-ocean coupled variability in the South Atlantic. **Journal of Climate**, v. 10, n. 11, p. 2904-2920, 1997. DOI

https://doi.org/10.1175/1520-0442(1997)010¡2904:AOCVIT¿2.0.CO;2.

VIZY, E. K.; COOK, K. H. Understanding long-term (1982-2013) multi-decadal change in the equatorial and subtropical South Atlantic climate. **Climate Dynamics**, v. 46, p. 2087-2113, 2016. DOI https://doi.org/10.1007/s00382-015-2691-1.

Appendix

Appendix A

Tables

Table A.1 - $SVD1_{SST}$ and $SVD1_{MSLP}$ correlations between different reanalysis and CMIP6 Historical Simulations models. The following subscripts are followed by their references: ERA5 - ERA5; ERA20 - ERA-20C; NOAA - NOAA-CIRES 20th Century; CMCCc - CMCC-CM2-SR5; CMCCe - CMCC-ESM2; FIOe - FIO-ESM-2-0. Correlations with a statistical confidence level above 95% are shown in bold

	SVD1 SST, ERA5	SVD1 MSLP, ERA5	SVD1 SST, ERA20	SVD1 MSLP, ERA20	SVD1 SST, MSLP	SVD1 MSLP, NOAA	SVD1 SST, CMCCc	SVD1 MSLP, CMCCc	SVD1 SST, CMCCe	SVD1 MSLP, CMCCe	SVD1 SST, FIOe	SVD1 MSLP, FIOe
SVD1 SST, ERA5	**1.000**	**0.299**	**0.955**	**0.327**	**0.908**	**0.365**	-0.036	-0.033	0.024	-0.004	**-0.078**	-0.018
SVD1 MSLP, ERA5	**0.299**	**1.000**	**0.295**	**0.879**	**0.291**	**0.898**	0.013	-0.063	-0.022	-0.025	-0.068	-0.013
SVD1 SST, ERA20	**0.955**	**0.295**	**1.000**	**0.320**	**0.906**	**0.363**	-0.058	-0.033	0.002	-0.025	**-0.120**	-0.036
SVD1 MSLP, ERA20	**0.327**	**0.879**	**0.320**	**1.000**	**0.303**	**0.890**	0.004	-0.030	-0.011	-0.020	-0.008	0.018
SVD1 SST, NOAA	**0.908**	**0.291**	**0.906**	**0.303**	**1.000**	**0.359**	-0.031	-0.016	0.021	-0.016	**-0.088**	-0.021
SVD1 MSLP, NOAA	**0.365**	**0.898**	**0.363**	**0.890**	**0.359**	**1.000**	0.021	-0.029	-0.010	-0.034	-0.013	0.025
SVD1 SST, CMCCc	-0.036	0.013	-0.058	0.004	-0.031	0.021	**1.000**	**0.429**	**0.129**	0.039	**0.094**	0.068
SVD1 MSLP, CMCCc	-0.033	-0.063	-0.033	-0.030	-0.016	-0.029	**0.429**	**1.000**	0.039	0.005	-0.015	0.034
SVD1 SST, CMCCe	0.024	-0.022	0.002	-0.011	0.021	-0.010	**0.129**	0.039	**1.000**	**0.343**	**0.120**	0.022
SVD1 MSLP, CMCCe	-0.004	-0.025	-0.025	-0.020	-0.016	-0.034	0.039	0.005	**0.343**	**1.000**	0.062	0.037
SVD1 SST, FIOe	**-0.078**	-0.068	**-0.120**	-0.008	**-0.088**	-0.013	**0.094**	-0.015	**0.120**	0.062	**1.000**	**0.372**
SVD1 MSLP, FIOe	-0.018	-0.013	-0.036	0.018	-0.021	0.025	0.068	0.034	0.022	0.037	**0.372**	**1.000**

Appendix B

Seasonal variability - NOAA CIRES and ERA-20C

B.1 NOAA CIRES 20th Century

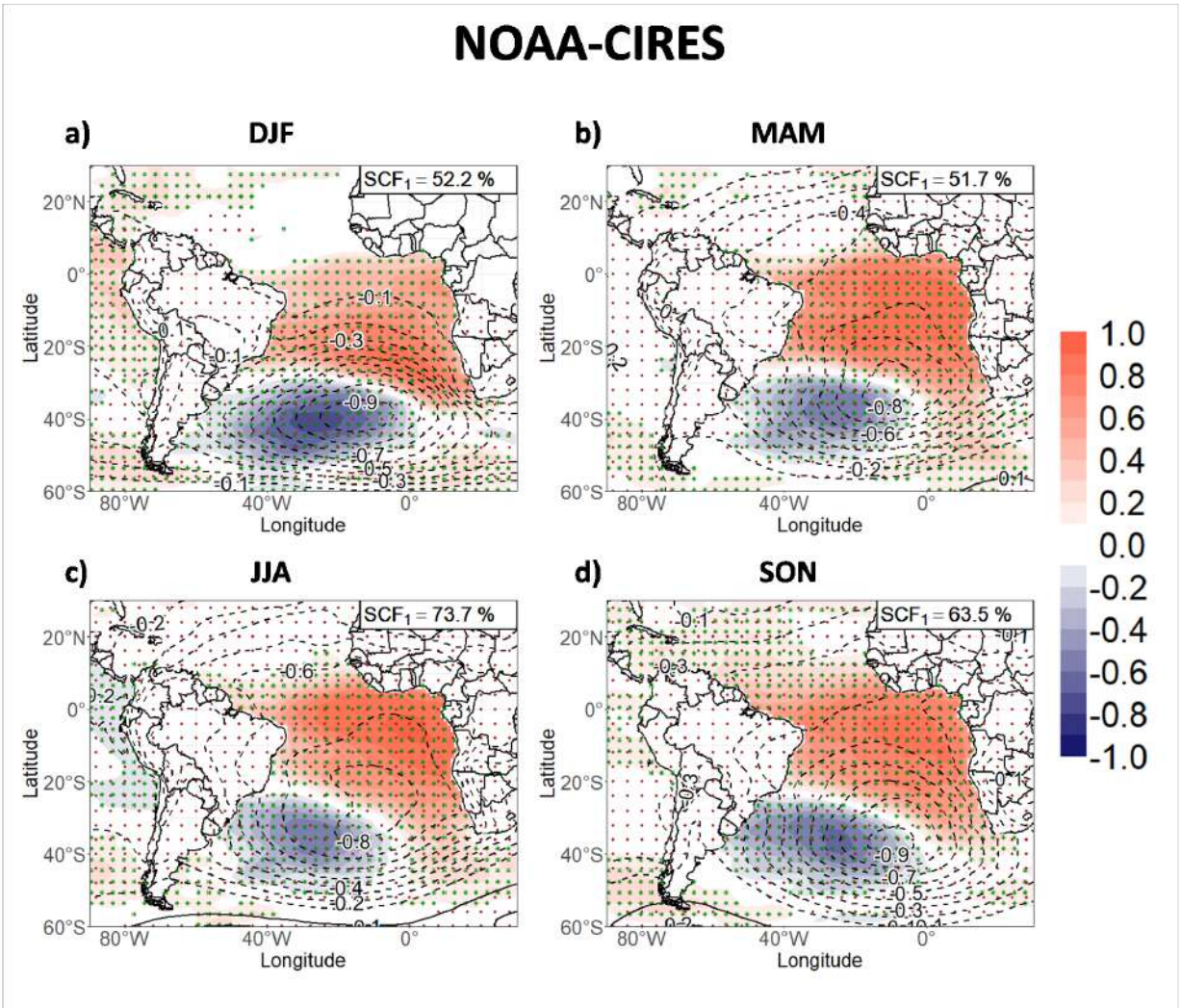

Figure B.1: The same as in Figure 3.7 except for the NOAA CIRES 20th Century reanalysis.

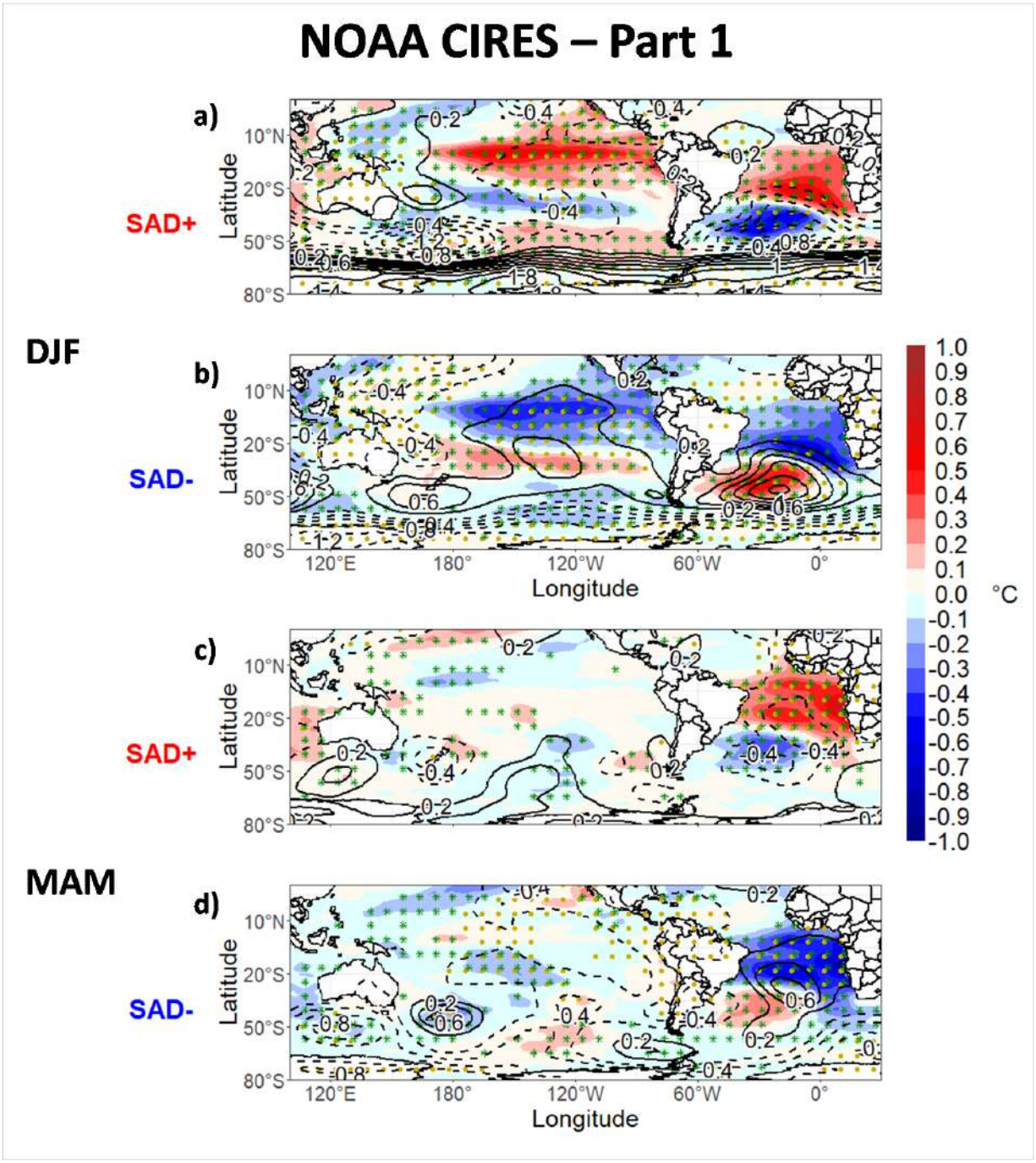

Figure B.2: The same as in Figure 3.8 except for the NOAA CIRES 20th Century reanalysis.

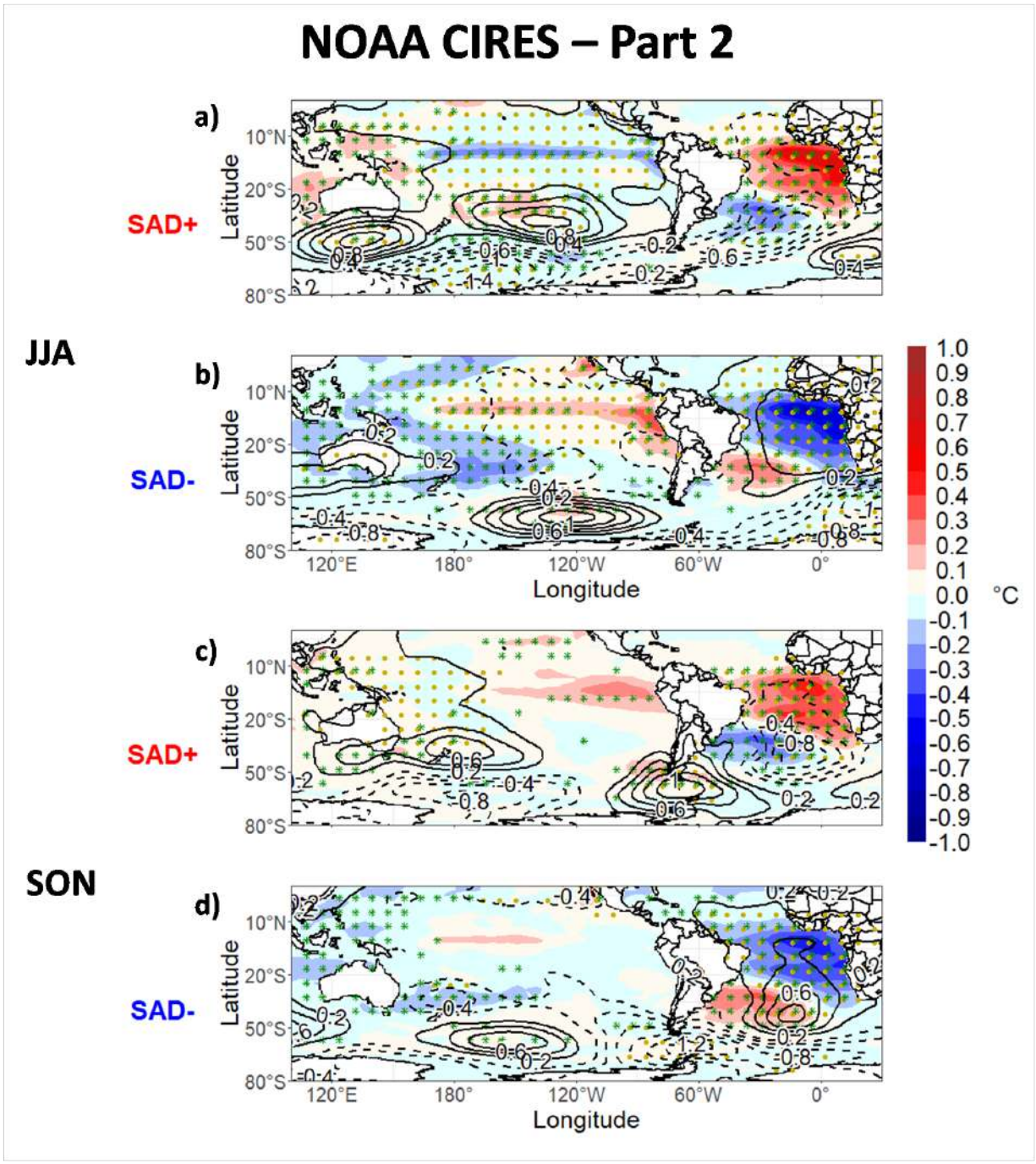

Figure B.3: The same as in Figure 3.9 except for the NOAA CIRES 20th Century reanalysis.

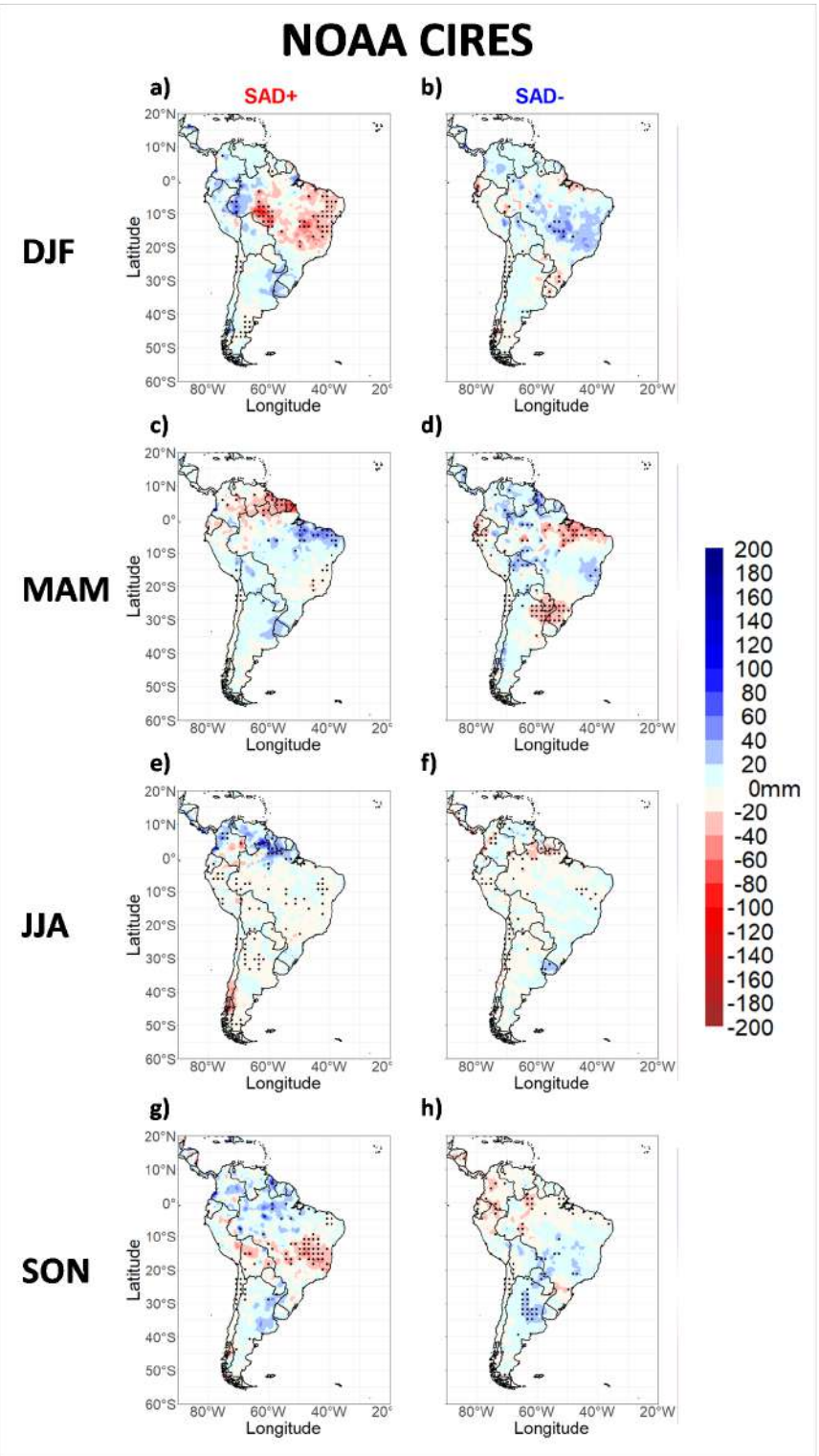

Figure B.4: The same as in Figure 3.10 except for the NOAA CIRES 20th Century reanalysis.

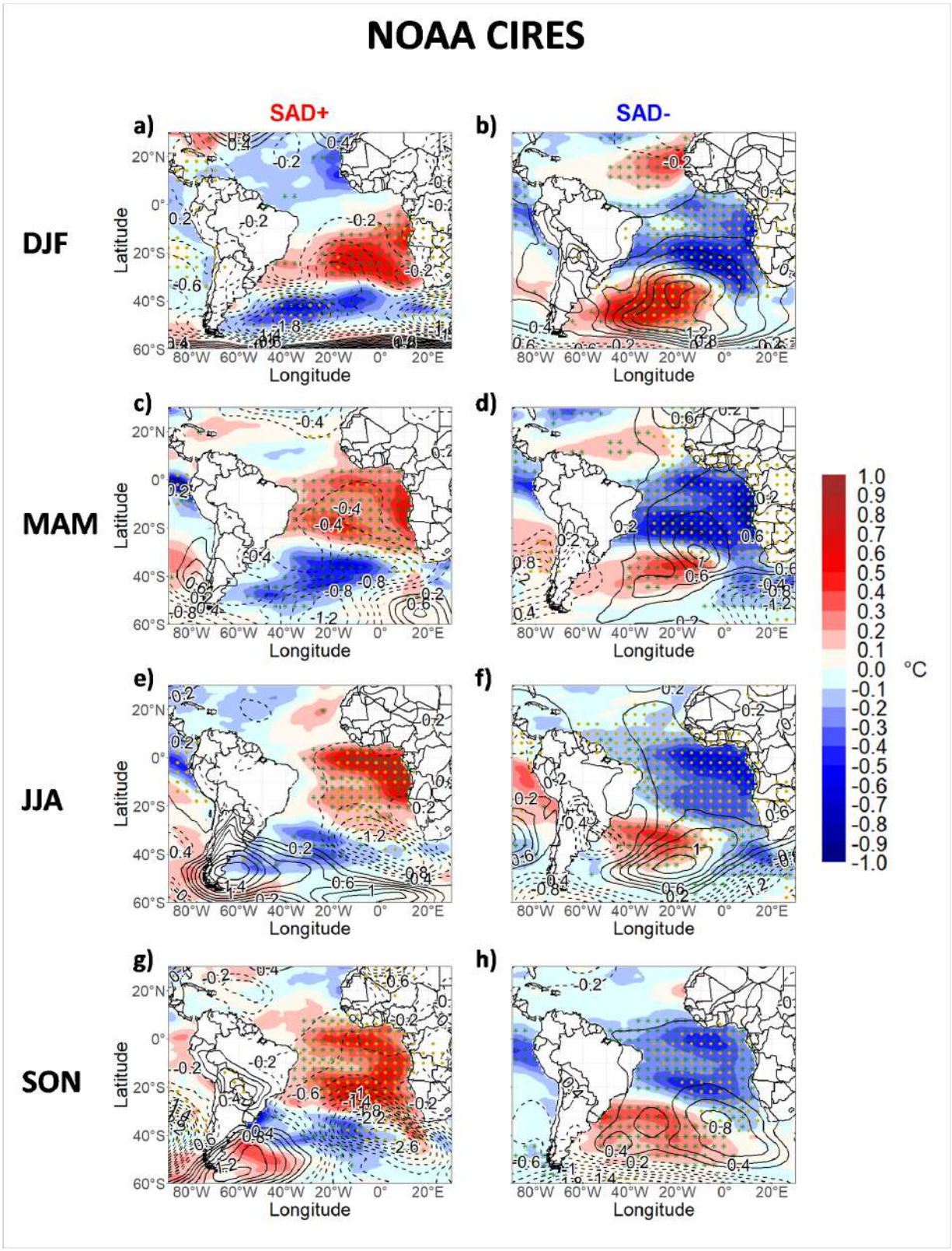

Figure B.5: The same as in Figure 3.11 except for the NOAA CIRES 20th Century reanalysis.

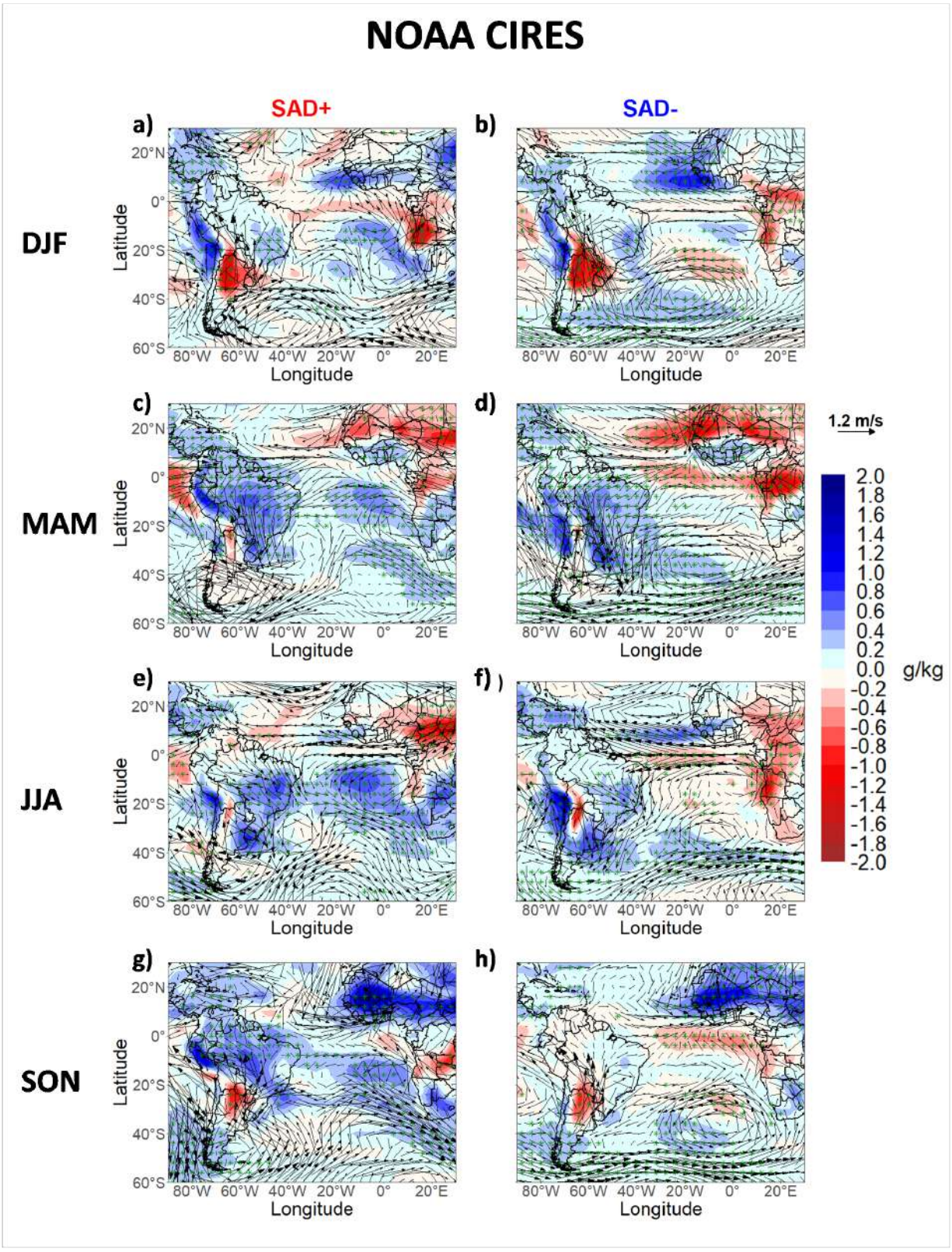

Figure B.6: The same as in Figure 3.12 except for the NOAA CIRES 20th Century reanalysis.

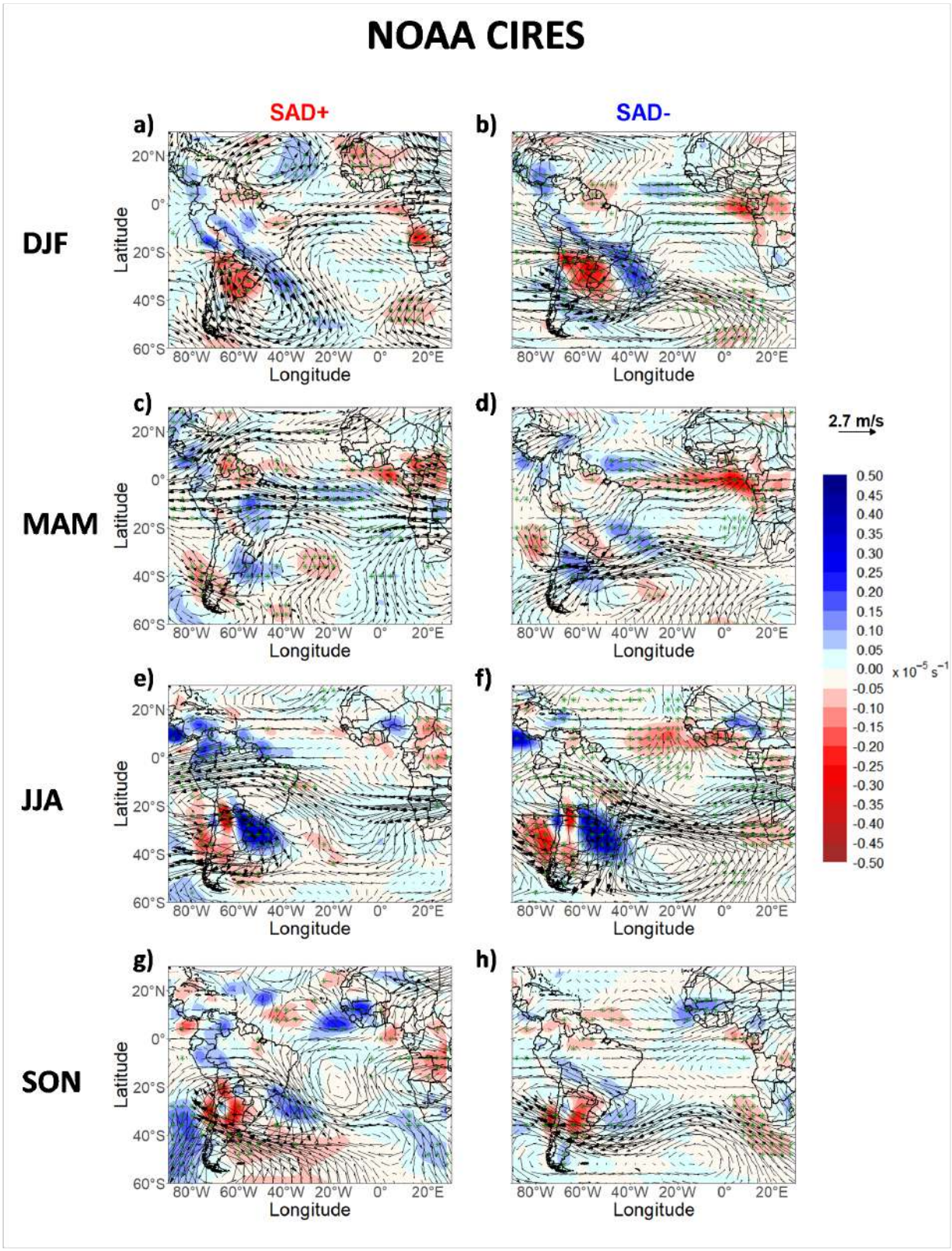

Figure B.7: The same as in Figure 3.13 except for the NOAA CIRES 20th Century reanalysis.

B.2 ERA-20C

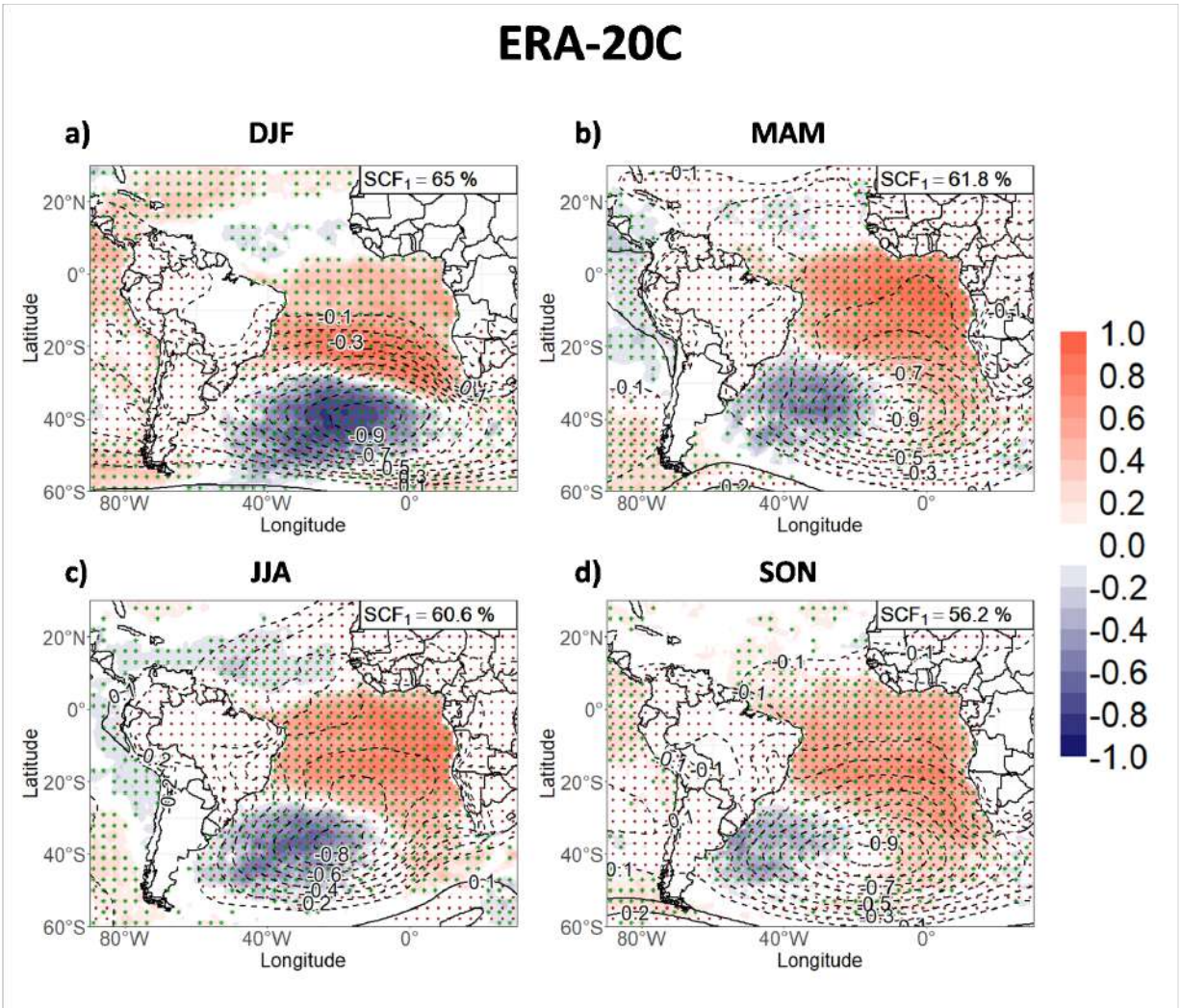

Figure B.8: The same as in Figure 3.7 except for the ERA-20C reanalysis.

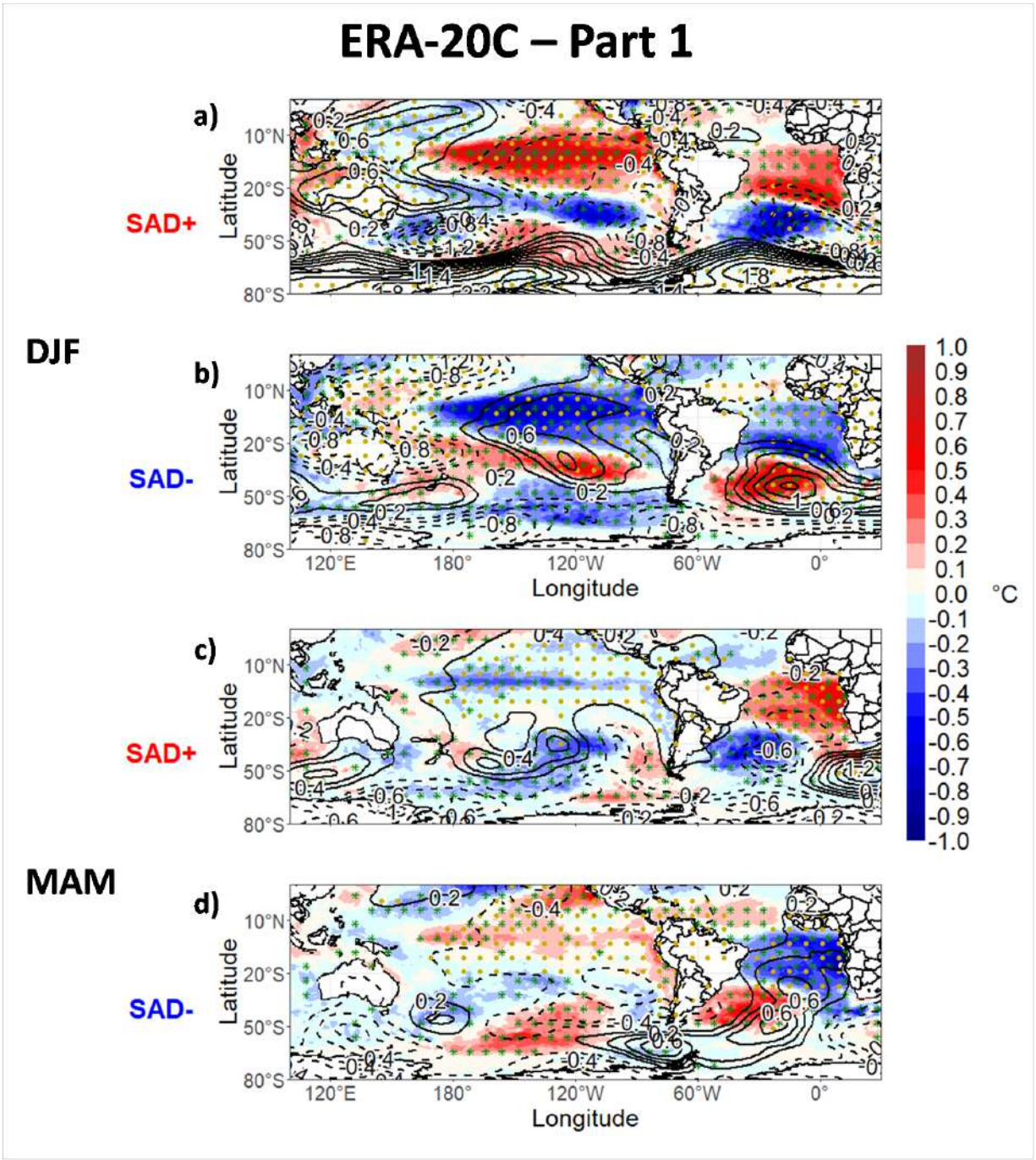

Figure B.9: The same as in Figure 3.8 except for the ERA-20C reanalysis.

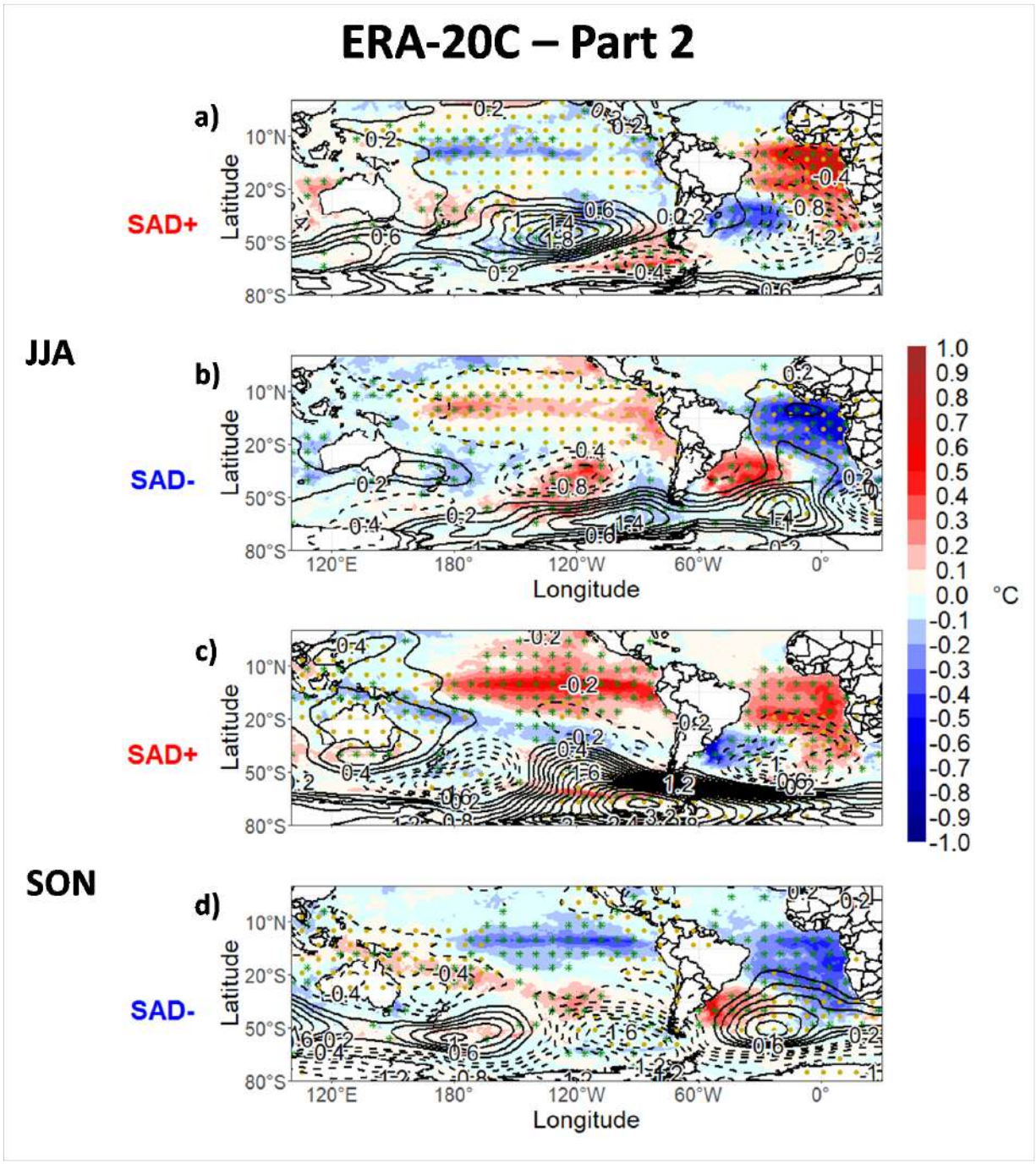

Figure B.10: The same as in Figure 3.9 except for the ERA-20C reanalysis.

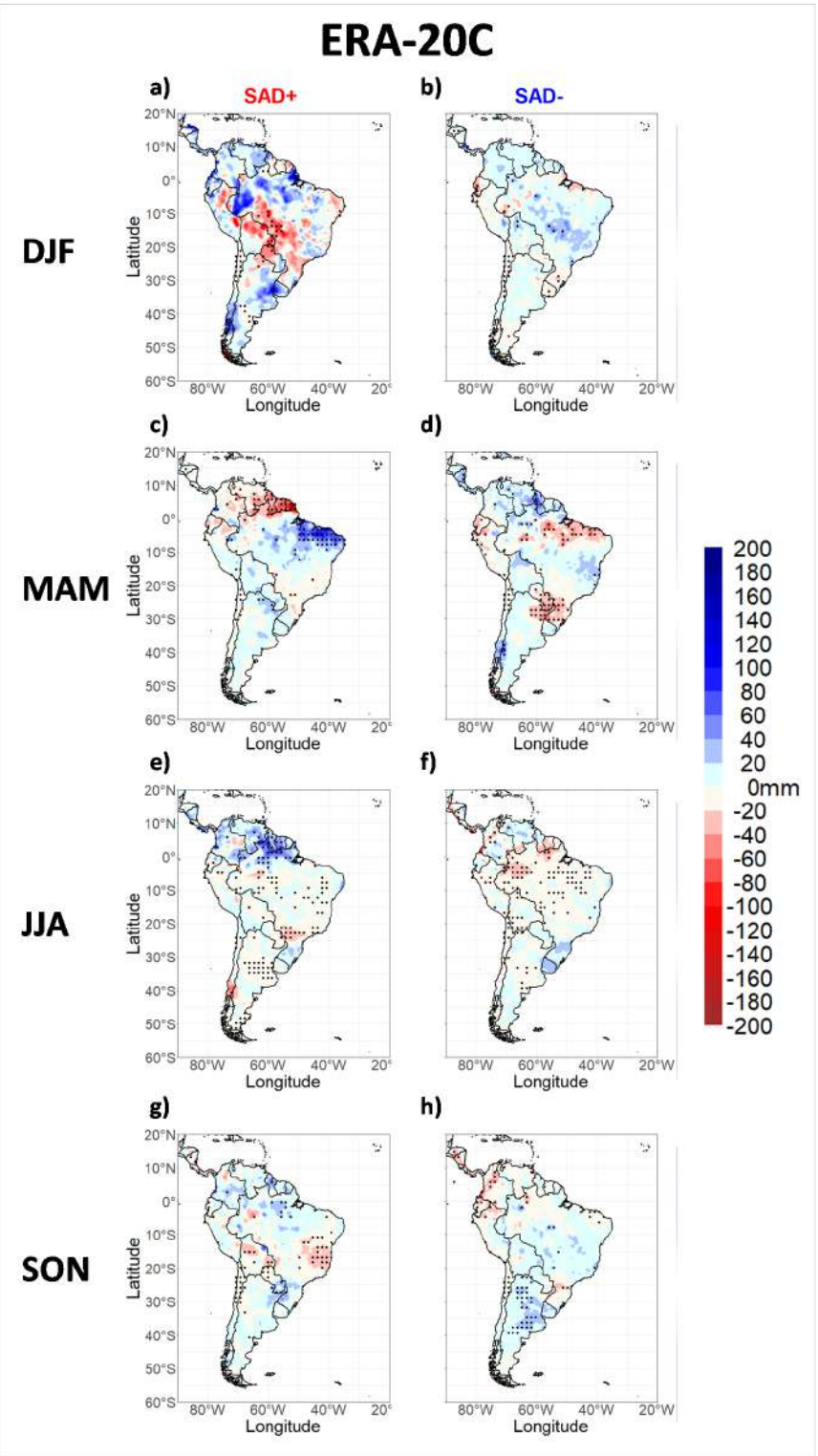

Figure B.11: The same as in Figure 3.7 except for the ERA-20C reanalysis.

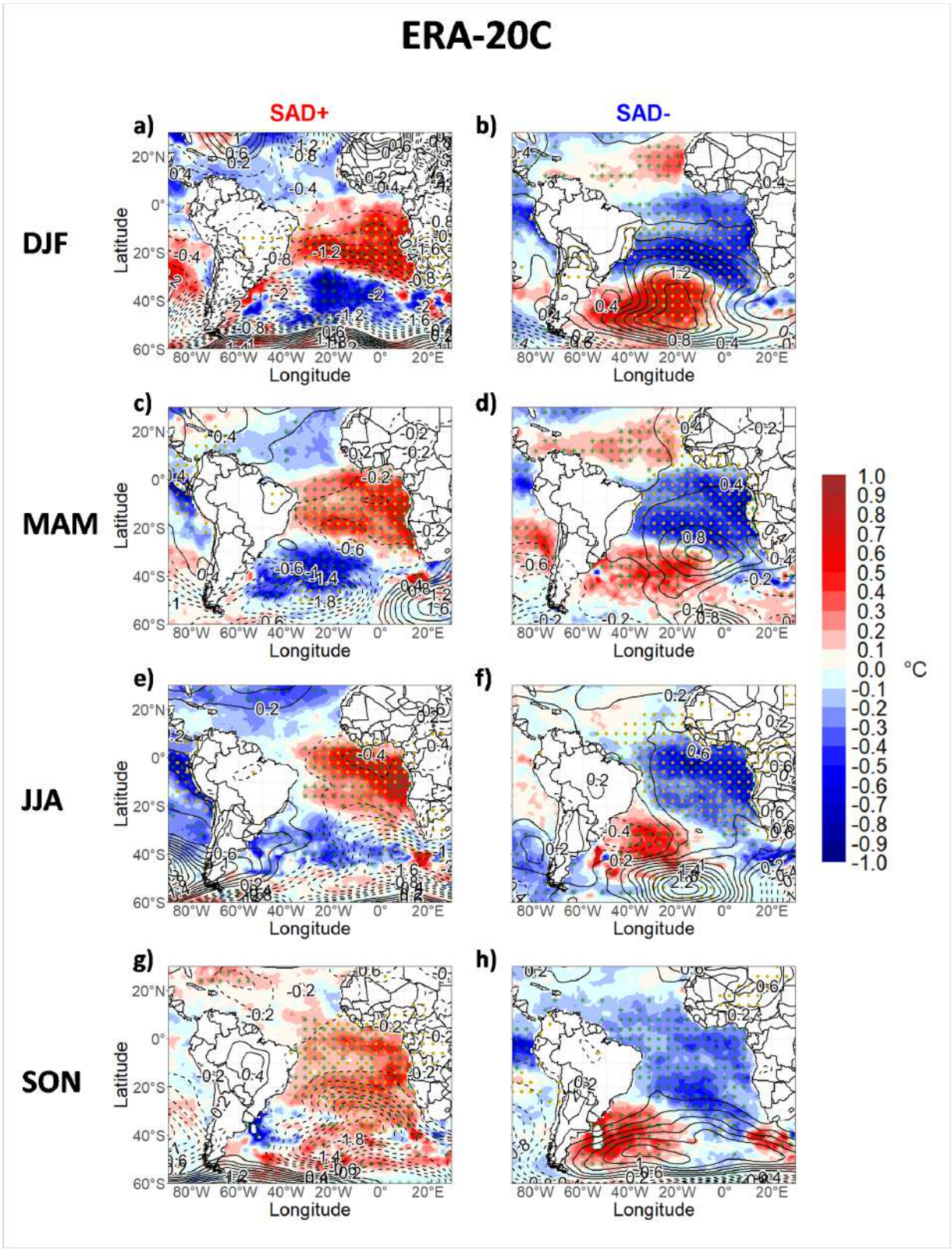

Figure B.12: The same as in Figure 3.11 except for the ERA-20C reanalysis.

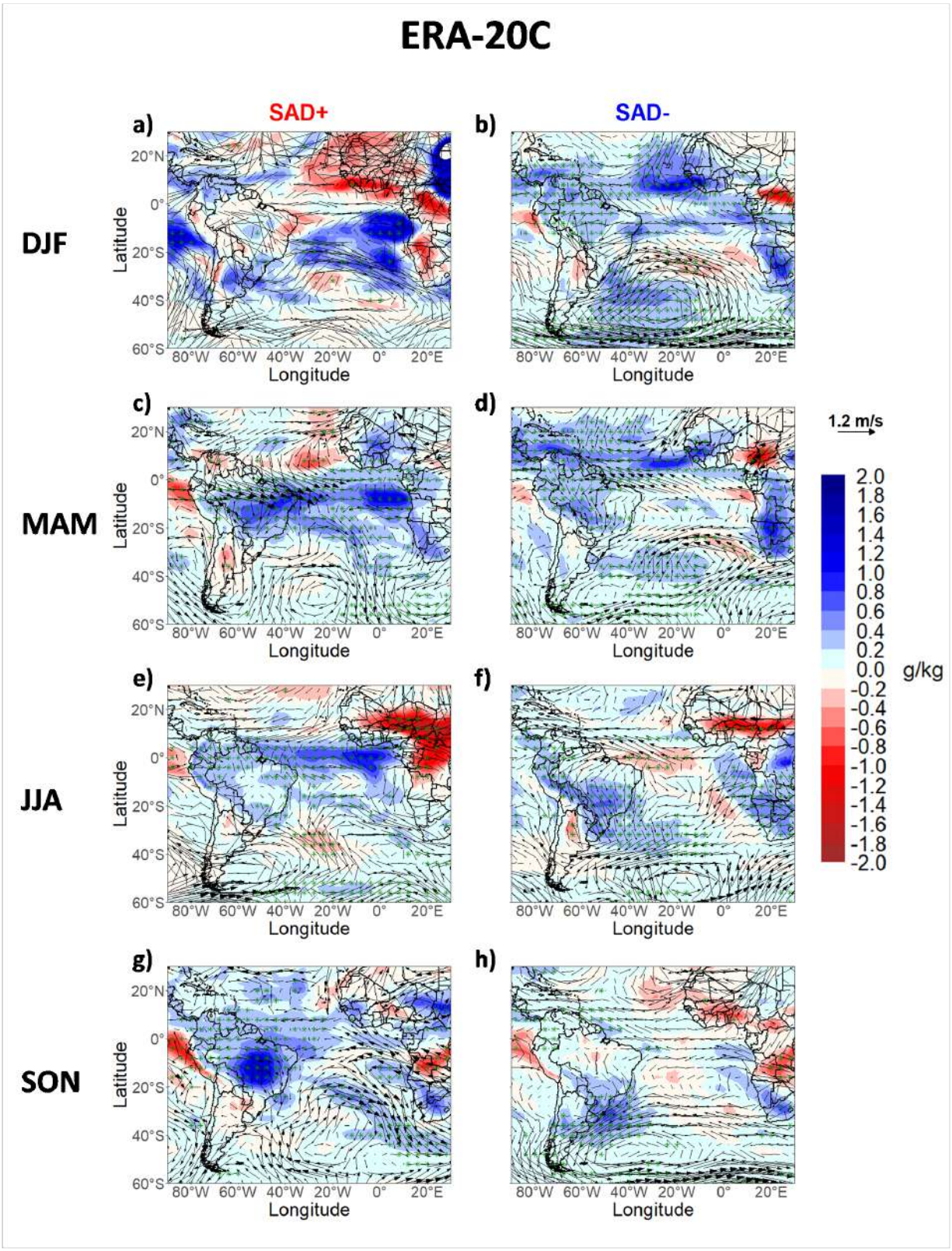

Figure B.13: The same as in Figure 3.12 except for the ERA-20C reanalysis.

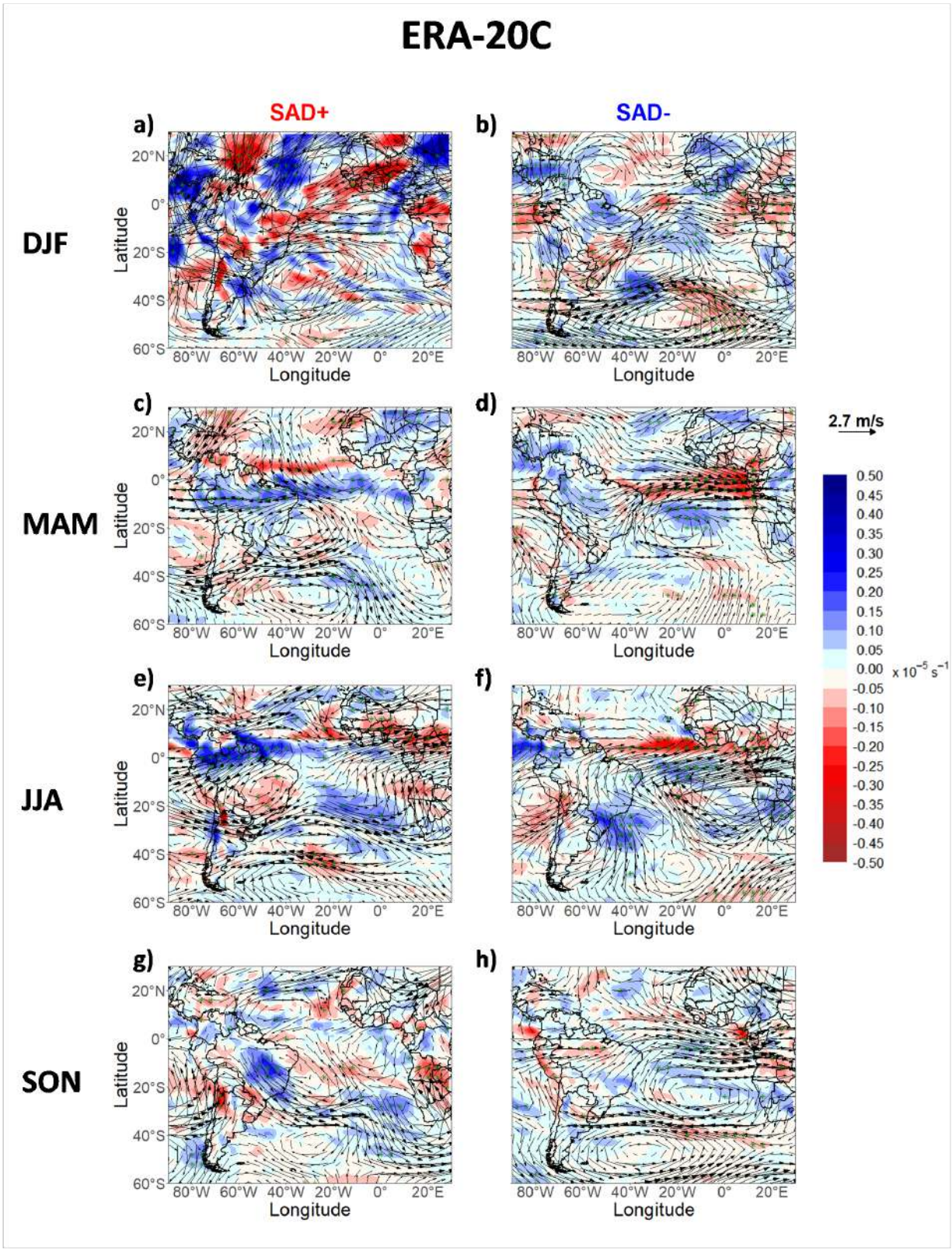

Figure B.14: The same as in Figure 3.13 except for the ERA-20C reanalysis.

Appendix C

Evolution over time based on the Interdecada Pacific Oscillation - NOAA-CIRES and ERA-20C

C.1 NOAA-CIRES 20th Century

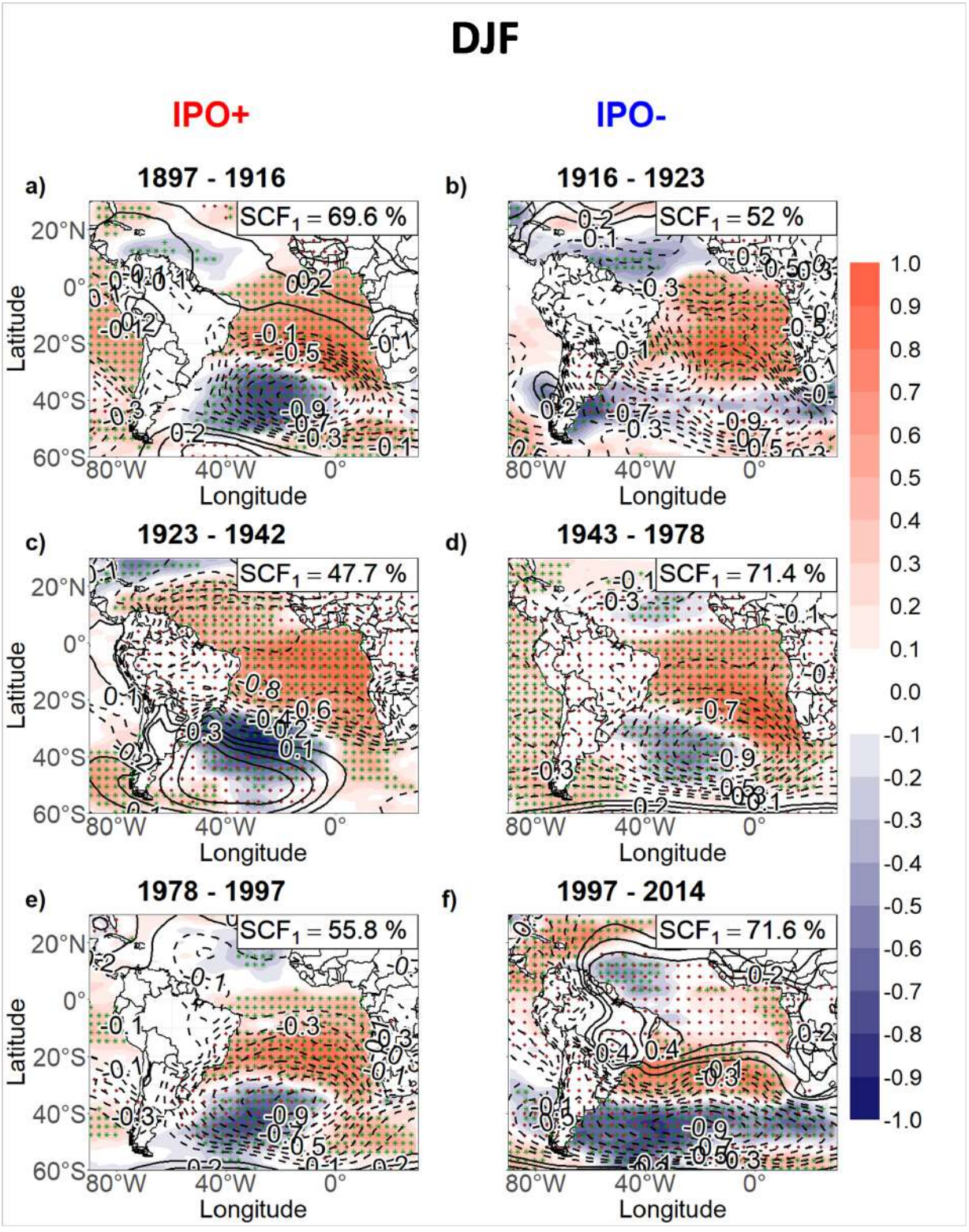

Figure C.1: Homogeneous correlation between $SVD1_{SST}$ and SST anomalies (shaded) and between $SVD1_{MSLP}$ and MSLP anomalies (contours) identified for December-February (DJF) months during the periods a) 1950-1978, b) 1978-1997 and c) 1997-2020, which are associated with the phases of the Interdecadal Pacific Oscillation (IPO). On the left side, there are fields corresponding to the positive IPO periods (IPO+) and to the right side the negative periods of the IPO (IPO-). Analyzes made with NOAA-CIRES 20th Century reanalysis. Correlations with a statistical confidence level above 95% are shown in green (yellow) dots for SST (MSLP) anomalies.

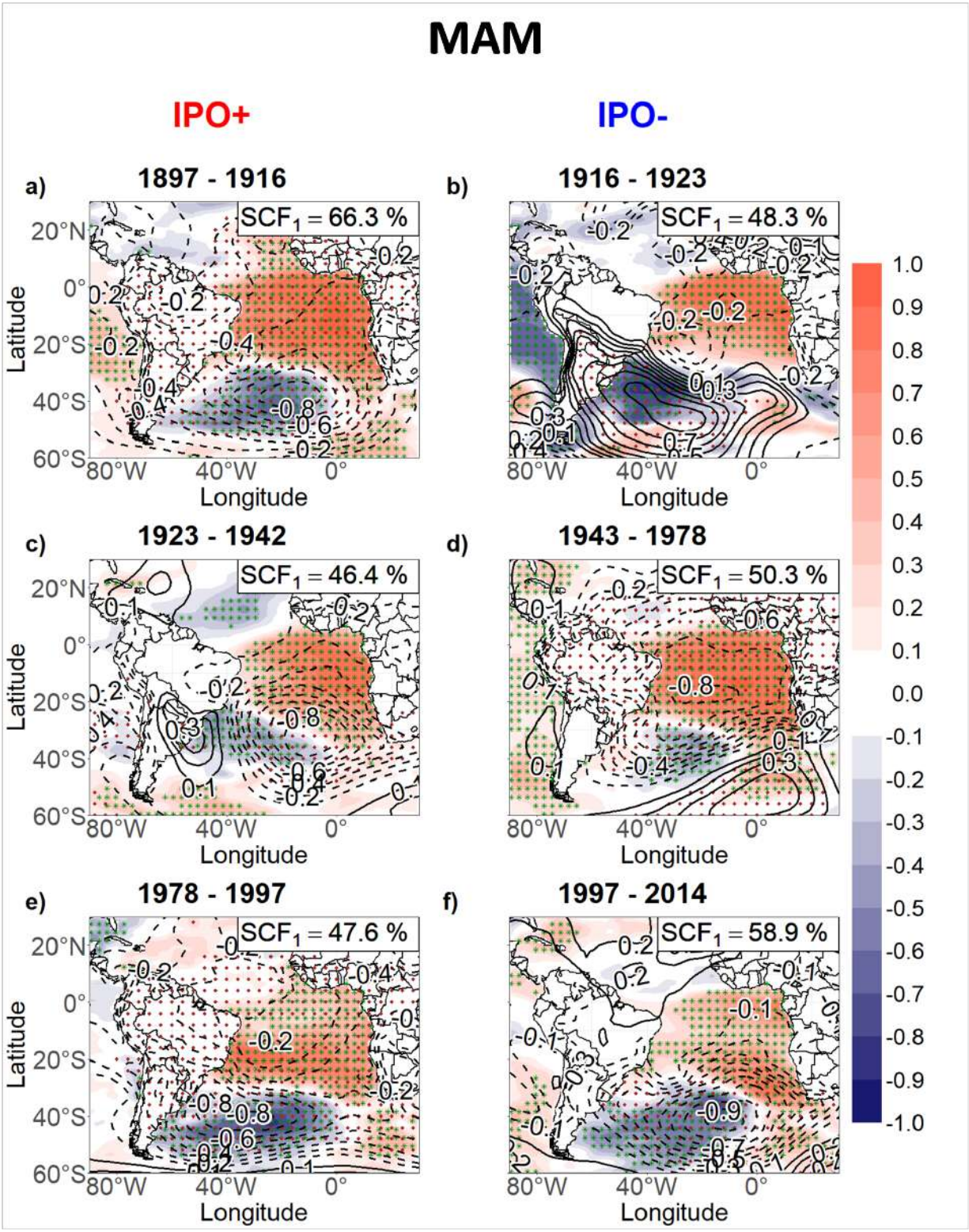

Figure C.2: The same as in Figure C.1 except for the MAM months.

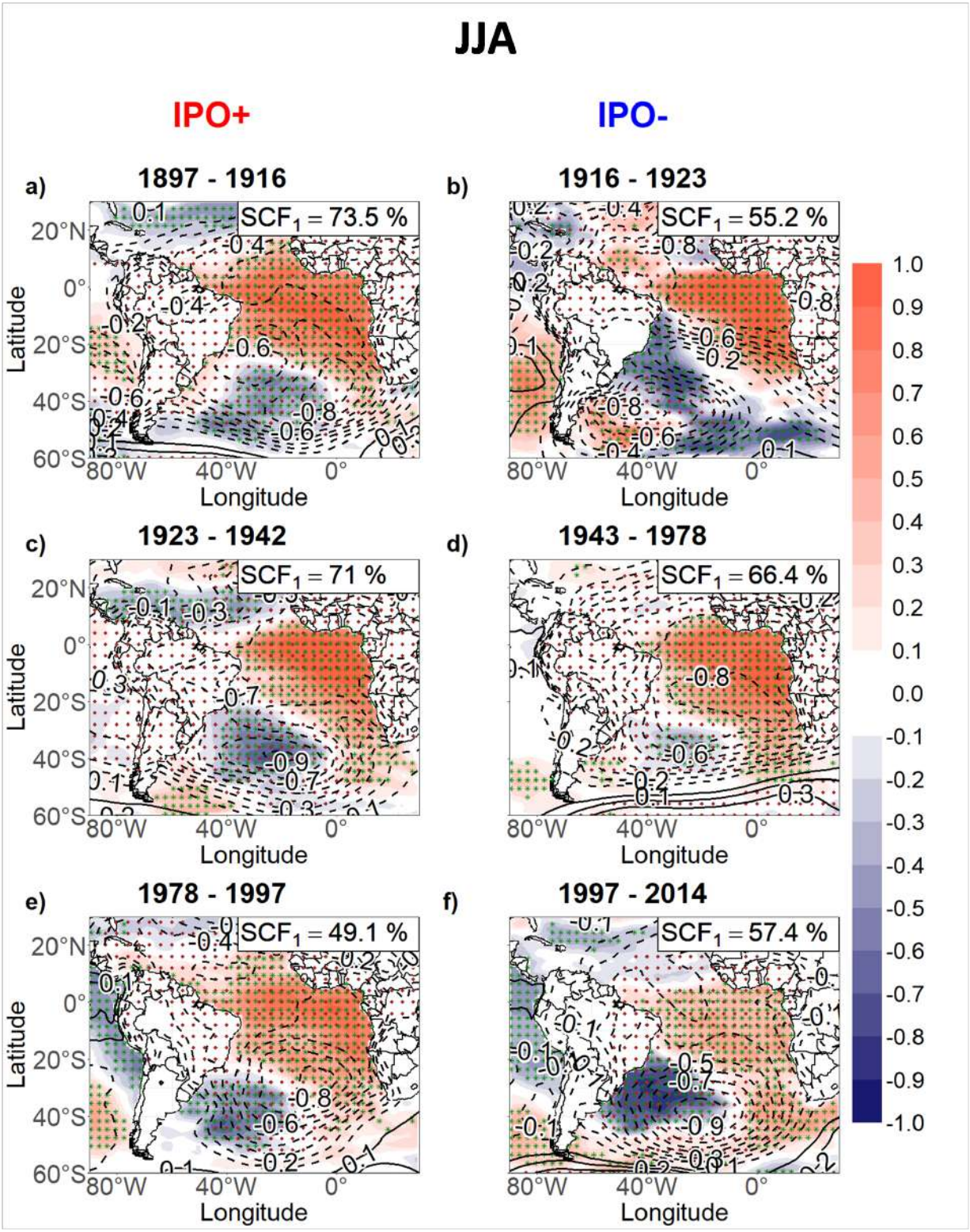

Figure C.3: The same as in Figure C.1 except for the JJA months.

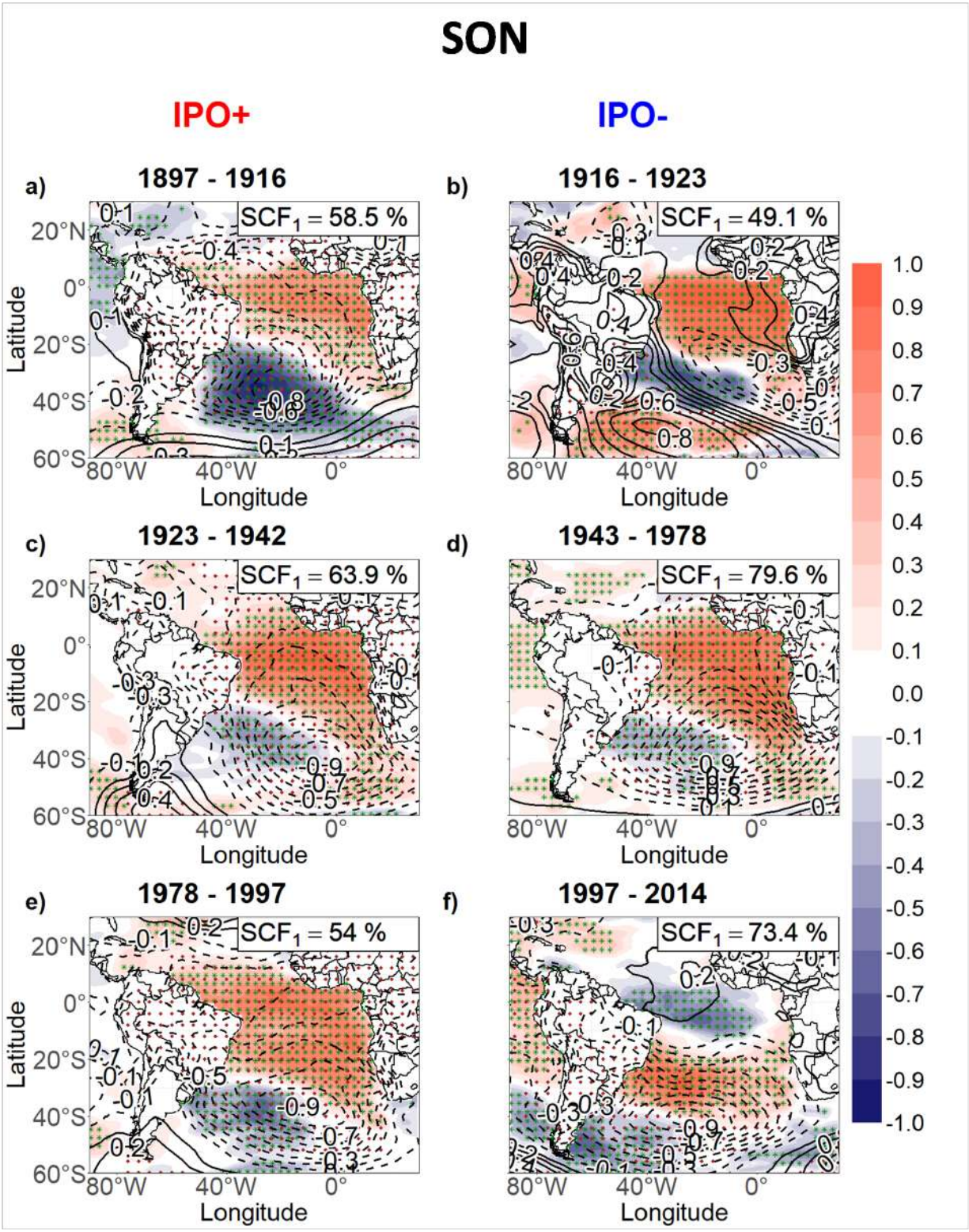

Figure C.4: The same as in Figure C.1 except for the SON months.

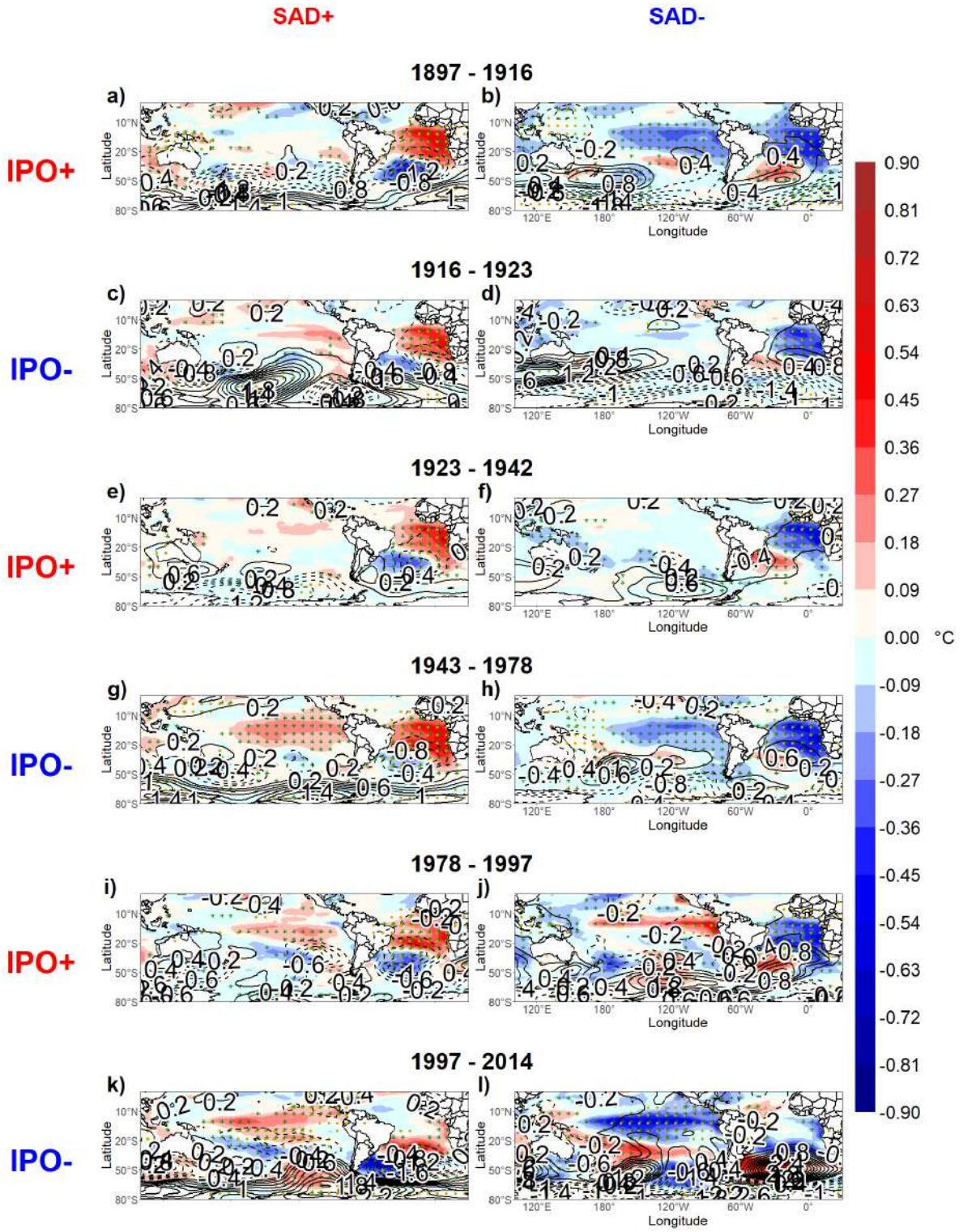

Figure C.5: Composites with SST anomalies (in colors) and MSLP anomalies (contours) for the positive (SAD+) and negative (SAD-) phases of the South Atlantic Dipole for the periods 1897-1916 (itens a) SAD+ and b) SAD-), 1916-1923 (itens c) SAD+ and d) SAD-), 1923-1942 (itens e) SAD+ and f) SAD-), 1943-1978 (itens g) SAD+ and h) SAD-), 1978-1997 (itens i) SAD+ and j) SAD-) and 1997-2020 (itens k) SAD+ and l) SAD-), which are associated with the phases of the Interdecadal Pacific Oscillation (IPO). IPO+ (IPO-) indicates a positive (negative) phase of IPO. The domain displayed is over the South Pacific and Atlantic basins. Calculated for the ERA5 reanalysis. Values with a statistical confidence level above 95% are shown in green (yellow) dots for SST (MSLP) anomalies.

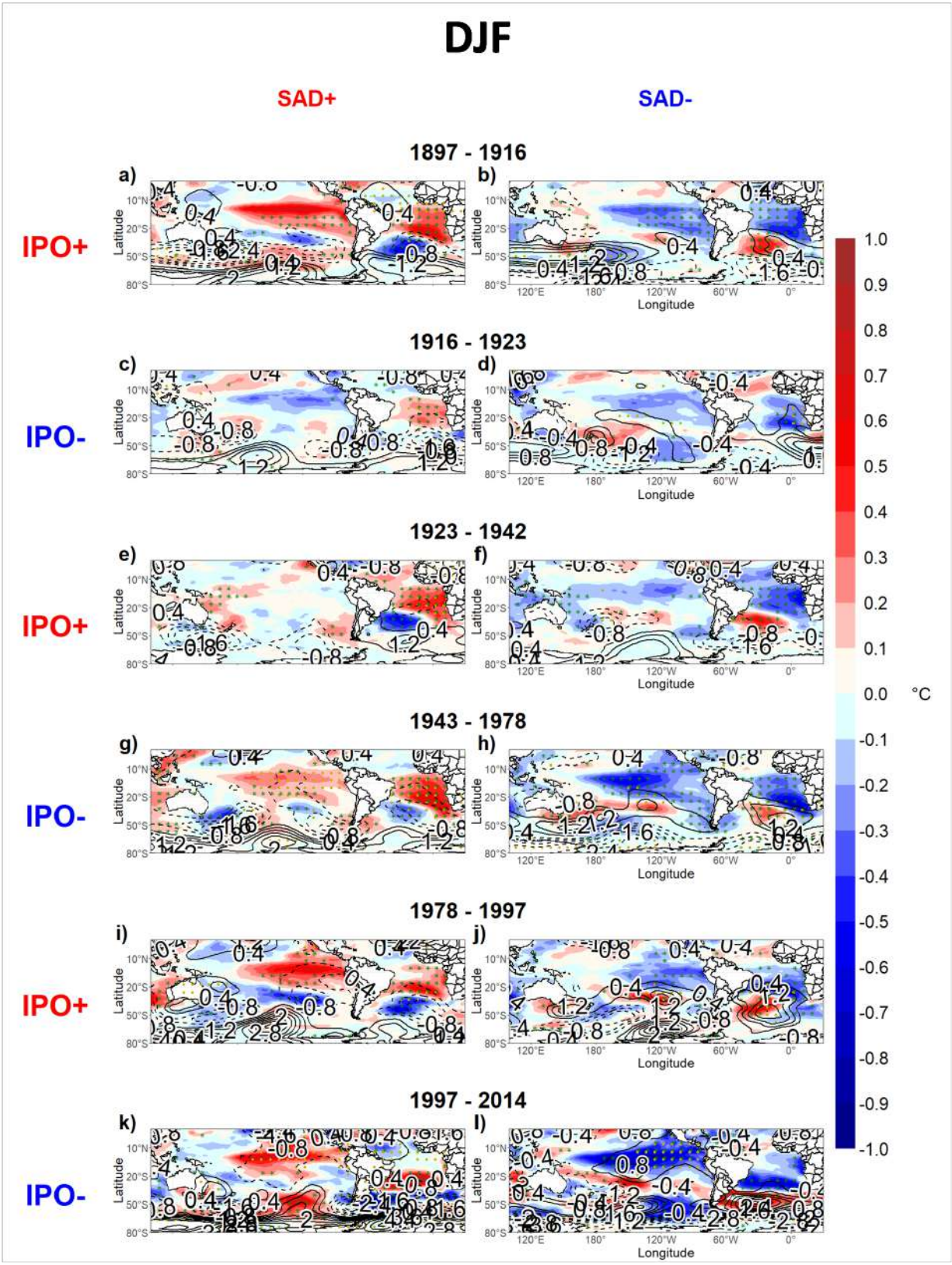

Figure C.6: The same as in Figure C.5 except for the DJF months.

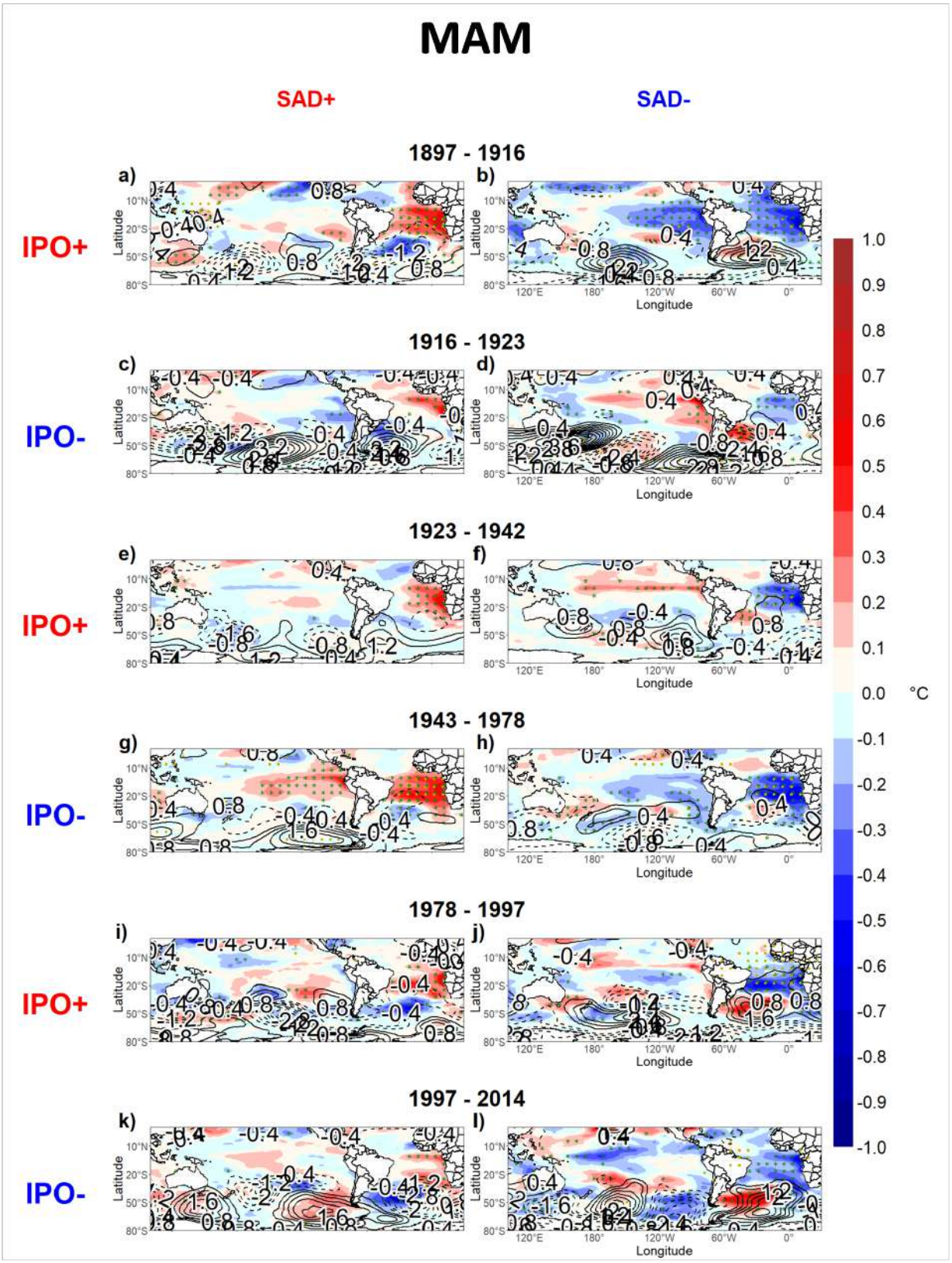

Figure C.7: The same as in Figure C.5 except for the MAM months.

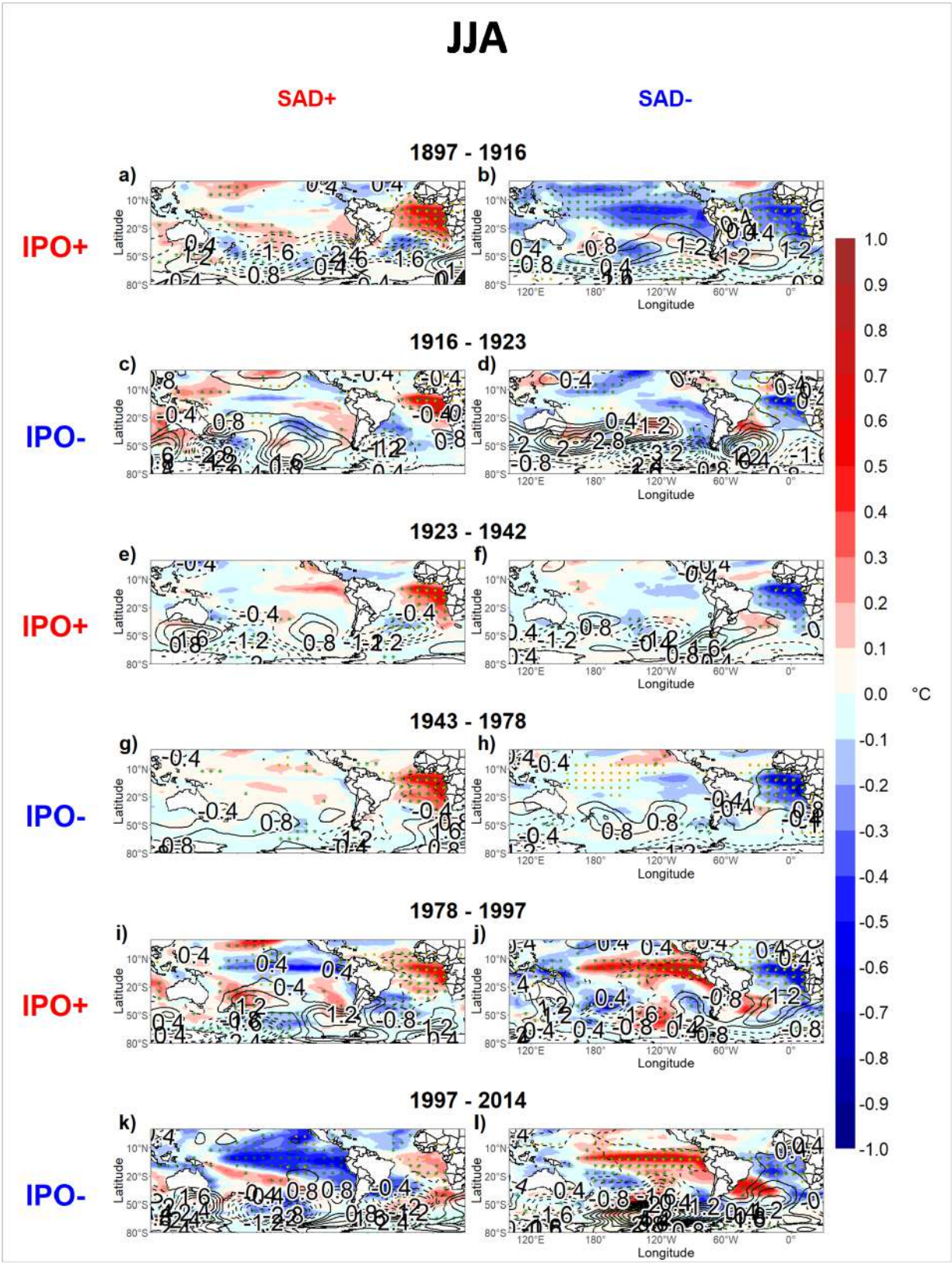

Figure C.8: The same as in Figure C.5 except for the JJA months.

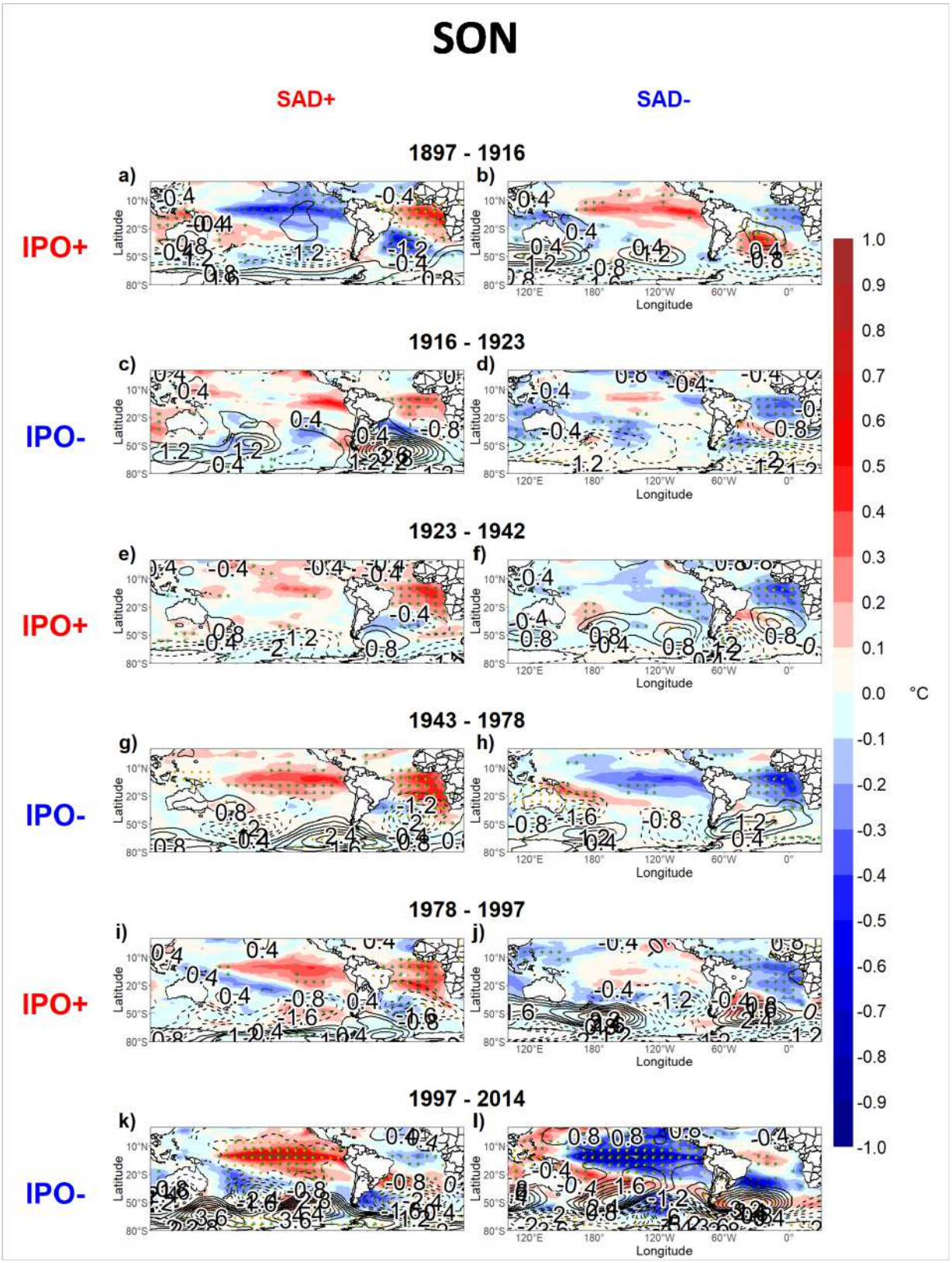

Figure C.9: The same as in Figure C.5 except for the SON months.

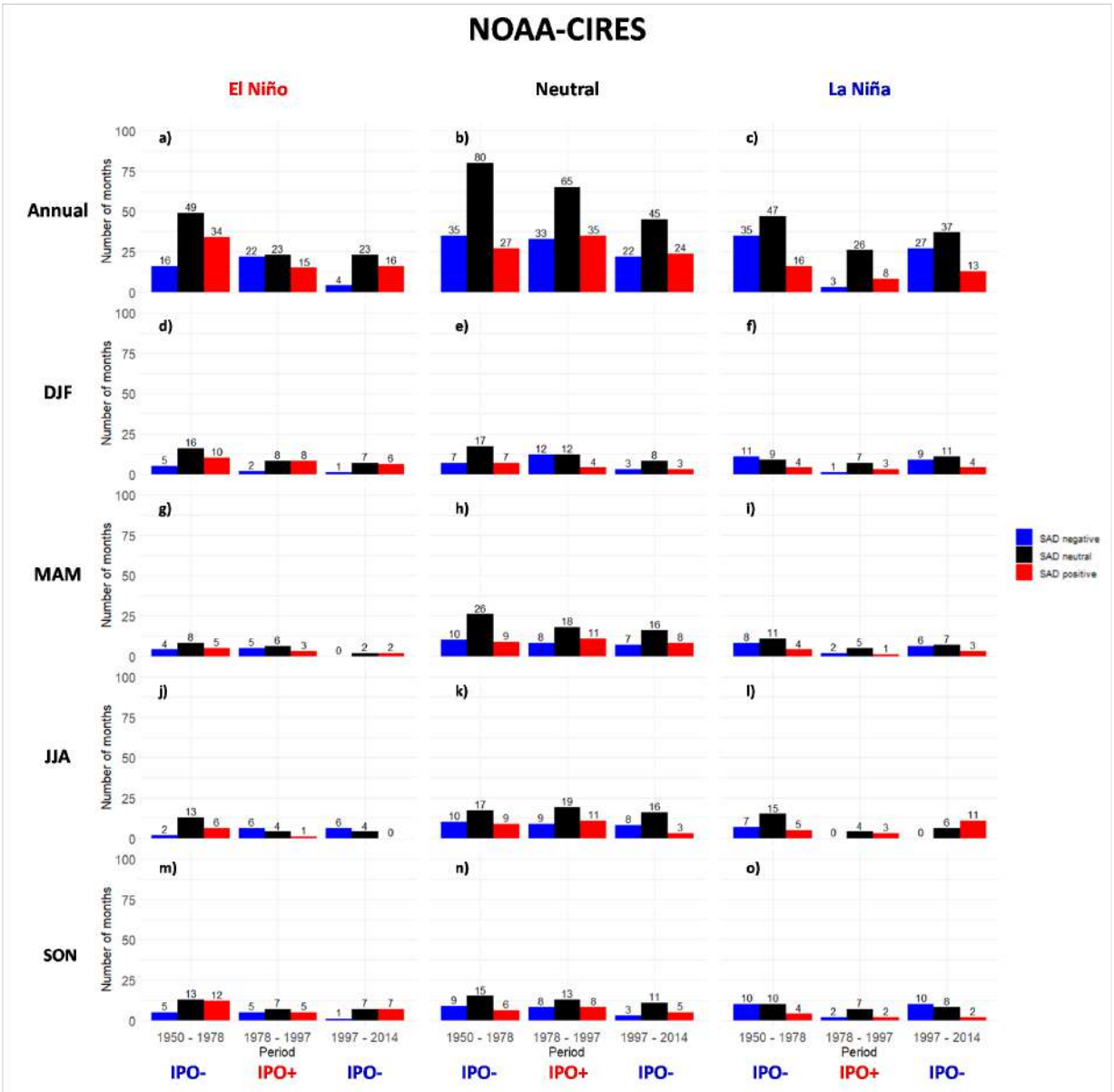

Figure C.10: The same as in Figure 3.21 except for the NOAA-CIRES 20th Century reanalysis.

C.2 ERA-20C

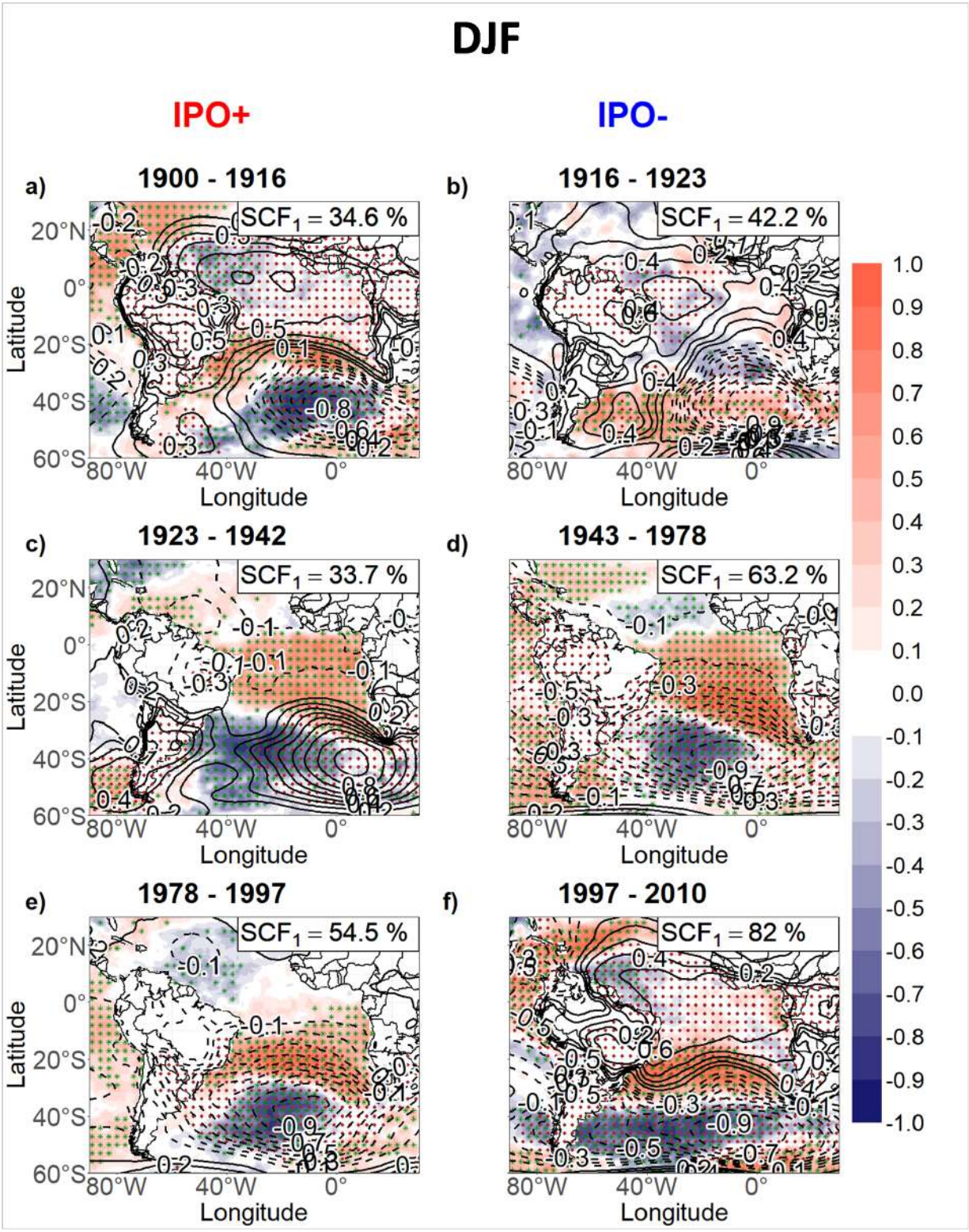

Figure C.11: The same as in Figure C.1 except for the ERA-20C reanalysis.

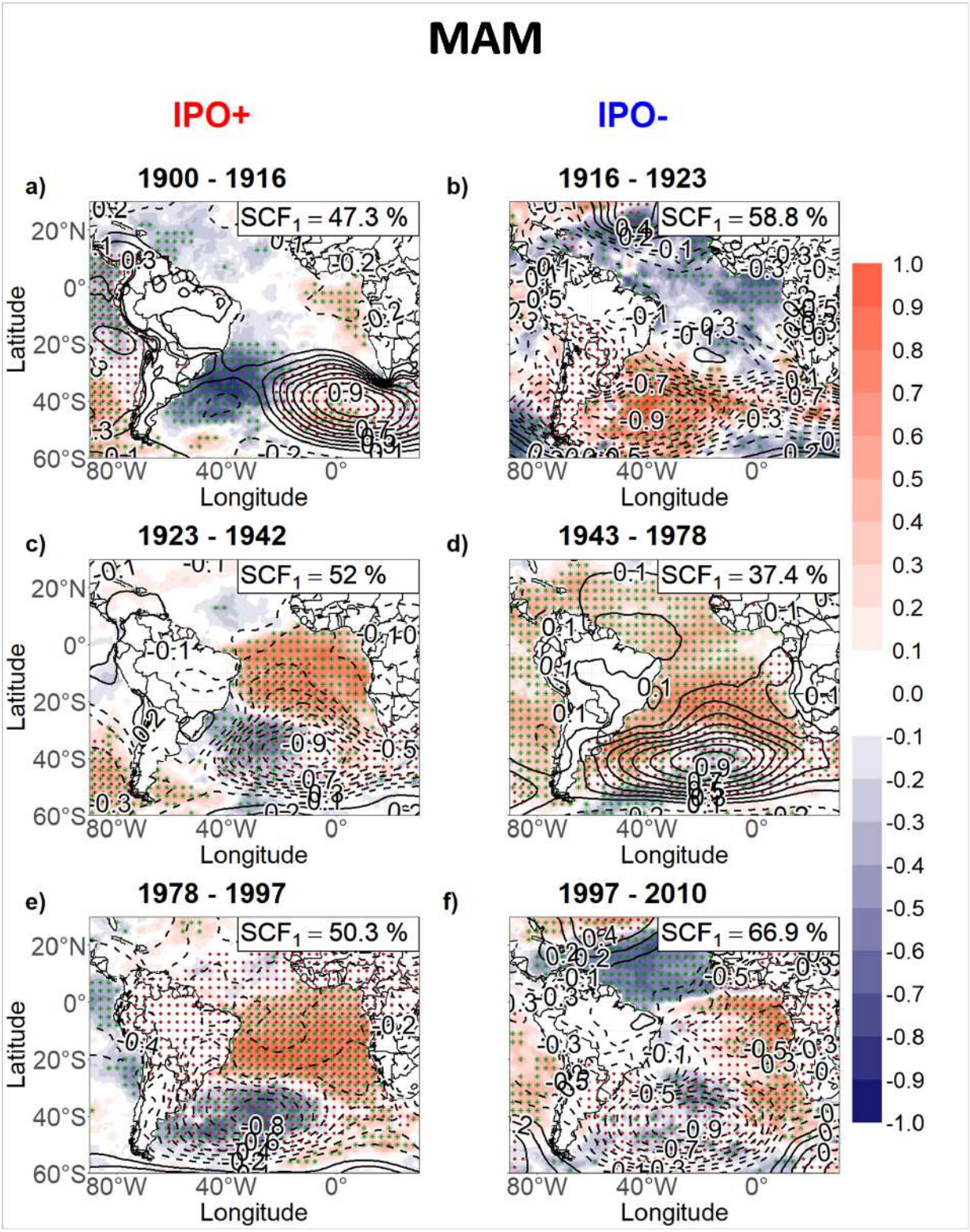

Figure C.12: The same as in Figure C.2 except for the ERA-20C reanalysis.

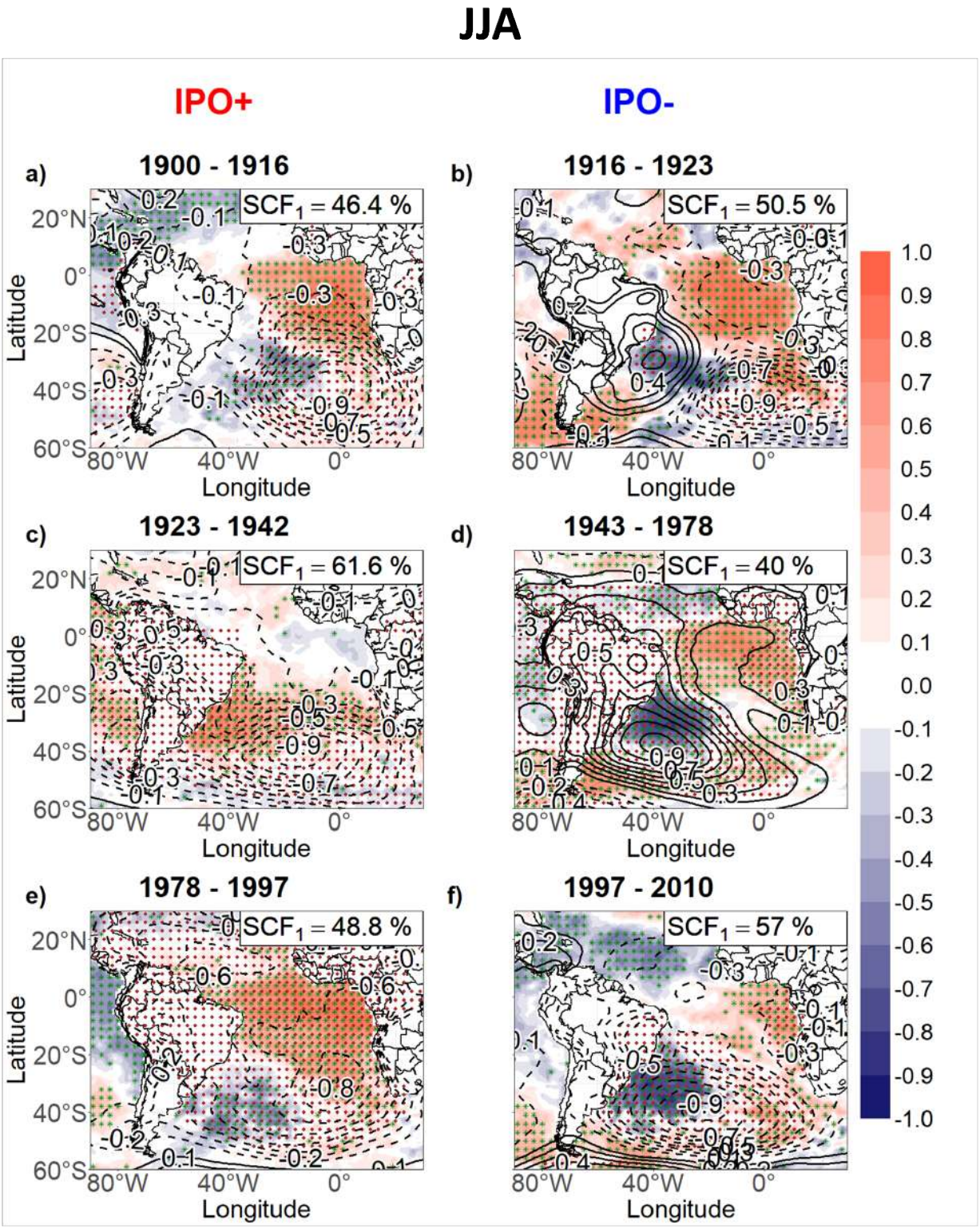

Figure C.13: The same as in Figure C.3 except for the ERA-20C reanalysis.

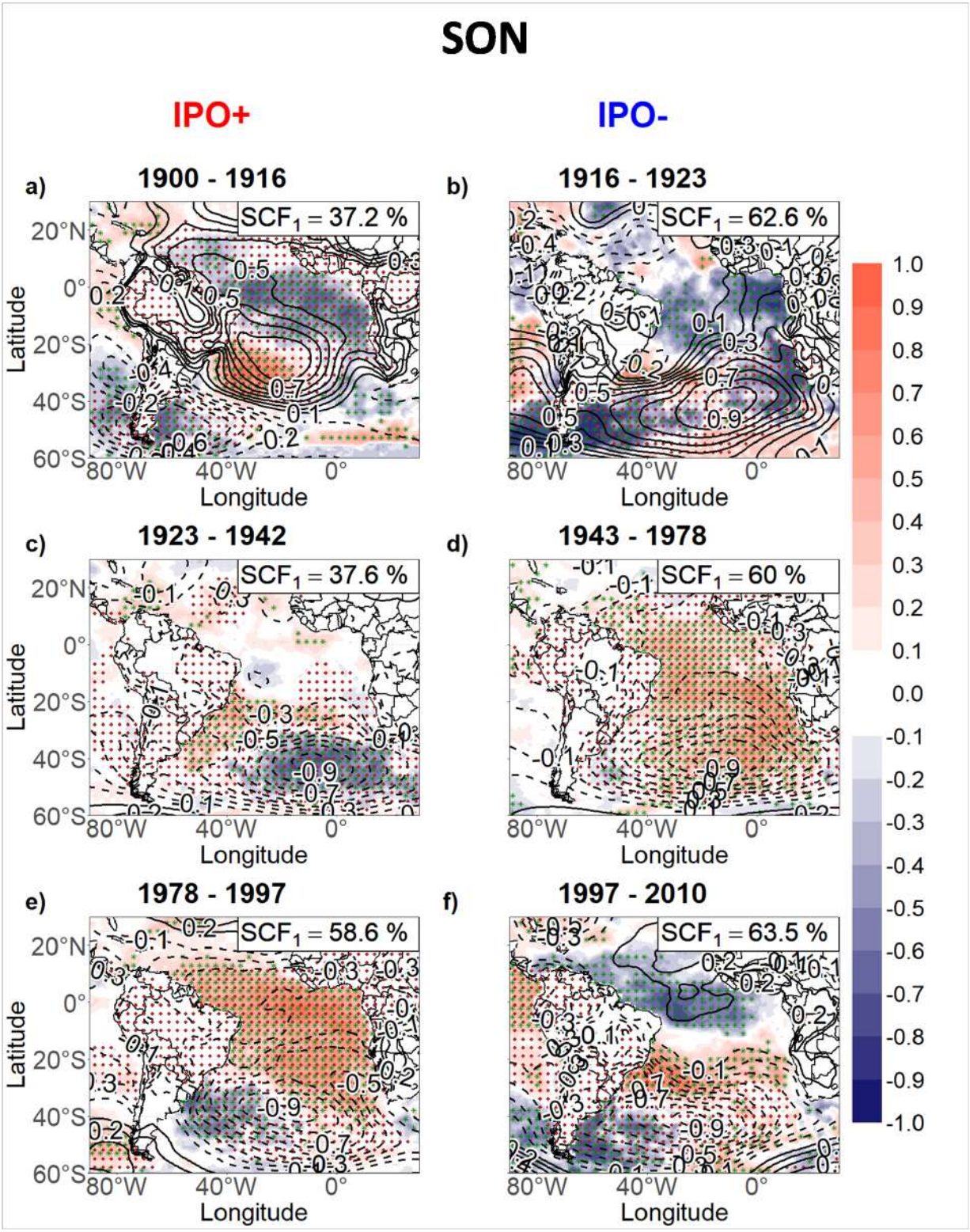

Figure C.14: The same as in Figure C.4 except for the ERA-20C reanalysis.

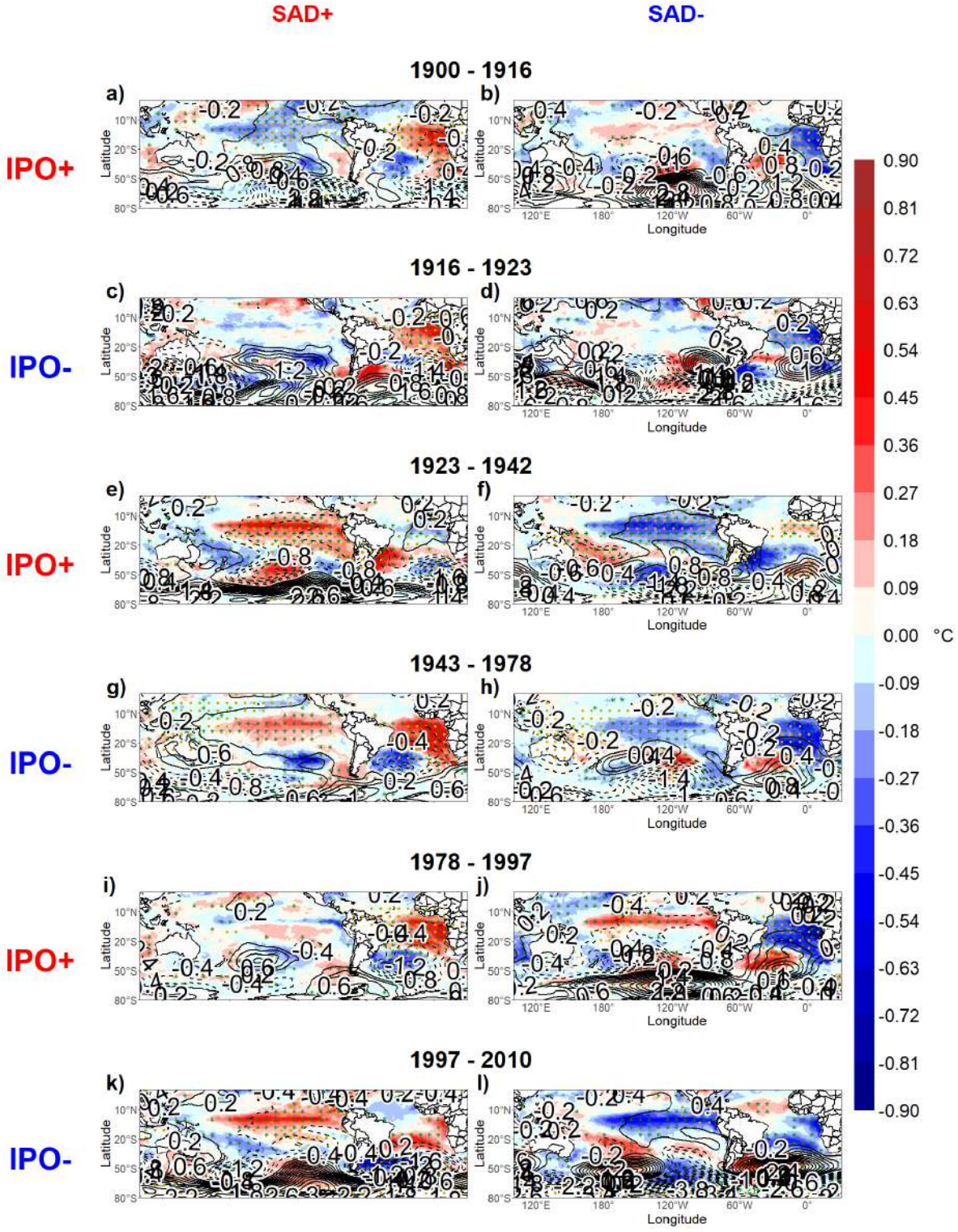

Figure C.15: The same as in Figure C.5 except for the ERA-20C reanalysis.

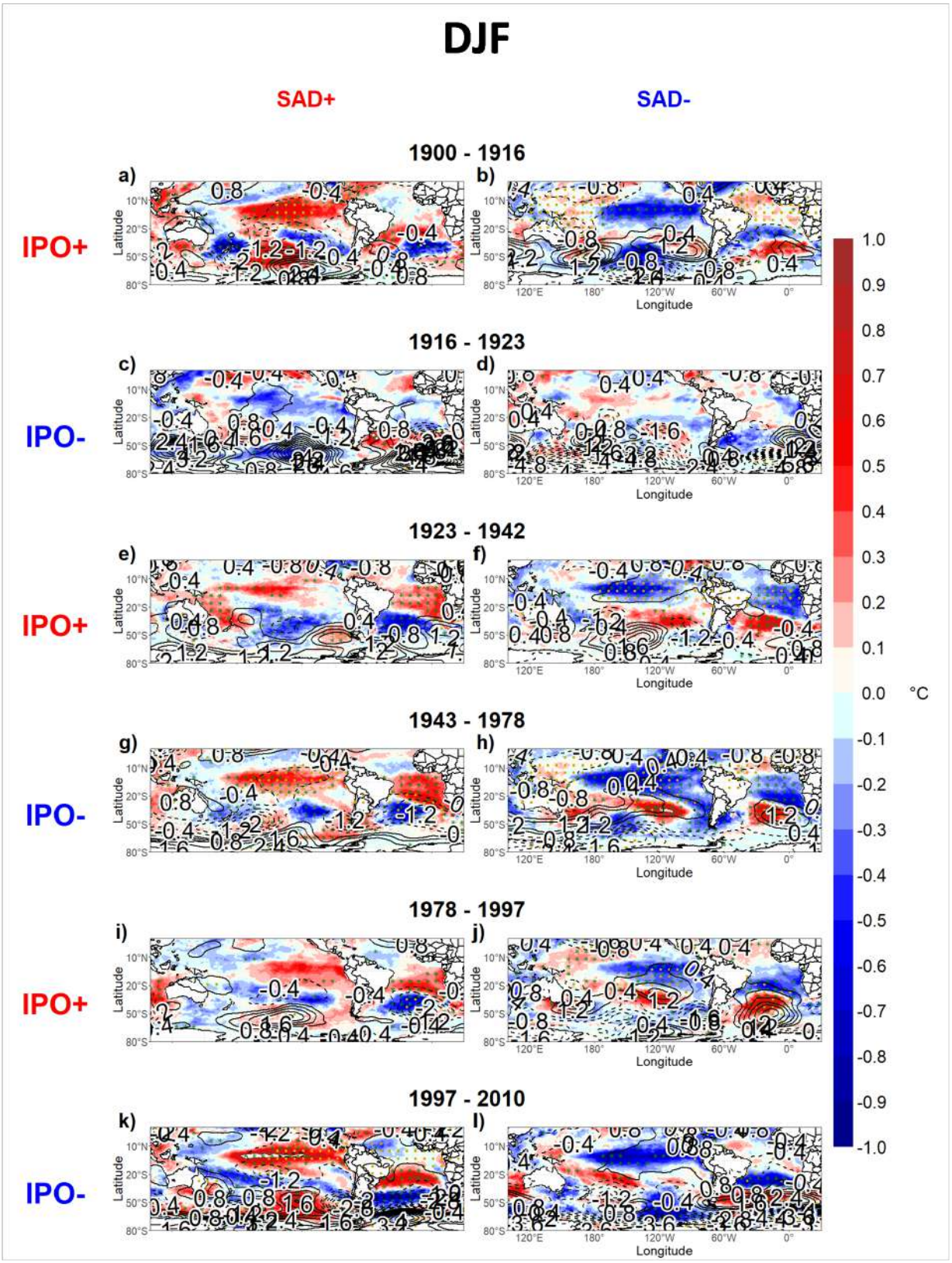

Figure C.16: The same as in Figure C.6 except for the ERA-20C reanalysis.

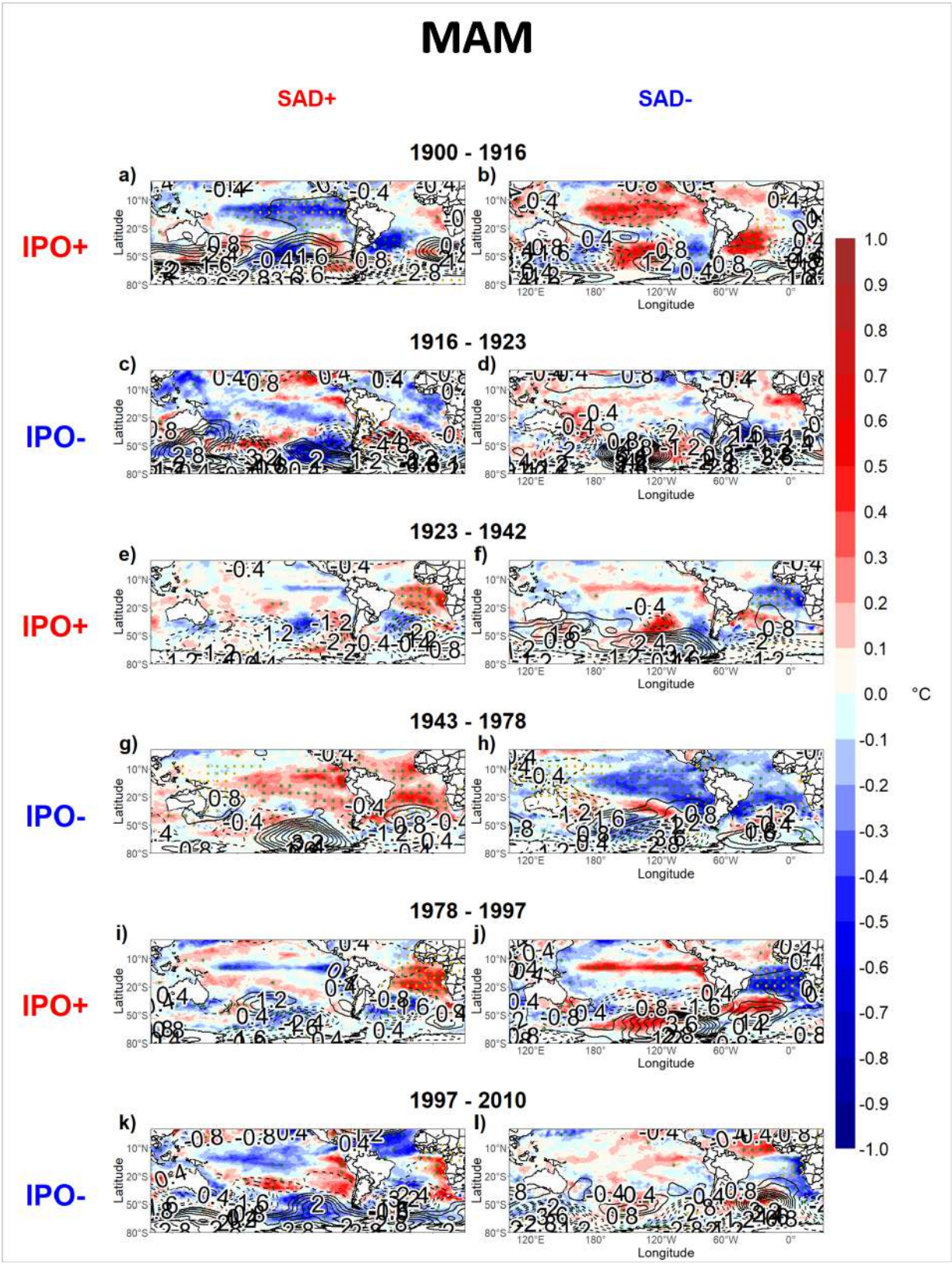

Figure C.17: The same as in Figure C.7 except for the ERA-20C reanalysis.

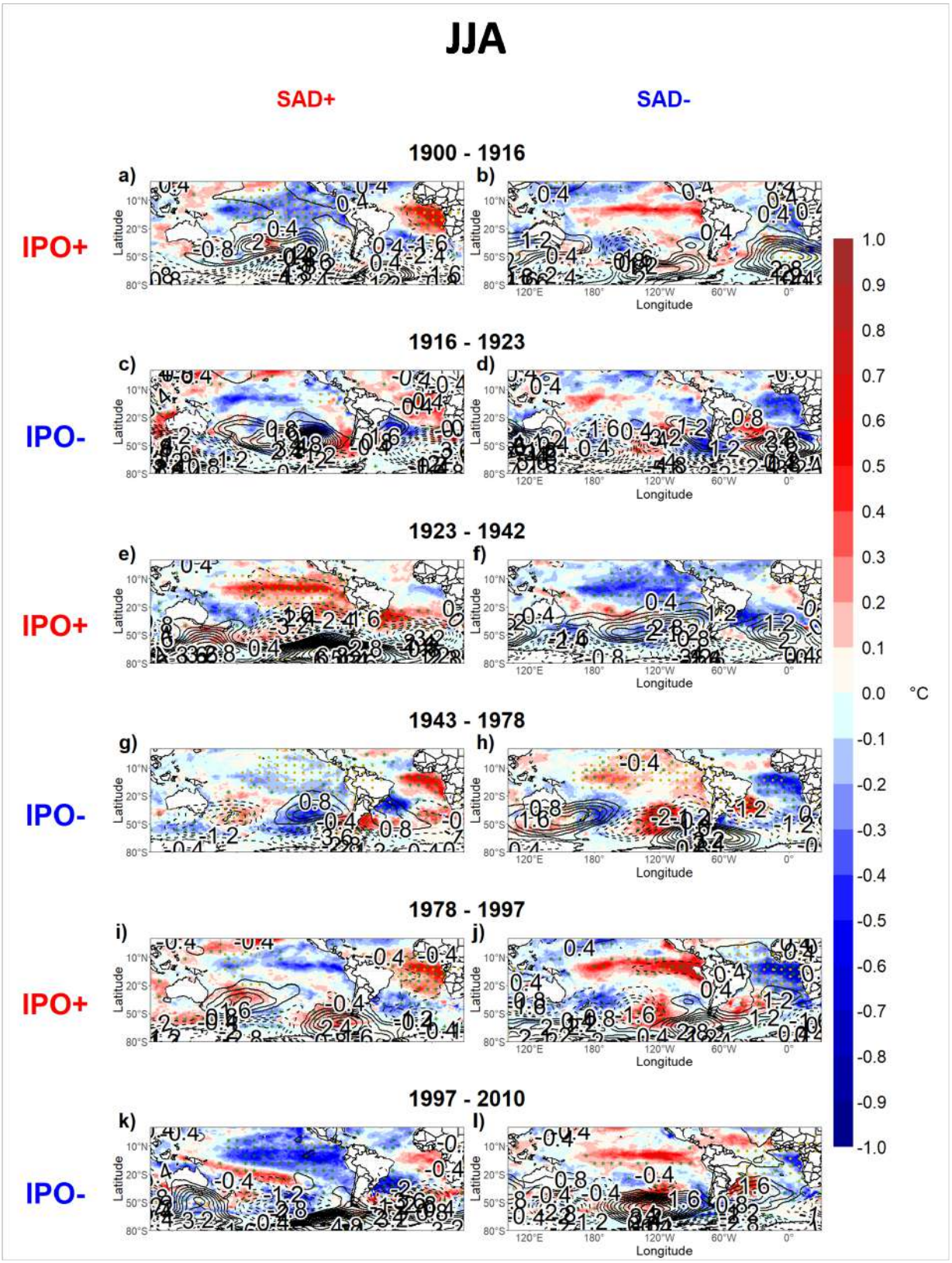

Figure C.18: The same as in Figure C.8 except for the ERA-20C reanalysis.

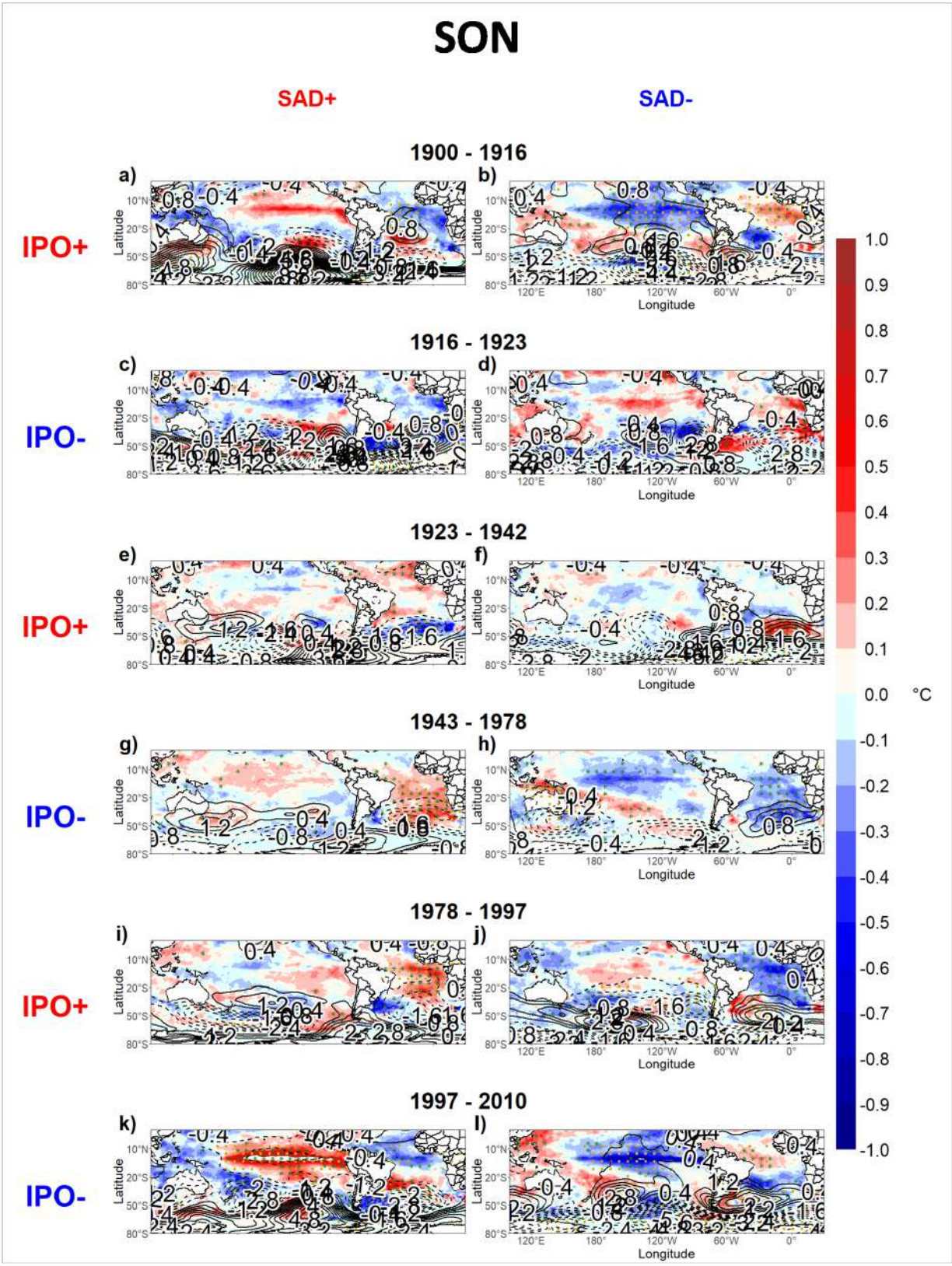

Figure C.19: The same as in Figure C.9 except for the ERA-20C reanalysis.

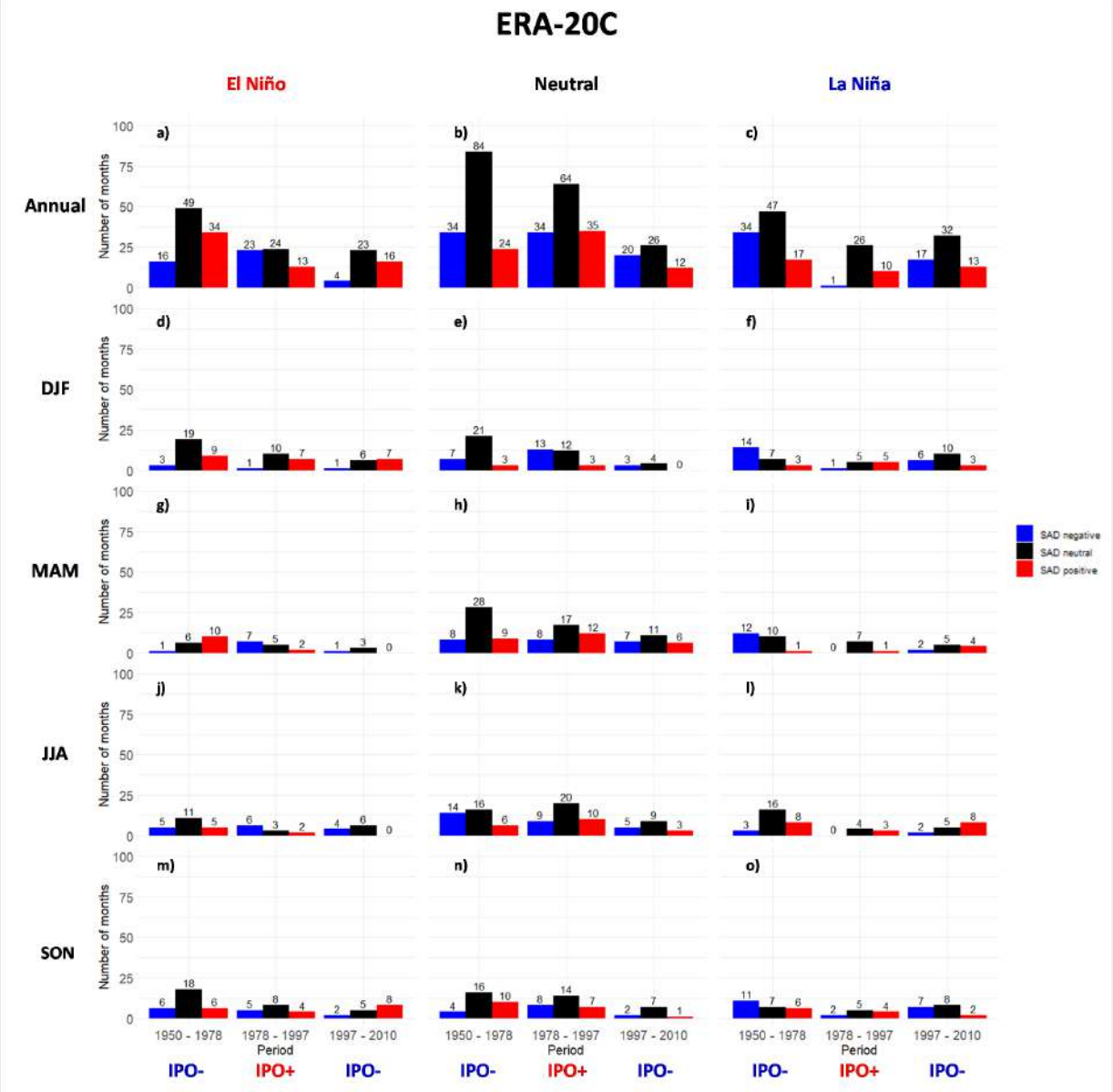

Figure C.20: The same as in Figure 3.21 except for the ERA-20C reanalysis.

Appendix D

Evolution of atmospheric characteristics of the South Atlantic Dipole in austral summer - NOAA CIRES and ERA-20C

D.1 NOAA CIRES 20th Century

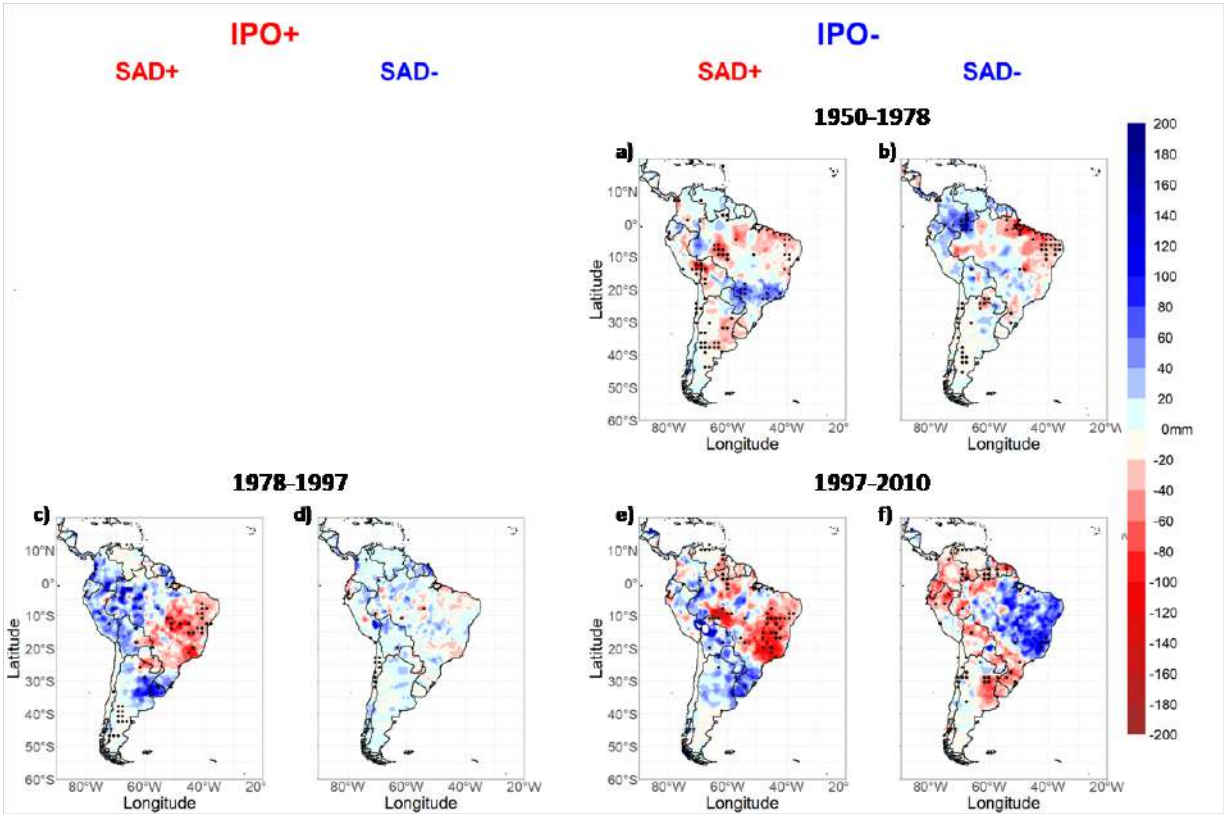

Figure D.1: The same as in Figure 3.22 except for the NOAA CIRES 20th Century reanalysis.

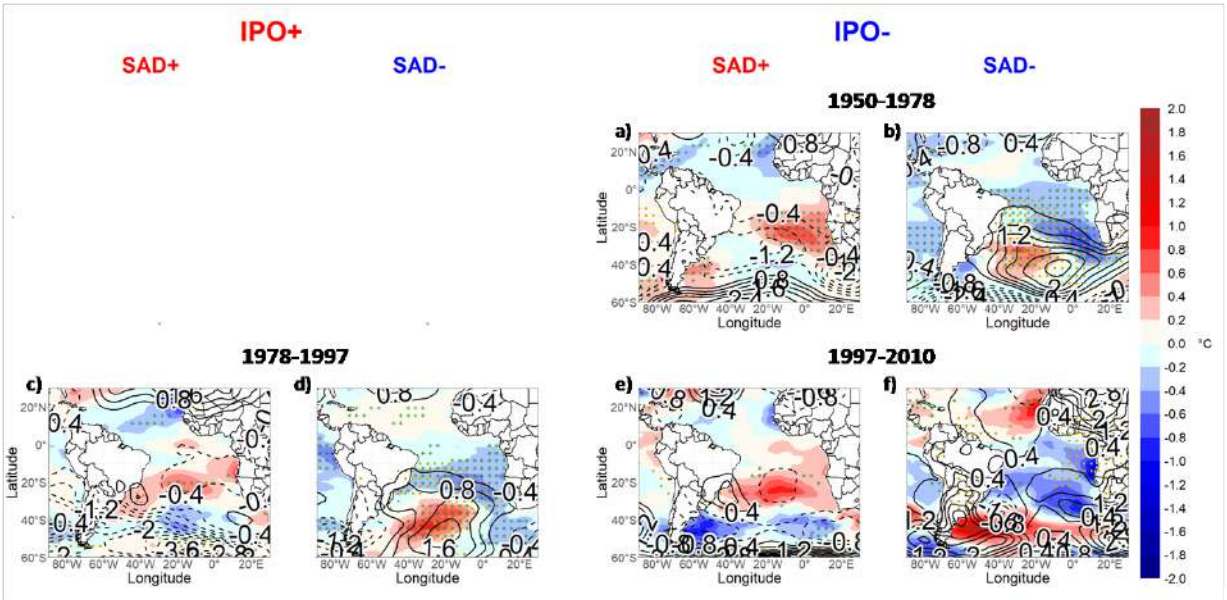

Figure D.2: The same as in Figure 3.23 except for the NOAA CIRES 20th Century reanalysis.

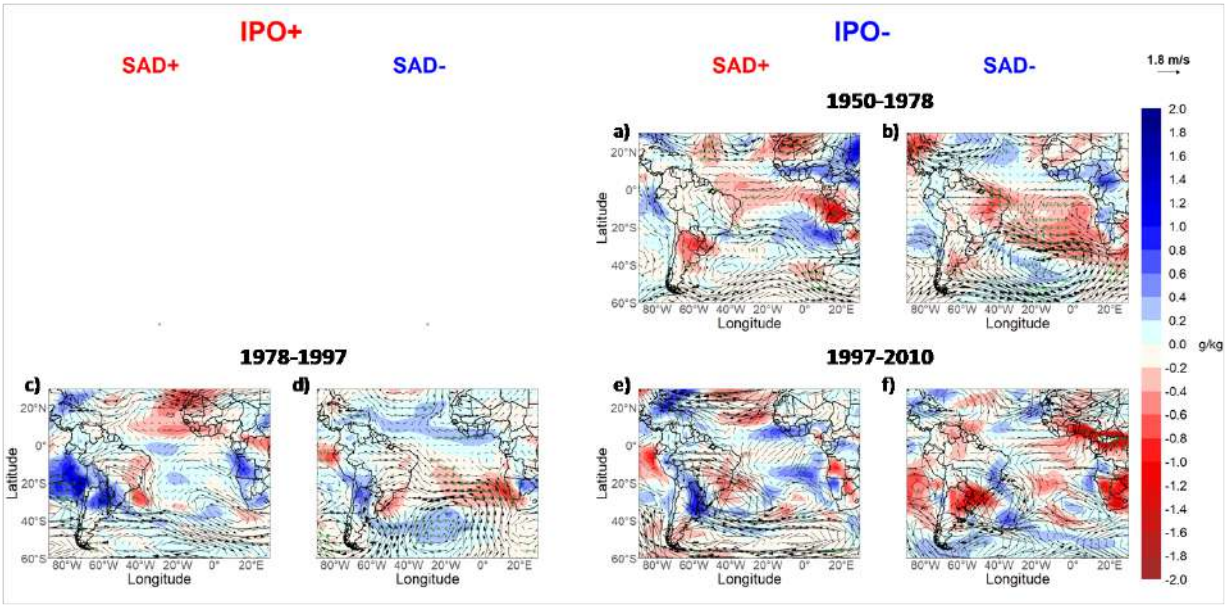

Figure D.3: The same as in Figure 3.24 except for the NOAA CIRES 20th Century reanalysis.

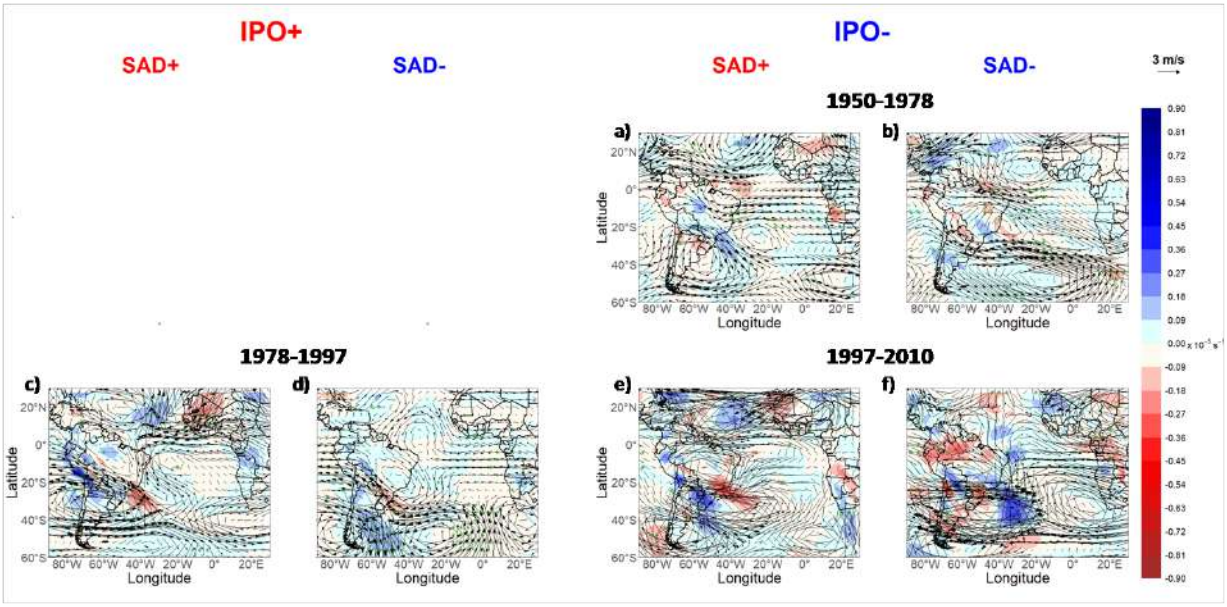

Figure D.4: The same as in Figure 3.25 except for the NOAA CIRES 20th Century reanalysis.

D.2 ERA-20C

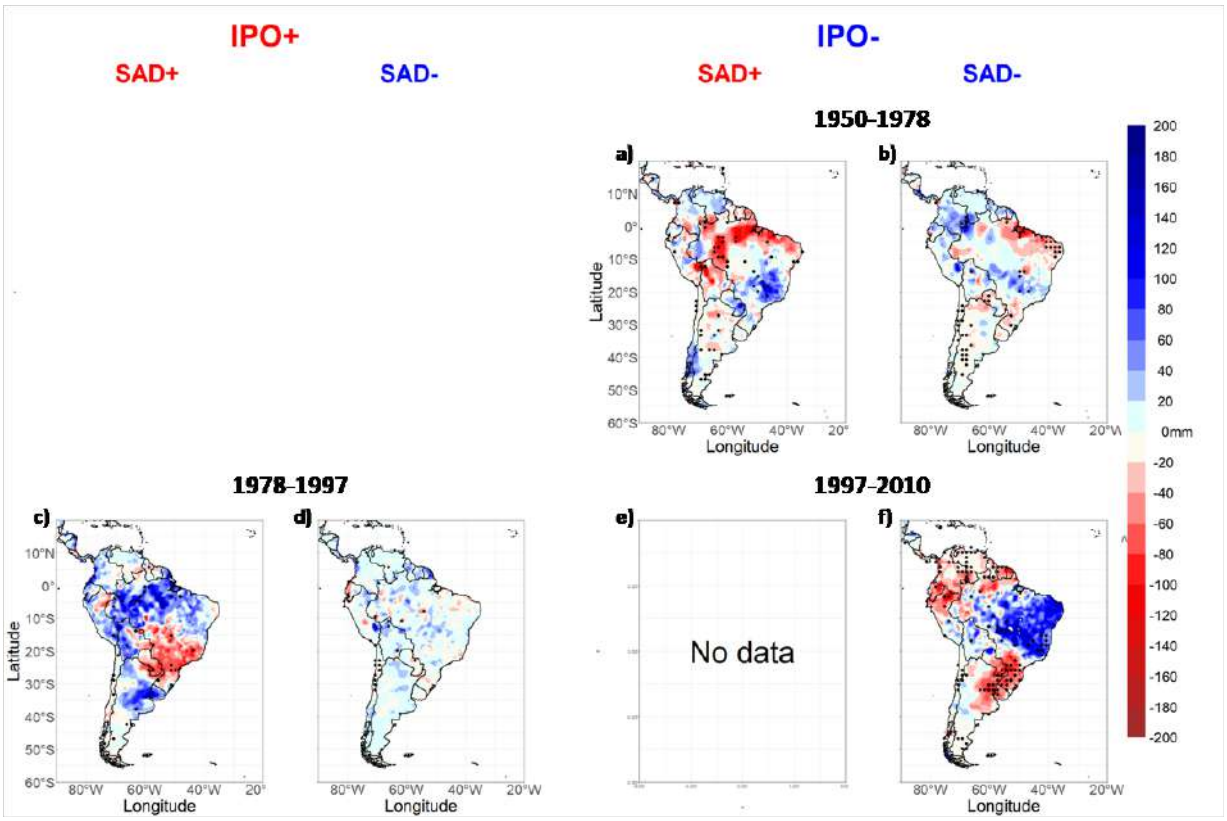

Figure D.5: The same as in Figure 3.22 except for the ERA-20C reanalysis.

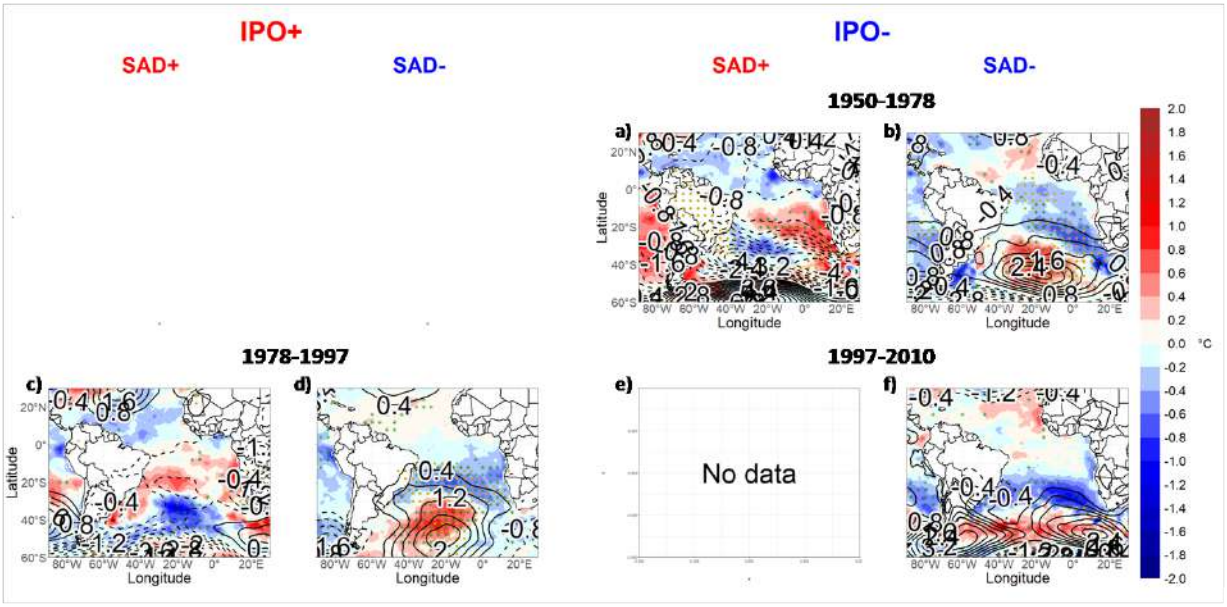

Figure D.6: The same as in Figure 3.23 except for the ERA-20C reanalysis.

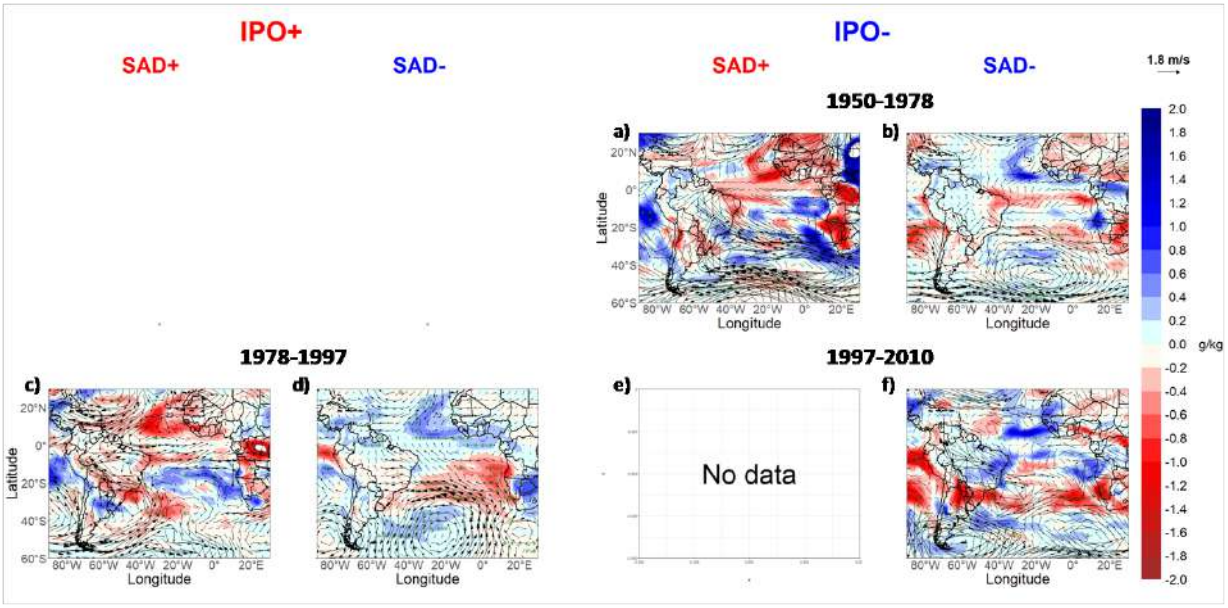

Figure D.7: The same as in Figure 3.24 except for the ERA-20C reanalysis.

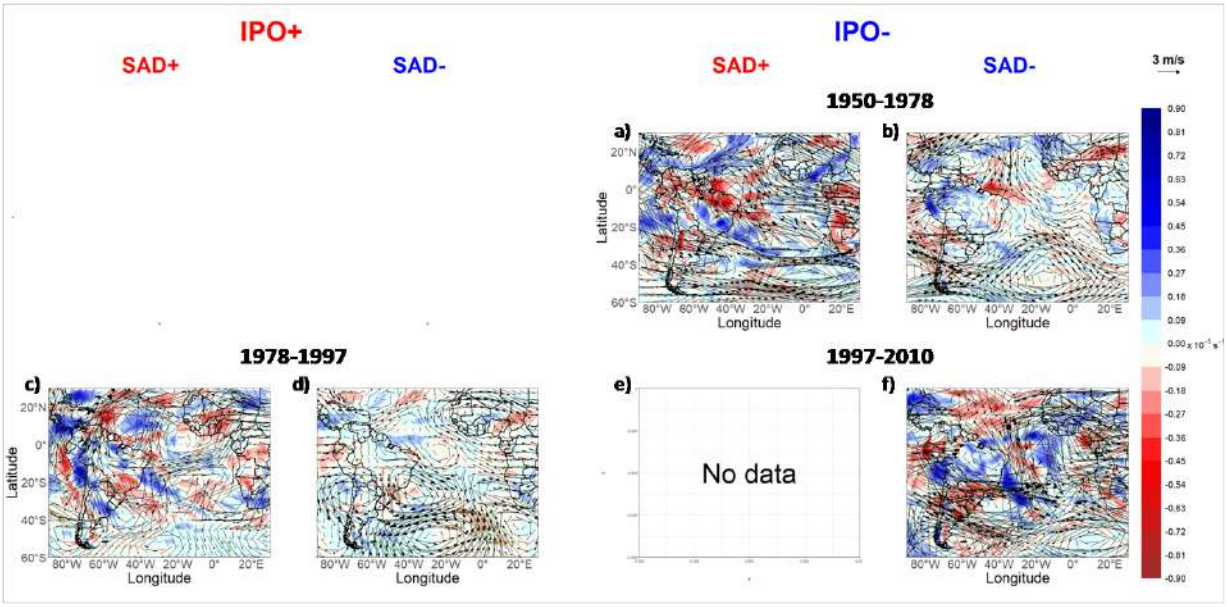

Figure D.8: The same as in Figure 3.25 except for the ERA-20C reanalysis.

Appendix E

The South Atlantic represented with CMIP6 Historical Simulations - NOAA CIRES and ERA-20C

E.1 NOAA CIRES 20th Century

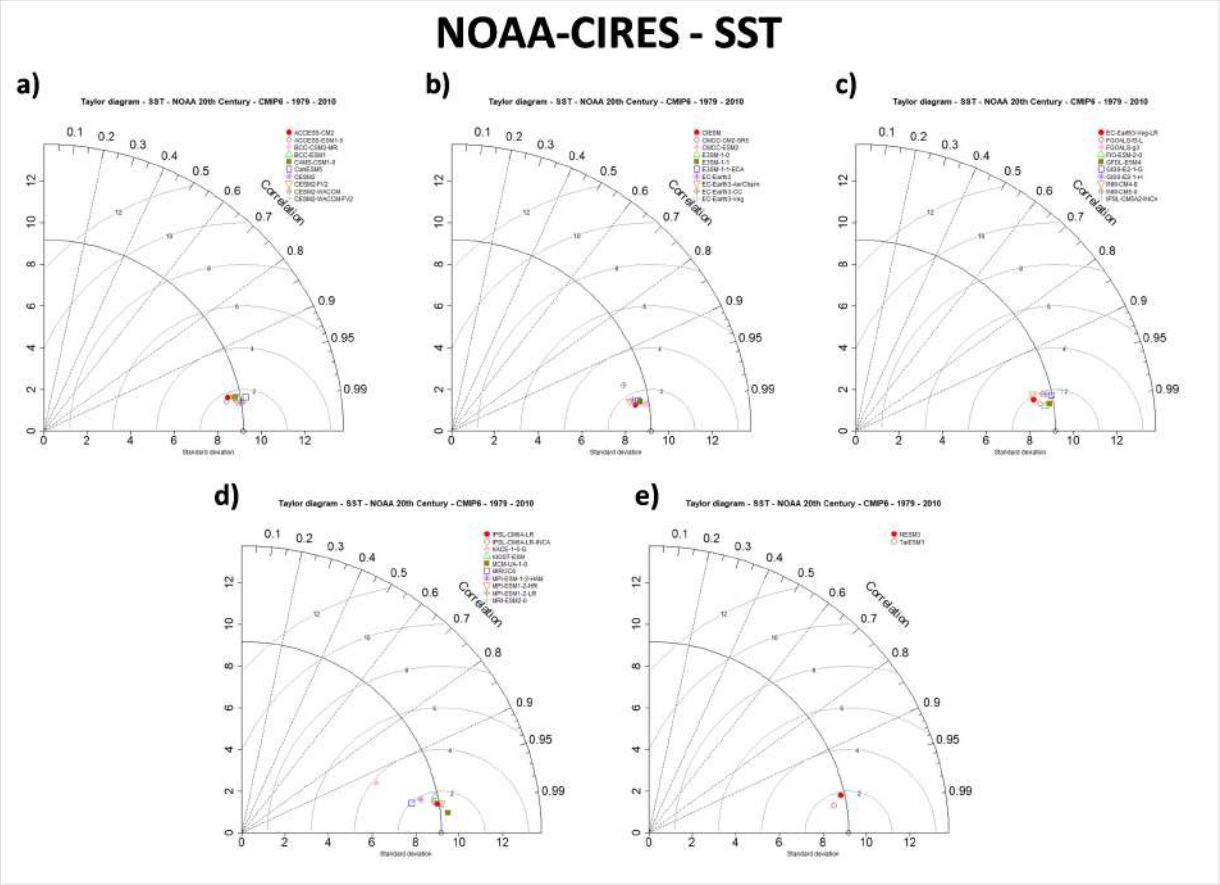

Figure E.1: The same as in Figure 3.26 except for the NOAA CIRES 20th Century reanalysis.

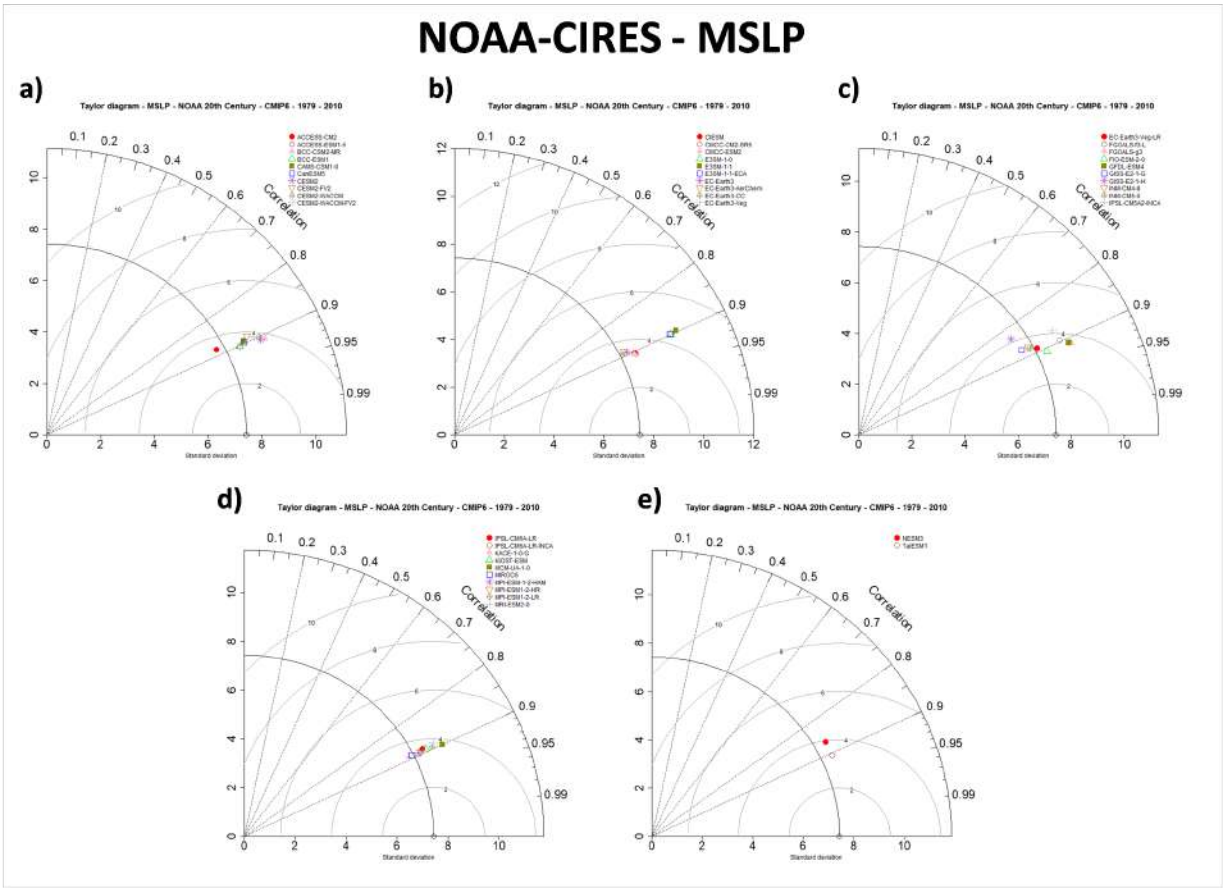

Figure E.2: The same as in Figure 3.27 except for the NOAA CIRES 20th Century reanalysis.

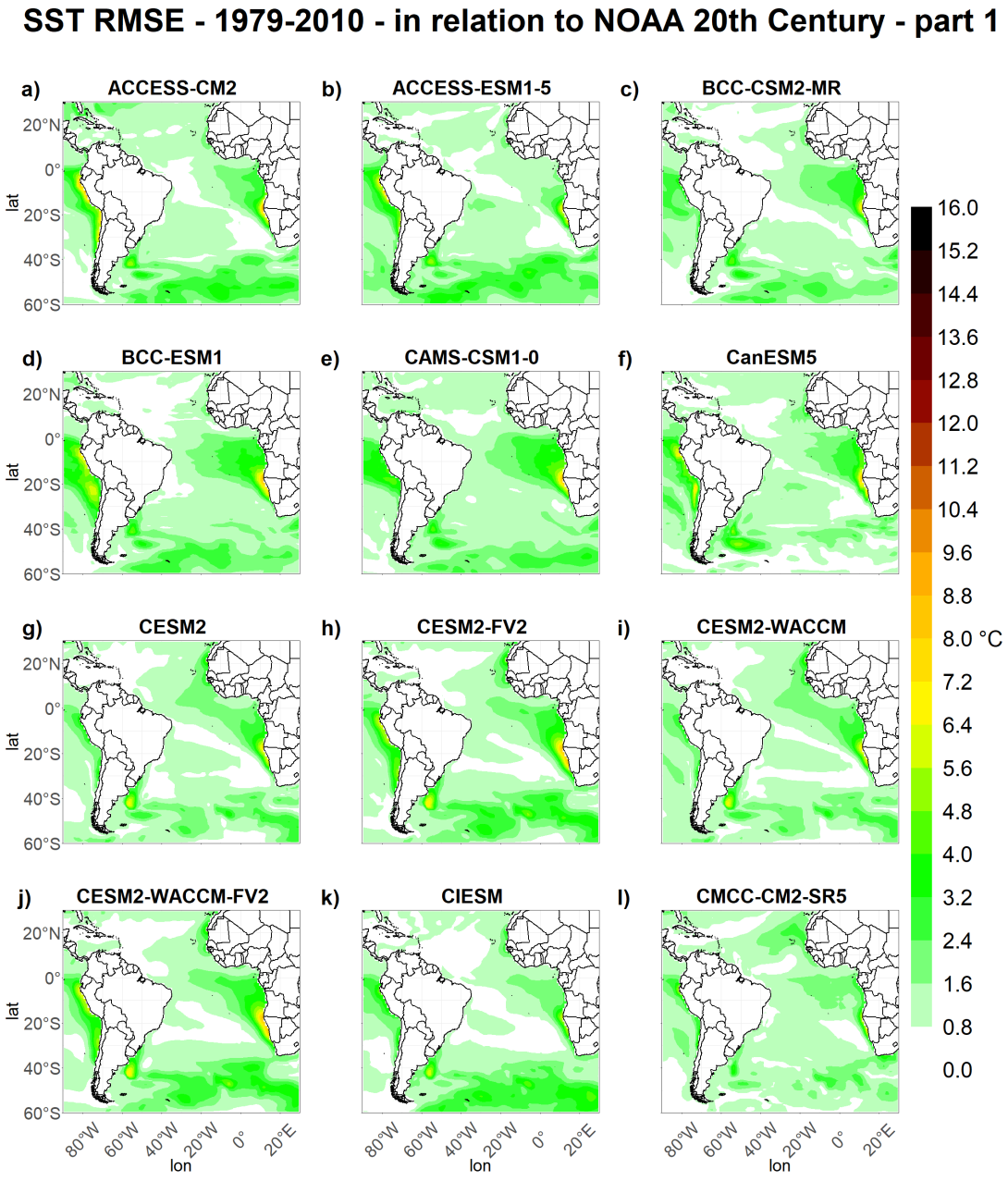

Figure E.3: The same as in Figure 3.28 except for the NOAA CIRES 20th Century reanalysis. Part 1.

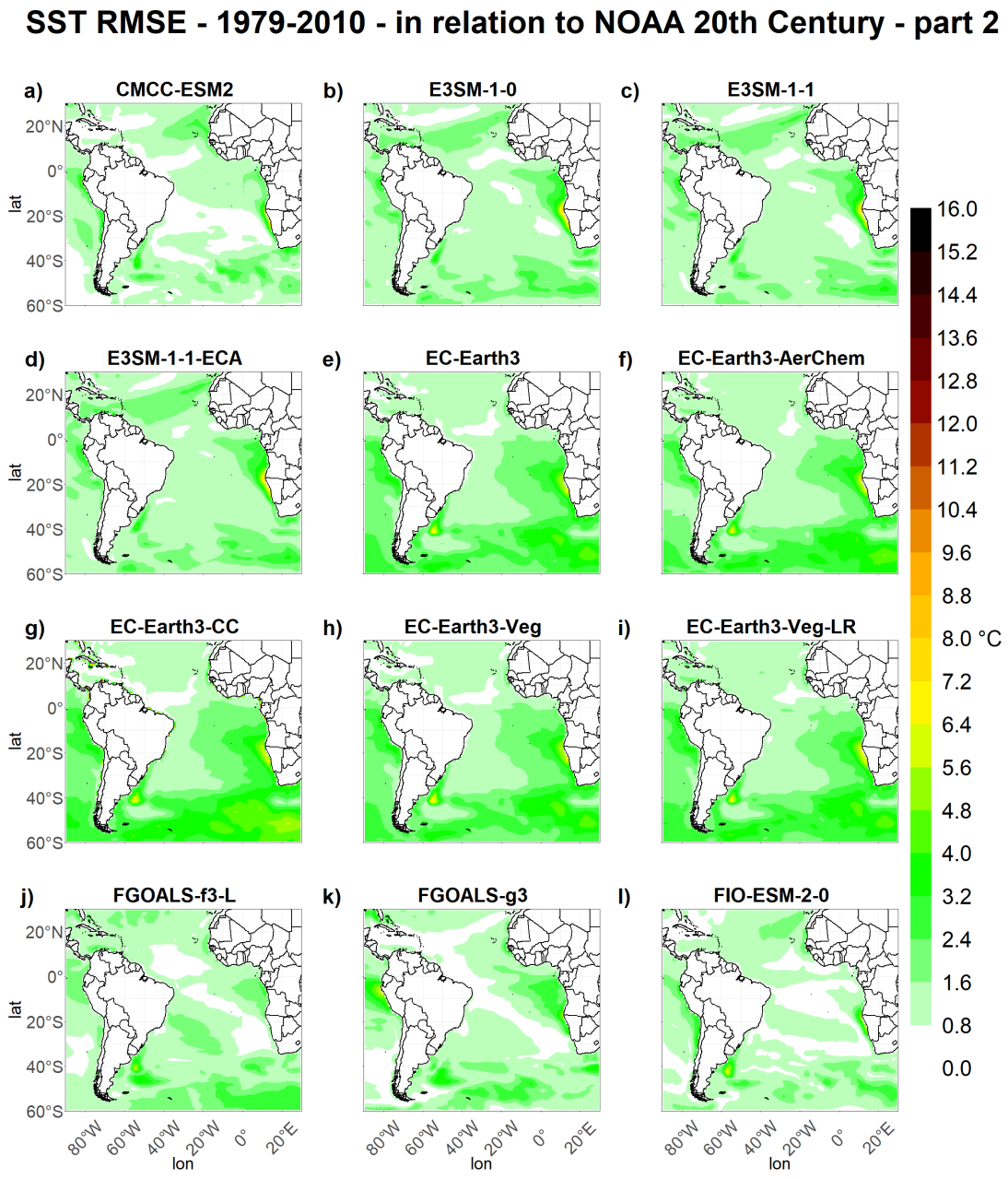

Figure E.4: The same as in Figure 3.28 except for the NOAA CIRES 20th Century reanalysis. Part 2.

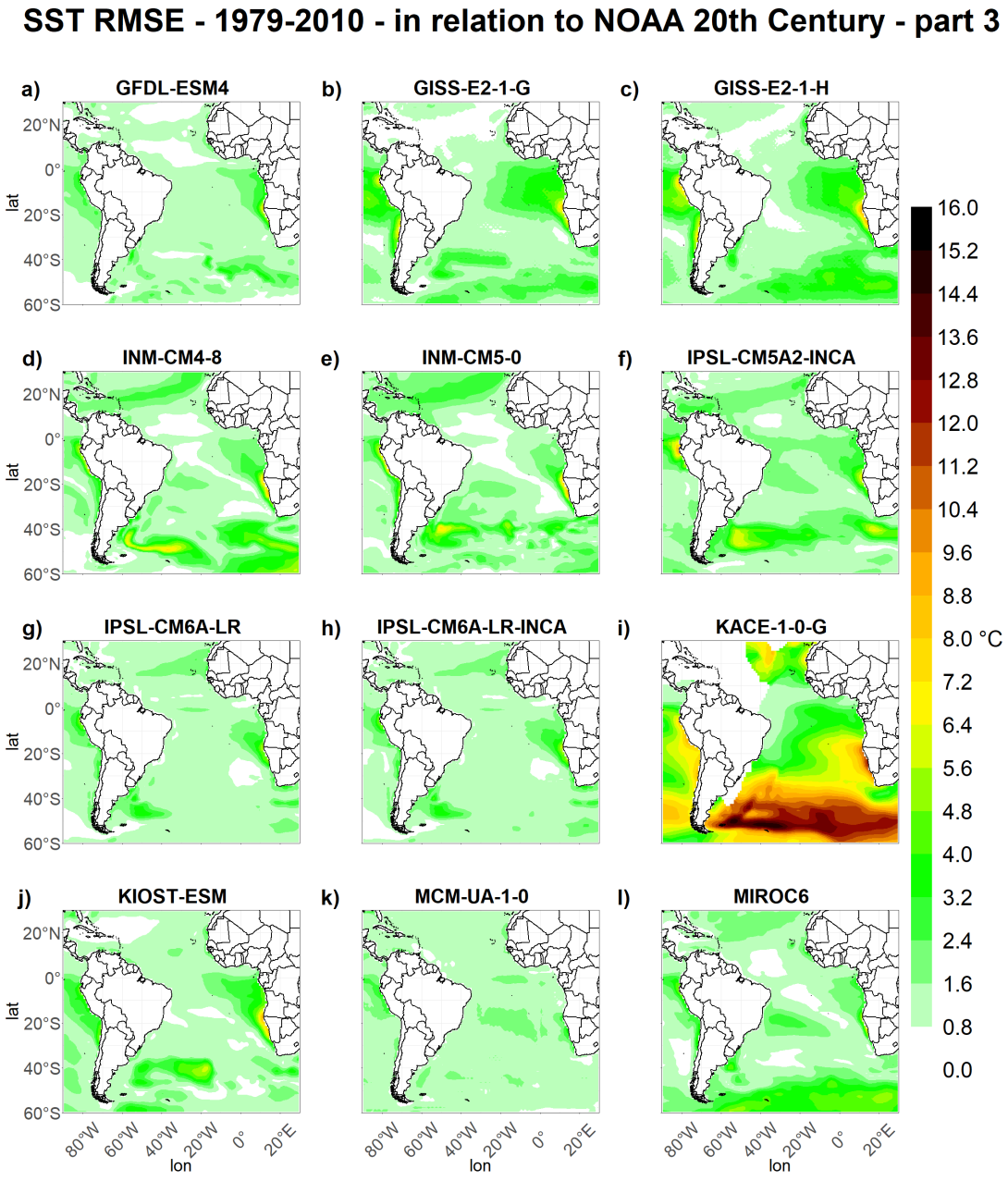

Figure E.5: The same as in Figure 3.28 except for the NOAA CIRES 20th Century reanalysis. Part 3.

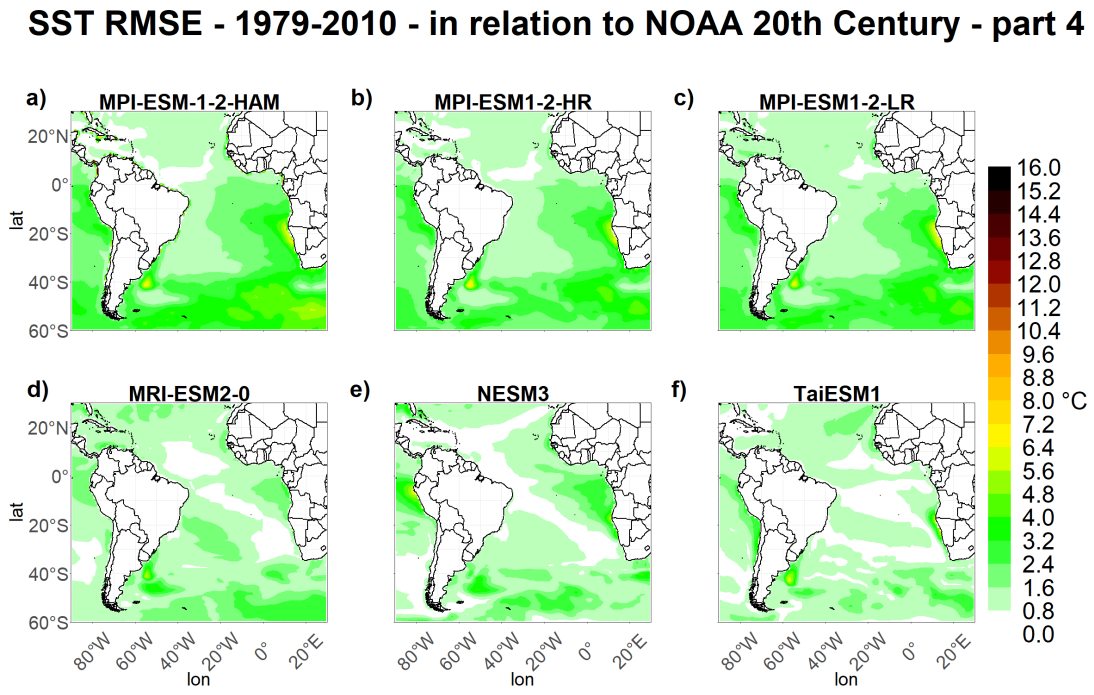

Figure E.6: The same as in Figure 3.28 except for the NOAA CIRES 20th Century reanalysis. Part 4.

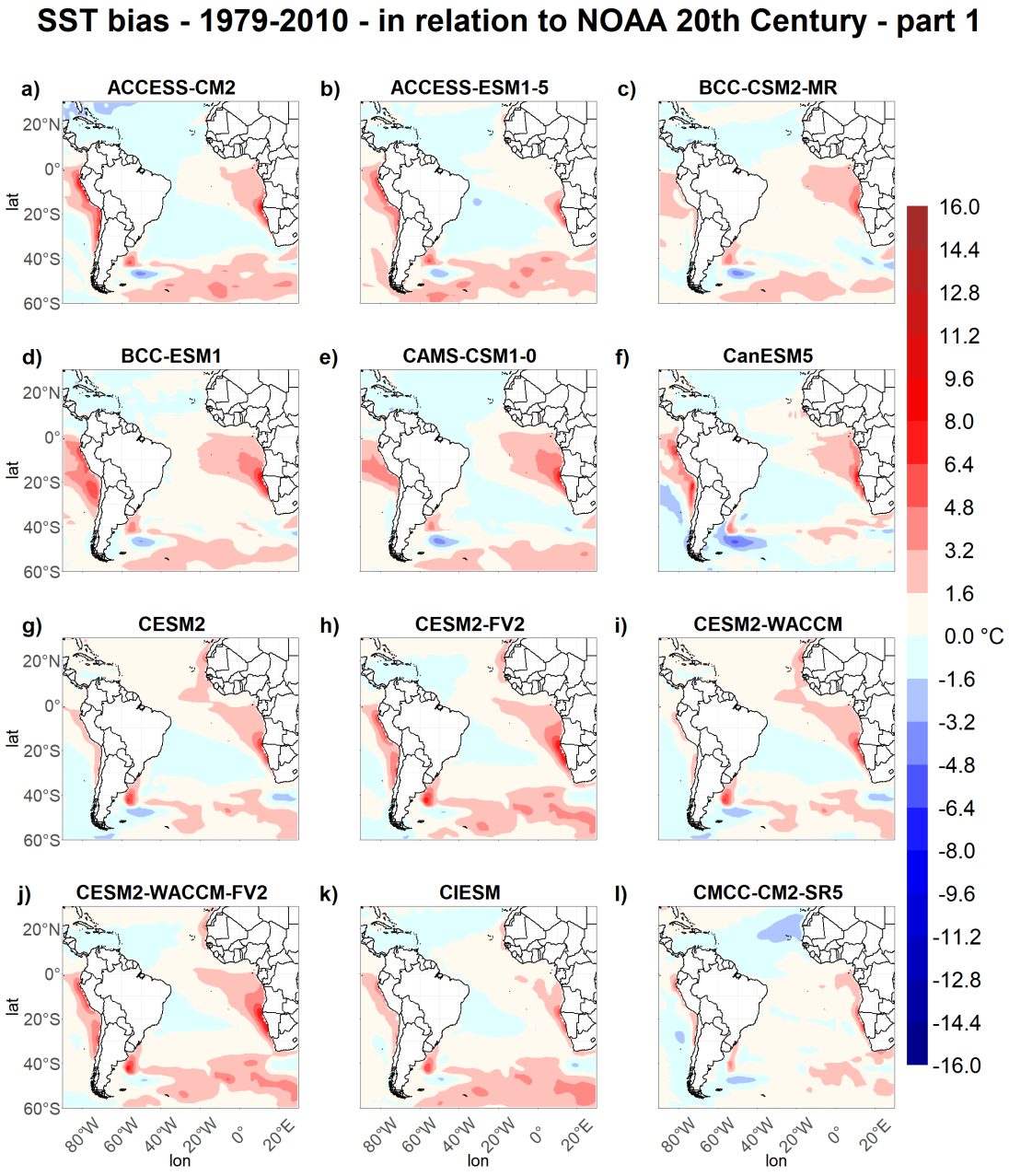

Figure E.7: The same as in Figure 3.32 except for the NOAA CIRES 20th Century reanalysis. Part 1.

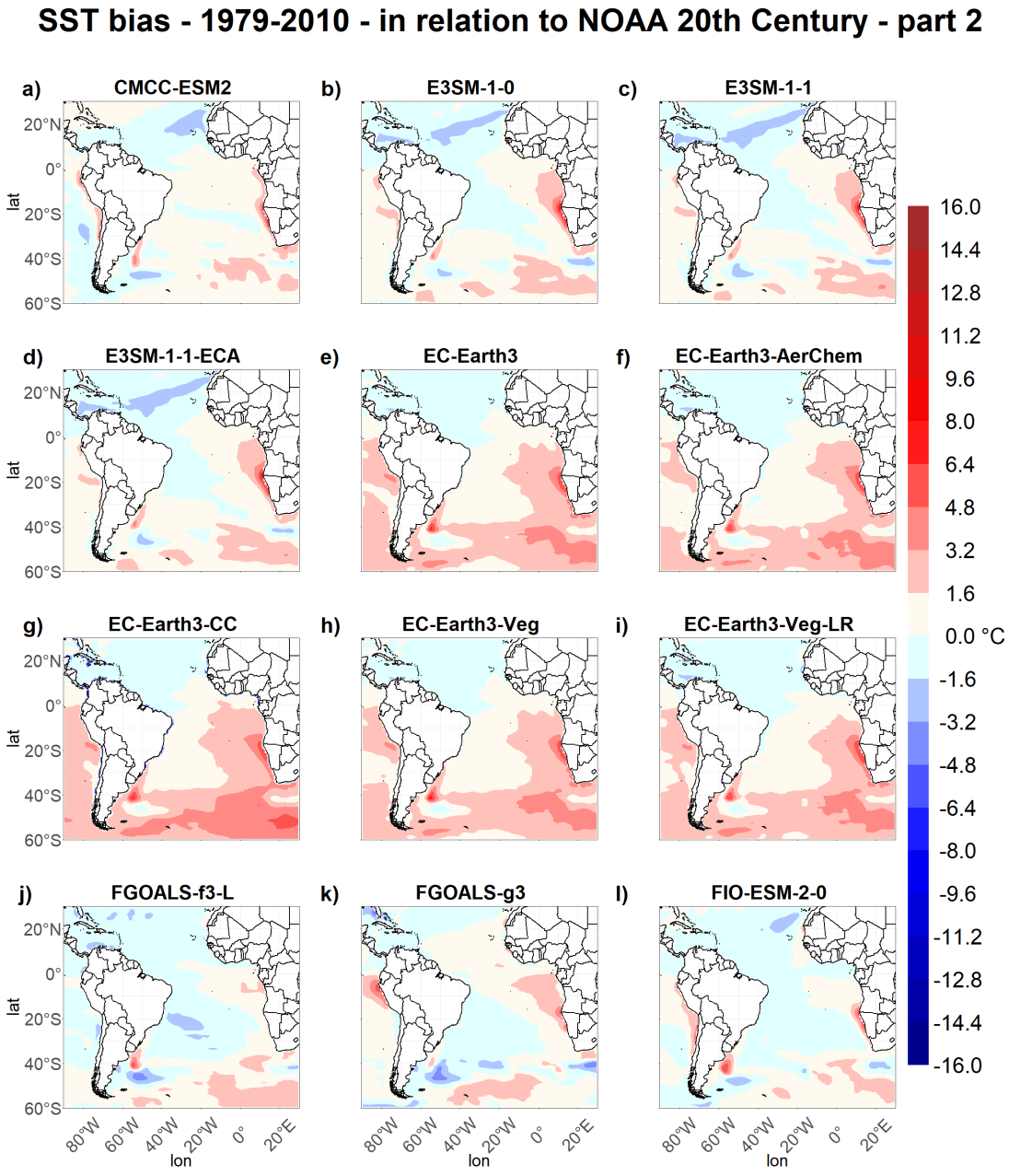

Figure E.8: The same as in Figure 3.32 except for the NOAA CIRES 20th Century reanalysis. Part 2.

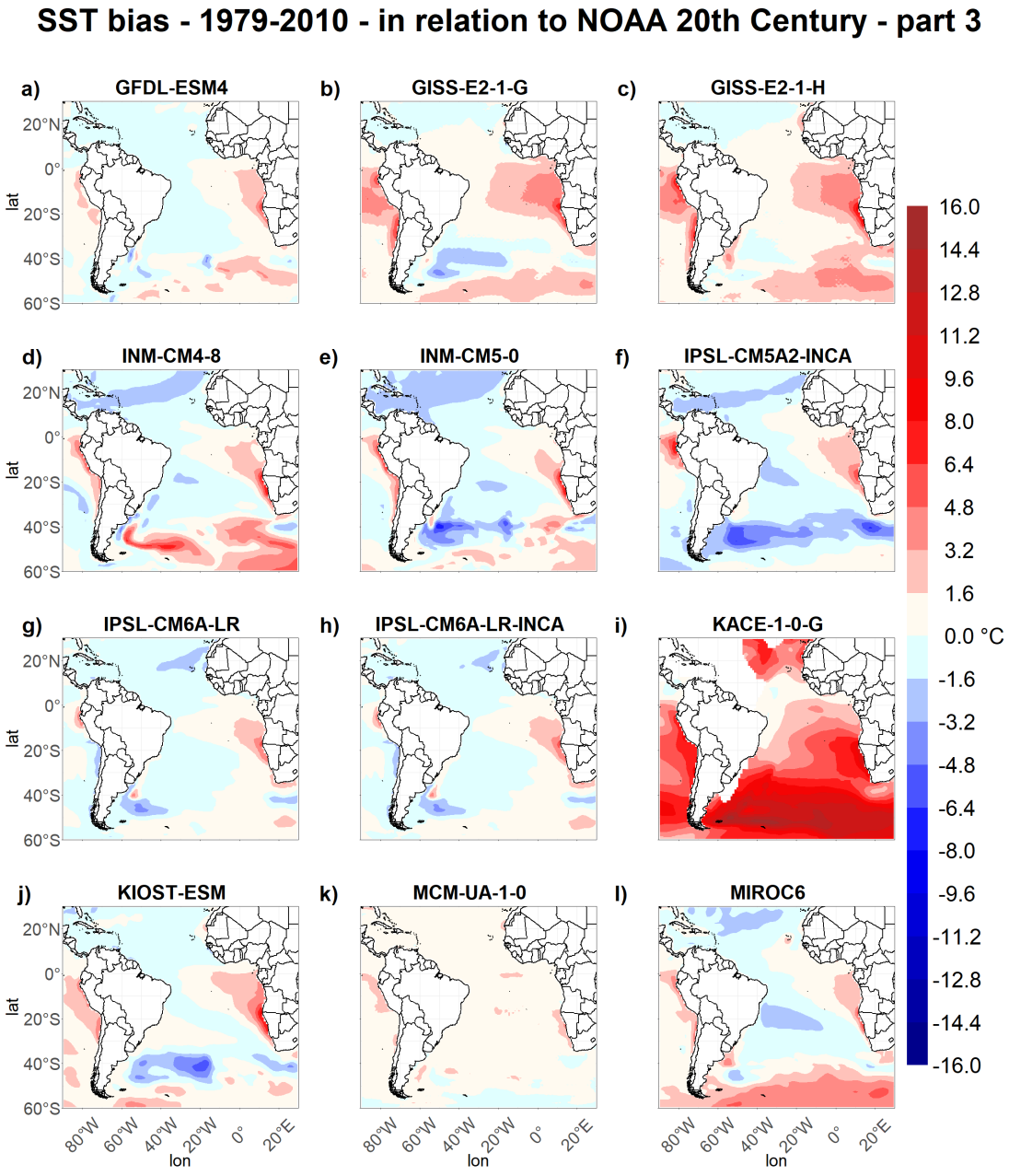

Figure E.9: The same as in Figure 3.32 except for the NOAA CIRES 20th Century reanalysis. Part 3.

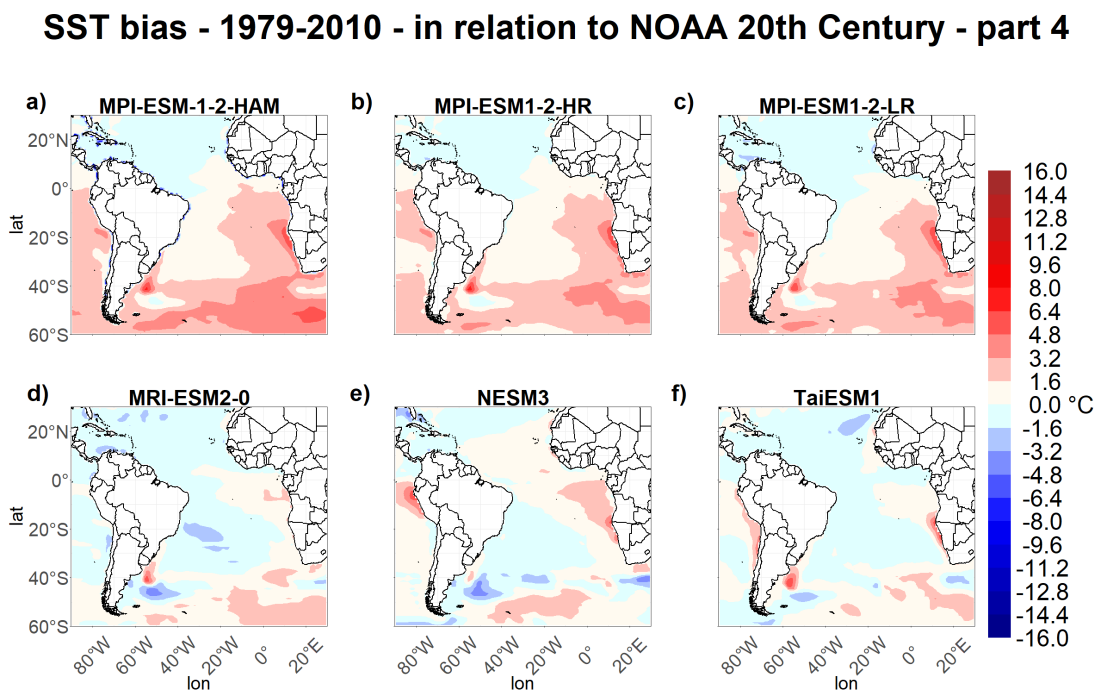

Figure E.10: The same as in Figure 3.32 except for the NOAA CIRES 20th Century reanalysis. Part 4.

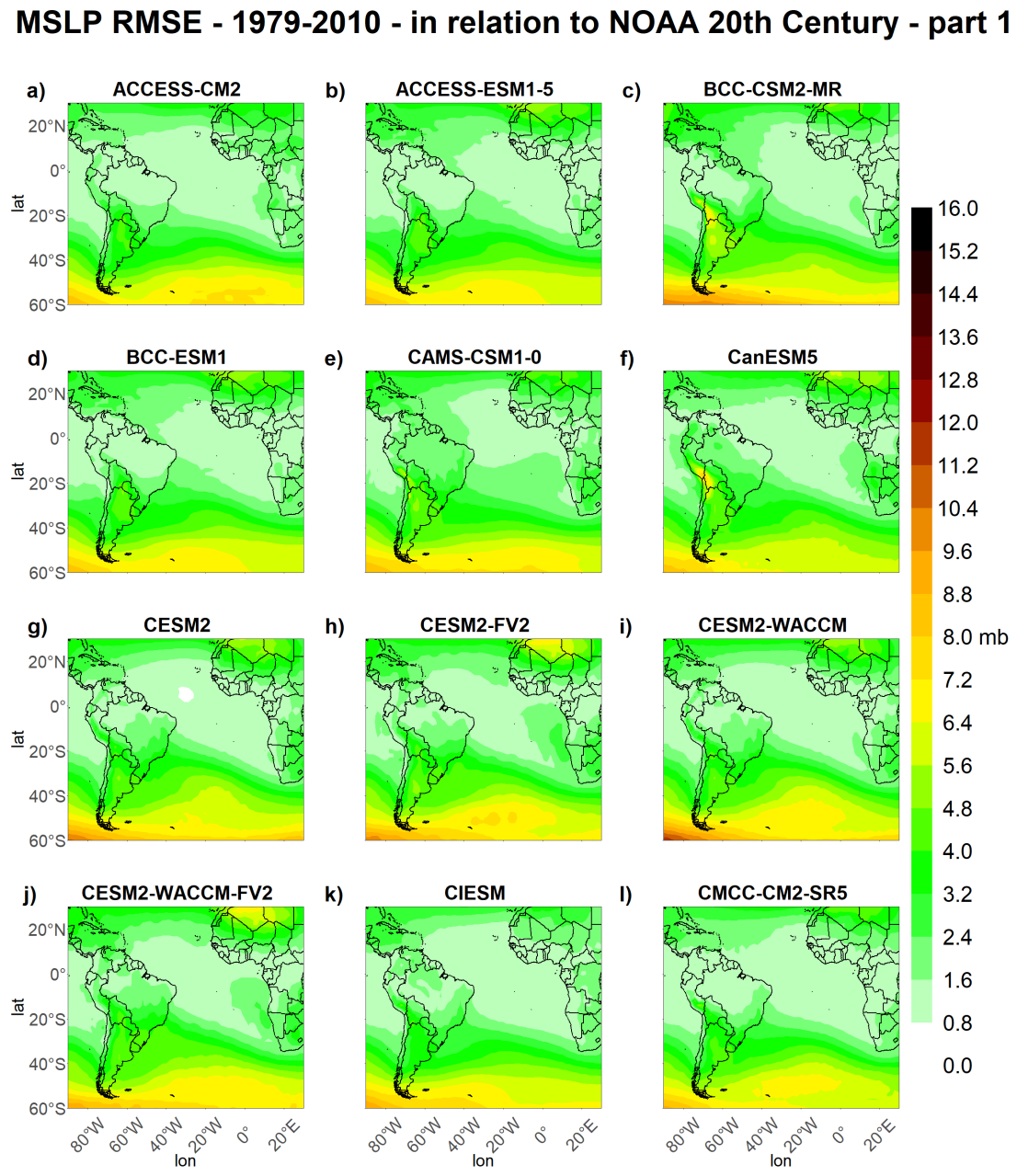

Figure E.11: The same as in Figure 3.36 except for the NOAA CIRES 20th Century reanalysis. Part 1.

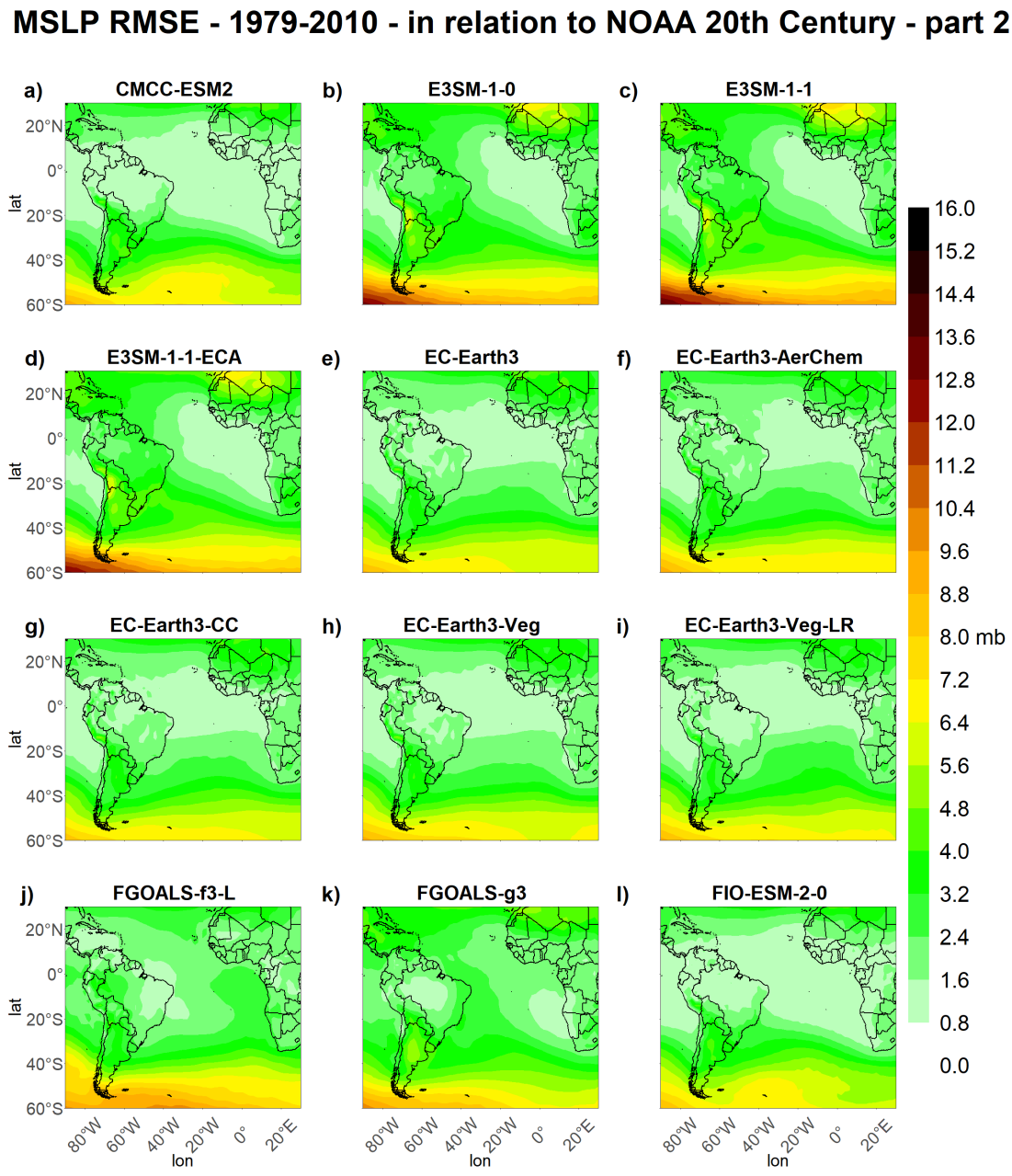

Figure E.12: The same as in Figure 3.36 except for the NOAA CIRES 20th Century reanalysis. Part 2.

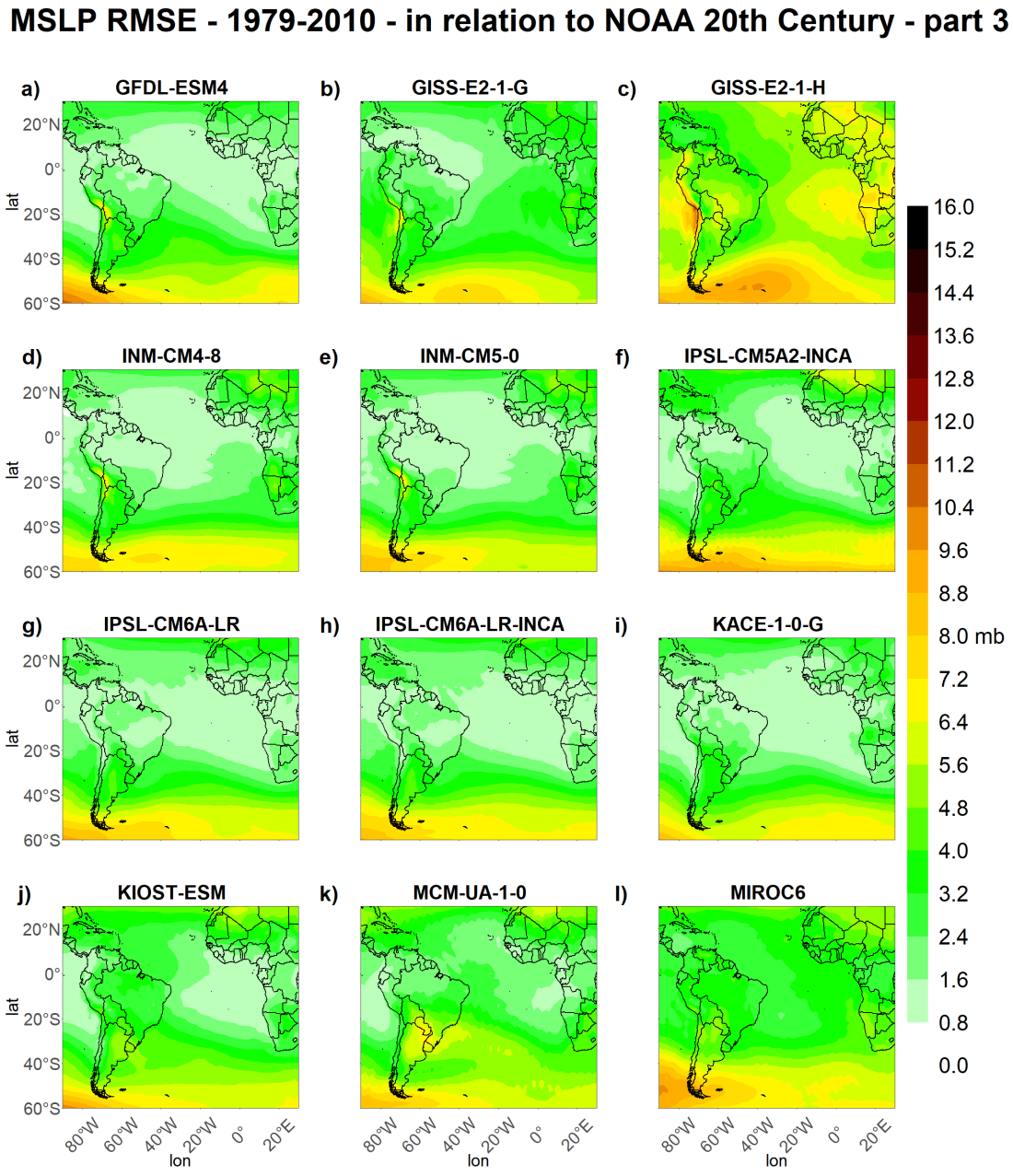

Figure E.13: The same as in Figure 3.36 except for the NOAA CIRES 20th Century reanalysis. Part 3.

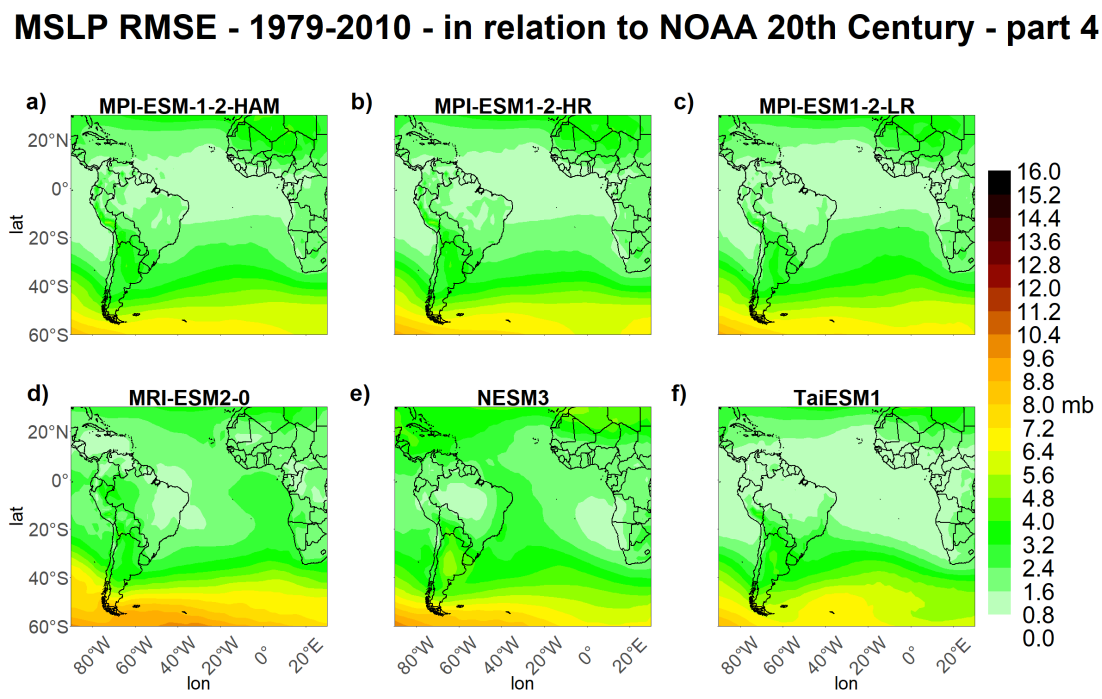

Figure E.14: The same as in Figure 3.36 except for the NOAA CIRES 20th Century reanalysis. Part 4.

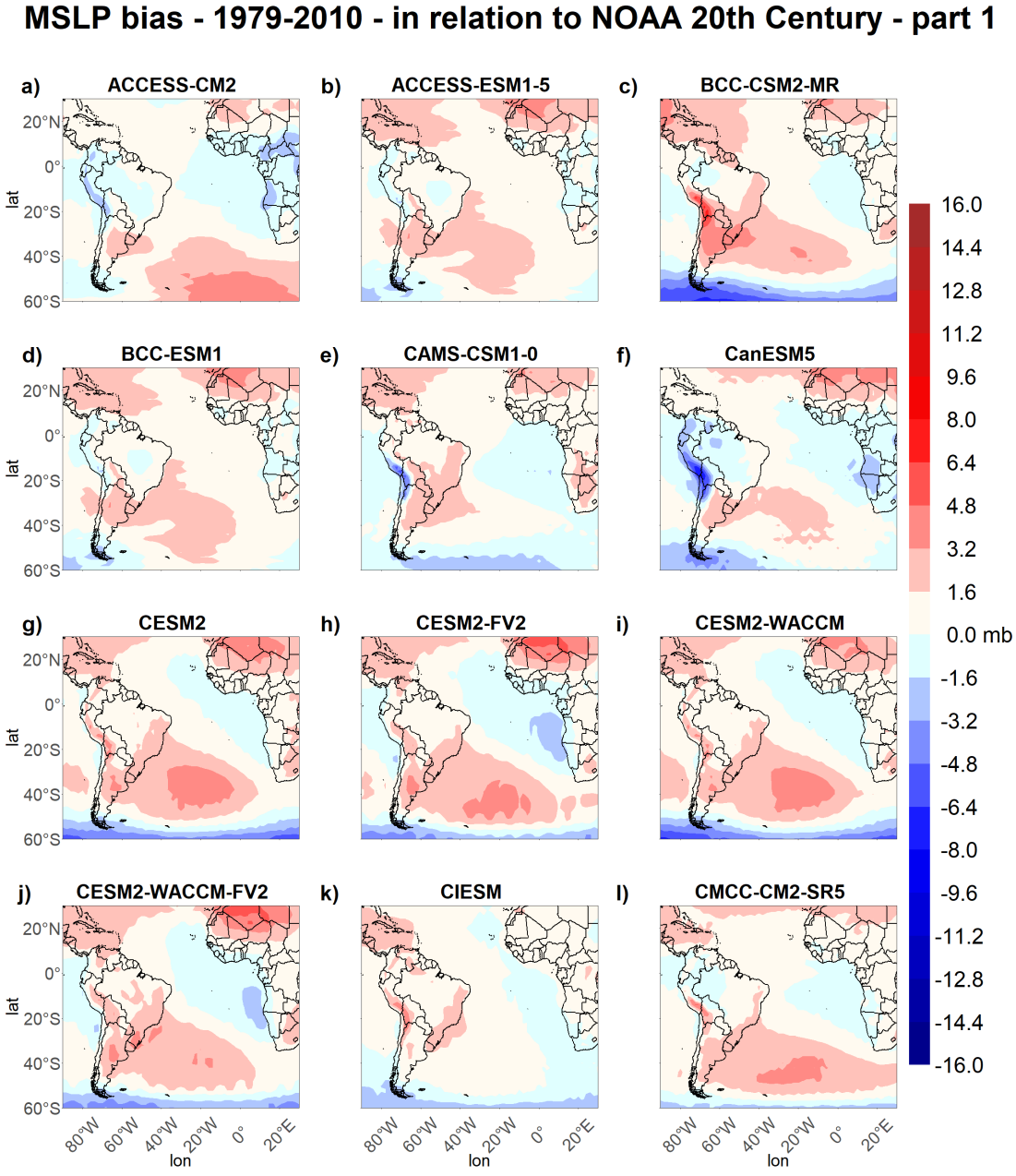

Figure E.15: The same as in Figure 3.40 except for the NOAA CIRES 20th Century reanalysis. Part 1.

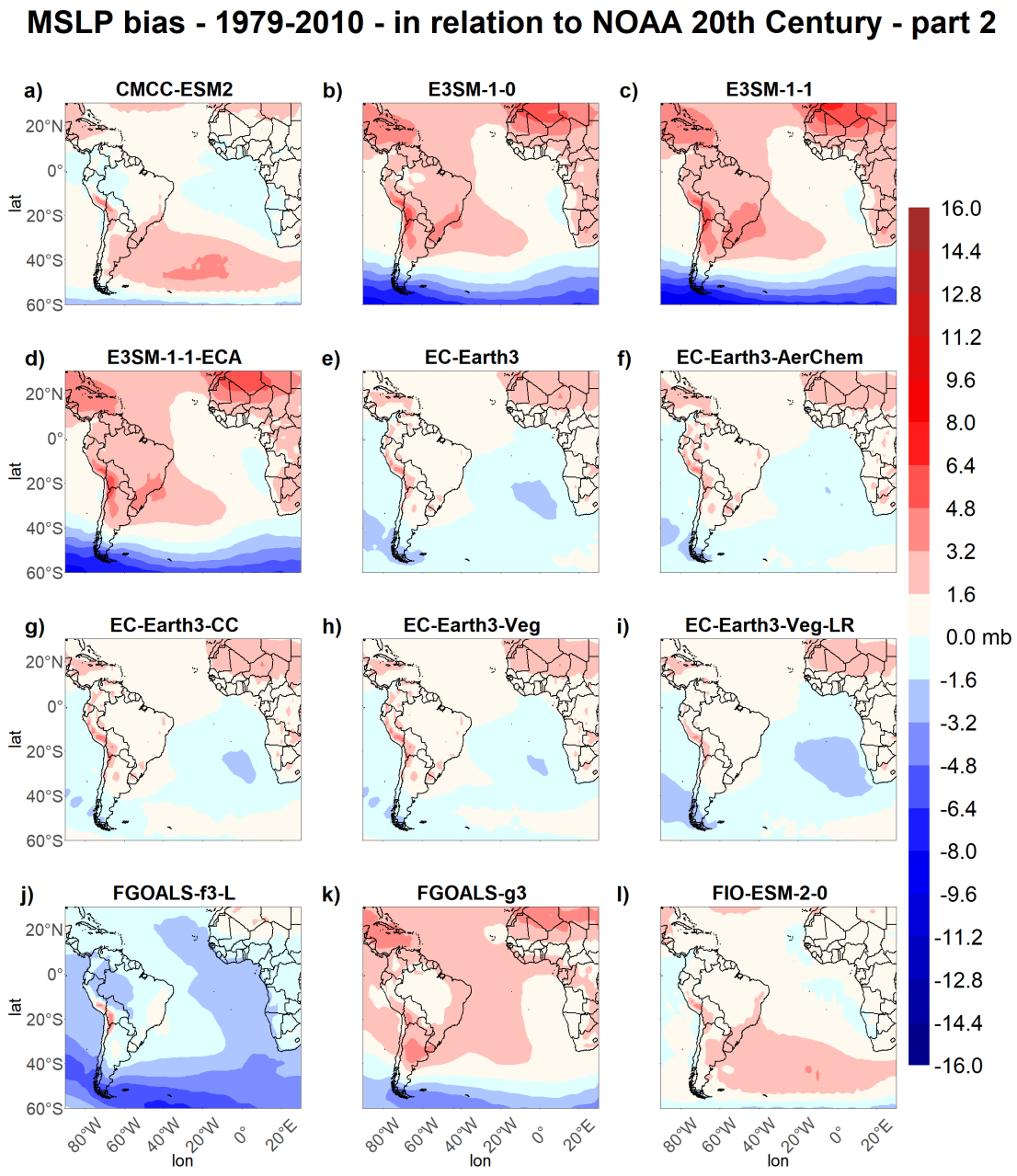

Figure E.16: The same as in Figure 3.40 except for the NOAA CIRES 20th Century reanalysis. Part 2.

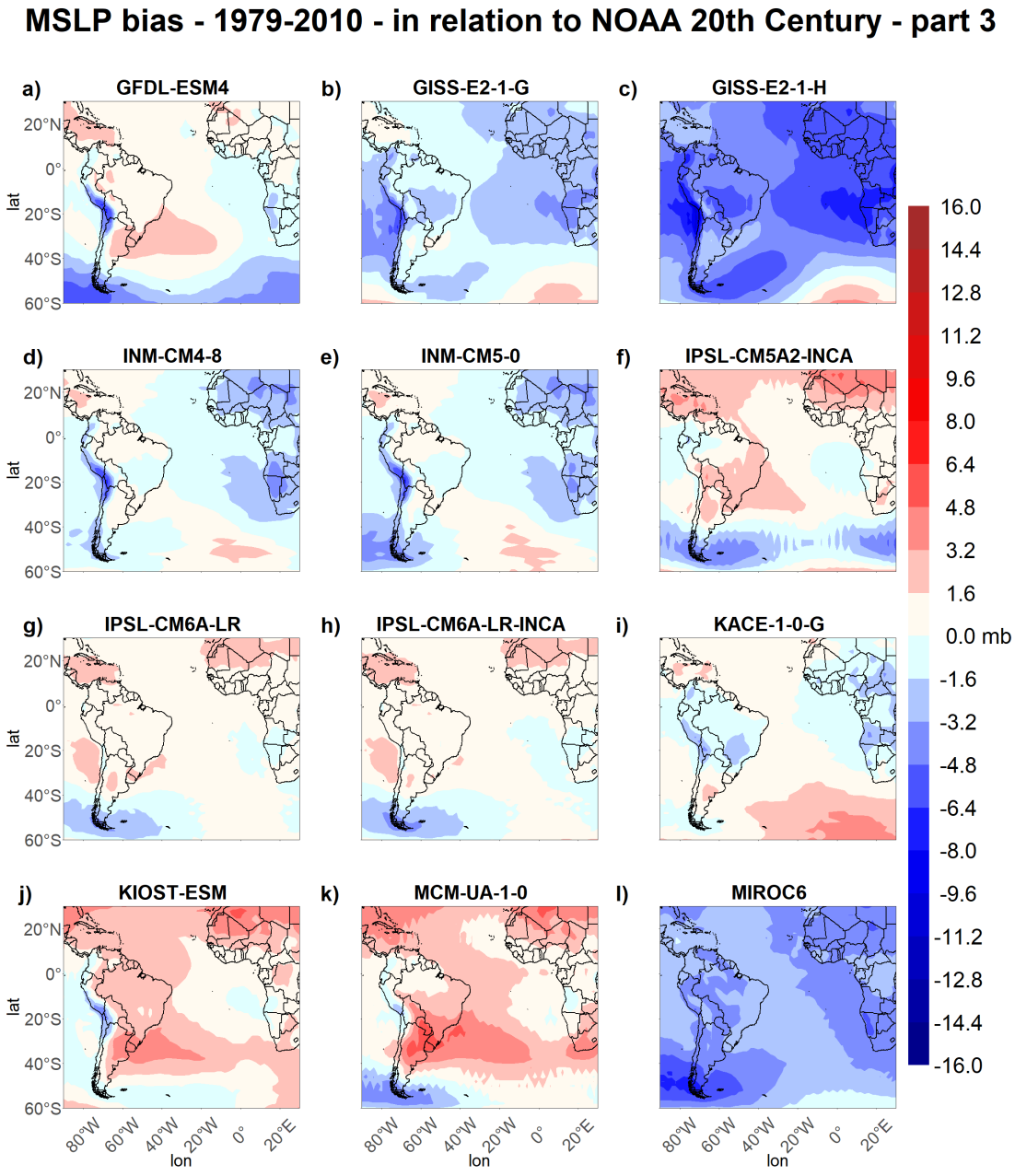

Figure E.17: The same as in Figure 3.40 except for the NOAA CIRES 20th Century reanalysis. Part 3.

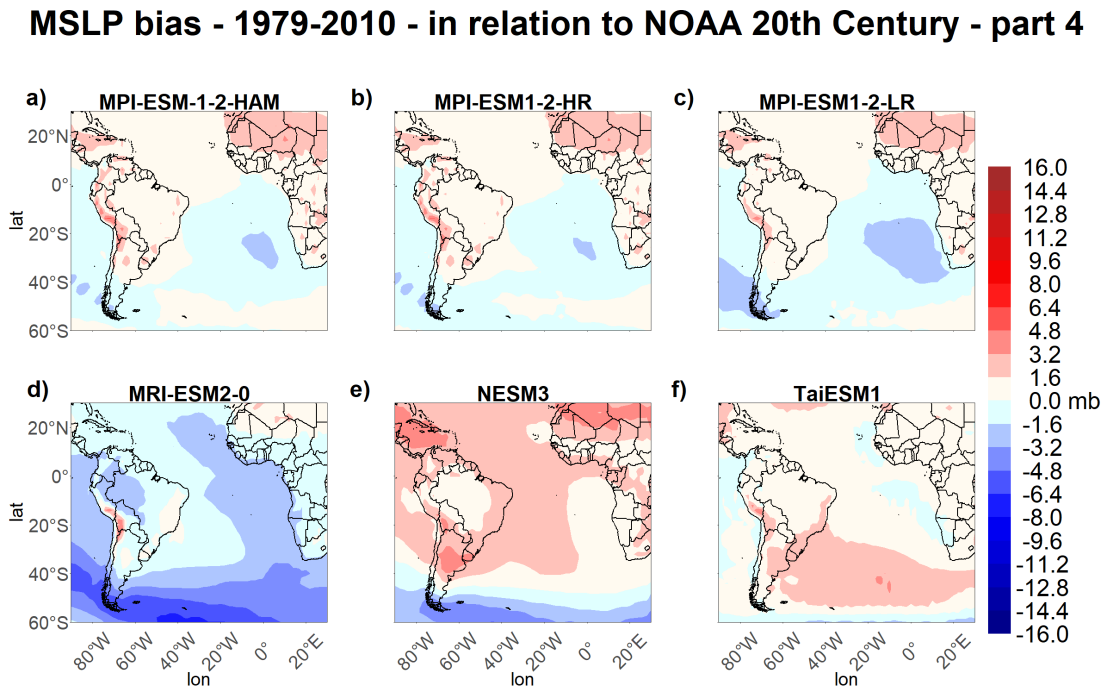

Figure E.18: The same as in Figure 3.40 except for the NOAA CIRES 20th Century reanalysis. Part 4.

E.2 ERA-20C

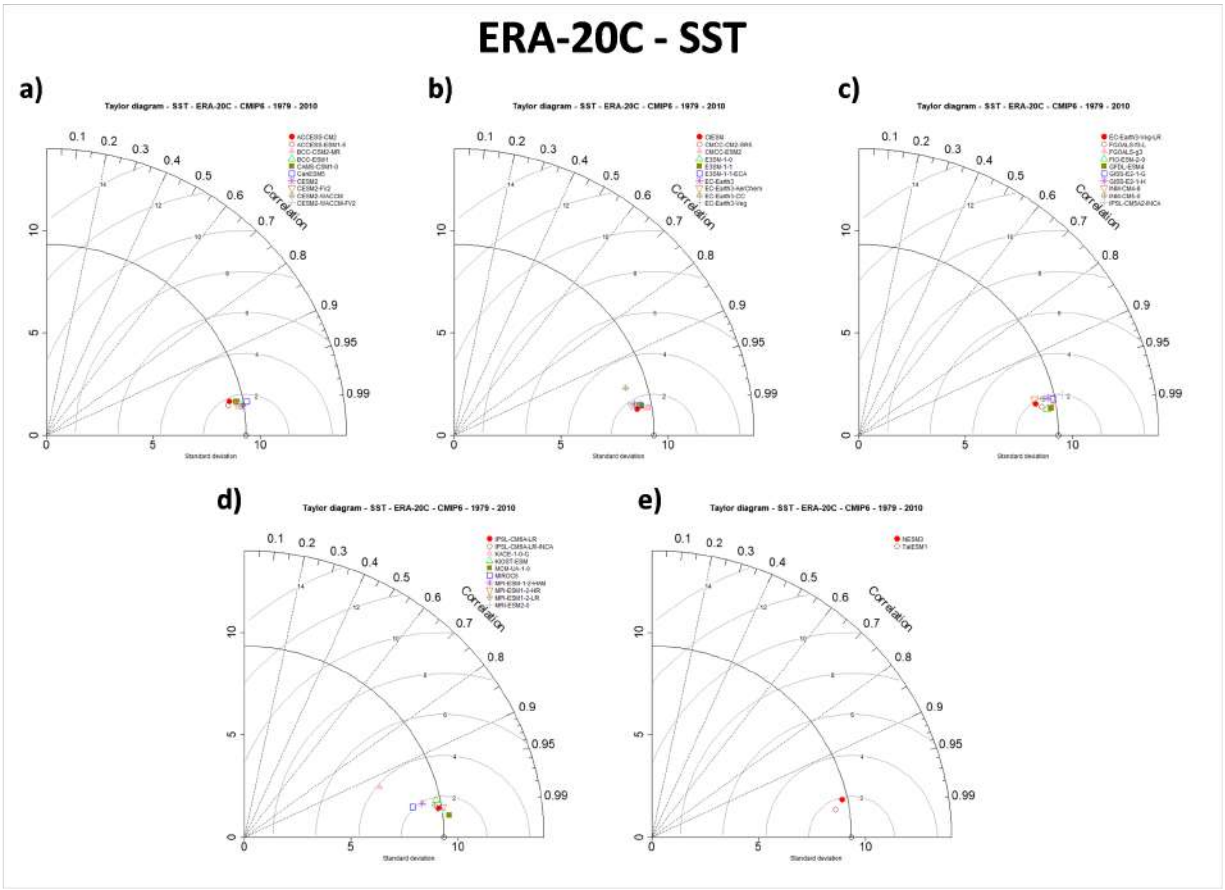

Figure E.19: The same as in Figure 3.26 except for the ERA-20C reanalysis.

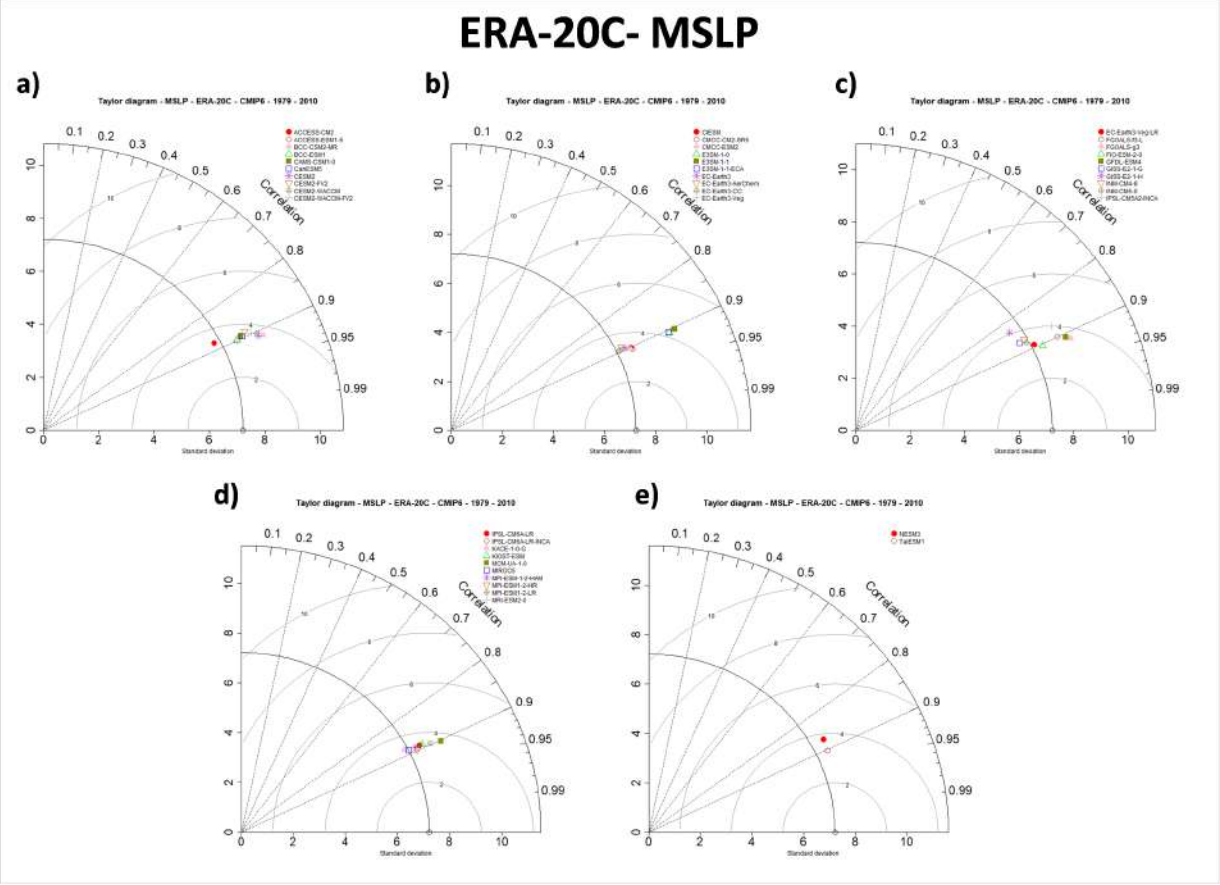

Figure E.20: The same as in Figure 3.27 except for the ERA-20C reanalysis.

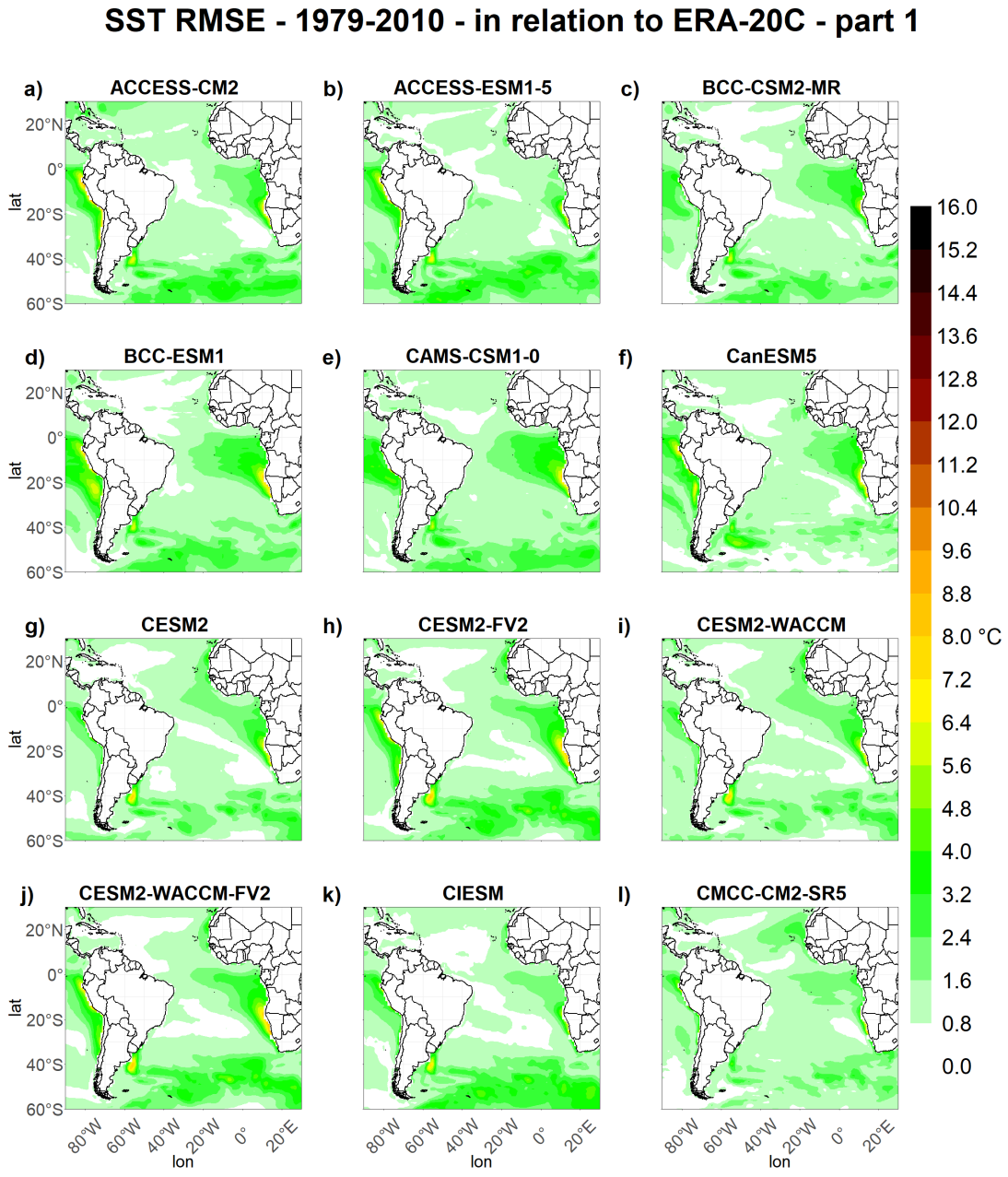

Figure E.21: The same as in Figure 3.28 except for the ERA-20C reanalysis. Part 1.

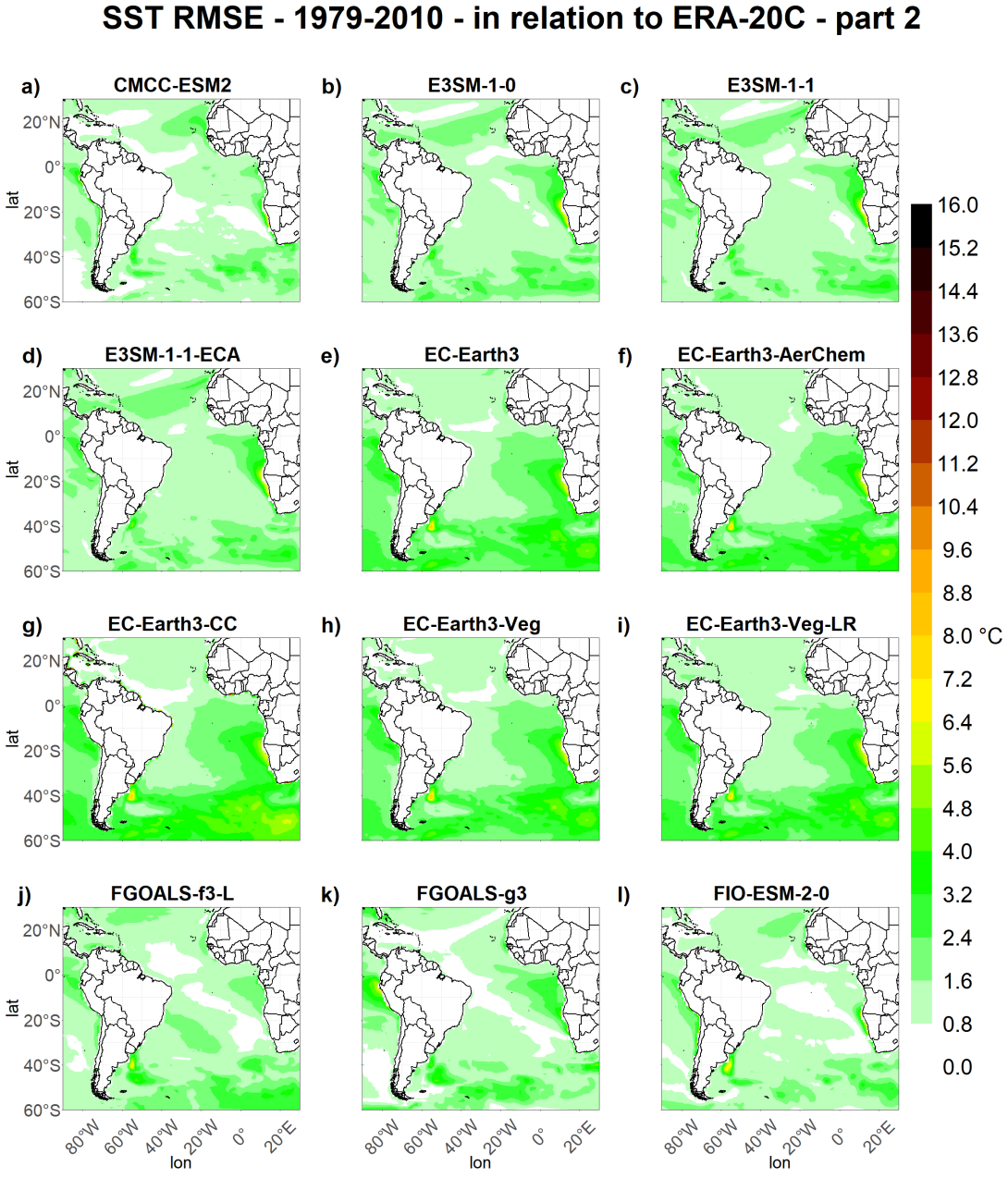

Figure E.22: The same as in Figure 3.28 except for the ERA-20C reanalysis. Part 2.

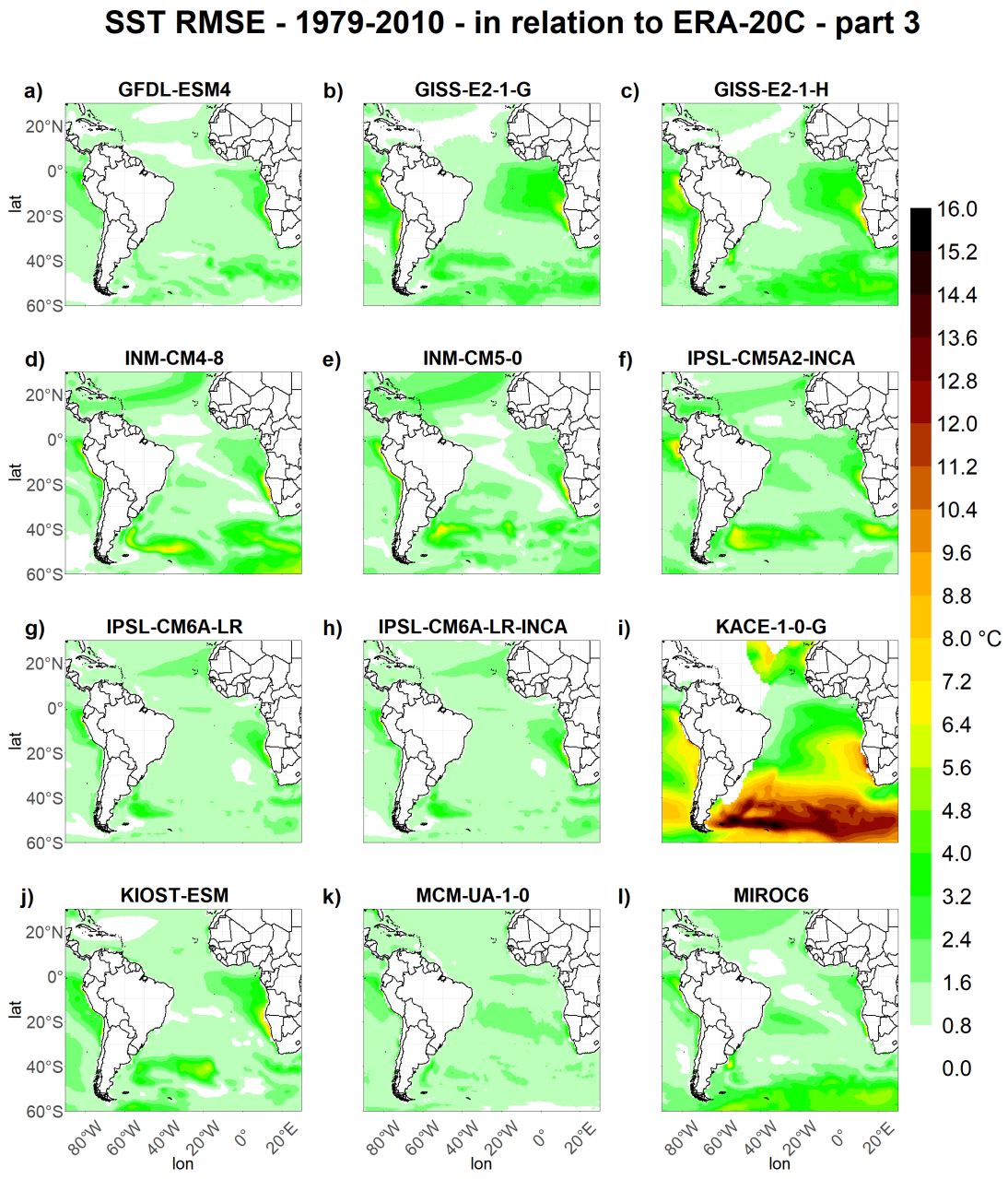

Figure E.23: The same as in Figure 3.28 except for the ERA-20C reanalysis. Part 3.

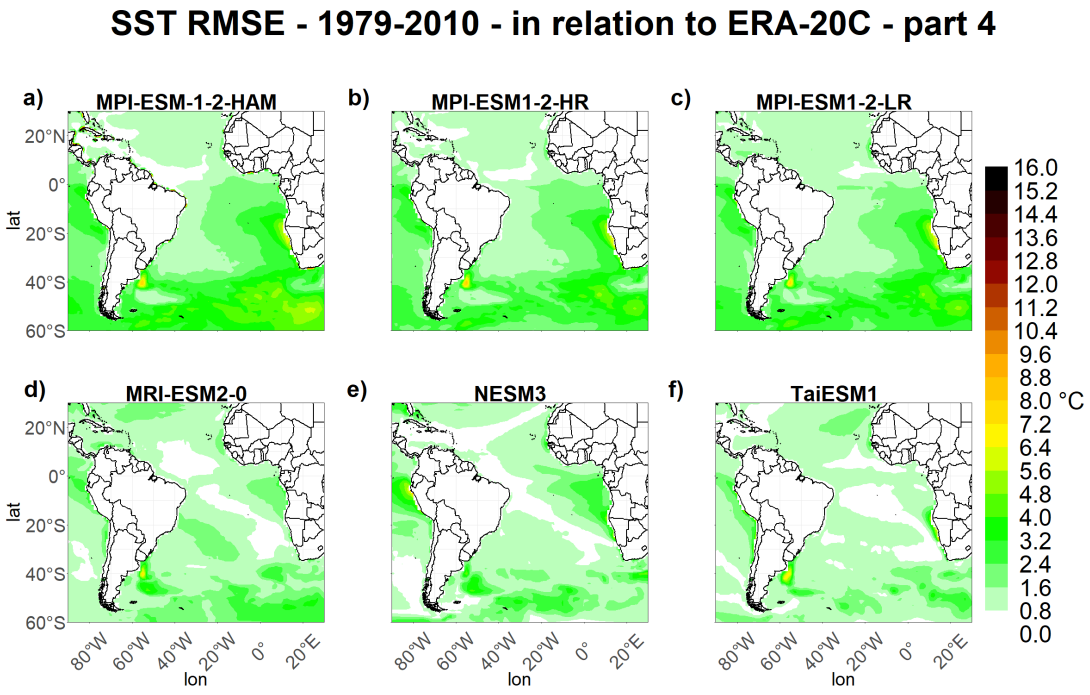

Figure E.24: The same as in Figure 3.28 except for the ERA-20C reanalysis. Part 4.

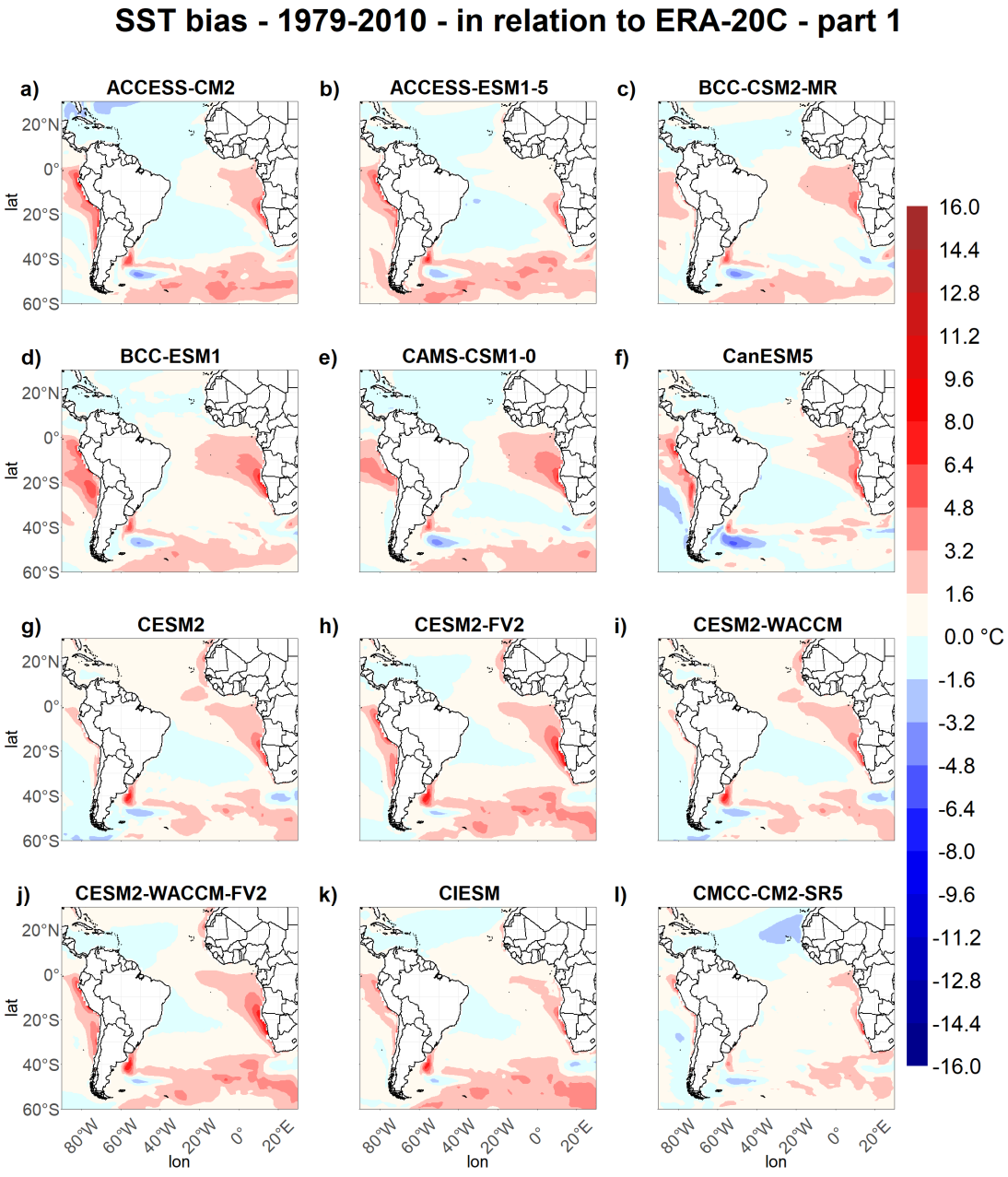

Figure E.25: The same as in Figure 3.32 except for the ERA-20C reanalysis. Part 1.

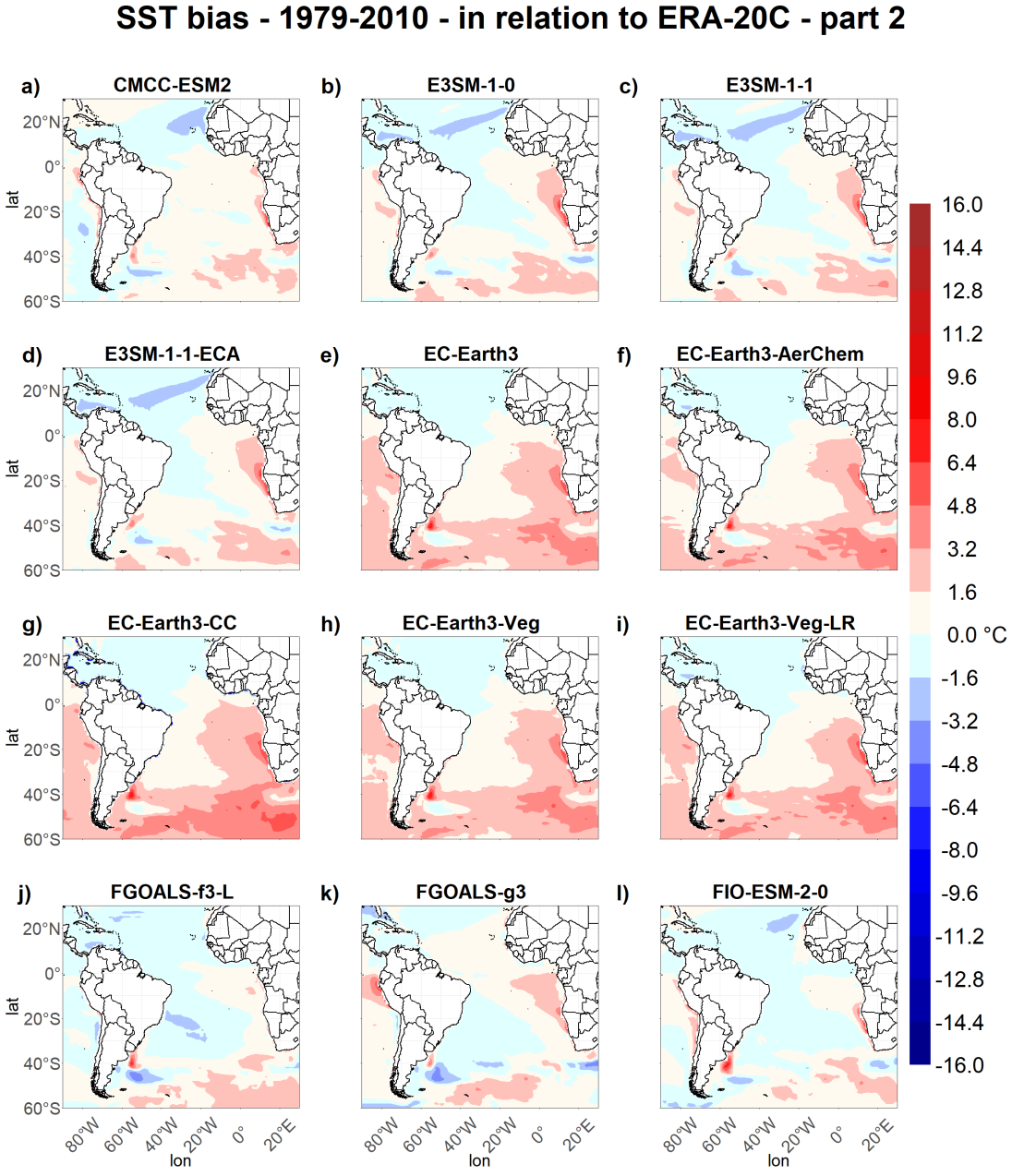

Figure E.26: The same as in Figure 3.32 except for the ERA-20C reanalysis. Part 2.

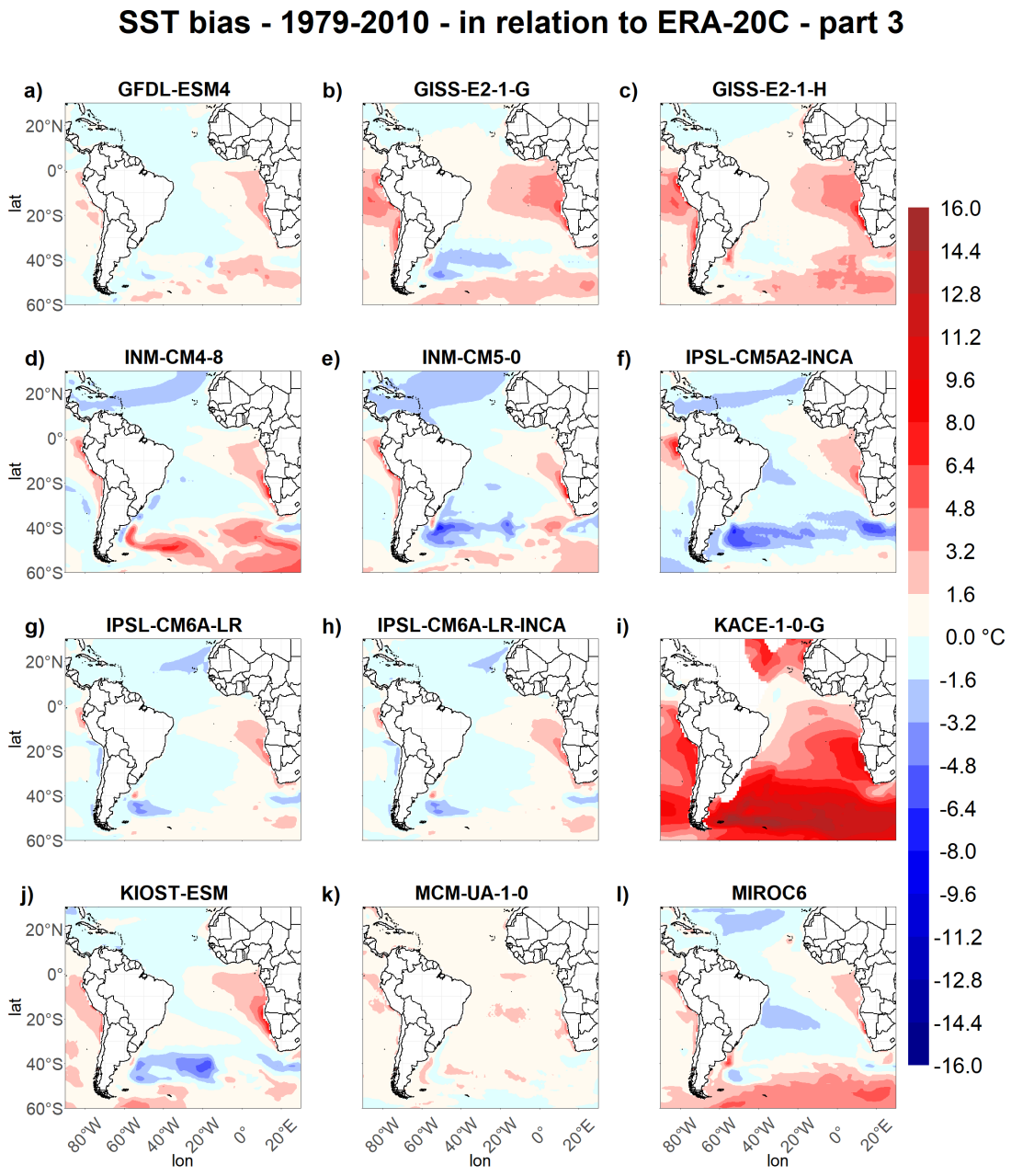

Figure E.27: The same as in Figure 3.32 except for the ERA-20C reanalysis. Part 3.

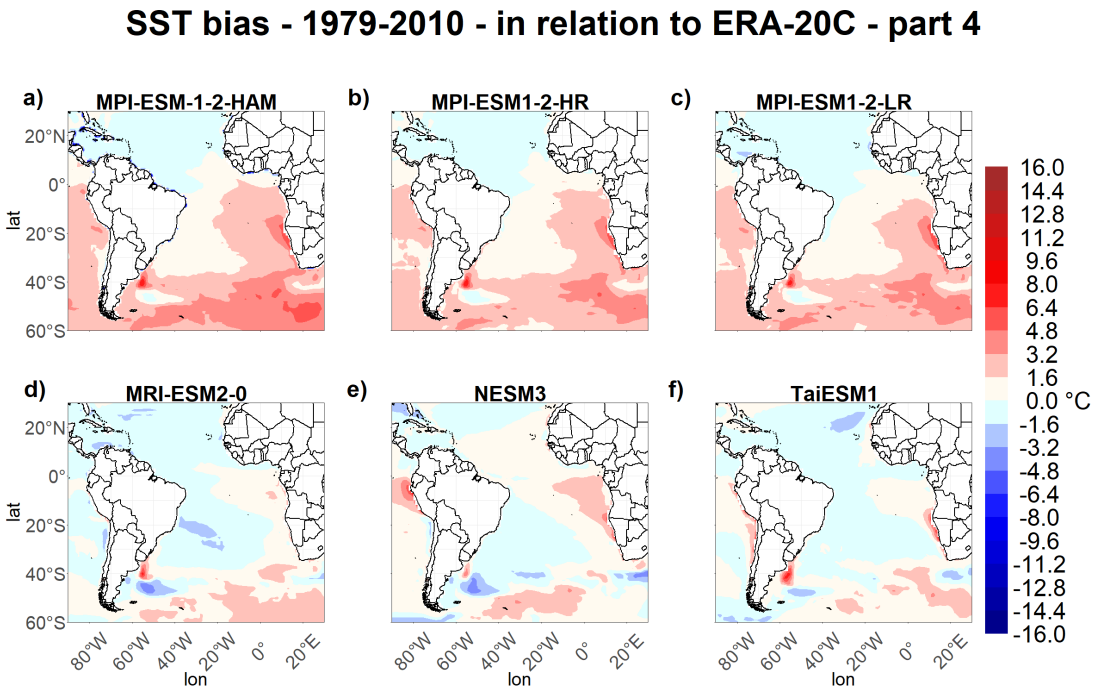

Figure E.28: The same as in Figure 3.32 except for the ERA-20C reanalysis. Part 4.

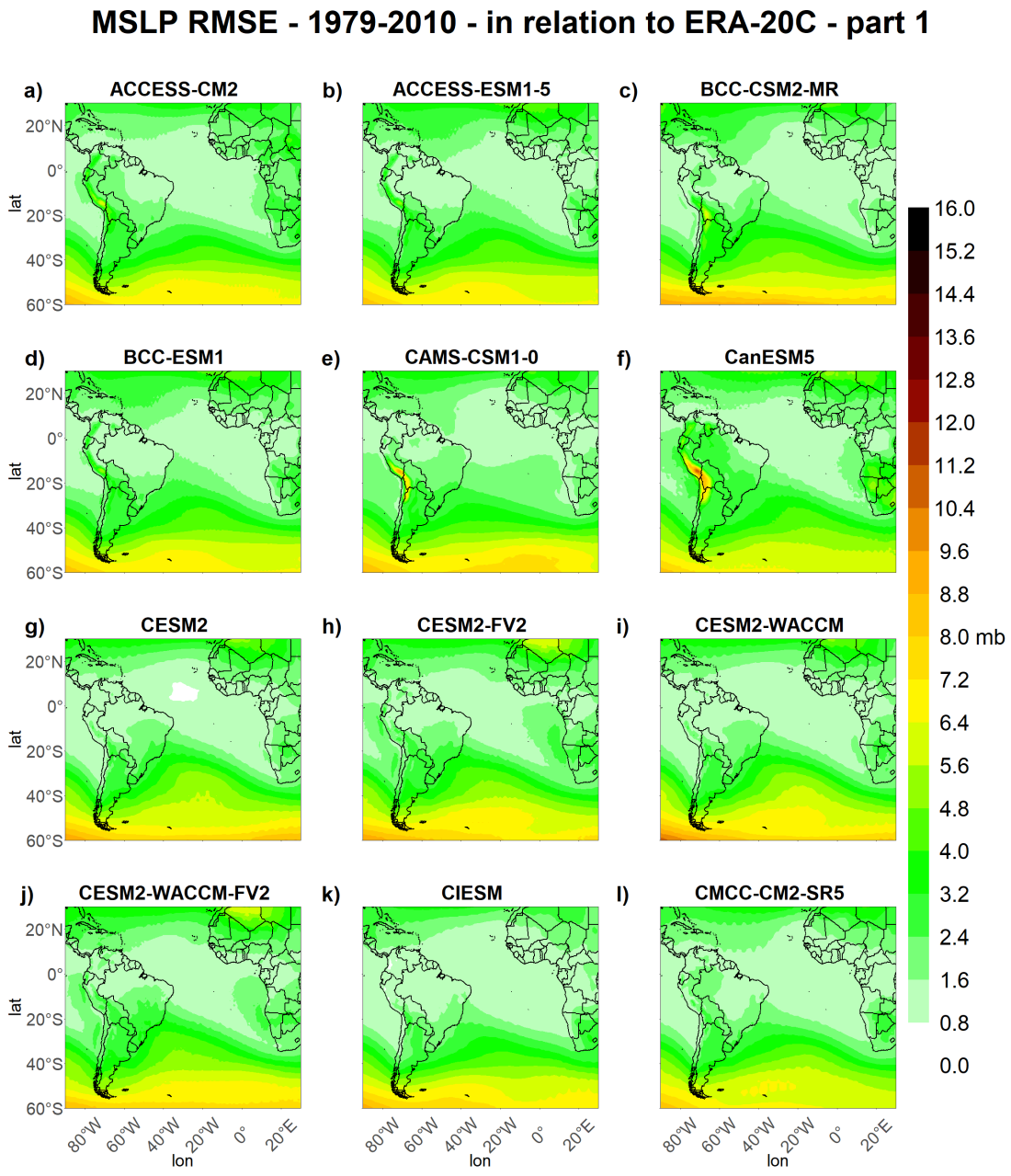

Figure E.29: The same as in Figure 3.36 except for the ERA-20C reanalysis. Part 1.

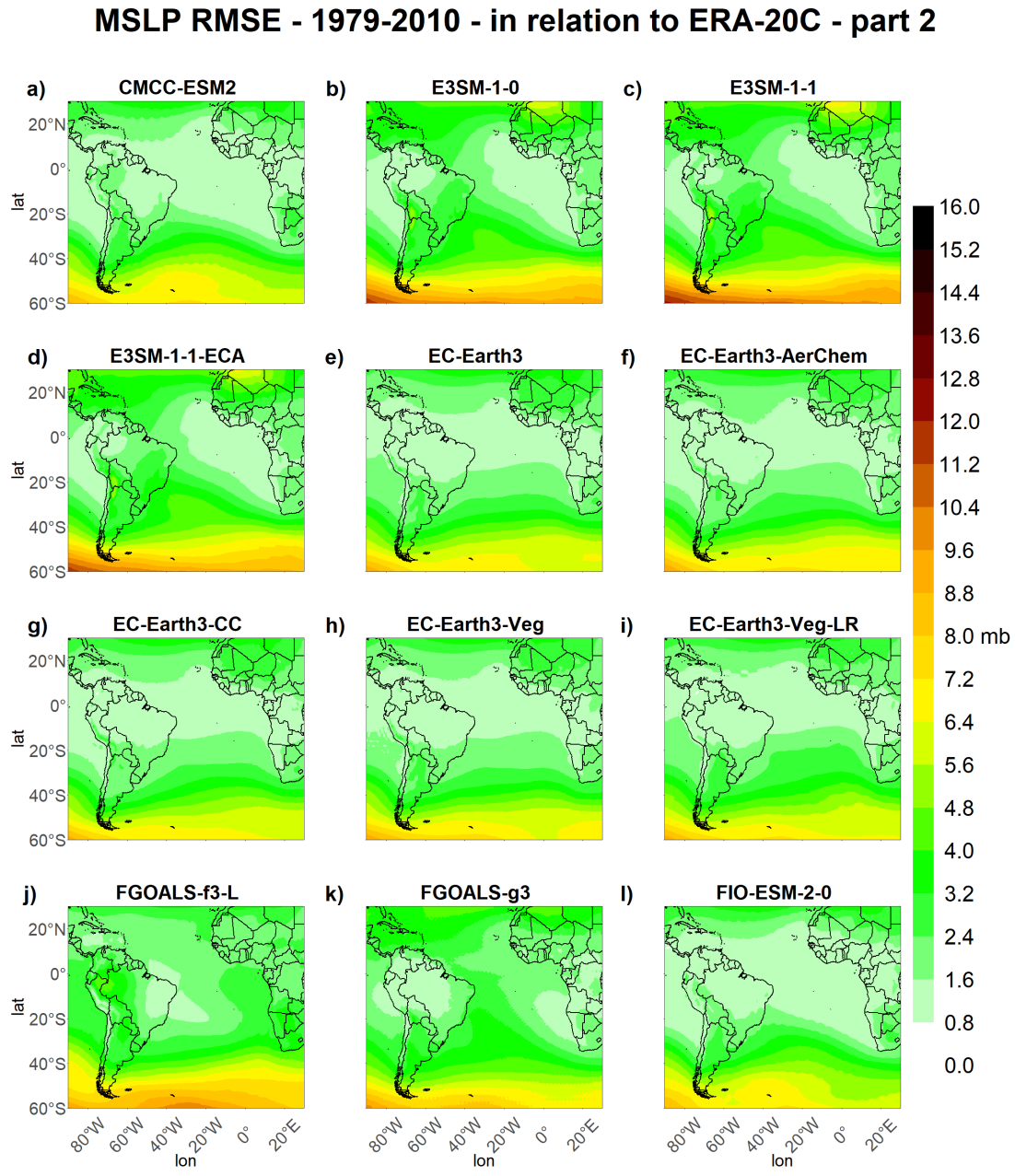

Figure E.30: The same as in Figure 3.36 except for the ERA-20C reanalysis. Part 2.

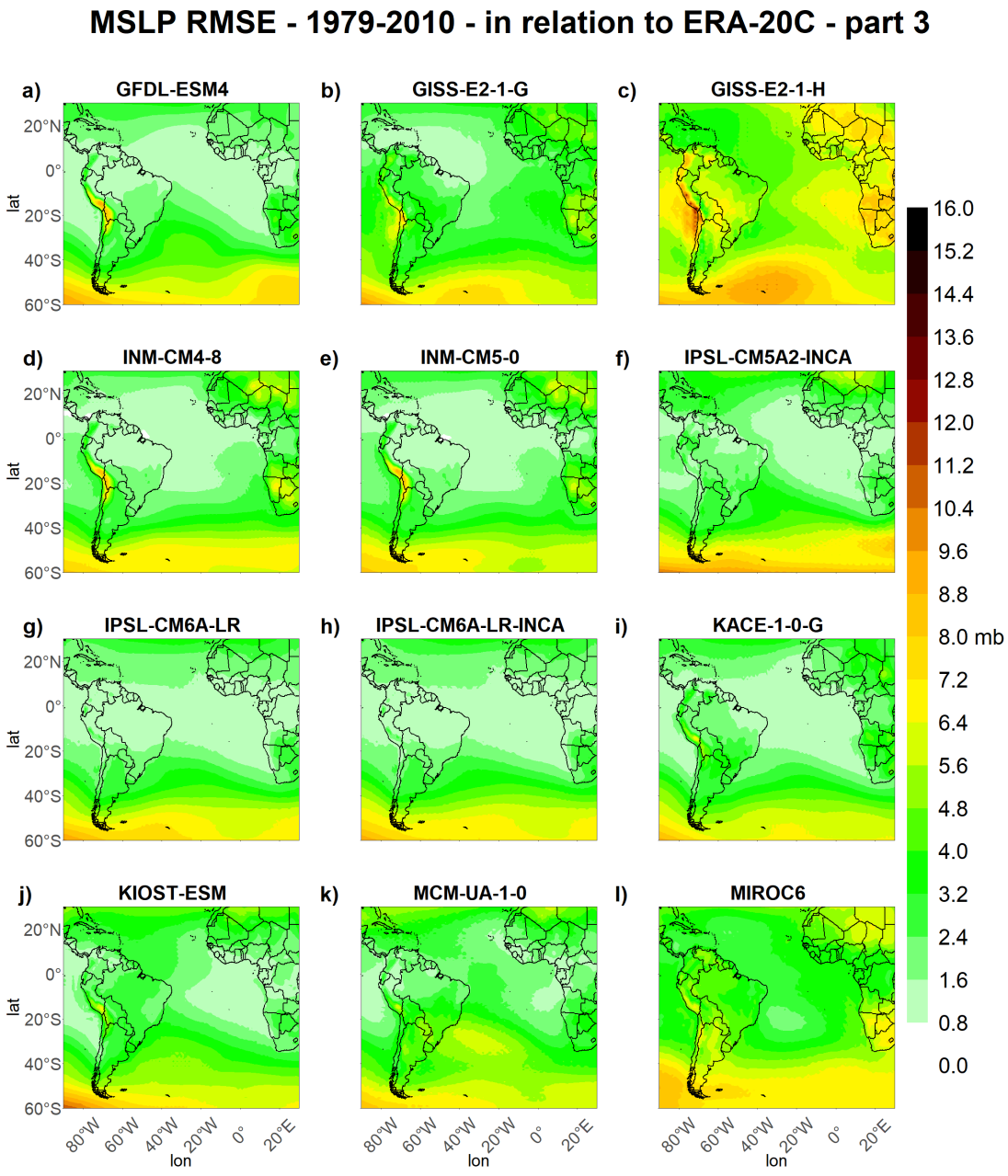

Figure E.31: The same as in Figure 3.36 except for the ERA-20C reanalysis. Part 3.

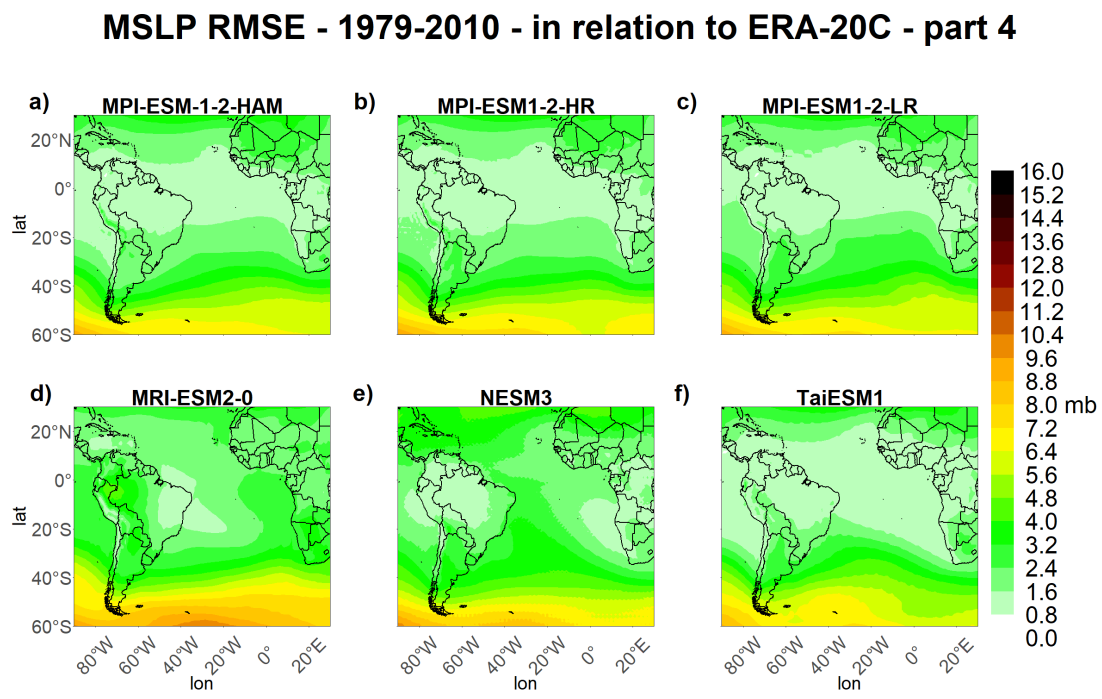

Figure E.32: The same as in Figure 3.36 except for the ERA-20C reanalysis. Part 4.

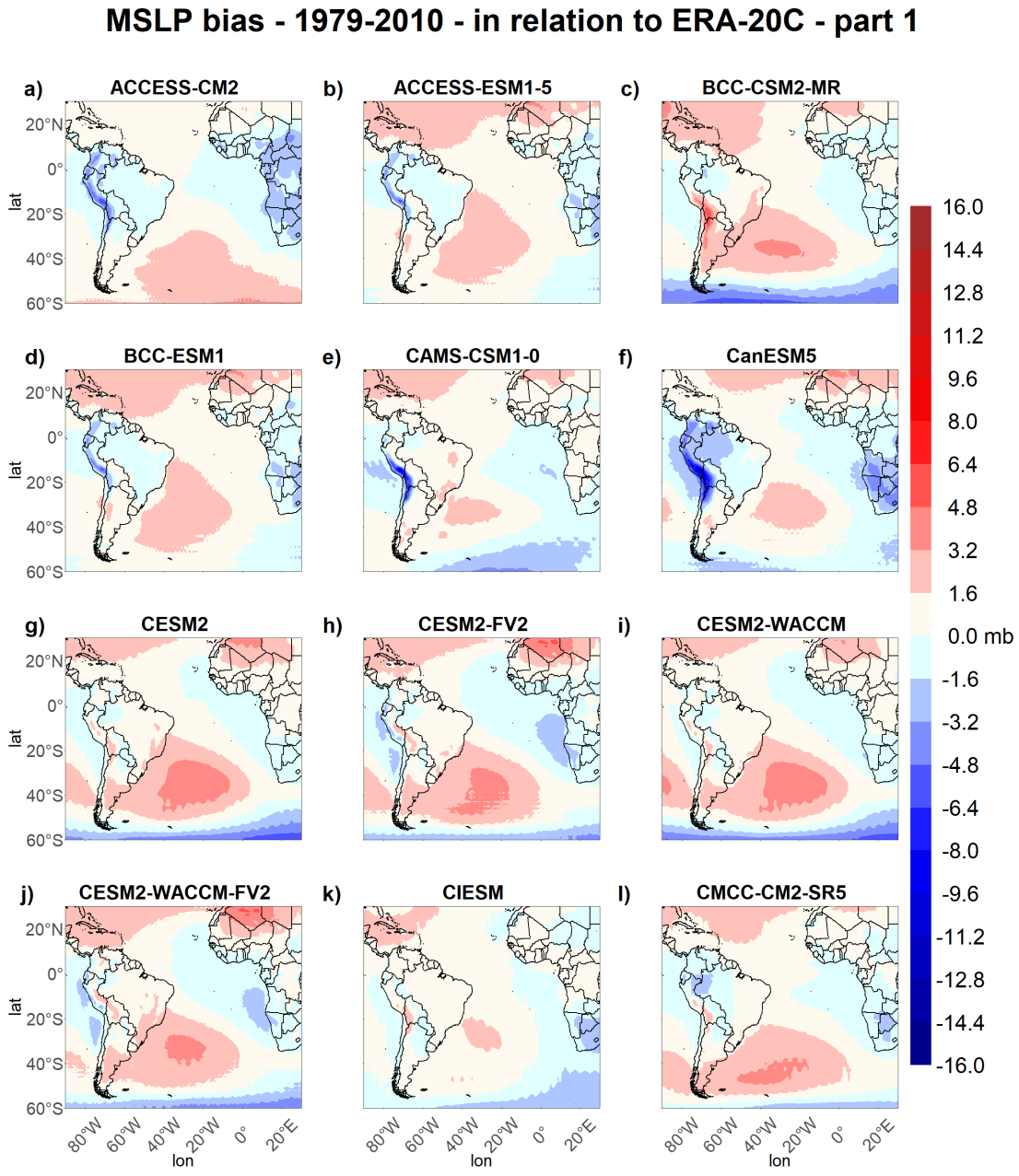

Figure E.33: The same as in Figure 3.40 except for the ERA-20C reanalysis. Part 1.

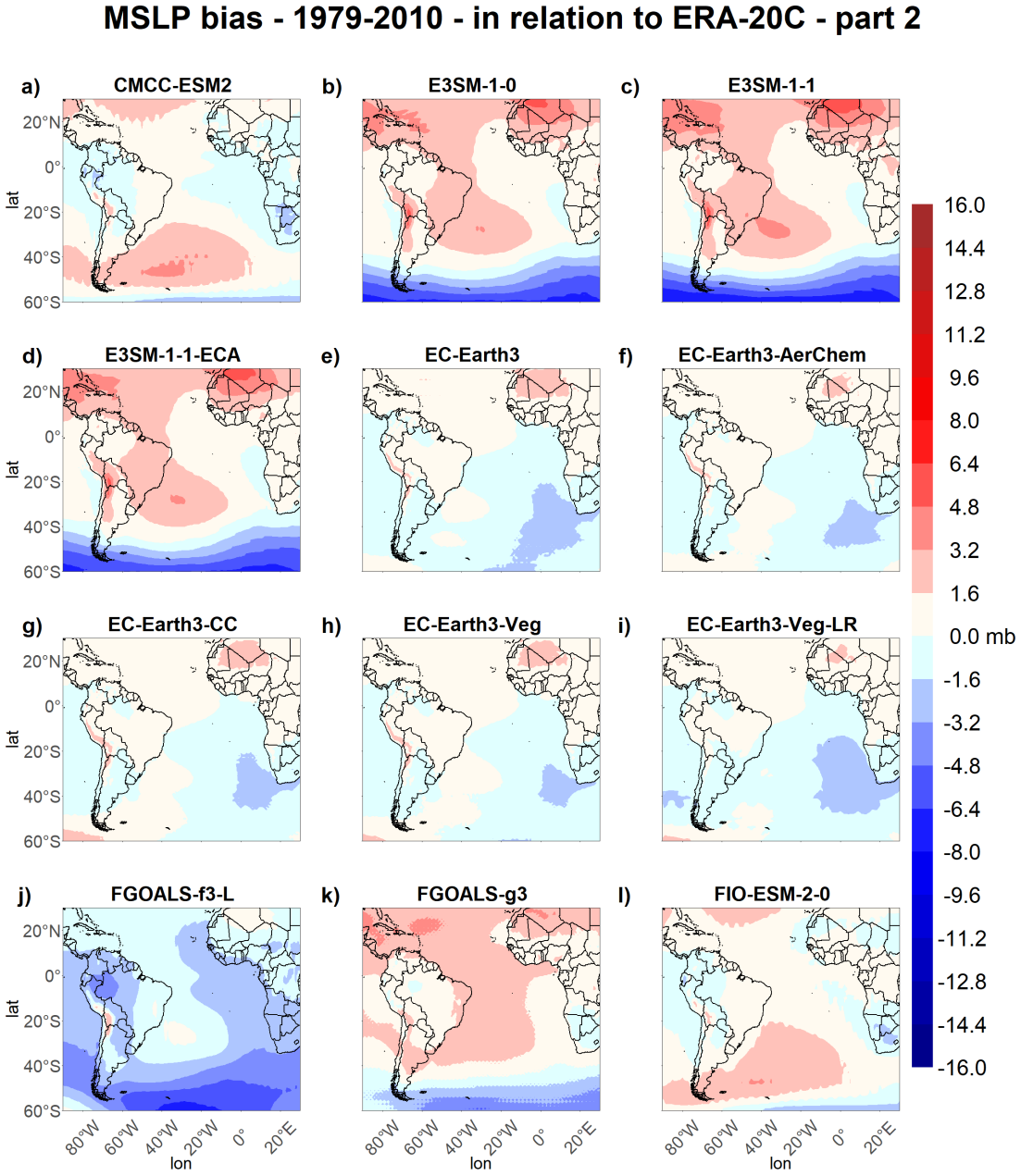

Figure E.34: The same as in Figure 3.40 except for the ERA-20C reanalysis. Part 2.

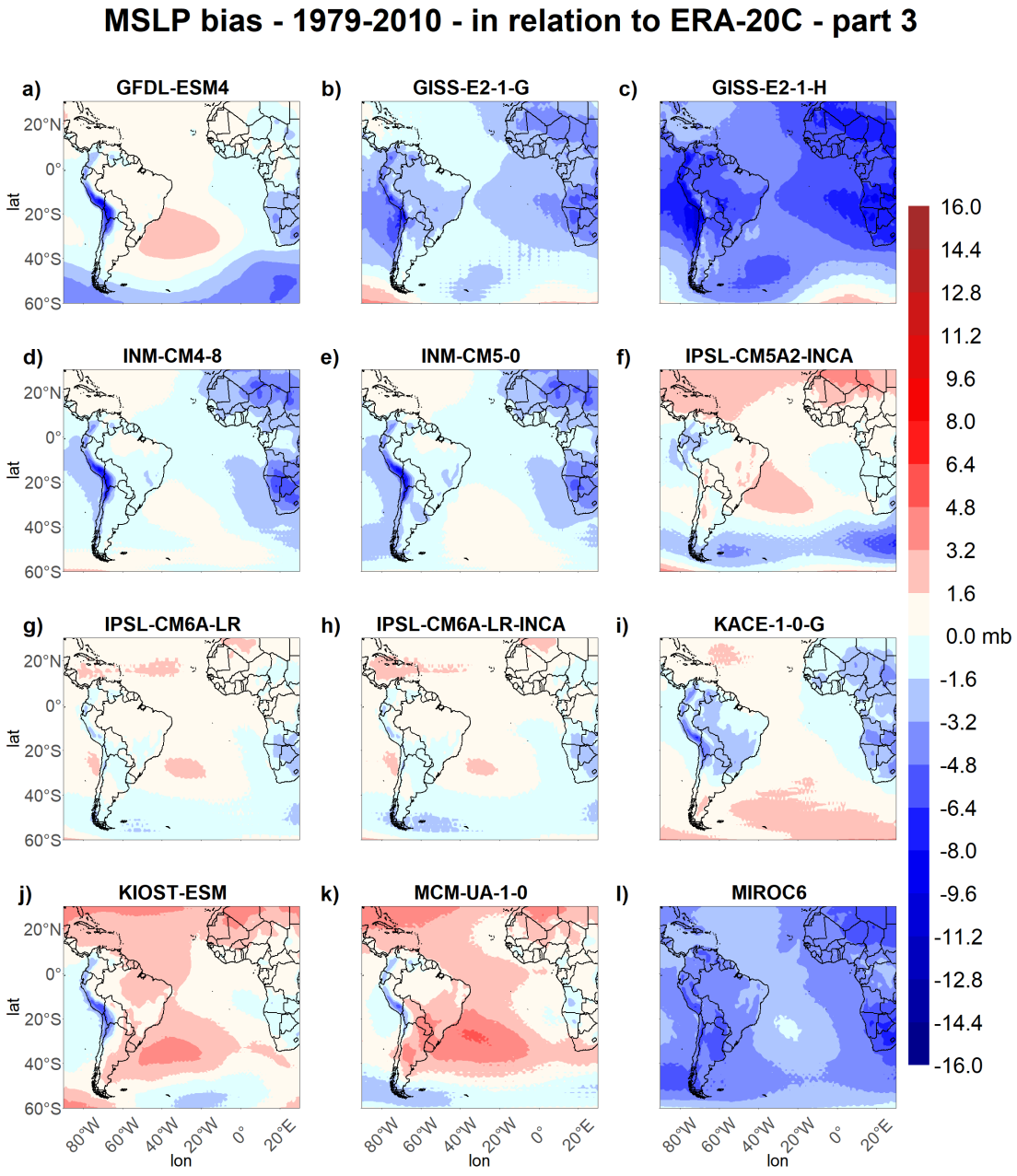

Figure E.35: The same as in Figure 3.40 except for the ERA-20C reanalysis. Part 3.

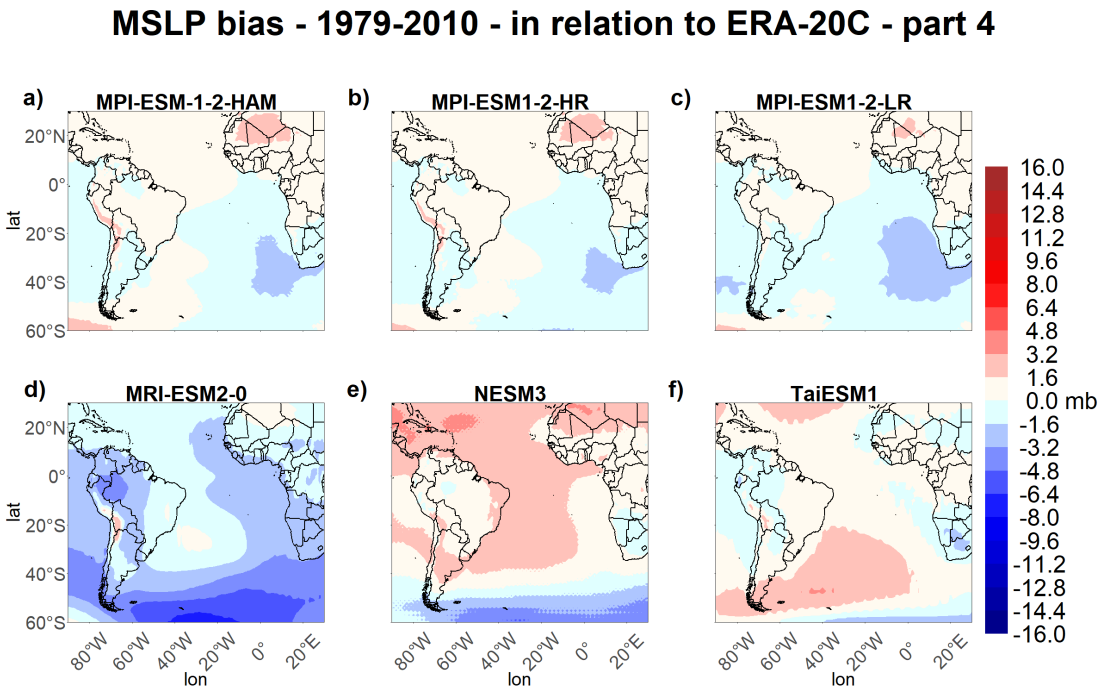

Figure E.36: The same as in Figure 3.40 except for the ERA-20C reanalysis. Part 4.

Appendix F

The South Atlantic Dipole representation by the CMIP6 Historical Simulations of the selected models - CMCC-ESM2 and CMCC-CM2-SR5

F.1 CMCC-ESM2

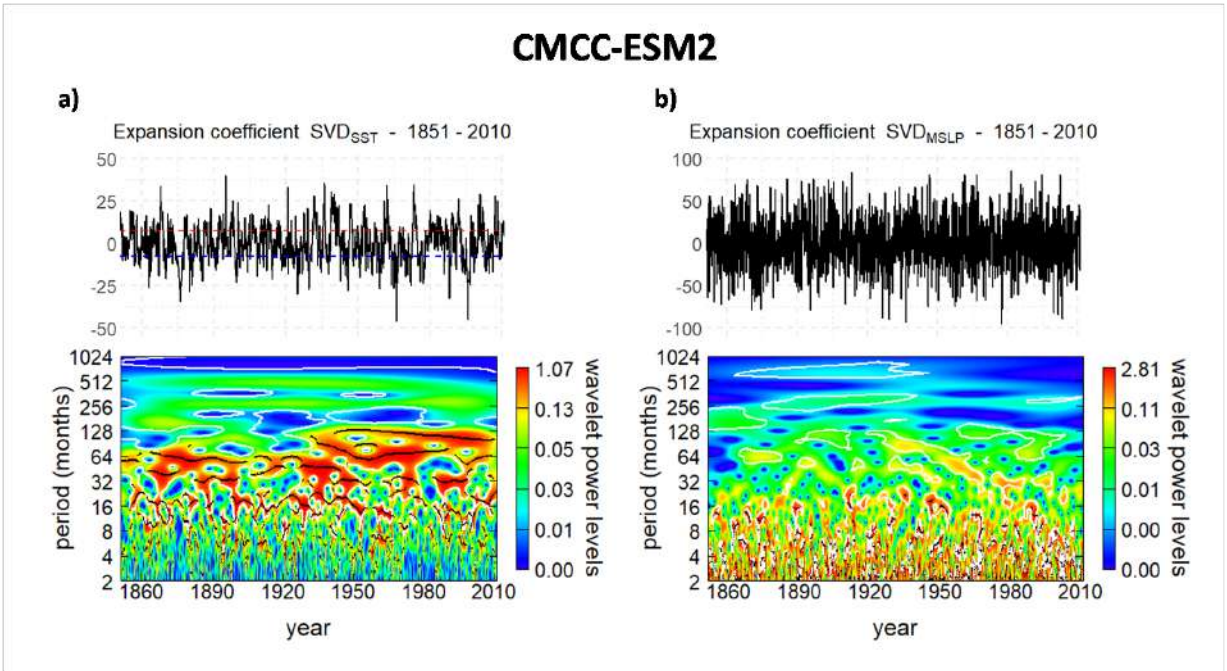

Figure F.1: The same as in Figure 3.45 except for the CMCC-ESM2 model CMIP6 Historical Simulations.

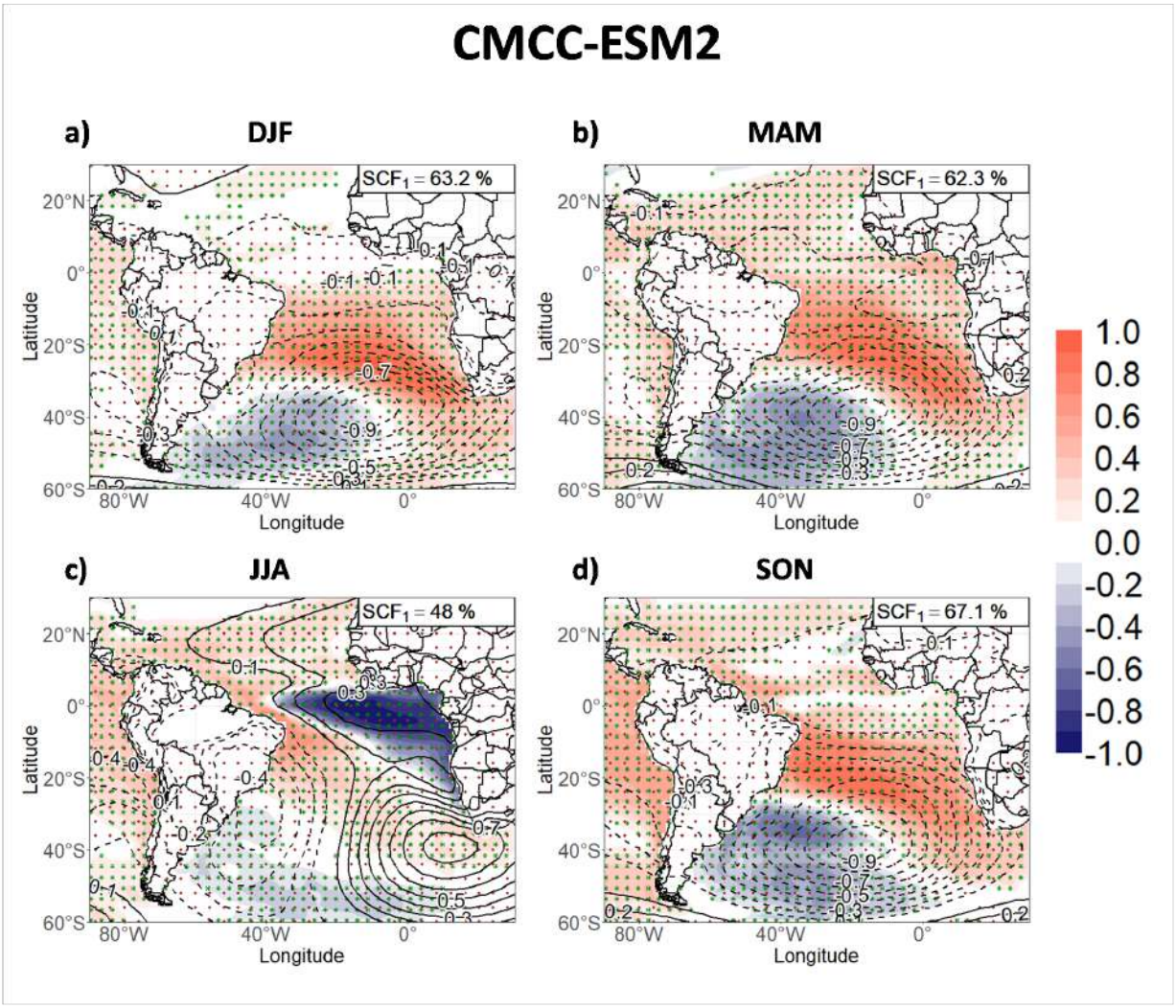

Figure F.2: The same as in Figure 3.7 except for the CMMC-ESM2 model CMIP6 Historical Simulations.

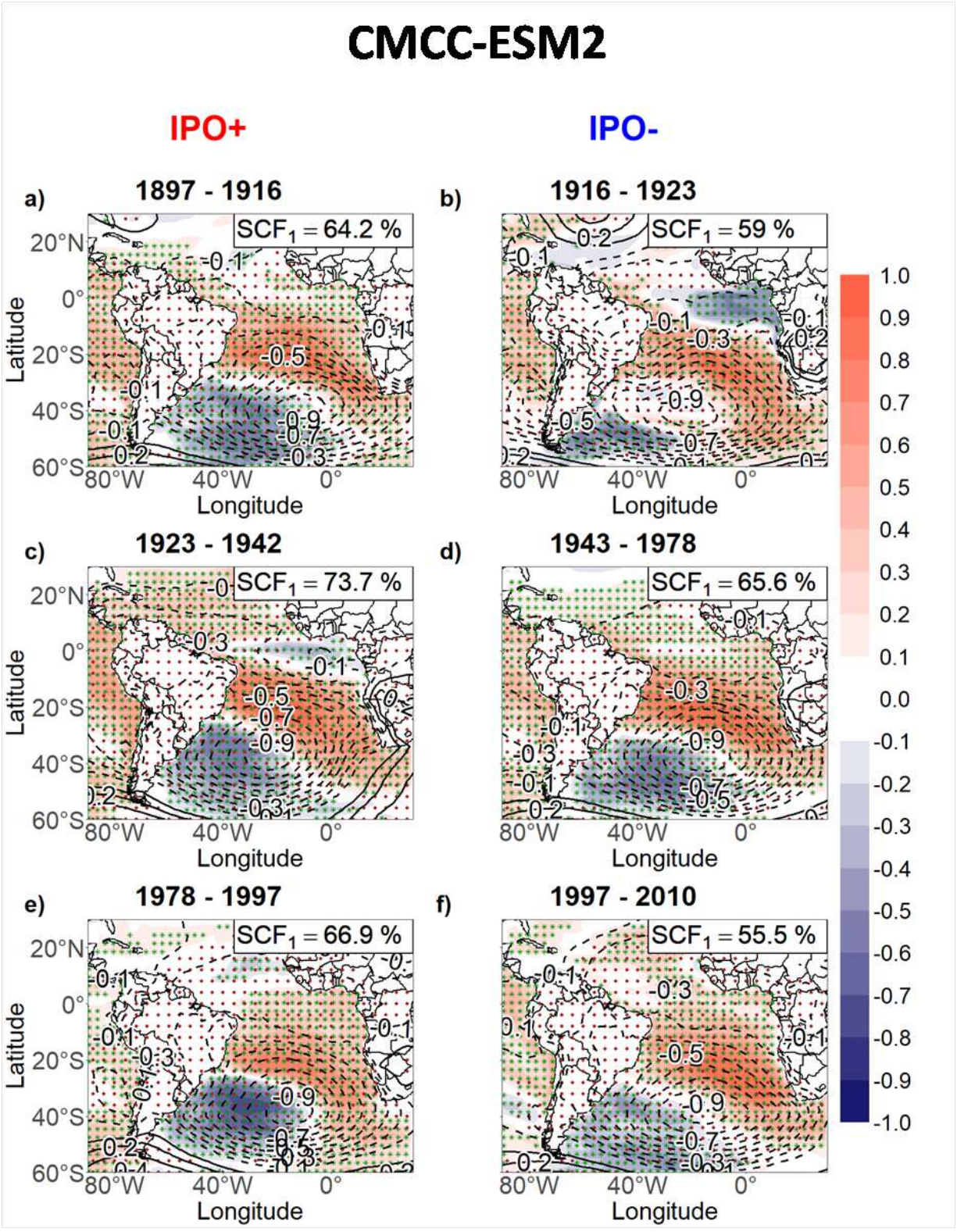

Figure F.3: The same as in Figure 3.14 except for the CMCC-ESM2 model CMIP6 Historical Simulations.

F.2 CMCC-CM2-SR5

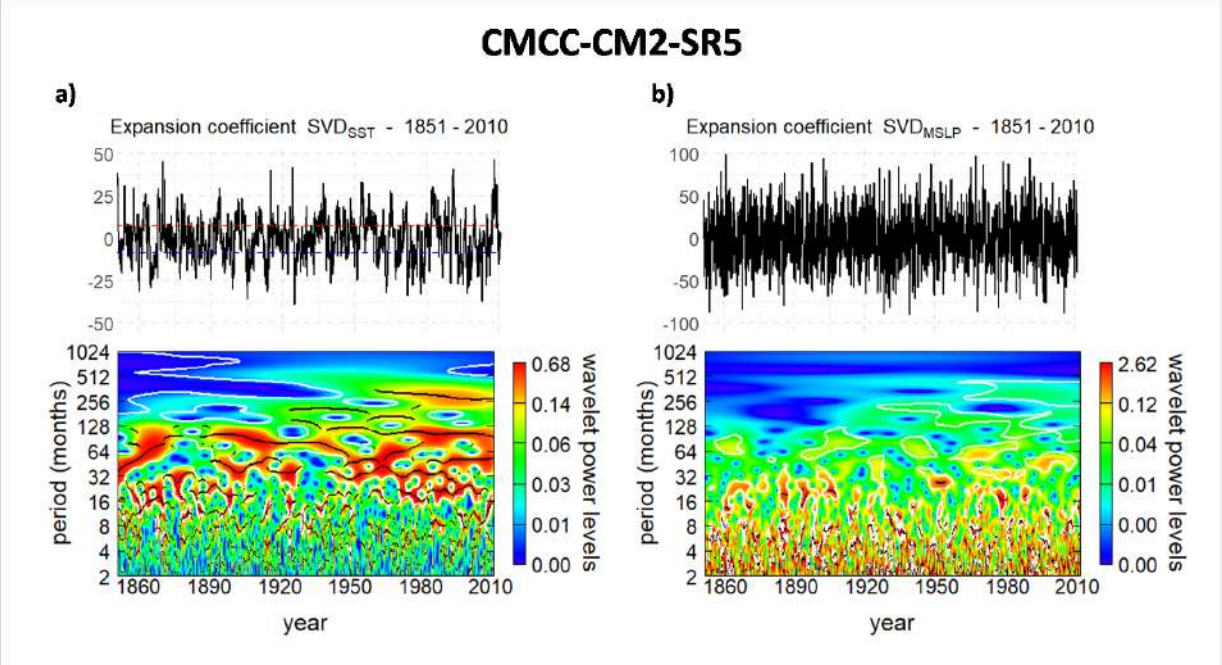

Figure F.4: The same as in Figure 3.45 except for the CMCC-CM2-SR5 model CMIP6 Historical Simulations.

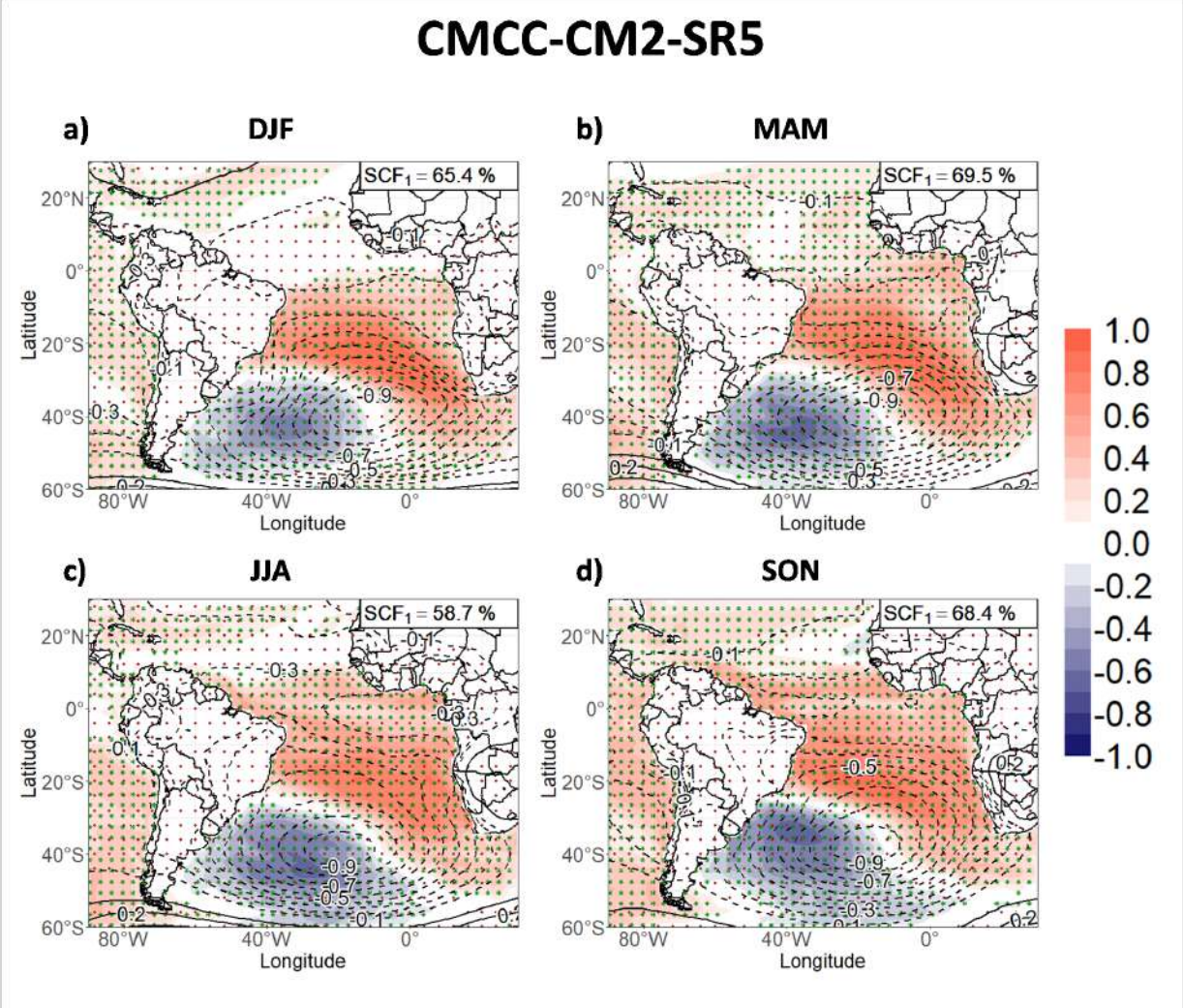

Figure F.5: The same as in Figure 3.7 except for the CMMC-CM2-SR5 model CMIP6 Historical Simulations.

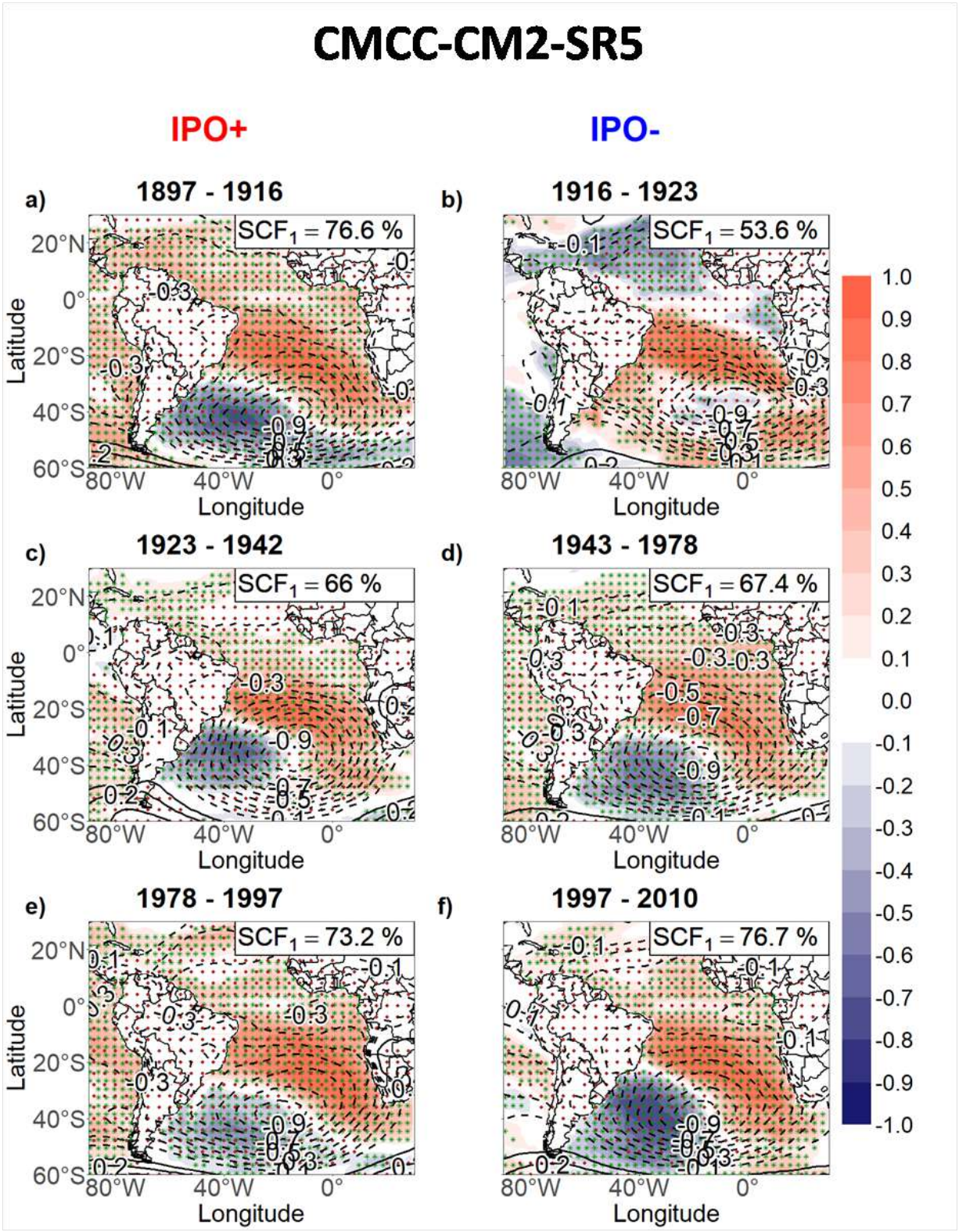

Figure F.6: The same as in Figure 3.14 except for the CMCC-CM2-SR5 model CMIP6 Historical Simulations.

Appendix G

The South Atlantic Dipole: Throughout the 21st century - CMCC-ESM2 and CMCC-CM2-SR5

G.1 CMCC-ESM2

G.1.1 SSP1-2.6

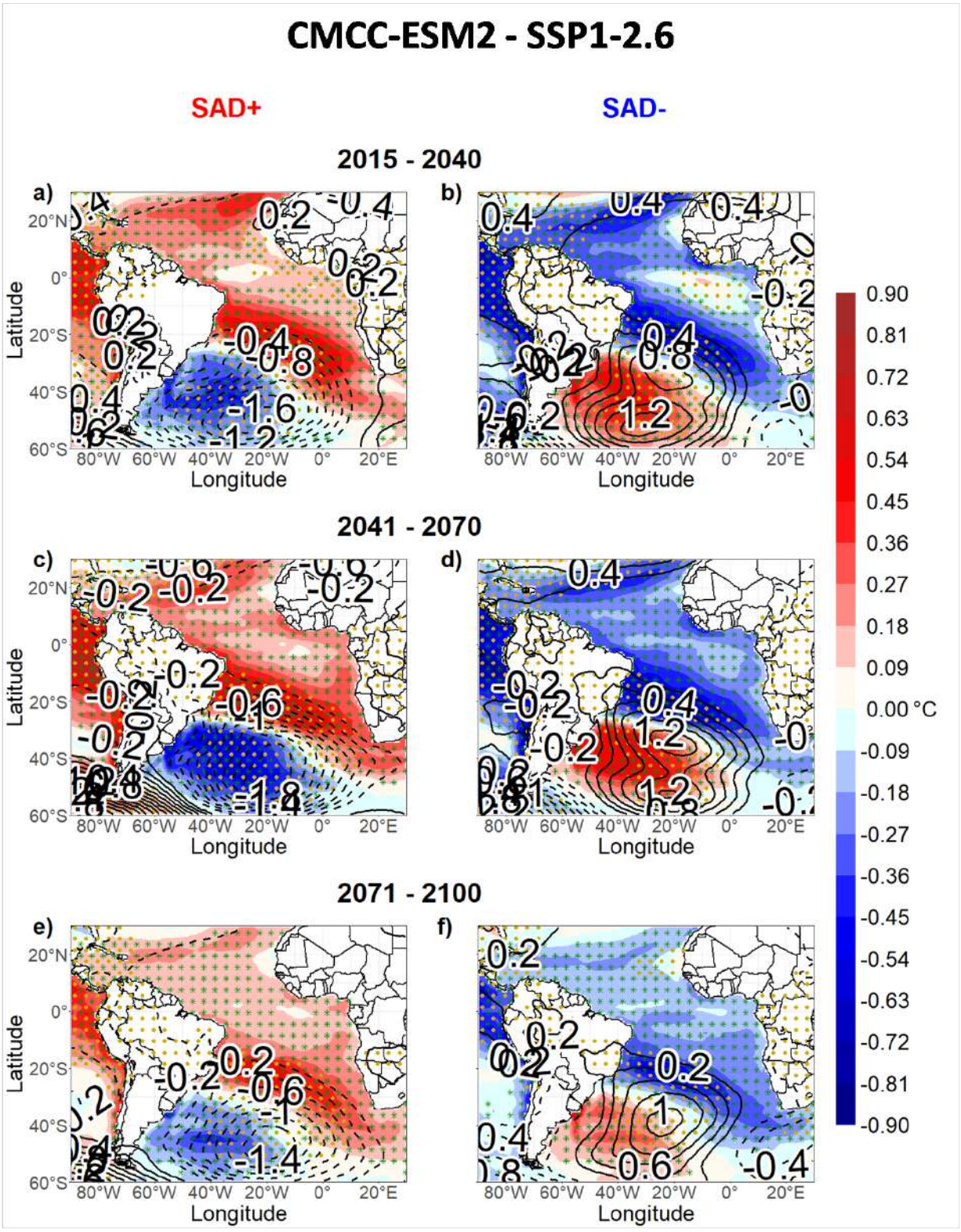

Figure G.1: The same as in Figure 3.50 except for the CMCC-ESM2 model.

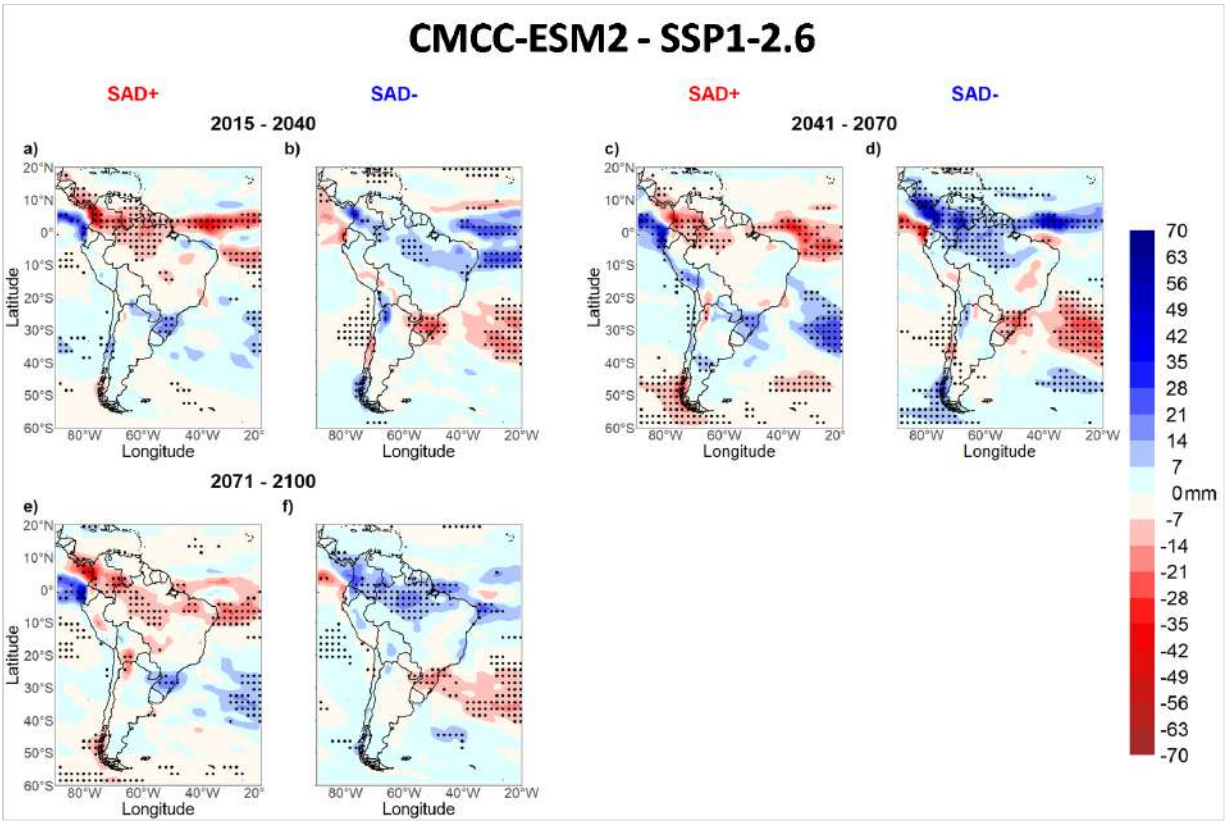

Figure G.2: The same as in Figure 3.51 except for the CMCC-ESM2 model.

G.1.2 SSP2-4.5

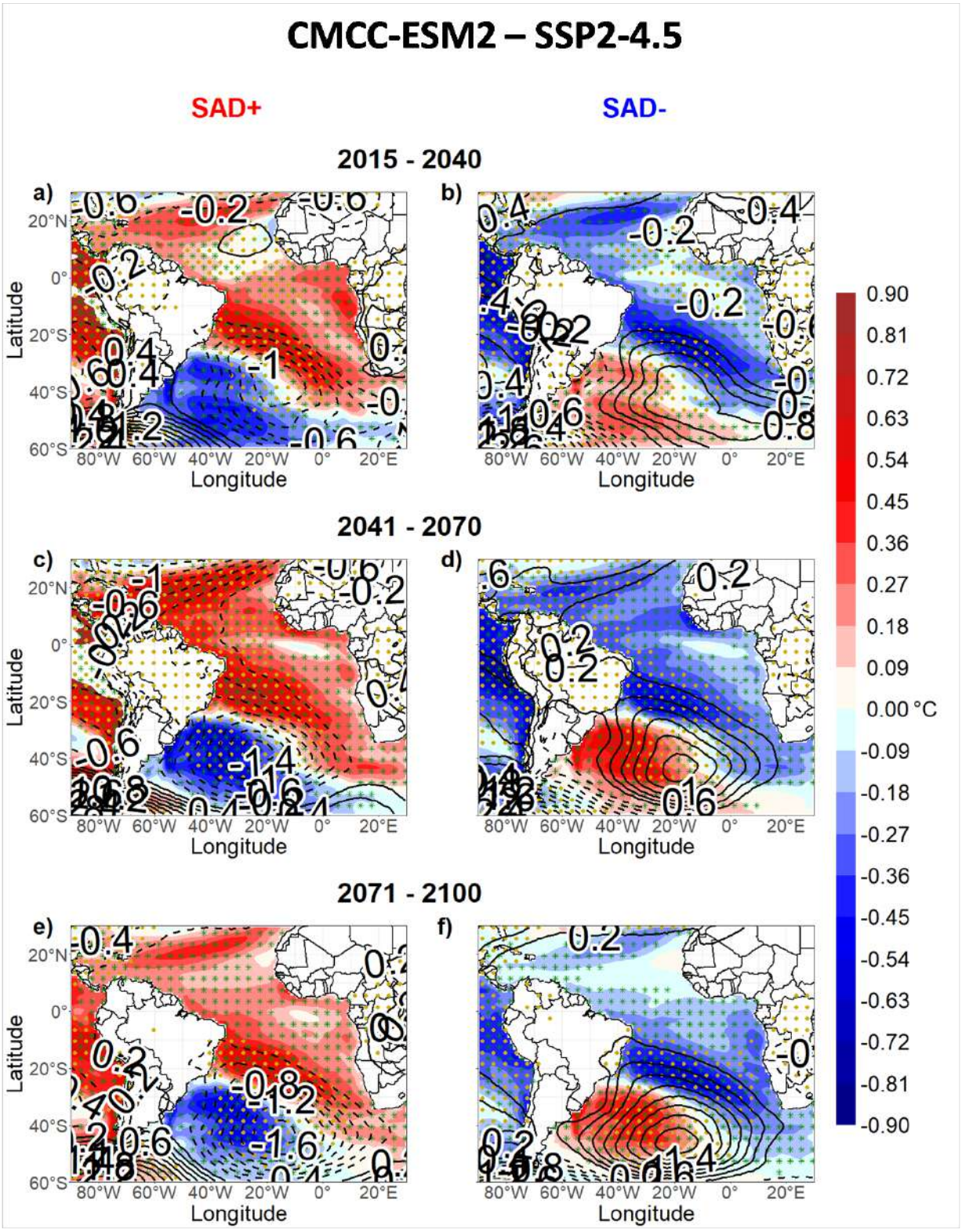

Figure G.3: The same as in Figure G.1 except for the SSP2-4.5 scenario.

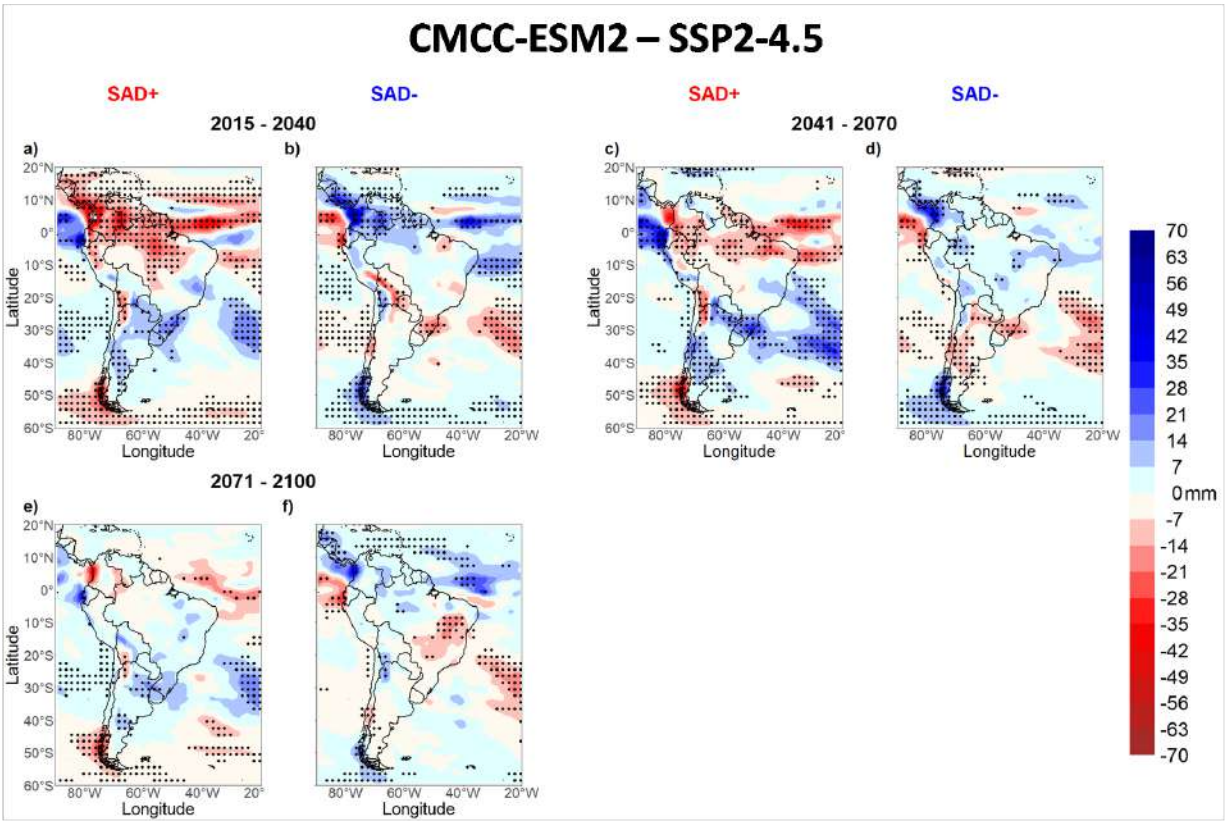

Figure G.4: The same as in Figure G.2 except for the SSP2-4.5 scenario.

G.1.3 SSP5-8.5

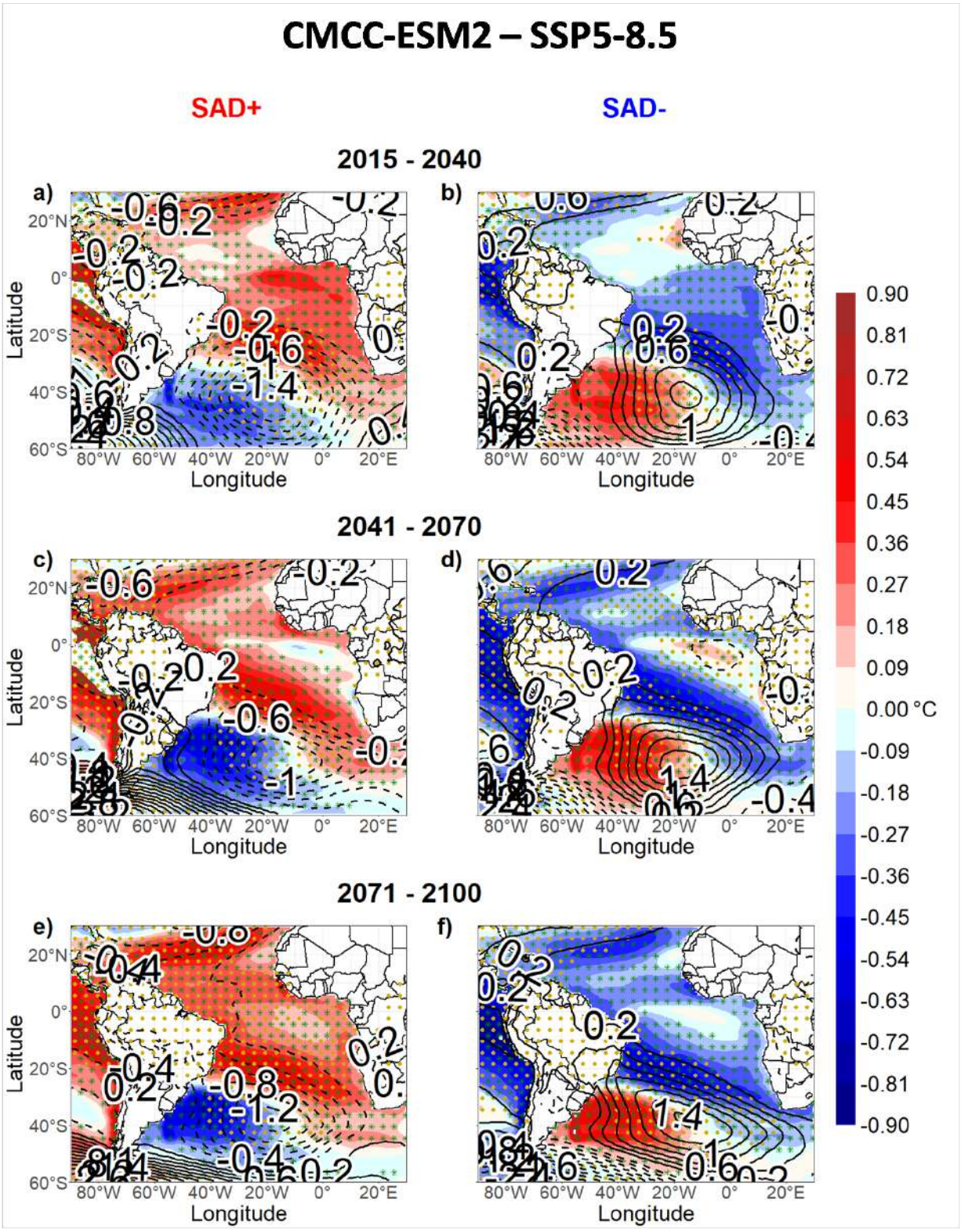

Figure G.5: The same as in Figure G.1 except for the SSP5-8.5 scenario.

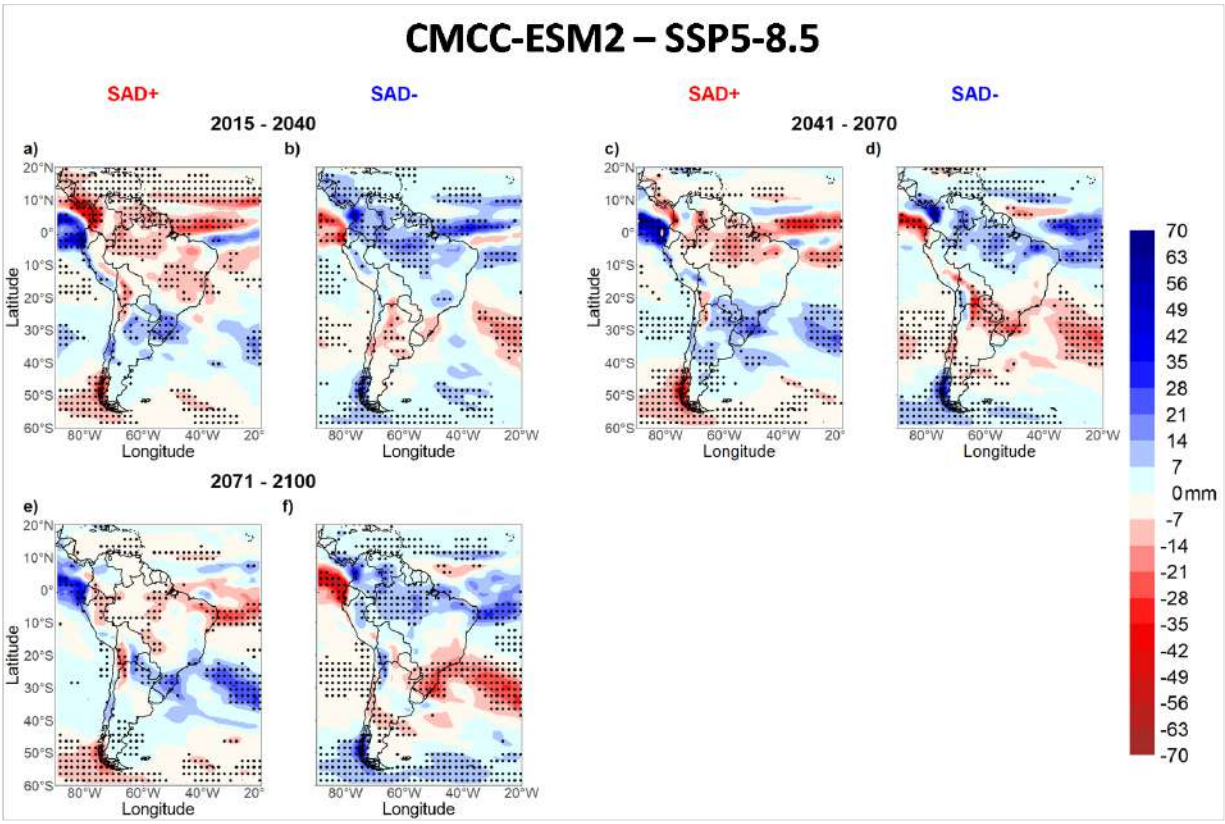

Figure G.6: The same as in Figure G.2 except for the SSP5-8.5 scenario.

G.2 CMCC-CM2-SR5

G.2.1 SSP1-2.6

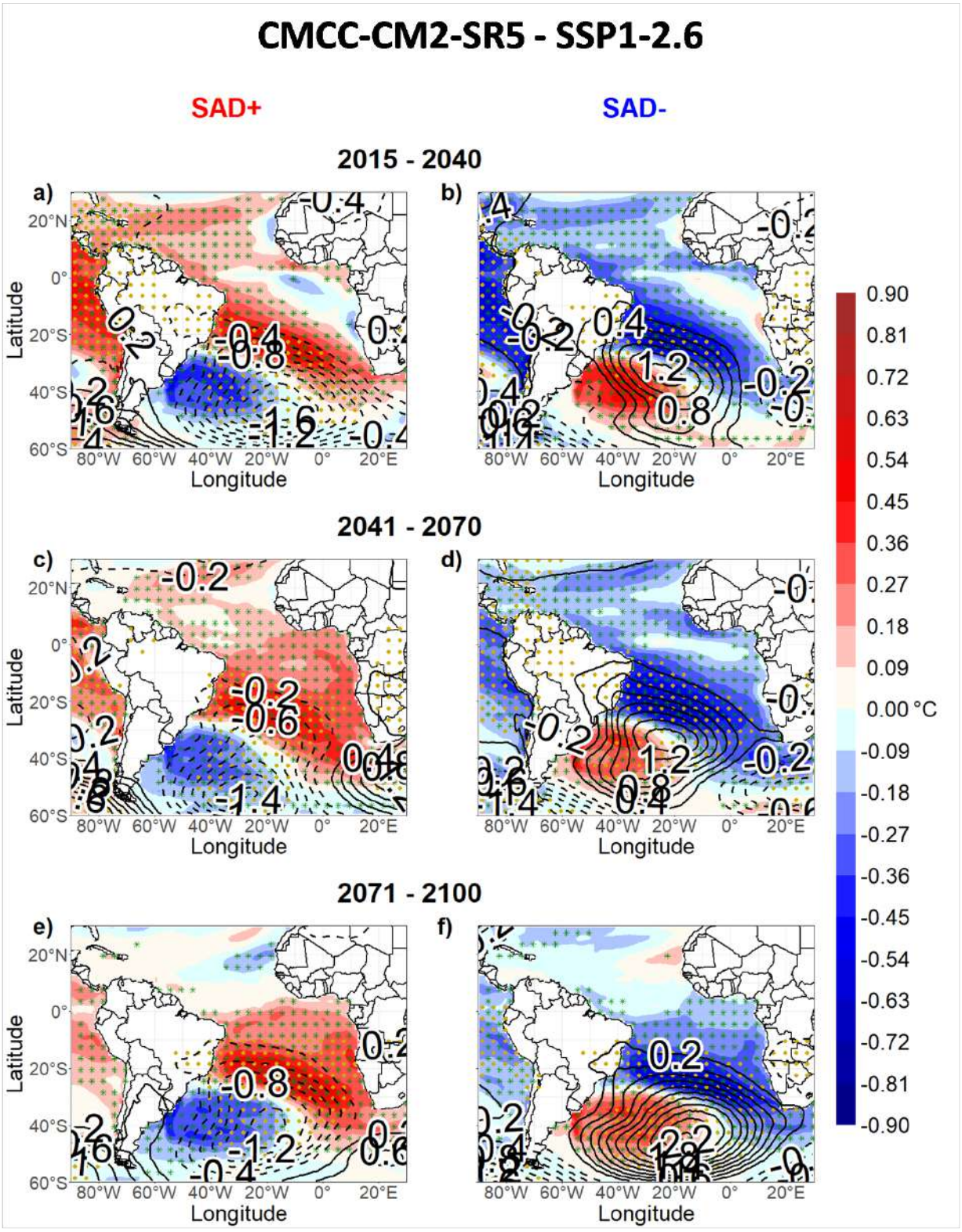

Figure G.7: The same as in Figure 3.50 except for the CMCC-CM2-SR5 model.

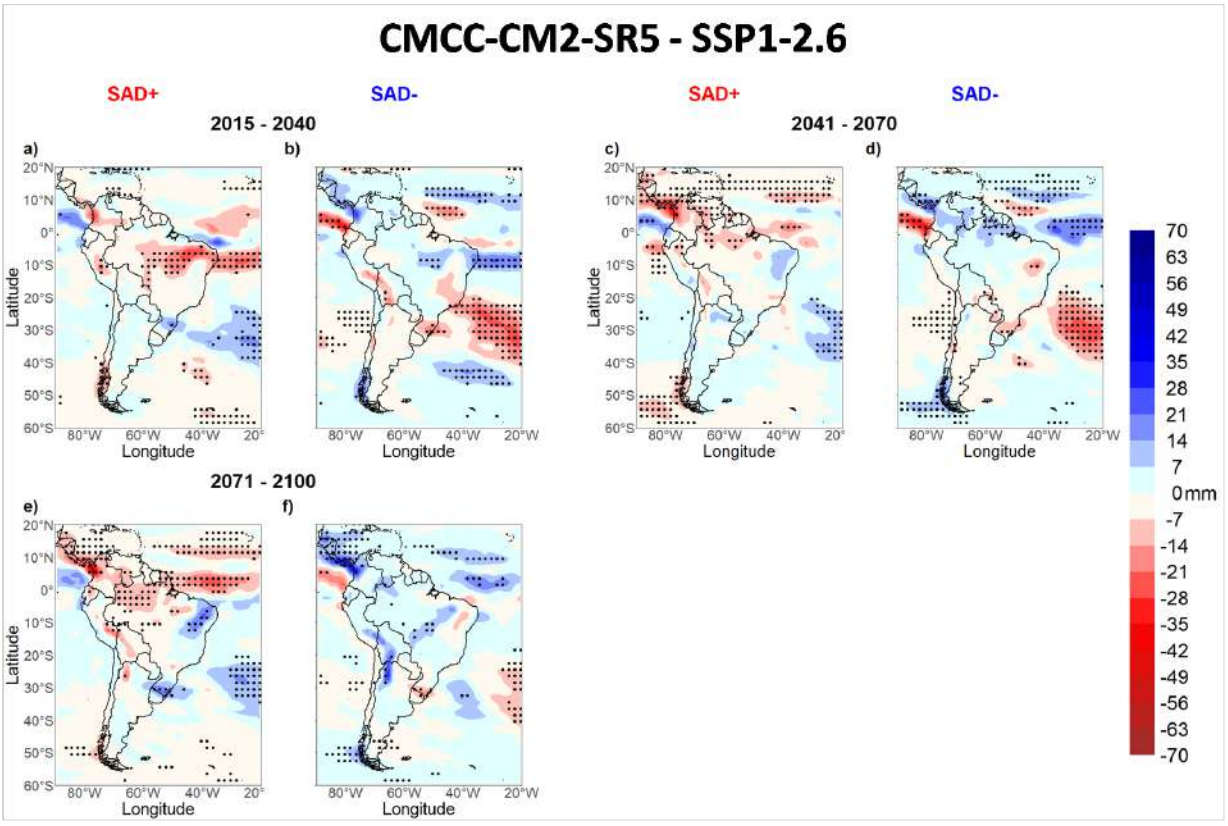

Figure G.8: The same as in Figure 3.51 except for the CMCC-CM2-SR5 model.

G.2.2 SSP2-4.5

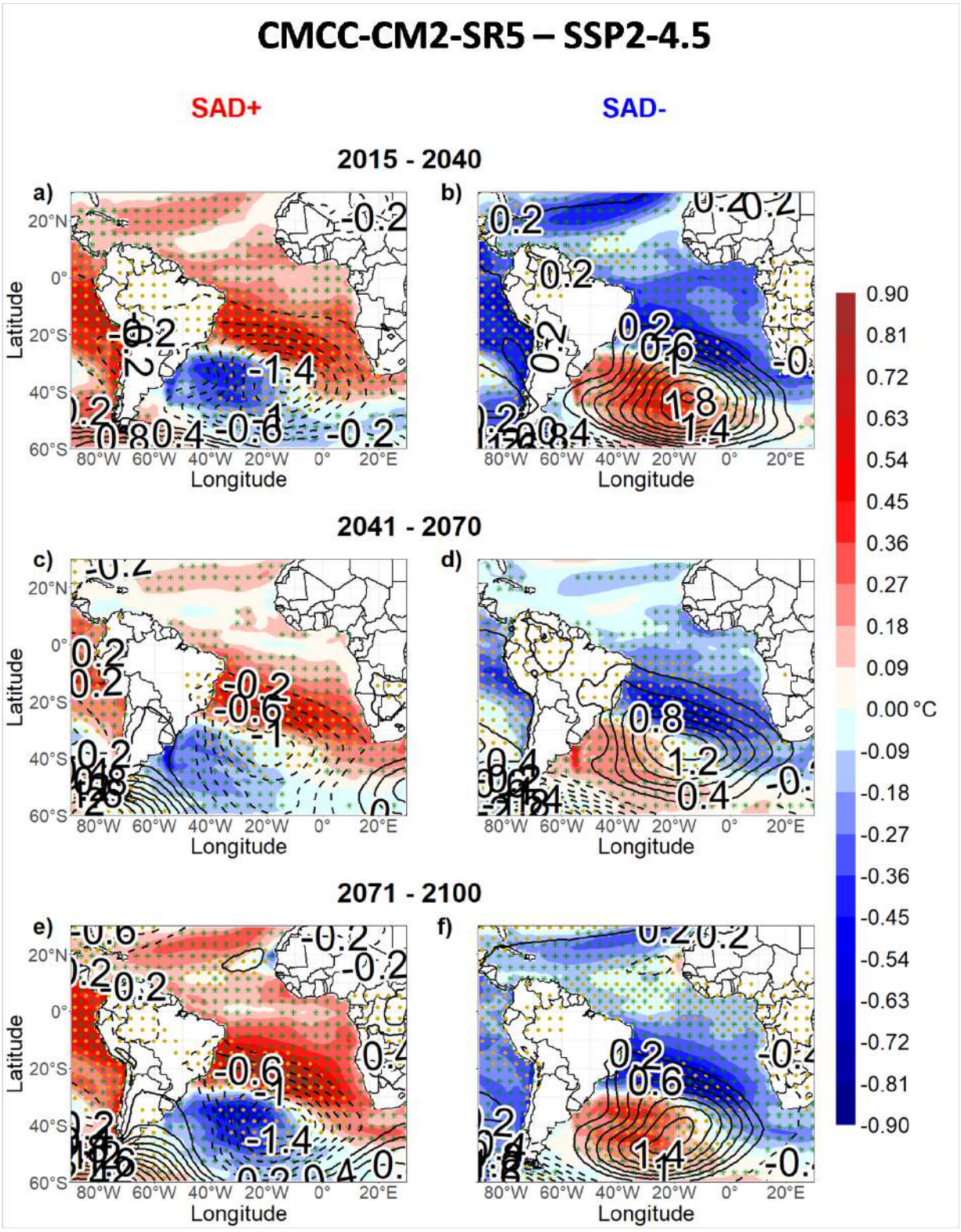

Figure G.9: The same as in Figure G.7 except for the SSP2-4.5 scenario.

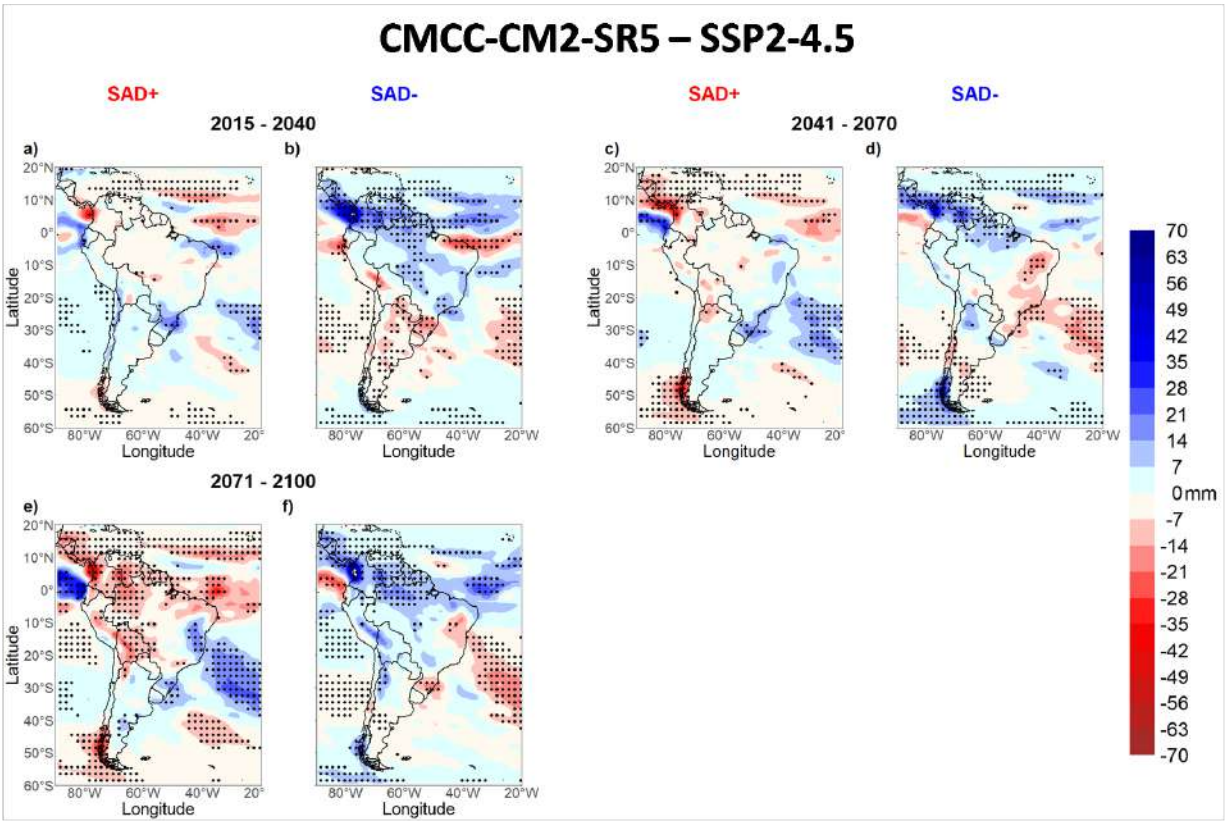

Figure G.10: The same as in Figure G.8 except for the SSP2-4.5 scenario.

G.2.3 SSP5-8.5

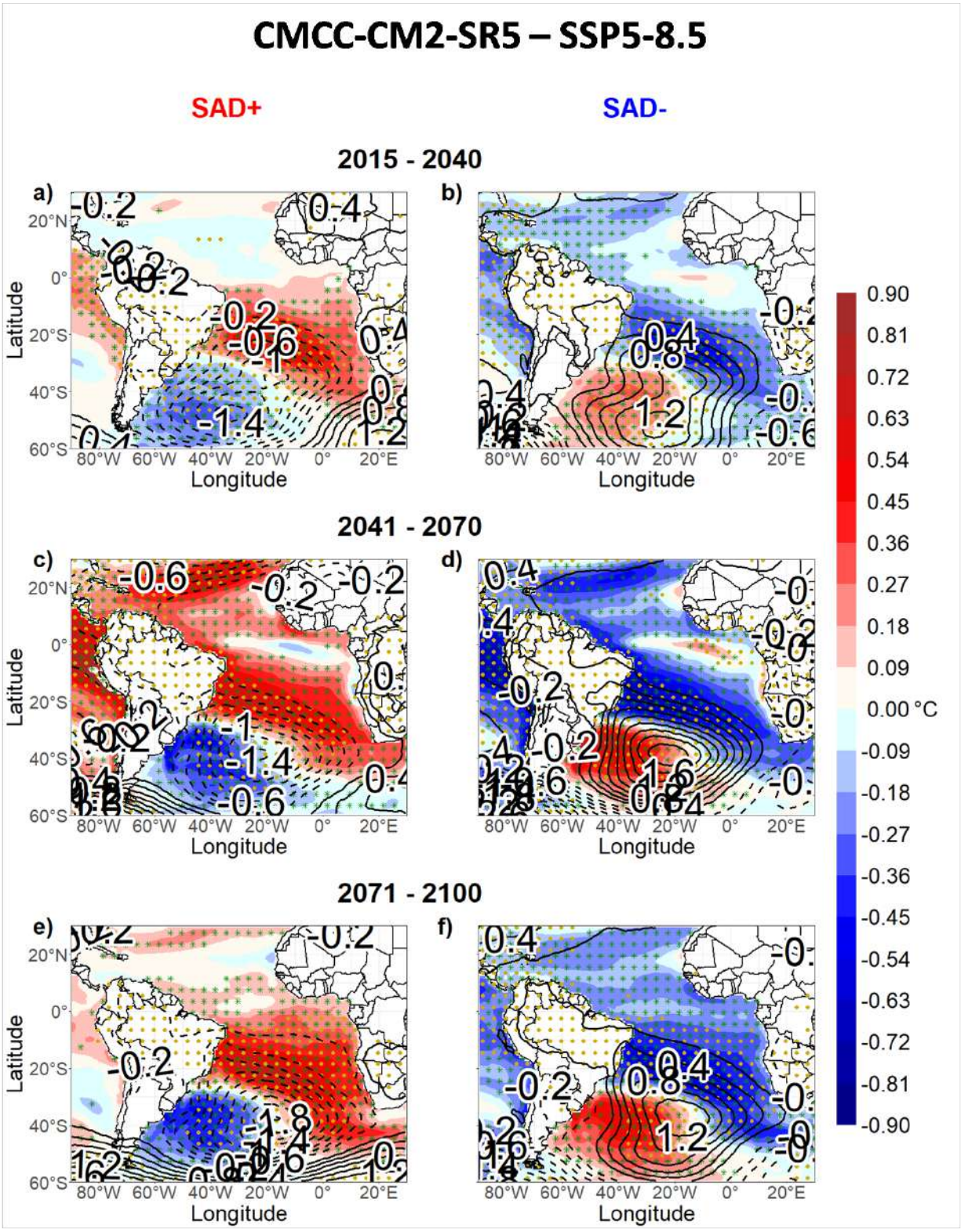

Figure G.11: The same as in Figure G.7 except for the SSP5-8.5 scenario.

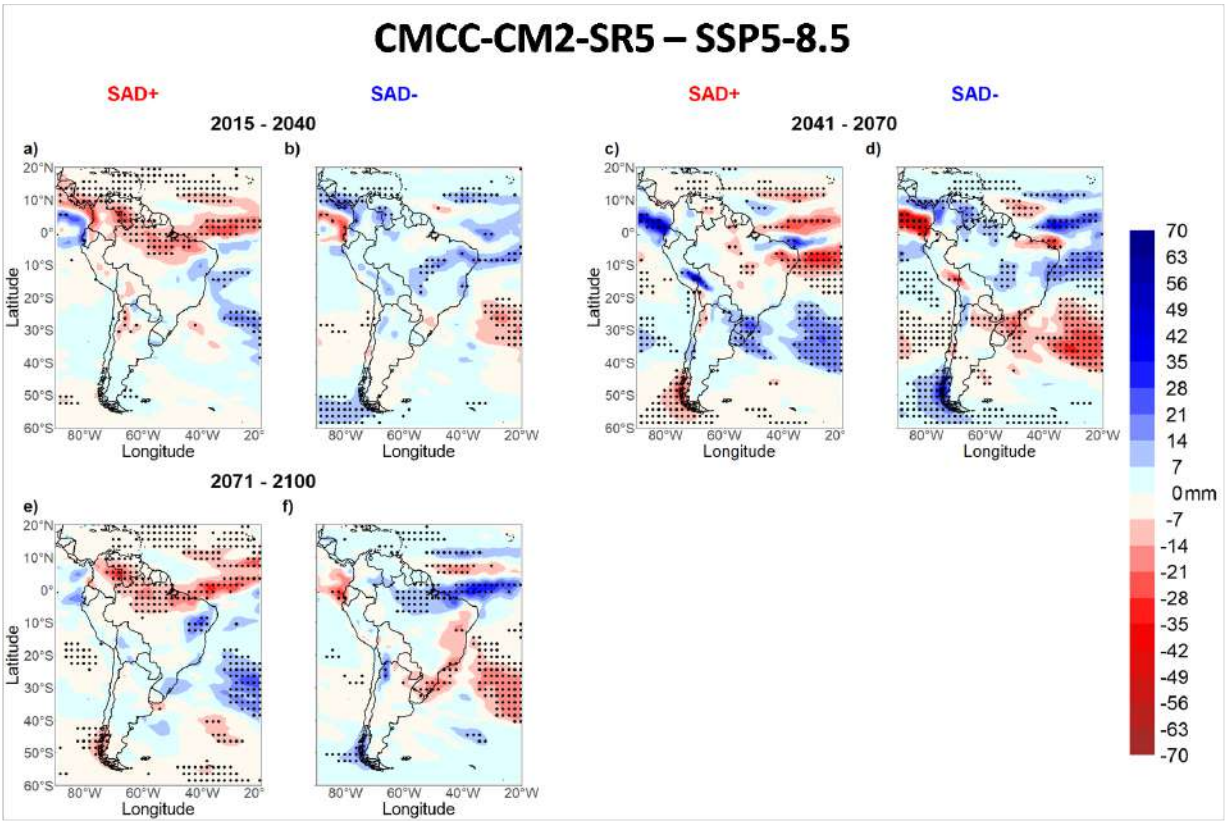

Figure G.12: The same as in Figure G.8 except for the SSP5-8.5 scenario.